Nanotechnology and Chiroptical Spectroscopy to Characterise Optically Active Chiral Metamaterials

By

Nadia Abdulkarim Abdulrahman

MSc. Physical Chemistry

Submitted in the fulfilment of the requirements for the Degree of Doctor of Philosophy in the

School of Chemistry
Collage of Science and Engineering
University of Glasgow

May 2014

Abstract

Work in this thesis involves manipulating the interaction between light and matter in order to retrieve important information from adsorbed molecules, such as their structure and/or function, and henceforth, to gain insight into highly sensitive detection capabilities for biosensor applications. Such manipulation might be achieved via rationalising the surfaces of optically active metamaterials by taking full advantage of the recent growth in a variety of nanotechnology disciplines. As such, the possibility of characterising biomolecules adsorbed on the surface of chiral and achiral plasmonic metamaterials, referred to as *chiral* and *achiral plasmonic nanostructures*, have been investigated. Also, illustration and applications for the so called `Superchiral Field`, which has been generated via circular polarised light (CPL), are presented. Microscopic origin of the chiroptical second harmonic generation (SHG) signal that originates from the surface of the chiral nanostructures has been investigated. Practical visualisation via femtosecond laser beam of regions of intense plasmonic activity, i.e., hot-spot mapping, has been performed. In general, the work described in this thesis involved the use of several linear and non-linear chiroptical techniques namely as extinction (absorption and scattering), CD, ORD and SHG spectroscopy, in addition to scanning imaging namely SEM and AFM microscopy. Given that most biomolecules contain either chiral molecules or adopt chiral structures, the plasmonic nanostructures presented in this work could be used to study a wide range of biological problems, from the structure of biomolecules associated with neurodegenerative illnesses such as Alzheimer's disease and Parkinson's disease, to DNA and viruses. As a regard, general classifications for aspects of chirality are presented in order to emphasise the association of the samples used in this chapter with some of these aspects. All samples are fabricated via Electron Beam Lithography (EBL) in JWNC cleanroom/UK; the associated fabrication techniques, the instruments and the experimental methods are described.

Contents

Abbreviations used in this thesis

Aβ	Amyloid β peptide
AFM	Atomic Force Microscope
APTS	3-Amino-Propyl-Triethoxy-Silane
CARS	Coherent Anti- Stokes Raman Scattering
CD	Circular Dichroism
CPL	Circularly Polarised Light
DNA	Deoxyribonucleic acid
2D	Two Dimensions
3D	Three Dimensions
EBL	Electron Beam Lithography
ECD	Electronic Circular Dichroism
EPL	Elliptically Polarised Light
FEG	Field Emitter Gun
FIB	Focused Ion Beam Lithography
FMN	Flavin Mononucleotide
fs	femto second
FWHM	Full-Width Half-Maximum
HSQ	Hydrogen Silses-Quioxane
IPA	Iso-Propyl Alcohol
IR	Infra- Red
L	Left
LSPR	Localized Surface Plasmon Resonance
MD	Molecular Dynamics
MIBK	Methyl Iso-Butyl Ketone

n	nano
Nd:YAG	Neodymium Doped Yttrium Aluminum Garnet
OA-SHG	Optically Active-Second Harmonic Generation
OR	Optical Rotation
ORD	Optical Rotary Dispersion
PMMA	Poly Methyl Meth-Acrylate
pp	paper page
ps	picosecond
R	Right
R4	Racemic 4
ROA	Raman Optical Activity
RSC	Resist Spin Coating
SDS	Sodium dodecyl sulphate
SE	Secondary Elactrons
SEM	Scanning Electron Microscopy
SERS	Surface-Enhanced Raman Scattering
SH	Second Harmonic
SHG	Second Harmonic Generation
SPPs	Surface Plasmon Poalretions
SPR	Surface Plasmon Resonance
UV	Ultra-Violet
vAC	Voltages Alternating Currents
vDC	Voltages Direct Currents
VRU	Variable Resolution Unit
VCD	Vibrational Circular Dichroism

Publications

1. Induced Chirality through Electromagnetic Coupling between Chiral Molecular Layers and Plasmonic Nanostructures

Abdulrahman N. A., Fan Z., Tonooka T., Kelly S. M., Gadegaard N., Hendry E., Govorov A. O. and Kadodwala M., Nano Lett., 2012, Vol.12, pp (977−983).

NANO LETTERS

Letter

pubs.acs.org/NanoLett

Induced Chirality through Electromagnetic Coupling between Chiral Molecular Layers and Plasmonic Nanostructures

Nadia A. Abdulrahman,[†] Z. Fan,[‡] Taishi Tonooka,[†] Sharon M. Kelly,[§] Nikolaj Gadegaard,[∥] Euan Hendry,*[,⊥] Alexander O. Govorov,*[,‡] and Malcolm Kadodwala*[,†]

[†]School of Chemistry, Joseph Black Building, University of Glasgow, Glasgow G12 8QQ, United Kingdom

[‡]Department of Physics and Astronomy, Ohio University, Athens, Ohio 45701, United States

[§]College of Medical, Veterinary and Life Sciences, Institute of Molecular, Cell and Systems Biology, University of Glasgow, Glasgow G12 8QQ, United Kingdom

[∥]Division of Biomedical Engineering, School of Engineering, Rankine Building, University of Glasgow, Glasgow G12 8LT, United Kingdom

[⊥]School of Physics, University of Exeter, Stocker Road, Exeter, EX4 4QL, United Kingdom

Supporting Information

ABSTRACT: We report a new approach for creating chiral plasmonic nanomaterials. A previously unconsidered, far-field mechanism is utilized which enables chirality to be conveyed from a surrounding chiral molecular material to a plasmonic resonance of an achiral metallic nanostructure. Our observations break a currently held preconception that optical properties of plasmonic particles can most effectively be manipulated by molecular materials through near-field effects. We show that far-field electromagnetic coupling between a localized plasmon of a nonchiral nanostructure and a surrounding chiral molecular layer can induce plasmonic chirality much more effectively (by a factor of 10^3) than previously reported near-field phenomena. We gain insight into the mechanism by comparing our experimental results to a simple electromagnetic model which incorporates a plasmonic object coupled with a chiral molecular medium. Our work offers a new direction for the creation of hybrid molecular plasmonic nanomaterials that display significant chiroptical properties in the visible spectral region.

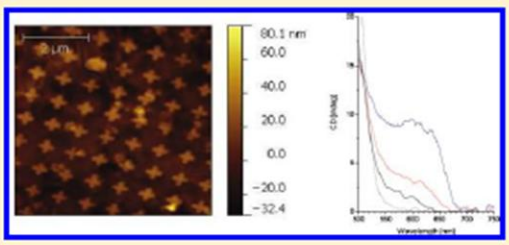

KEYWORDS: *Chiral, plasmonic, metamaterials, optics, nanostructures*

Chiral plasmonic nanomaterials[1−3] are a remarkable new class of engineered materials, whose unique chiroptical properties have been used to create negative refractive index media,[4,5] broadband circular polarisers,[1] and superchiral electromagnetic (EM) fields for ultrasensitive structural characterization of biomaterials.[6] The optical properties of these lithographically created chiral nanostructures are governed by their forms and symmetries (i.e., they are created with very specific shapes which have no mirror symmetry) and are inherently constrained by design. Such nanomaterials can be complex and, particularly in the case of three-dimensional (3-D) chiral structures, difficult to fabricate.[1] Here, we demonstrate a previously unconsidered mechanism by which chiroptical behavior can be induced in the resonances of achiral plasmonic nanostructures, driven by radiative electromagnetic coupling between metallic particle plasmons and a surrounding chiral isotropic medium. This is fundamentally different from previously reported phenomena caused either by orbital hybridization[7−9] or near-field, dipole dipole interactions between chiral molecules and particle plasmons.[10−14] Due to its long range of interaction, the new effect reported here can be three orders of magnitude more effective at inducing circular dichroism (CD) in the absorption resonances of achiral nanostructures than near-field, dipole dipole interactions. As well as discovering a new and interesting fundamental effect, we suggest that the hybrid nanoplasmonic materials studied, once optimized, could be a route to, for example, negative refractive index media. This approach offers flexibility in both fabrication and application of chiral metamaterials by combining the physical engineering of the metal structure with the molecular properties of the dielectric medium in which they are embedded. Crucially, such an approach is not limited by design constraints of the nanostructures themselves.

It has been previously shown[10,11,14] that CD can be induced in plasmonic resonances of spherical particles through short-range coupling between the nanoparticle and a surrounding,

Received: November 17, 2011
Revised: January 11, 2012
Published: January 20, 2012

dx.doi.org/10.1021/nl204055r | Nano Lett. 2012, 12, 977−983

2. The origin of off-resonance non-linear optical activety of a gold chiral nanomaterial.

Nadia A. Abdulrahman, Christopher D.Syme, Calum Jack, Affar Karimuallh, Laurence D.Barron, Nikolaj Gadegaard and Malcolm Kadodwala. The Royal Society of Chemistry, Nanoscale, 2013, Vol.5, pp(12651-12657).

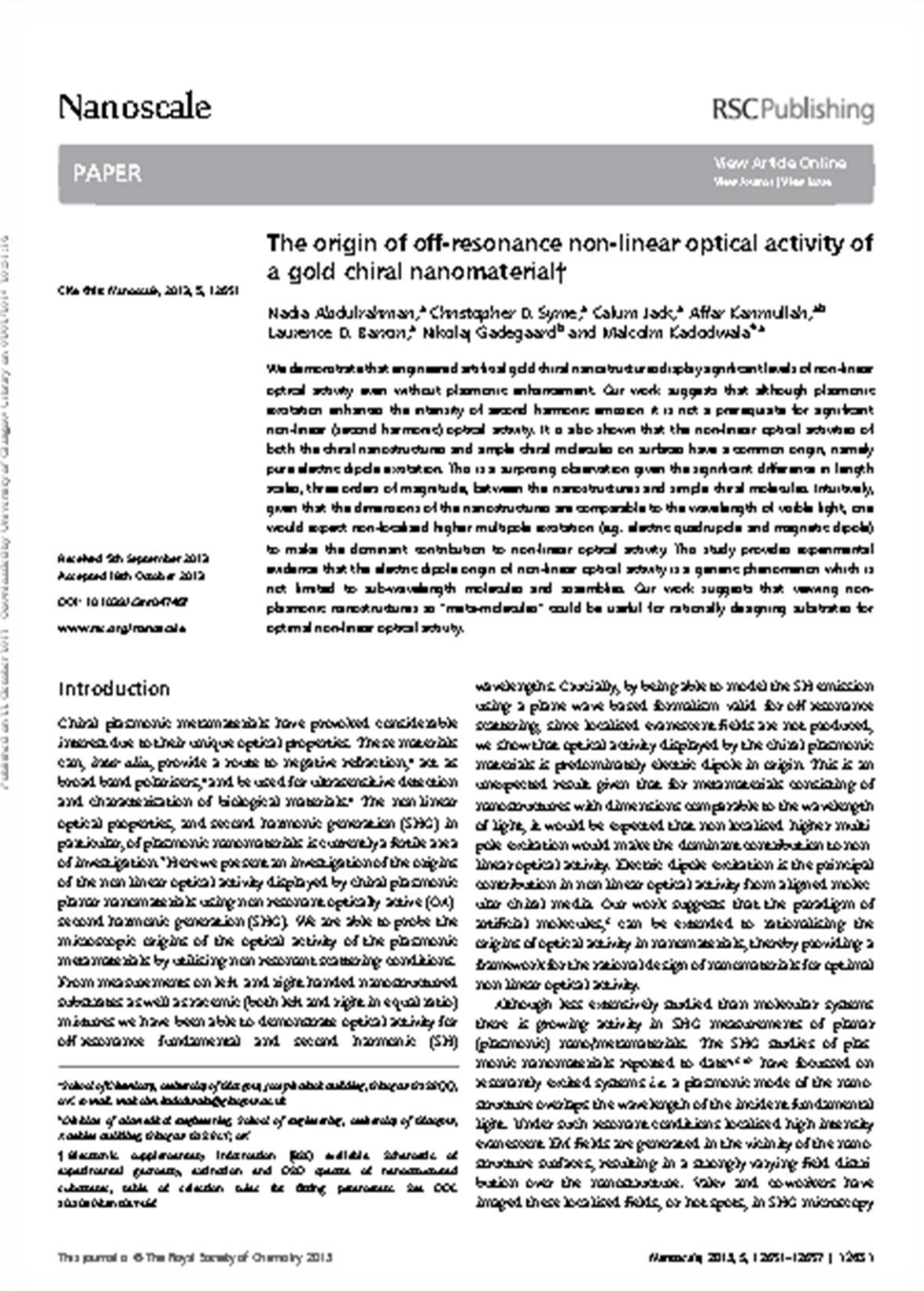

Nanoscale

RSC Publishing

PAPER

View Article Online

View Journal | View Issue

The origin of off-resonance non-linear optical activity of a gold chiral nanomaterial†

Nadia Abdulrahman,[a] Christopher D. Syme,[a] Calum Jack,[a] Affar Karimullah,[ab] Laurence D. Barron,[a] Nikolaj Gadegaard[b] and Malcolm Kadodwala*[a]

Cite this: Nanoscale, 2013, 5, 12651

We demonstrate that engineered artificial gold chiral nanostructures display significant levels of non-linear optical activity even without plasmonic enhancement. Our work suggests that although plasmonic excitation enhances the intensity of second harmonic emission it is not a prerequisite for significant non-linear (second harmonic) optical activity. It is also shown that the non-linear optical activities of both the chiral nanostructures and simple chiral molecules on surfaces have a common origin, namely pure electric dipole excitation. This is a surprising observation given the significant difference in length scale, three orders of magnitude, between the nanostructures and simple chiral molecules. Intuitively, given that the dimensions of the nanostructures are comparable to the wavelength of visible light, one would expect non-localised higher multipole excitation (e.g. electric quadrupole and magnetic dipole) to make the dominant contribution to non-linear optical activity. The study provides experimental evidence that the electric dipole origin of non-linear optical activity is a generic phenomenon which is not limited to sub-wavelength molecules and assemblies. Our work suggests that viewing non-plasmonic nanostructures as "meta-molecules" could be useful for rationally designing substrates for optimal non-linear optical activity.

Received 5th September 2013
Accepted 16th October 2013

DOI: 10.1039/c3nr04746f

www.rsc.org/nanoscale

Introduction

Chiral plasmonic metamaterials have provoked considerable interest due to their unique optical properties. These materials can, inter alia, provide a route to negative refraction,[1] act as broad band polarisers,[2] and be used for ultrasensitive detection and characterisation of biological materials.[3] The non linear optical properties, and second harmonic generation (SHG) in particular, of plasmonic nanomaterials is currently a fertile area of investigation.[4] Here we present an investigation of the origins of the non linear optical activity displayed by chiral plasmonic planar nanomaterials using non resonant optically active (OA) second harmonic generation (SHG). We are able to probe the microscopic origins of the optical activity of the plasmonic metamaterials by utilising non resonant scattering conditions. From measurements on left and right handed nanostructured substrates as well as racemic (both left and right in equal ratio) mixtures we have been able to demonstrate optical activity for off resonance fundamental and second harmonic (SH) wavelengths. Crucially, by being able to model the SH emission using a plane wave based formalism valid for off resonance scattering, since localised evanescent fields are not produced, we show that optical activity displayed by the chiral plasmonic materials is predominately electric dipole in origin. This is an unexpected result given that for metamaterials consisting of nanostructures with dimensions comparable to the wavelength of light, it would be expected that non localised higher multipole excitation would make the dominant contribution to non linear optical activity. Electric dipole excitation is the principal contribution in non linear optical activity from aligned molecular chiral media. Our work suggests that the paradigm of artificial molecules,[5] can be extended to rationalising the origins of optical activity in nanomaterials, thereby providing a framework for the rational design of nanomaterials for optimal non linear optical activity.

Although less extensively studied than molecular systems there is growing activity in SHG measurements of planar (plasmonic) nanophotonic materials. The SHG studies of plasmonic nanomaterials reported to date[4,6–9] have focused on resonantly excited systems i.e. a plasmonic mode of the nanostructure overlaps the wavelength of the incident fundamental light. Under such resonant conditions localised high intensity evanescent EM fields are generated in the vicinity of the nanostructure surfaces, resulting in a strongly varying field distribution over the nanostructure. Yuko and co-workers have imaged these localised fields, or hot spots, in SHG microscopy

[a]School of Chemistry, University of Glasgow, Joseph Black Building, Glasgow G12 8QQ, UK. E-mail: malcolm.kadodwala@glasgow.ac.uk

[b]Division of Biomedical Engineering, School of Engineering, University of Glasgow, Rankine Building, Glasgow G12 8LT, UK

†Electronic supplementary information (ESI) available: Schematic of experimental geometry, extraction and CAD images of nanofabricated substrates, table of calculation values for fitting parameters. See DOI: 10.1039/c3nr04746f

Acknowledgements

I would like to thank my supervisor Dr. Malcolm Kadodwala for his constant assistance and guidance during the course of my PhD. Likewise, I would like to thank my second supervisor Professor Greame Cooke; also my supervisor in the School of Engineering; Dr. Nikolaj Gadegaard and my mentor Professor Stephen Wimperis for their constant assistance, advice and support during my PhD course. A special thank should go to the head of our Chemistry school; Professor James Stephen Clark for his constant assistance, advice and support during my PhD course.

Also, I would like to thank my examiners: Professor Klass Wynne (Chair in Chemical Physics in our Chemistry school) and Professor Christian Johannessen (Professor in Molecular Spectroscopy at University of Antwerp/ Belgium) for their essential suggestions and theoretical corrections.

A special thank also should go to my supervisor in biochemistry section (Life Sciences), Dr. Sharon Kelly, for her constant and generous assistance during my experimental work and my thesis writing, especially for essential training on CD and UV spectroscopy, also for her essential assistance to prepare the fibrils that we used in our studies, as well, for her voluntarily assistant to proof read this thesis. Many thanks certainly should go to research assistant Dr. Christopher Syme for his essential training on SHG, Raman and ROA spectroscopy, also for his general assistance and support during my PhD course, as well as for his assistance in proof reading this thesis. I sincerely thank my colleague Dr. Martin King for his immediate assistance, reliability and constant support during my PhD course, also for his assistance to proof read several chapters in this thesis.

I would also like to thank Professor Euan Hendry from University of Exeter/UK for theoretical simulations associated with electromagnetic modelling for our gammadion-like shapes. Also, I would like to thank Professor Alexander Govorov from University of Ohio/ USA for theoretical simulations and treatment for plasmonic core- chiral shell systems.

Appreciative thanks also go to academics in our school of chemistry, Dr. Adrian Lapthorn and Dr. Justin Hargreaves for effective help to my experimental work and for useful advice on thesis writing. Also, my acknowledgements should go to Stuart Mackay for generous help with computer troubleshooting and IT problems. Also, I would like to acknowledge research assistant Dr. David Turton for his assistance with the sample irradiations using the femtosecond laser beam; I would also like to acknowledge research assistant, Dr. Affar Karimullah for his help with ORD measurements for SHG samples. I would also acknowledge my fellow PhD student, Calum Jack for general help.

My grateful thanks should go to all JWNC staff in Electrical and Electronic Engineering at Glasgow University, especially, Dr. Stephen Thoms for advice in producing high quality nanostructures. Also, many thanks for Mrs. Hellen Mcllen, for extensive training on Plassys II, modefide evaporator, FEI and SEM microscopy. Likewise, for Mr. Robert H Harkins and Mr. Donald Nicolson, for their constant assistance and training on nanofabrication work.

Many thanks to academics and research assistants in Electric and Electronic Engineering in Glasgow University, especially: Dr. Matthew Steer for generous help for training on AFM microscopy, Dr. Rasmus Pederson and Dr. Kevin Docherty for training and assistance for my nanofabrication work. Also, many thanks essentially go to Dr. Kamil Rudnicki for immediate and voluntarily help with my nanofabrication work in general, and for long term accompanying on late working in JWNC, including weekends; accompanying which was essential to satisfy safety and security policy in the JWNC cleanroom.

I could not, and will never be able to, find words to thank my God, ALLAH, for his great gift; this is my family. Many thanks should go to a patient and supportive mother and father; sister and two brothers, it`s much appreciated. Without doubt, great thanks should go to my husband, Dr. Karwan Sahibqran, who suffered for a long time, on daily basis, from a student wife; likewise, my two young daughters, Sarah and Maryam, who suffered, almost five years now, from a student mum. Again, it`s much appreciated. Thanks god for having such a great gift.

Finally I would like to thank the Iraqi government for my PhD scholarship funding. I would also like to thank *Engineering and Physical Sciences Research Council EPSRC*, *BBSRC bioscience* well as *Medical Research Council MRC* for research funding. Surely, I would like to thank Glasgow University for giving me the opportunity to finish my PhD degree within its academia, my great honour.

Author`s Declaration

I declare that, except where explicit reference is made to the contribution of others, that this thesis is the result of my own work and has not been submitted for any other degree at the University of Glasgow or any other institution.

Chapter 1: Introduction

1.1. Overview

Chirality, or handedness, is the key phenomenon of interest in this thesis. The building blocks of life such as DNA, proteins, amino acids, sugars etc. are chiral molecules whose structures are inextricably linked to function. A molecule consisting of four different groups bonded to a central atom is described as a chiral molecule; which cannot be superimposed upon its mirror image. Figure 1 illustrates this concept; the molecule can have right handed chirality referred to as d (also written as (+)- [from *dextrorotatory*. Latin *dexter*: right hand-side]) or left handed chirality referred to as l- (also written as (-)- [from *laevorotatory*. Latin *laevus*: left hand-side]). In addition, Figure 1 illustrates how the absolute configurations (the spatial orientation) of the chiral centre could be assigned, following Cahn-Ingold-Prelog system, to be either R (from *rectus* in Latin meaning right) or S (from *sinister* in Latin meaning left). In principle, the chirality observed in molecules can be attributed to four types of atomic configurations, namely: ***Chiral centre***; ***Chiral axis***; ***Chiral Helix***; and ***Chiral plane***. For ***Chiral centre***, Figure 1 illustrates an example of this configuration which is represented by the tetrahedral C atom. For ***Chiral axis***, when substituents spatially arranged around a fixed axis with a chiral fashion (i.e. the mirror image of the final structure cannot be superimposed on its original one) then this axis is called *chiral axis*. In this case it is not necessary for the substituents to differ. An example of a molecule with a chiral axis is 2,2′-dimethoxy-binaphtyl, shown in Figure 5e. A **Chiral *helix***, can be described as a molecule with a simple helical shape. An example of this element is helicinebisquinone, shown in Figure 5c. For ***chiral plane***: This is `*a structural plane in a molecule with a group substituted in the plane that destroys a symmetry plane perpendicular to the structural plane*` [1 ch3 pp75]. An example of this element is the cyclophane molecule, shown in Figure 2a. In this Figure, without carboxyl group, one could imagine two orthogonal symmetry planes (shown with dashed red lines) both are perpendicular (denoted by the red dot circle) on the plane of the molecule (plane of the page). However, upon attaching the carboxyl group to the benzene ring these two symmetry planes that are perpendicular to the plane of the benzene ring will be destroyed. Here,

the plane of the benzene ring is described as a *chiral plane*. In order to assign the absolute configuration for cyclophane, which follows the R/S system mentioned above, first, we should choose a reporter atom (either above or below the chiral plane) which is an atom that is attached to an atom in the chiral plane, e.g. for cyclophane, the C of methylene chain that lies above the plane of the molecule could be chosen as a reporter atom, see Figure 2b. Then, following the rules of mass priority system described in Figure 1, we should create an arc from the atom attached to the reporter to the atom of the substituted group, and see (view the arc path from the reporter atom toward the chiral plane) if the arc orientation is clockwise or anticlockwise. For cyclophane the orientation of the arc is clockwise and hence, the absolute configuration of this molecule is R, see Figure 2b below [1-5].

Molecules with opposite chirality are described as *enantiomers* which are indistinguishable in terms of physical properties such as density and molecular weight. However, they interact differently and hence become distinguishable, with other chiral objects [6]. As will be explained later, this is a key property of chiral molecules. In this thesis, we used 2D chiral nanostructures which support what is known as *planar chirality*. Figure 3 illustrates how our 2D nanostructures are assigned to be either right handed, (referred to as R) or left handed, (referred to as L). For example for the gammadions, the four arms are equal because they are made out of gold with the same thickness and dimensions, however if we number the end of each arm e.g. starting from number 1 for the first arm (this could be arbitrarily chosen) to end up with number 4 for the fourth arm and then join up these numbers with the dashed arrows we will end up with lines orientating in left-handed fashion or right-handed fashion, see Figure 3a. The actual configuration was evidenced using the CD spectra shown in Figure 73 in chapter 2. For J`s nanostructures which support what we refer to as a *superstructural chirality* (we chose this name in parallel to *Supermolecular chirality* illustrated in Figure 5) we used to number the twisted end for any J by number 1 and the other twisted end for the other J by number 2 and then we join up these numbers with the dashed arrows to end up with lines orientating in left-handed fashion or right-handed fashion, see Figure 3b. Again, this configuration was evidenced using the CD spectra shown in Figure 74 in chapter

2. The G`s nanostructures are another example of superstructural chirality. Here we used to number the negative tone areas (the black areas) in a way similar to that we illustrated in Figure 3c, then by joining up these numbers by the red dashed arrows shown in the same Figure we end up with lines orientating in left-handed fashion or right-handed fashion. This configuration was indirectly evidenced via SHG spectra shown in Figure 4. In this Figure we present SHG spectra for right handed gammadions (R-gammadions (red)) and left handed gammadions (L-gammadions (blue)) as well as for right handed G`s (R-G`s (red)) and left handed G`s (L-G`s (blue)). From this Figure, it is clear that the intensity of SHG signal generated via nanostructures with right handed orientation (for both: G`s and gammadions) are characterised by very similar spectra (Butterfly like shape). Also, the intensity of SHG signal generated via nanostructures with left handed orientation (again for both: G`s and gammadions) are characterised by similar spectra also. The fact that our G`s were deposited on a silicon wafer (i.e. a non-transference surface) means that only spectra that are collected from reflected light could be used to characterise it. Therefore we used the spectra of Figure 4 to evidence the handedness of our G`s since the handedness of our gammadion were clearly evidenced via CD spectra presented in Figure 73 chapter 2. Furthermore, Valve group have evidenced the handedness of these G`s with SHG spectroscopy and SHG microscopy, which are in agreement with our configurations [7].

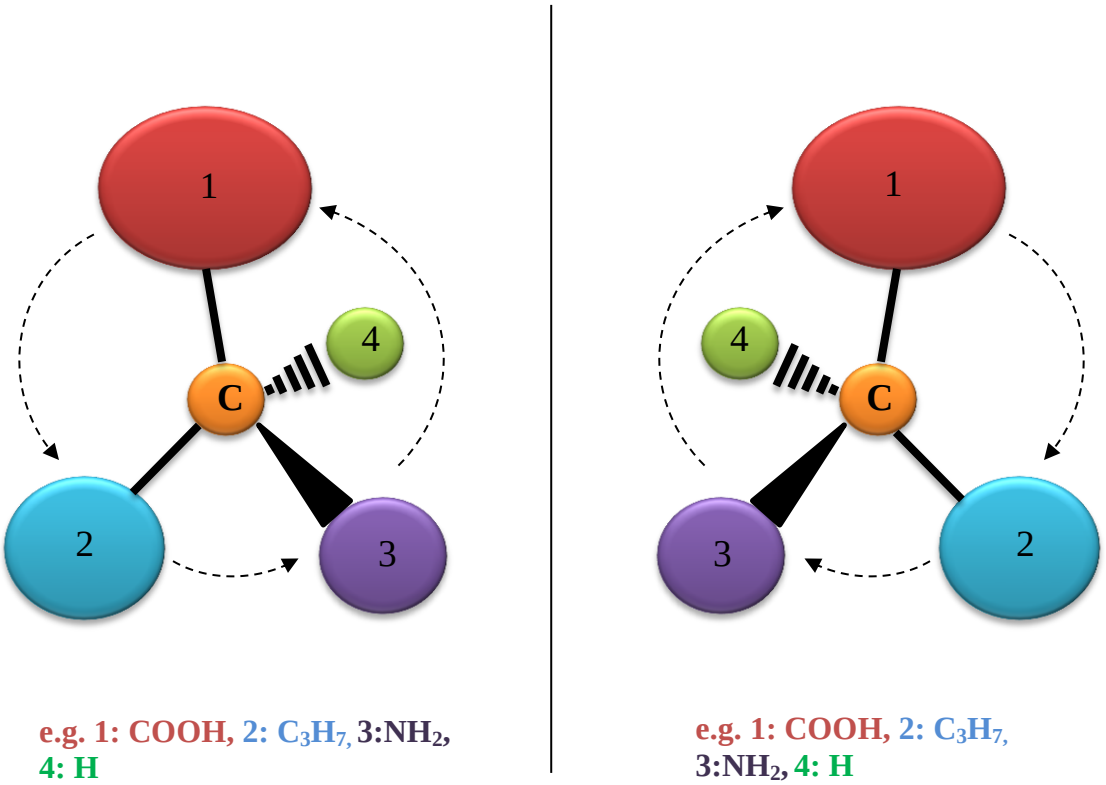

Figure 1: A chiral molecule is a molecule of four different groups, represented here by 1, 2, 3 and 4, these groups are bonded to a central atom (such as tetrahedral carbon), a whole molecule cannot be superimposed upon its mirror image. Different rearrangements for 1, 2, 3 and 4 will end up with only two absolute configurations; these are: an original configuration and its mirror image. The four groups are ordered according to its priority (importance) which is assigned here by the atomic numbers (or atomic masses) of the molecules of these groups, i.e. the most important group is the group with bigger atomic number. Considering the smallest group (i.e. group no.4) being always behind this page, and via joining up the other groups by the dashed arrows shown above one would decide the chiral centre (i.e. C atom) to have a right handed orientation R (from *rectus* in Latin means right) which means to have a molecule being characterised as a d- or (+)- (this is a representation of an optical rotation induced by this molecule for a plane polarised incident light in a clockwise direction) or to have a left handed orientation S (from *sinister* in Latin means left) which means to have a molecule being characterised as an l- or (-)- (this is a representation of an optical rotation induced by this molecule for plane polarised incident light in anti-clockwise direction). Note that R/ S system is used to characterise the chiral centre (which is represented here by C atom), while d-/l- system is used to characterise whole molecule.

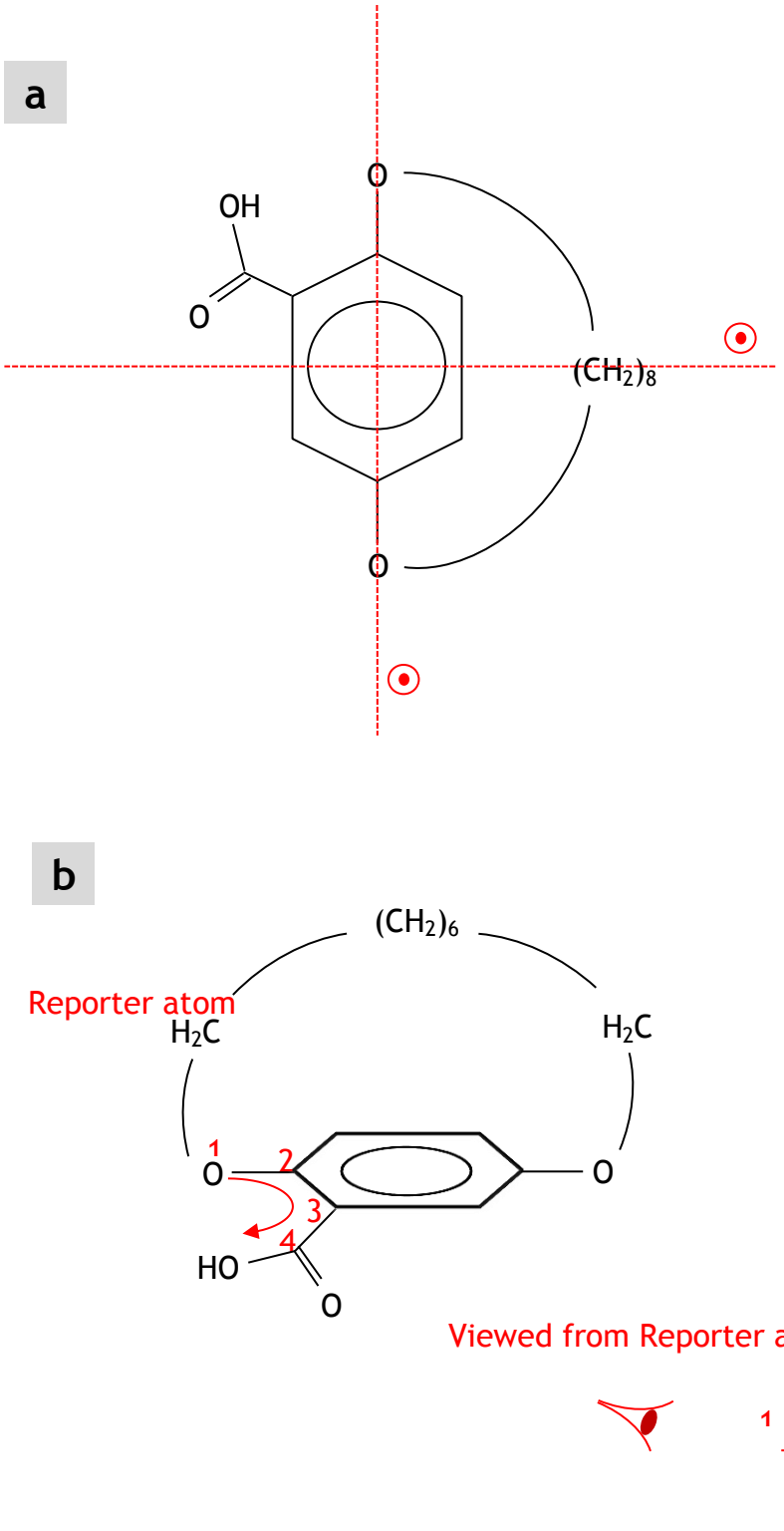

Figure 2: Chiral plane and its absolute configuration for cyclophane. **a** shows the molecule with two perpendicular (denoted by the red dot circle) planes (red dashed lines). **b** shows the chiral plane which is the plane of the benzene ring. Note how Carboxyl group attachment destroys the two perpendicular symmetry planes. The absolute configuration of the chiral plane could be assigned via R/S system if one viewed the arc path from the reporter atom.

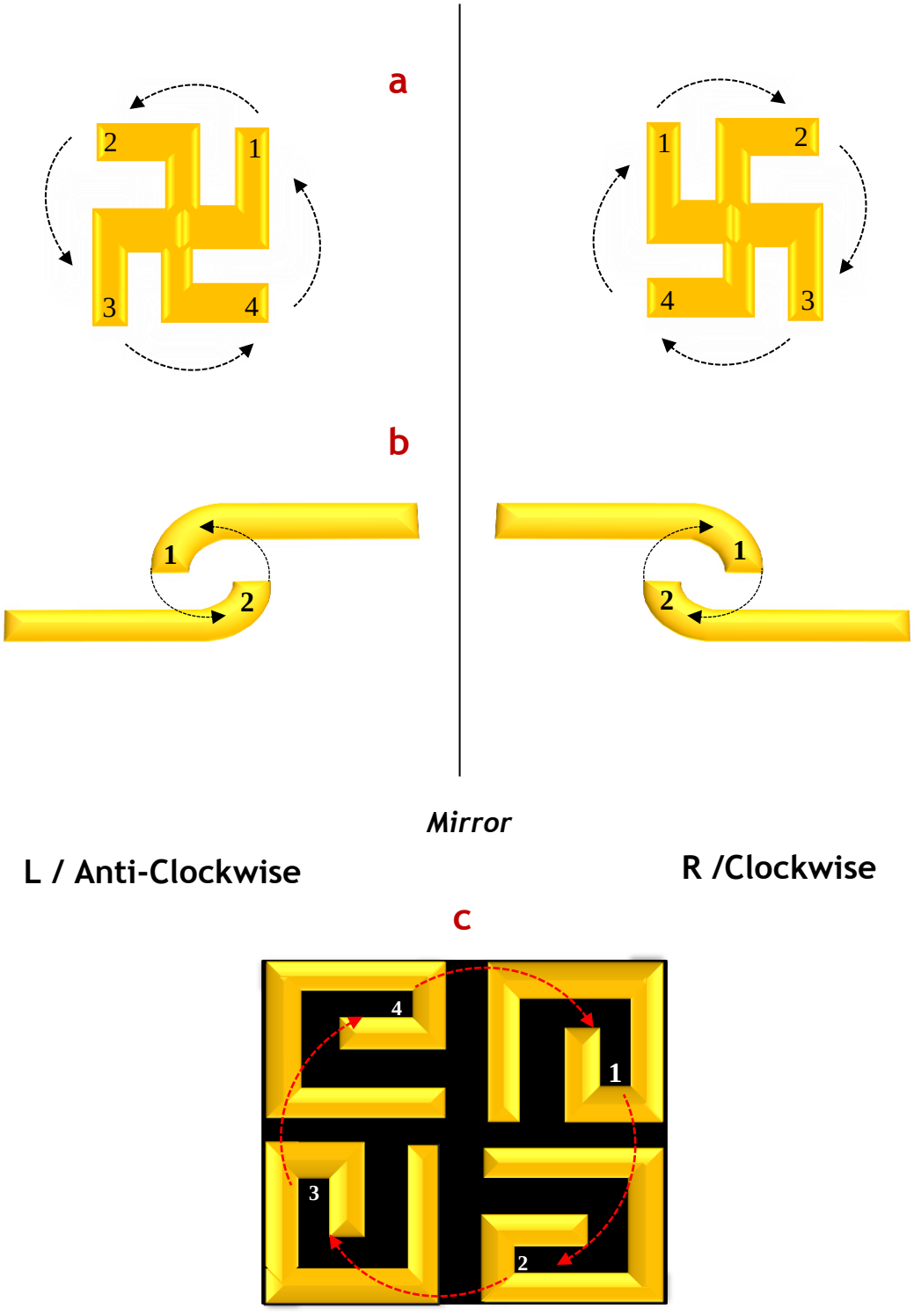

Figure 3: Our methodology to determine the chirality of our nanostructures. **a** illustrates how the four arms of the gammadion could be numbered and joined up by the black arrows to end up with either right handed handedness (R) or left handed handedness (L) configuration. **b** illustrates how the two twisted ends of the J`s nanostructures could be numbered and then joined up by the black arrows to end up with either right handed handedness (R) or left handed handedness (L) configuration. **c** illustrates how the negative tone areas (the black areas) for the G`s nanostructures could be numbered and then joined up by the red arrows to end up with either right handed handedness (R) or left handed handedness (L) configuration.

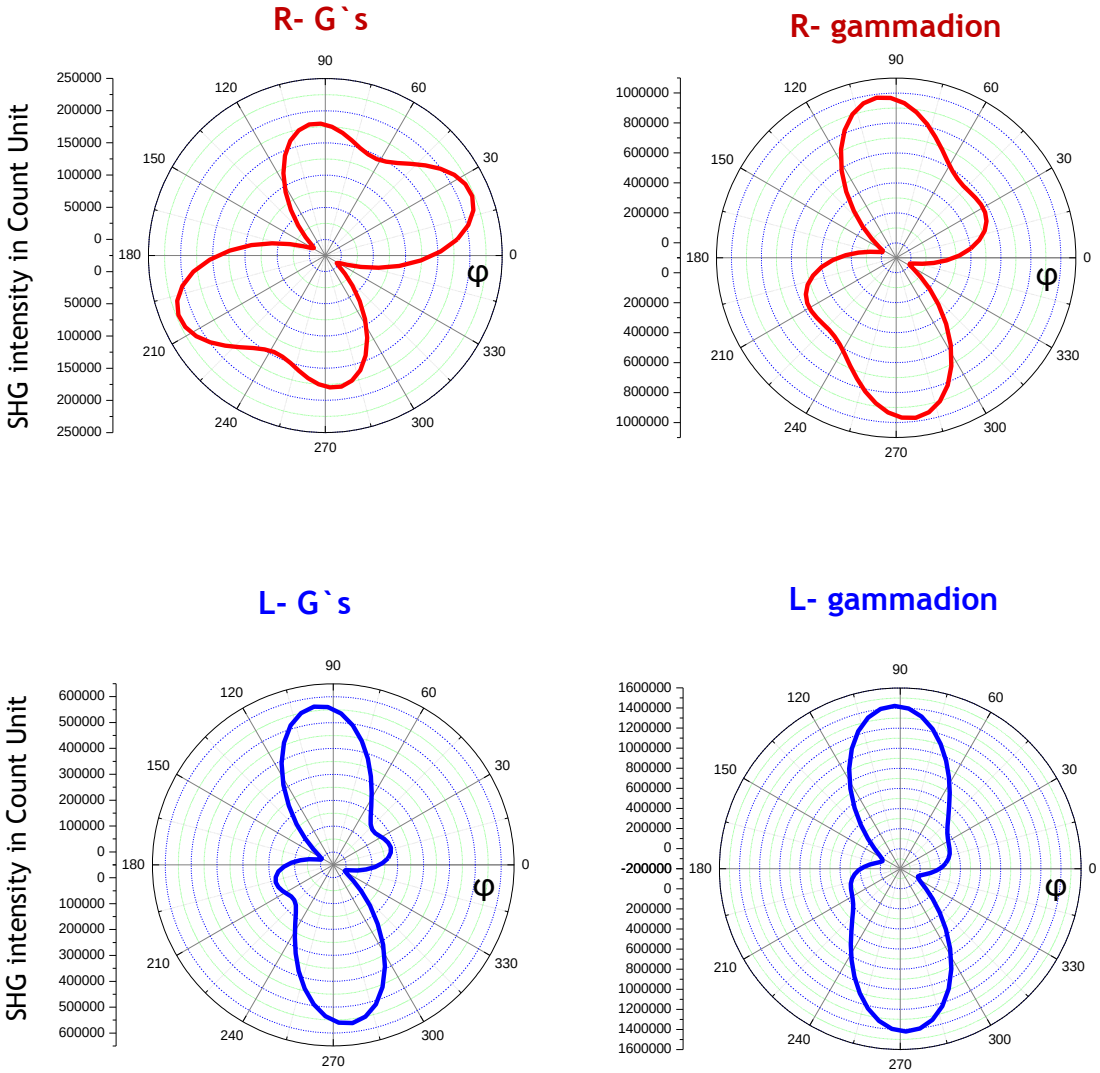

Figure 4: SHG spectra for right handed gammadions(R-gammadions (red)) and left handed gammadions (L-gammadions (blue)) as well as for right handed G`s (R-G`s (red)) and left handed G`s (L-G`s (blue)). Clearly, nanostructures with right hand handedness have very comparable spectra (Butterfly like shape). Similarly, nanostructures with left hand handedness have very comparable spectra.

An increasing number of spectroscopic techniques that are sensitive to chirality have emerged in recent years e.g. OR, ORD, CD (or ECD), VCD and ROA (or VROA) [1-3]. Chirality is also a key property in the pathogenic detection of biological species that are associated with amyloidal diseases, such as Alzheimer's disease and Parkinson's disease [8]. Chirality is also of significant interest in the pharmaceutical and drug industries, particularly due to the difference in physiological activity of different enantiomers. For instance, thalidomide is a drug that was used against morning sickness and was administrated to pregnant women, however only one enantiomer had the desired therapeutic effect, while the other enantiomer linked itself to the DNA of the growing foetus and inhibited the development of limbs, causing a spate of birth defects. Also, ethambutol is a drug that was administrated to patients with tuberculosis; however its enantiomer caused blindness. Therefore, the characterisation of optically pure molecular compounds, i.e. single enantiomer molecular compounds, is essential in the pharmaceutical and drug industries [9]. In essence, the characterisation of optically pure molecular compounds means to gain insight into the chiroptical effect associated with chiral compounds. Chiral plasmonic nanostructures are potentially useful platforms to sense chiroptical effects. As such, chiral plasmonic nanostructures are of considerable interest and this is one of the main reasons for the work described in this thesis.

In order to investigate the chiroptical properties of chiral molecules, one may transpose the concepts of natural chirality to artificial nanostructured surfaces. In principle, the general concepts of chirality (natural and artificial) have been termed in six classes so far, namely as: ***helical* chirality/propellers**, ***helical chirality/spirals***, ***chiral coupling***, **supermolecular chirality**, ***pseudo/extrinsic chirality*** and ***chiral scaffolds*** [7, 9-23]. The work in this thesis is associated with the first four classes only. In principle, ***Helical chirality/propellers*** is when the overall aspect shows a shape of a three-armed helix e.g. perchlorotriphenylamine (Figure 5 a), or, a shape of a four armed helix e.g. our left and right handed gammadions (Figure 5 b), likewise, examples are shown in references [9-11]. ***Helical chirality/spiral*** is when the molecule is expanded over its spiral span e.g. helicinebisquinone (Figure 5 c), as well as our G-like shapes (Figure 5 d); more examples are shown in references [7,9,12]. ***Chiral coupling*** applies when two achiral elements are coupled to exhibit a chiroptical

effect. e.g. 2,2′-dimethoxy-binaphtyl (Figure 5e) and our J-like shapes (Figure 5 f), again, more examples can be found in references [9, (13-15)]. ***Supermolecular chirality*** applies when at least two chiral elements are coupled to exhibit a chiroptical effect e.g. the DNA double helix, and also if molecules in 5c are stacked in a super-chiral fashion (Figure 5 g), likewise for quadric units of our right-handed G-like shapes (Figure 5 h), again, more examples are found in references [9,13,16]. ***Pseudo and/or extrinsic chirality*** is shown when the geometry of the experimental setting is arranged for a chiral environment. As such, it is required to have the wave vector $\hat{k}$, the surface normal $\hat{n}$, and the light polarization vector $\hat{s}$ arranged together to exhibit pseudochirality, as shown by 2-docosylamino-5-nitropyridine molecules (Figure 6 a) [9, 17], or further, to exhibit extrinsic chirality which was shown in split ring nanostructures (Figure 6 b) [9, 18], and more examples can be found in references [9, 19]. Finally, ***chiral scaffolds*** are blocks consisting of chiral and achiral elements, here either the chiral molecules bind to a cluster of the nanoparticles to enhance the optical chirality of the cluster (Figure 6 c) [9, 20], or oppositely, the nanoparticles are binding to helical molecules, such as strands of DNA, to follow its chiral arrangement (Figure 6 d) [9, 21], otherwise, 3D chiral metamaterials are driven to large scale self-assembling scaffolds to have nanostructures with gyroid networks (Figure 6 e) [9, 22, 23].

Generally speaking, the work of this thesis has been presented in seven different chapters; including this one. In chapter 2, the nanofabrication work is presented. Nanofabrication work was carried out in the James Watt Nanofabrication Centre (JWNC) cleanroom facilities at Glasgow University/UK. Samples (i.e chiral and/or achiral plasmonic nanostructures) were fabricated via Electron Beam Lithography (EBL). All fabrication techniques, instruments and experimental methods are described in this chapter. In chapter 3, circular polarised light (CPL) was used to generate the so-called `Superchiral Field` by illuminating a surface of the chiral plasmonic nanostructures. The aim was to reduce the pitch length scale of the incident light to that approaching the pitch length scale of the biomolecules that are adsorbed on the surfaces of the chiral plasmonic nanostructures; this in order to enable the detection and structural characterisation of very low concentrations of biomolecules e.g. picogram quantities. Three main techniques were used for this purpose: CD spectroscopy,

SEM and AFM microscopy. In chapter 4, the possibility of characterising biomolecules adsorbed on the surface of achiral plasmonic nanostructures is explored. The work in this chapter is based on the far field electromagnetic field coupling between the electromagnetic field of the plasmonic surface and the electromagnetic field of the adsorbed chiral molecules, a coupling essentially to be achieved by the aid of the incident light. In chapter 5, the origin of the chiroptical second harmonic generation (SHG) signal that originates from the surface of the chiral plasmonic nanostructures upon irradiation with intense linearly polarised light has been investigated. From the work presented in this chapter, it may be concluded that the non-linear optical activity of the chiral plasmonic nanostructures share a common microscopic origin with that of aligned chiral molecules, which was established to be electric dipolar excitation. This is an unexpected result since it might have been expected that non-localised higher multipolar excitation (e.g. electric quadrupole and magnetic dipole contributions) would dominate the optical activity of such relatively large plasmonic nanostructures. Importantly, measurements were performed in off-resonance conditions for reasons discussed throughout the chapter. In chapter 6 the practical visualisation of regions of intense plasmonic activity, referred to as `hot spots` has been described. After irradiation with a femtosecond laser beam, SEM microscopy was used to map chiral plasmonic nanostructures surfaces to show which areas have been damaged, and hence reveal where the plasmonic hot spots are. Finally, in chapter 7, we derived our conclusion and hence present our anticipation for future work.

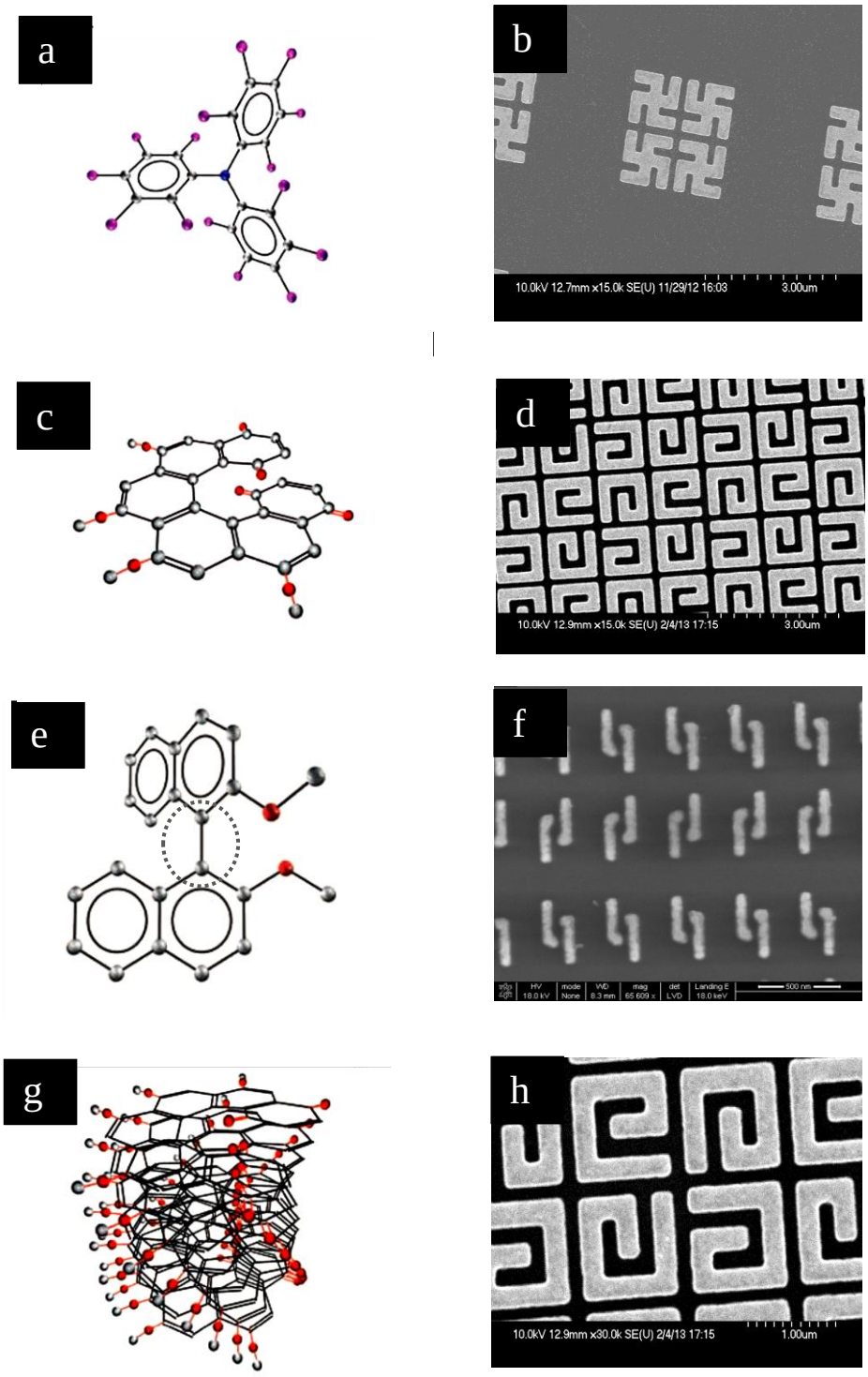

Figure 5: Four concepts of chirality are demonstrated here, these are: ***propeller*** is demonstrated in **a** for perchlorotripheylamine and in **b** for the left and Right handed gammadions, ***spiral*** is demonstrated in **c** for helicinebisquinone and in **d** for G like shapes, ***chiral coupling*** is demonstrated in **e** for 2,2′-dimethoxy-binaphtyl and in **f** for J like shapes, finally, ***supermolecular chirality*** is demonstrated in **g** for molecules in **c** stacked in super chiral fashion and in **h** for quadric units of G like shapes. Grey dashed circle illustrates *chiral axis*.

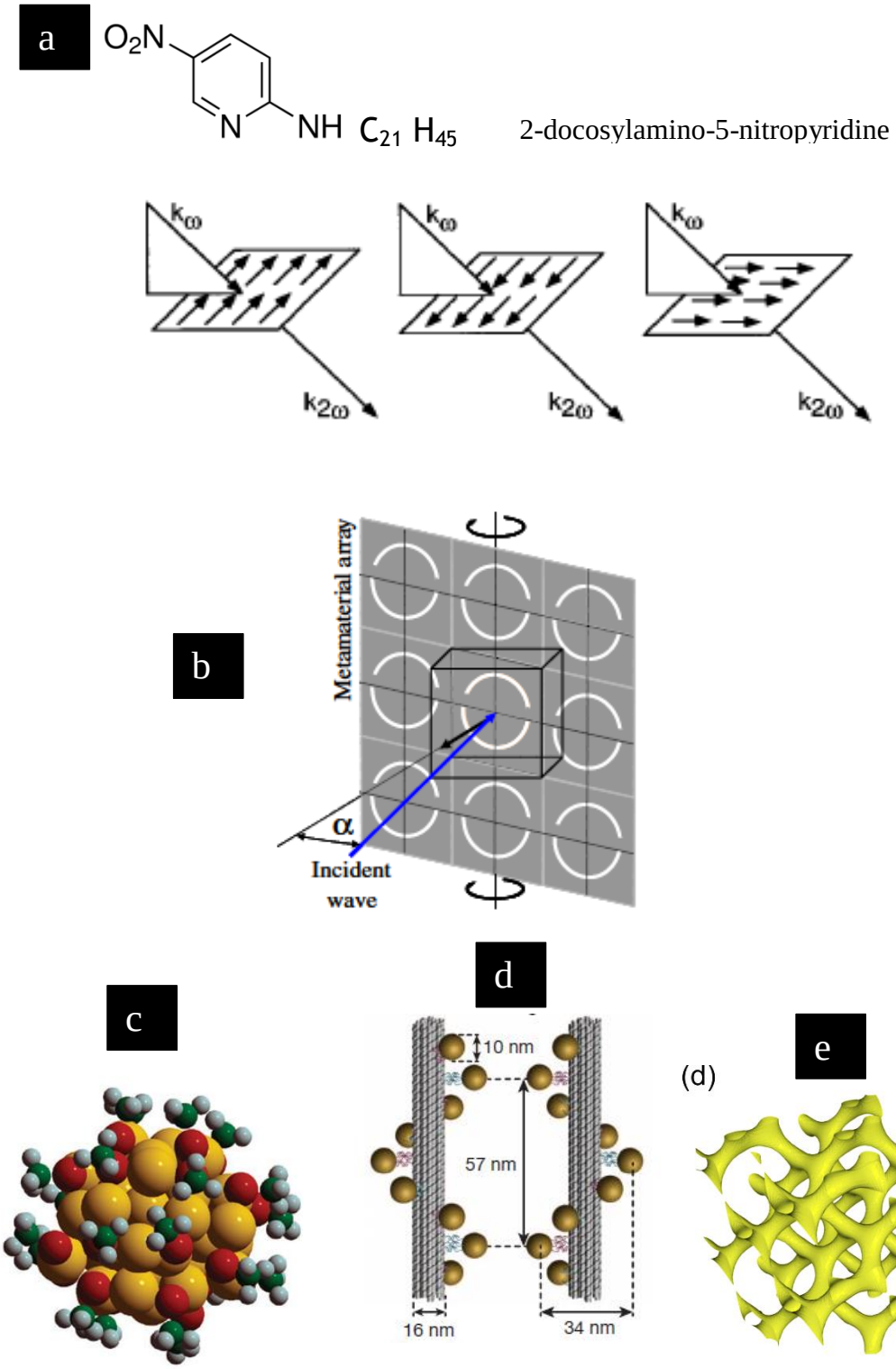

Figure 6: Five concepts of chirality are demonstrated here, these are: ***pseudo chirality*** in **a** for different experimental set up for 2-docosylamino-5-nitropyridine molecule, ***extrinsic chirality*** in **b** for different experimental set up for split rings nanostructures, ***chiral scaffolds*** in **c** for chiral molecules that are binding to a cluster of nanoparticles, ***chiral scaffolds*** in **d** for nanoparticles that are binding to helical molecules, such as strands of DNA, and finally, ***chiral scaffolds*** in **e** for 3D chiral metamaterials that are fabricated to gyroid networks.

1.2. Historical review

The study of optical activity and its possible applications has a long and distinguished history dating back more than 200 years. Early observations of optical activity was recorded by Arago in 1811, when he observed the rotation of plane polarised sunlight by a piece of quartz, located between two crossed polarisers, thus demonstrating the optical rotation measurements (OR) for the first time. Several years later in 1815, a French physicist called Jean Biot verified the optical rotation for several liquids varied between organic liquid like turpentine, alcoholic solution of camphor and aqueous solutions of sugars [1,2$^{ch1\ pp2}$]. He then managed to record the optical rotation for the second form of quartz, the amethyst, in 1818 which showed the opposite effect to the one used by Arago above. Furthermore, in 1832 he tested the optical rotation for tartaric acid, to pioneer the idea of optical activity as a distinguishing of a single molecule; since he couldn`t find it in molten quartz i.e. in molecule attached to its own crystal structure[2$^{ch1\ pp2}$]. Meanwhile, in 1825 Frensel discovered the circular polarised beam which was then used in 1847 by Haiding to resolve CD measurements of violet amethyst [1,2$^{ch1\ pp5}$]. A year later, in 1848, Louis Pasteur had formulated the concept of dissymmetry and that mirror image molecules shared the same formula but have a different spatial arrangement, when he successfully isolated and characterised CD measurements for enantiomeric solutions of tartaric acid crystals [2$^{ch1\ pp25}$,24,25]. With this achievement, the idea of three dimensional molecular structures had become an important breakthrough; as long as two dimensional structures are incapable to support such studies [26]. Fifty years later, in 1895, Aimé Cotton substantiated CD measurements for liquids comprised of chiral metallic complexes of copper and chromium tartarate, to reveal the relationship between the optical rotation and the wavelength of incident light for the first time, which is now known as a Cotton effect, a phenomena that was first theoretically predicted and distinct by Biot in 1812 as an optical rotary dispersion ORD [1, 2$^{ch1\ pp2}$].

By the early 20th century, CD spectroscopy was considered to be a useful tool to quantify objects with specific spatial geometry named for the first time in 1904 by Lord Kelvin as `chiral` objects, when he said: `I call any geometrical figure, or group of points, *chiral*, and say that it has chirality if its image in a plane

mirror, ideally realized, cannot be brought to coincide with itself `[2ch1 pp25, 27]. Thereafter, biological molecules like proteins and DNA, the building block of life, began to be studied by CD spectroscopy [8]. Yet, CD measurements of biomolecules remained challenging, particularly for small molecules because of their weak response [28].

More than a century ago in 1908, Nobel laureate Gustav Mie published his solutions to Maxwell`s equations of electromagnetic scattering by homogenous and isotropic spheres, giving the first theoretical explanation for the colourful appearance of colloidal gold solutions. Effectively, it is the electromagnetic field surrounding the spherical particles which is responsible for the colours seen. This field is the result of conductive electrons oscillations which arise when excited by incident light. Recent literature refers to this principle as `Mie Theory` [29,30] and for the field in question as SPPs (explained in more details in Chapter 2).

In last four decades, great efforts have been devoted to extend the scattering modelled above to spheres immersed in an adsorbing host medium [31,32]. More recently, in 2010, Cohen`s group from Harvard university, extended it to a metamaterials made out of gold, when they theorised their surface plasmonic resonance by Maxwell`s equations for the first time, to show that in a certain circumstances this field could be twisted and therefore make it chiral, so they called it `Superchiral field` (explained in more details in chapter 3) [33].

1.3. References

1. Nafie L. A., "Vibrational Optical Activity Principles and Applications", *Jhon Wiley& Sons Ltd*., 2011, printed book.
2. Barron L. D., "Molecular Light Scattering and Optical Activity", *Cambridge University press, Cambridge*, 2nd edition, 2004, printed book.
3. Berova N., Polavarapu P. L., Nakanishi K. and Woody R. W., "Comprehensive Chiroptical Spectroscopy/ Instrumentation, Methodologies, and Theoretical Simulations", *John Wiley & Sons, Inc., Hoboken*, 2012 Vol.1, printed book.
4. Moss P. G., *Pure & Appl. Chem., 1996* , Vol. 68, pp (2193-2222).
5. http://chemistry.umeche.maine.edu/CHY556.html (cited in 2014).
6. Yang N.,Tang Y. and Cohen A., *Nano Today* , 2009, Vol.4, pp (269-279).
7. Valev V. K., Smisdom N., Silhanek A. V., De Clercq B., Gillijns W., Ameloot M., Moshchalkov V. V. and Verbiest T., *Nano Lett.*, 2009, Vol.9, pp (3945- 3948)
8. Hendry E., Carpy T., Johnston J., Popland M., Mikhaylovskiy R. V., Lapthorn A. J., Kelly S. M., Barron L. D., Gadegaard N. and Kadodwala M., *Nature Nanotechnology*, 2010, Vol.5, pp (783-787).
9. Valev V. K., Baumberg J. J., Sibilia C. and Verbie T., *Advanced Materials*. **2013**, Vol.25, pp (2517–2534).
10. Kuwata-Gonokami M., Saito N., Ino Y., Kauranen M., Jefimovs K., Vallius T., Turunen J. and Svirko Y., *Phys. Rev. Lett.*, 2005, Vol. 95, pp(227401(1- 4)).
11. Valev V. K., De Clercq B., Zheng X., Denkova D., Osley E. J., Vandendriessche S., Silhanek A. V., Volskiy V., Warburton P. A. ,Vandenbosch G. A. E., Ameloot M., Moshchalkov V. V. and Verbiest T., *Opt. Express*, 2012, Vol.20, pp(256 -264).
12. Gansel J. K., Thiel M., Rill M. S., Decker M., Bade K., Saile V., Von Freymann G., Linden S. and Wegener M., *Science*, 2009 , Vol. 325, pp (1513- 1515).
13. Decker M., Ruther M., Kriegler C. E., J. Zhou J., Soukoulis C. M., Linden S. and Wegener M., *Opt. Lett.* 2009, Vol.34, pp (2501-2503) .
14. Huttunen M. J., Bautista G., Decker M., Linden S., Wegener M. and Kauranen M., *Opt. Mat. Express*, 2011, Vol.1, pp (46-56).
15. Liu N., Liu H., Zhu S. and Giessen H., *Nat. Phot.*, 2009, Vol.4, pp (1-2).
16. Decker M., Zhao R., Soukoulis C. M., Linden S. and Wegener M., *Opt. Lett.*, 2010, Vol.35, pp (1593-1595) .
17. Verbiest T., Kauranen M., Van Rompaey Y. and Persoons A., *Phys. Rev. Lett.*, 1996, Vol.77, pp (1456-1459) .
18. Plum E., Liu X. X., Fedotov V. A., Chen Y., Tsai D. P. and Zhelude N. I., *Phys. Rev. Lett.*, 2009, Vol.102, pp (113902-(1-4)) .
19. Belardini A., Larciprete M. C., Centini M., Fazio E. and Sibilia C., *Phys. Rev. Lett.*, 2011, Vol.107, pp (257401-(1-5)) .
20. Noguez C. and Garzon I. L., *Chemical Society Reviews*, 2009, Vol.38, pp (757-771).
21. Kuzyk A., Schreiber R., Fan Z., Pardatscher G., Roller E. M., Hogele A., Simmel F. C., Govorov A. O. and Lied T., *Nature* 2012, Vol.483, pp(311-314).

22. Vignolini S., Yufa N.A., Cunha P. S., Guldin S., Rushkin I., Stefik M., Hur K., Wiesner U., Baumberg J. J. and Steiner U., *Advenced Optical Materials*, 2012, Vol.24, pp (OP23–OP27).
23. Hur K., Francescato Y., Giannini V., Maier S. A., Hennig R. G. and Wiesner U., *Angewandte Chemie International Edition*, 2011, Vol.50, pp (11985-11989).
24. Flack H. D., "Louis Pasteur`s discovery of molecular chirality and spontaneous resolution in 1848, together with a complete review of his crystallographic and chemical work", *Acta Crystallographica*, 2009, Vol.65, pp (371-389).
25. Gal J., "Louis Pasteur, Language, and Molecular Chirality/ Background and Dissymmetry", *Chirality*, 2011, Vol.23, pp (1-16).
26. Corrêa D. H. and Ramos C. H., *African J. of Biochemistry Research*, 2009, Vol.3, pp (164-173).
27. Lord Kelvin, "Baltimore Lectures on Molecular Dynamics and the Wave Theory of Light", *Clay C.J. and Sons, Cambridge University Press Warehouse, London*, 1904.
28. Tang Y. and Cohen A. E., *Science*, 2011, Vol.332, pp (333-336).
29. Kosuda K. M., Bingham J. M., Wustholz K. L. and Van Duyne R. P., *Comprehensive Nanoscience and Technology*, 2011, Vol.3, pp (263-301).
30. Hergert W., Wriedt T., "The Mie Theory, Basics and Applicatons", *Springer*, 2012, e-book.
31. Mundy W. C., Roux J. A. and Smith A. M., *Journal of the Optical Society of America*, 1974, Vol.64, pp (1593-1597).
32. Bohren C. F. and Gilra D. P., *Journal of Colloid Interface Science*, 1979, Vol.72, pp (215-221).
33. Tang Y. and Cohen A. E., *Phys. Rev. Lett.*, 2010, Vol.104, pp (163901-163904).

Chapter 2: The Nanofabrication of plasmonic nanostructures by Electron Beam Lithography

Abstract

This chapter describes the nanofabrication of the plasmonic nanostructures which have been fabricated during the project. The nanofabrication work was carried out in the JWNC cleanroom in the Department of Electronic and Electrical Engineering/ School of Engineering/ Glasgow University. All the samples were fabricated via Electron beam lithography (EBL). An outline of Electron beam lithography technique is included together with a discussion of the factors which affect the interactions between the electron beam and sample surfaces. The instruments used and experimental methods employed are described.

2.1. Introduction:

2.1.1. Electron Beam Lithography

Electron Beam Lithography (EBL) is the technique of using a focused electron beam as a means of drawing geometrical features on a polymer matrix of a supporting substrate. The idea is to exploit the capability of the electron beam to interact with the molecules of this matrix. This interaction can be directed to produce a specific pattern consisting of thousands of features scaled to nanometer sizes. The pattern is then revealed by the development process, which removes the exposed area of the matrix and retains the unexposed area. Then, a metallic layer is deposited on the matrix to fill up the exposed area (the patterned area) with a specific thickness layer of the metal. Eventually, the metallic pattern is revealed by the lifting off process, in which the metallic layer is removed from the unexposed area to retain the area with the metallic pattern [1 Chapter(2) pp142, 2 Chapter(2) pp(11-12)].

Electron beam lithography (or E-beam writing) is one of many other lithographical techniques, these are: The Deep UV (200-290nm), extreme UV (<200nm) photolithography and Phase-shift photolithography, the X-ray lithography, focused ion beam (FIB) lithography, scanning probe lithography and others. EBL has the advantages of: high resolution performance that approaches less than 10nm feature size; reproducibility and high quality throughout. It is a direct writing routine and does not require a mask or a template to transform the desired pattern. The only disadvantage is that the procedure is time-consuming since the writing practice is performed as a dot by dot system [3-12]. In general, EBL can be used to manufacture electronic devices like semiconductors, circuits and biosensors. The functionality in such electronics requires a very high resolution performance e.g. of the order of 10nm or less which is comparable to the size of large molecules. This can only be achieved by techniques like Electron Beam Lithography; because the spot size of the electronic beam using this technique is ~4 nm in diameter [1[Chapter2 pp142],2[Chapter(2) pp12],3]. Table 1 illustrates the length scales of common objects [13 [chapter(1) pp1]]. In fact, the manufacture of nanoscale patterns is challenging, especially when considering ways in which the electron beam (the writing tool) interferes with the substrate surfaces.

On the other hand, the nanometer scale is small enough to be comparable with invisible dust particles. Thus, contamination by dust is the main concern in the nanofabrication industry. Therefore, the technique is usually performed within special `cleanroom environments` which are designed to ensure a dust-free working area. The maintenance of such cleanroom environments requires huge funding, efforts, expertise and a restricted entrance with special suits to maintain the cleanroom status.

Table 1: These are approximate sizes for some common objects with SI metric scale units.

Object	Typical diameter	SI metric scale
Grain of sand	1 mm = 1000 μm	1μm = 10^{-6} m 1nm = 10^{-9} m 1pm = 10^{-12} m
Human hair	150 μm	
Red blood cell	10 μm	
Bacterium	1 μm	
Virus	20 nm	
DNA molecule	2 nm	
Uranium atom	0.2 nm = 200 pm	

For this project, 2D plannar chiral metamaterials have been manufactured using EBL with nanofeatures ranging between 200-1000nm. The size of such features is comparable with the scale of the wavelength of the spectroscopic light. This is important to study the interferences between the nanoscale features and the nanoscale wavelength of the spectroscopic light; which is the basis of this thesis. Some bespoke 2D plannar chiral metamaterials were used in this thesis; however all designs are presented in section 2.4.1. Wire widths of 40nm, 60nm, 80nm and 200nm have been achieved. All patterns were written by an ultrahigh resolution writing machine at the JWNC cleanroom of Glasgow University. The aim of the nanofabrication work in this chapter is to make plasmonic nanostructures that are considered to be sorts of `radiant signal domain` sensors. These sensors depend on the signal properties of the electromagnetic waves such as intensity, wavelength, polarisation and phase. From literatures, sensors; are classified into six categories [14 Chapter7 pp381], these are: `*1.The thermal signal domain sensors: functionalised through temperature, heat and heat flow 2. The mechanical signal domain sensors: functionalised through force, pressure velocity, acceleration and position 3.The chemical signal domain sensors: measure the internal quantity of the matter such as concentrations of materials, composition and reaction rate 4. The magnetic signal domain sensors: functionalised through magnetic field intensity, flux density and magnetisation*

5.The radiant signal domain (which our sensors are characterised under)*: here the signals are quantities of the electromagnetic waves, such as intensity, wavelength, polarisation and phase 6.The electrical signal domain sensors: measuring voltage, current and charge*`.

Historically, EBL was first demonstrated over 50 years ago following the development of Scanning Electron Microscopy (SEM) and the addition of a pattern generator and blanker plates to the column of the scanning electron microscope [1[Chapter(2) pp142],2[Chapter(2) pp12],15,16]. The subsequent discovery of high resolution resists like PMMA (poly methyl methacrylate), ZEP 520 (11% methyl styrene + chloromethyl acrylate copolymer (solid) + 89% anisole (solvent)) and HSQ (hydrogen silsesquioxane) has contributed significantly to this development since they represent the platform for pattern deposition [1 [Chapter(2) pp142], 17-19]. The concept of EBL was first introduced by Buck et.al in 1959 when they decided to use the contamination layer, known as a side effect in electron microscopy at that time, as an etching mask for the 100nm patterns. This layer forms as a result of polymerisation of the hydrocarbon or siloxane exiting under vacuum by the electron beam of the microscope [15]. EBL terminology came from the idiom *Lithography,* which is `*The process of printing from a flat metal (formerly stone) surface treated so as to repel the ink except where it is required for printing*`. Origin Greek ` *lithos* ` is stone, and `*graphic*` is writing or drawing [20 (Concise English Dictionary)]. Another reference defines *Lithography* as `*A method of printing from a metal or stone surface on which the printing areas are not raised but made ink-respective while the non-image areas are made ink-repellent*` [21 (Collins English Dictionary)].

2.1.2. Metamaterials

Metamaterials can be described as an array of artificially sculpted materials [22], patterned in a two or three dimensional periodic lattice, distributed over a dielectric substrate, sized in smaller than a certain wavelength, spaced by sub-micron and frequented in order larger than 100s x 100s of d nm thick features. Their advantage of possessing negative values for both dielectric permittivity (ε

< 0) and magnetic permeability (μ < 0) simultaneously (see Figure 1 which illustrates materials classification based on materials dielectric permittivity and materials magnetic permeability), lead to imply negative refractive index ($n= -\sqrt{\varepsilon\,\mu}$), where `*the phase velocity is opposite to the energy flux*`, a unique characteristic causes to change opaque materials (with negative value for either ε or μ) to transparent materials (with positive value for both ε or μ), which is unlikely to be found naturally. Changing opaque materials to transparent materials can be explained as follows: when electromagnetic waves reflect from the surface of an object hidden behind a metamaterial plate, the electromagnetic waves are bended negatively at the interface between A (e.g. air) and B (e.g. the metamaterial plate) (see Figure 3), and hence, a focal point is formed inside the metamaterial plate. This in turn, and similarly to the original source, acts as a new source of light. Hence, once again, the electromagnetic waves are bended negatively at the interface between B (the metamaterial plate) and A (the air), as such, a focal point is formed outside the metamaterial plate this time; which means the object behind the metamaterial plate become visible, see Figure 3. Generally speaking, due to this novel phenomena, when an electromagnetic field with a visible frequency incident the metamaterial surfaces; it will twisted in the `wrong` direction, and hence such materials are termed as `Left Handed Materials` or `Double Negative Materials` or even `Backward Wave Materials` [23-26], see Figure 2 which illustrates examples of a solution with normal refractive index (left) and a solution with negative refractive index (right). This description has provoked a considerable number of aspects to use it successfully (applications have increased within a decade) and yet are being researched, Thus, since 1999 when first manufactured by Pendry group [27] others start to employ it in a variety of schemes, like, Terahertz metamaterials [28], photonic metamaterails [29], plasmonic metamaterias [30], chiral metamaterials[31], non-linear metamaterials [32] and more [33-35]. Indeed, it is a virtue back to the theoretical model pioneered by the Russian physicist V.G Veselago in 1967 [23]. Recently, light scattering using metamaterials has become a vital concept that could be used to improve diagnostic devices like biosensors. This is because the functionality of these biosensors is highly optimised by the metamaterials optical properties [36]. Hence, the optical properties of metamatrials with plasmonic surfaces and negative refractive indices have become an important field in bio sensing

techniques and pathogenic detections [37,38]. Advancements in scanning electronic and scanning atomic force microscopy, also in techniques such as, electron beam lithography, CD spectroscopy and laser based tools, in addition to computing devices that enable sophisticated numerical calculations to be achieved quickly and precisely, all together are playing a key role to support such studies with adequate details.

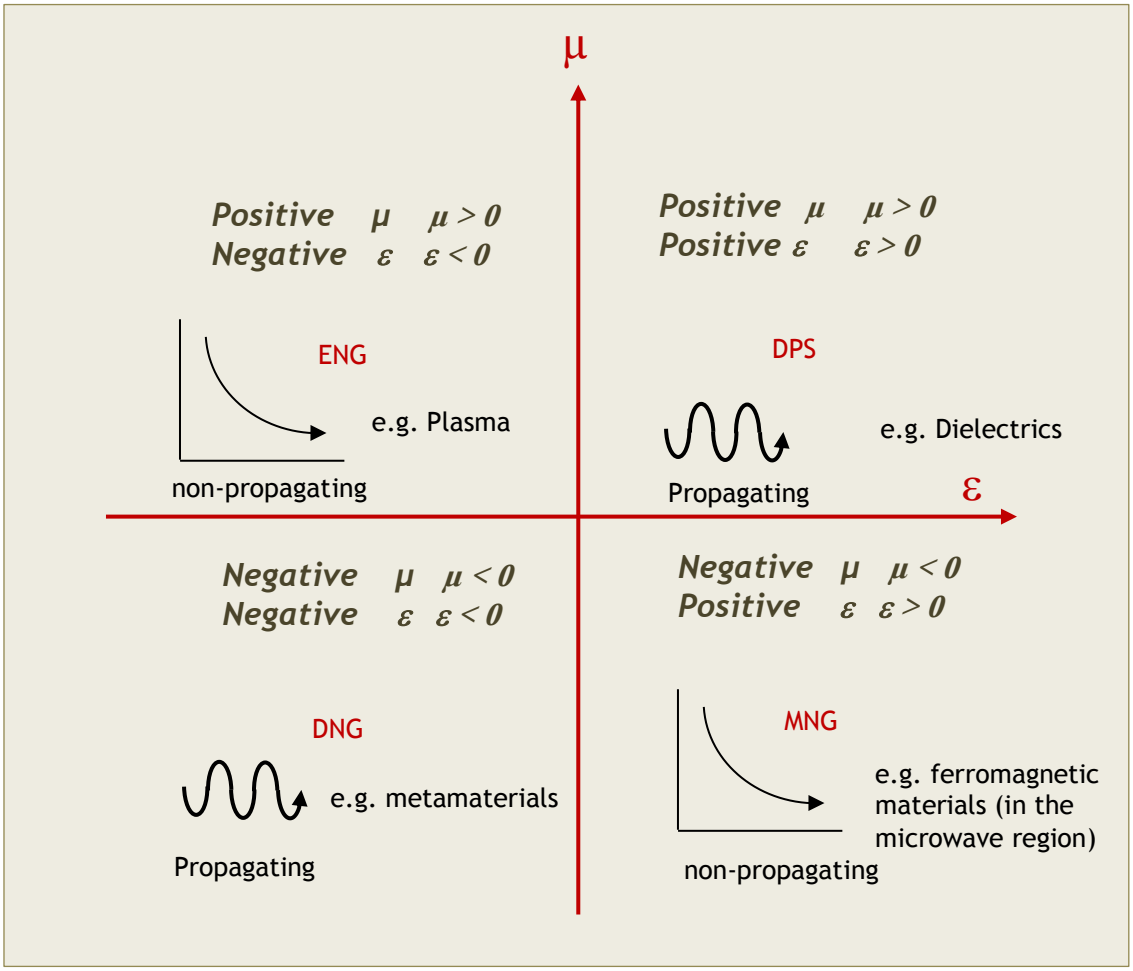

Figure 1: Illustration of materials classification that is based on negative and positive dielectric permittivity ε in addition to negative and positive magnetic permeability μ. DPS is double positive materials, ENG is epsilon negative materials, DNG is double negative materials and MNG is mu negative materials.

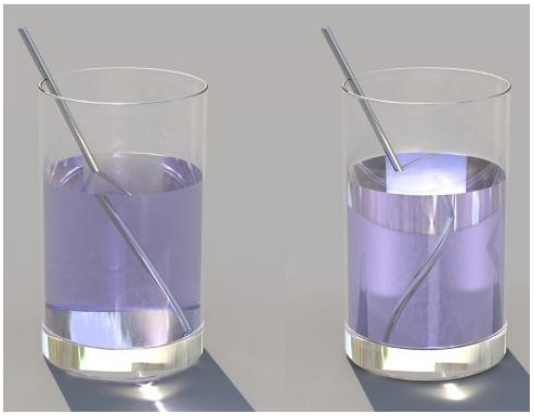

Figure 2: Examples of a solution with normal refractive index (left) and a solution with negative refractive index (right). This Figure was taken from reference [39].

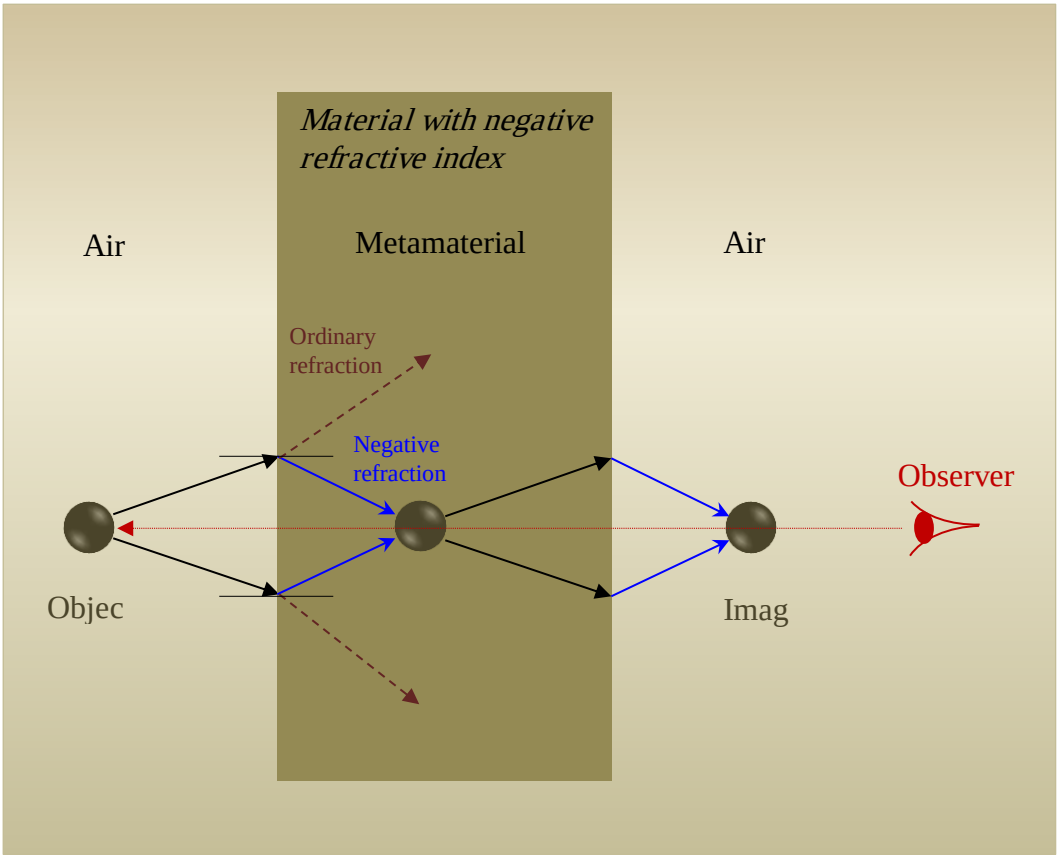

Figure 3: the electromagnetic waves are bended negatively at the interface between A (air) and B (metamaterial) and therefore, a focal point is formed inside the metamaterial, which in turn, and in the same way to the original source, acts as a new source of light. Then, once again, the electromagnetic waves are bended negatively at the interface between B (metamaterial) and A (air), hence, a focal point is formed outside the metamaterial this time; which means the object behind the metamaterials become visible [40].

2.1.3. Surface Plasmons

At a definite wavelength, light can excite metal-dielectric surfaces since metals have free electrons on their outside orbitals (e.g. visible light is able to excite gold-air and silver-air surfaces under certain experimental conditions). This is an important phenomenon as when light excites such surfaces it will induce coherent oscillations associated with the metal's free electrons along the metal-dielectric interface. Such oscillations are known as `Surface Plasmons` or SPs and the collective of oscillations is known as `Surface Plasmon Resonance`, or SPR. For the reason that SPR propagates along metal-dielectric interface, researchers also refer to the propagating SPR as `Propagating Surface Plasmon Resonance` or PSPR. Such oscillations are usually excited on continuous metal thin film (e.g. 50nm gold film) through prism couplers that follow Kretschmann excitation configuration, Figure 4. Essentially, SPR induces quasiparticles known as ` Surface Plasmon Polaritons`, or SPPs, which arise as surface longitudinal, p-polarized, electric field waves that propagate along the metal-dielectric interface. In principle, SPPs are near fields, also known as *evanescent fields*, with a maximum intensity at 1/3 λ from the surface of its formation (Figure 5a) and exponentially decay towards the dielectric medium and inside the metal (Figure 5b). For example, for 50nm gold film, the SPPs propagate 10-100 microns along the metal-dielectric interface in the x- and y- directions and decay exponentially over a distance on the order of 200nm in the z-directions. Concerning the nanoparticle and the nanostructure surfaces, there is another variation of SPR known as `Localised Surface Plasmon Resonance` or LSPR, in which the SPR is localised around the nanoparticles (Figure 6) and the nanostructures. Importantly, the actual sizes of the nanoparticle and the nanostructure should be smaller than the wavelength of the incident light. SPPs from such surfaces are confined by the LSPR which is itself confined by the shape of the nanoparticles and the nanostructures [37,(41-44)]. The advantages of such confinements will be explained below. Generally speaking, SPPs originate when electromagnetic waves of an incident light couples to the oscillations of the surface plasmon. Such coupling requires the electromagnetic waves of the incident light to be p-polarised; it also requires having the electromagnetic waves of the incident light and the oscillations of the surface plasmon propagating at the same frequency. In addition, for continuous thin

film, it requires having the electromagnetic waves of the incident light to be incident on the metal surface through a dielectric medium (e.g. a prism) at an incident angle greater than the critical angle for total internal reflection (Kretschmann configuration). However, for nanoparticles and nanostructures it requires having the electromagnetic waves of the incident light to be incident on the metal surface through air (i.e. prism is not required) at a normal incident angle. In fact, all these requirements are necessary to be maintained in order to increase the K (wave vector) value of the incident light inside the optically denser medium (i.e. prism for PSPR or structure confinements for LSPR) to match the K value of the SPR. To clarify this issue, from the dispersion plot for continuous metal thin film (i.e. PSRR) shown in Figure 7, it is clear that the K value of the incident light ($k_d = \omega / c\sqrt{\varepsilon_d}$) is much smaller than the counterpart K value of the surface plasmon ($k_{dm} = \frac{\omega}{c}\sqrt{\frac{\varepsilon_d\,\varepsilon_m}{\varepsilon_d + \varepsilon_m}}$), meaning that light will not be able to propagate through the plasmon. But with Kretschmann excitation configuration (in addition to other excitation configurations such as Otto excitation configuration and diffraction effect) it is possible to increase K value for the incident light to satisfy perfect matching between the wave vector of the incident light and the wave vector of the surface plasmon to generate efficient SPPs. The reason of such requirements is that the traveling waves of the SPPs only originate if the *exponent term* appears in equation1 as a complex term, i.e. a fraction of the incident light is absorbed. Indeed, light absorption is essential here in order to excite the free electrons of the metal which therefore excites SPR. The latter will not induce SPPs unless the bespoke wave vectors are perfectly coupled; simply because the newly generated SPPs waves need to follow this vector. This is expressed by the equation:

$$E = E_o \exp\left(j\omega t - jk.r\right) \qquad \text{.....1}$$

Where *E* is the amplitude of the evanescent waves (SPPs) which propagate along the wave vector *k*. E_o is the amplitude of the incident electric field, ω is the

angular frequency ($2\pi f$), t is time, r is the propagation axis (x or y or z) and $j=\sqrt{-1}$ [45].

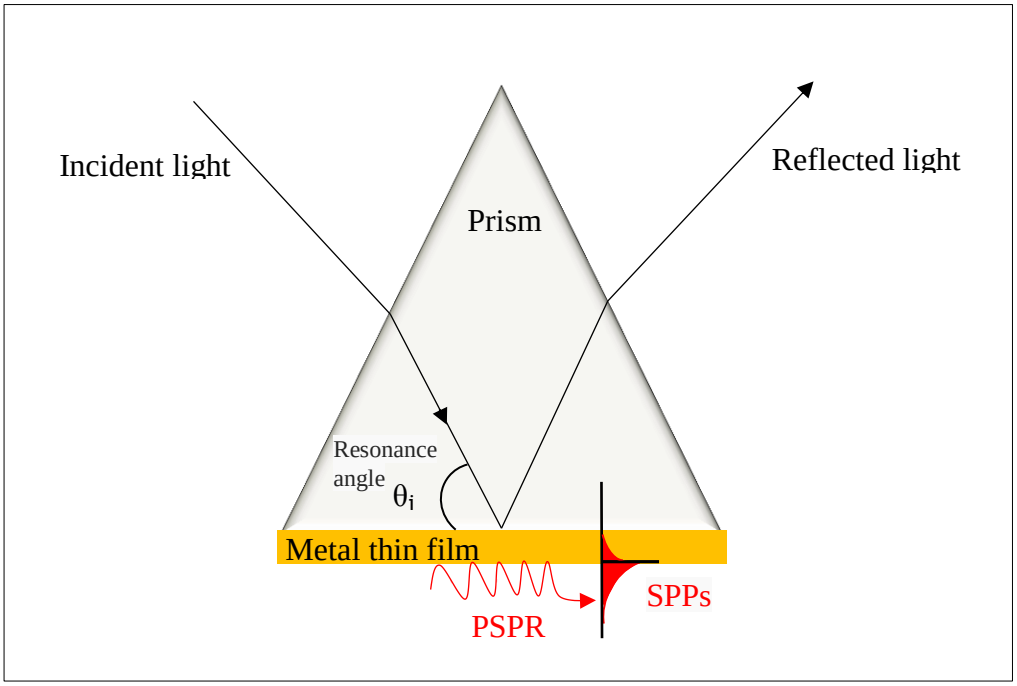

Figure 4: Schematic illustration for Kretschmann excitation configuration. PSPR can be excited on a metal thin film attached to the surface of a prism. PSPR can be excited if p-polarised light is incident by a certain angle called *resonance angle*, denoted by θ_i, which allows light to be absorbed by the free electrons of the metal, and hence, arising coherent oscillations represented by PSPR. The prism slows down the wave vector of the incident light to have it comparable to the wave vector of the PSPR oscillations. PSPR induce SPPs along the metal-dielectric interface. SPPs exponentially decay in the dielectric medium as well as in the metal.

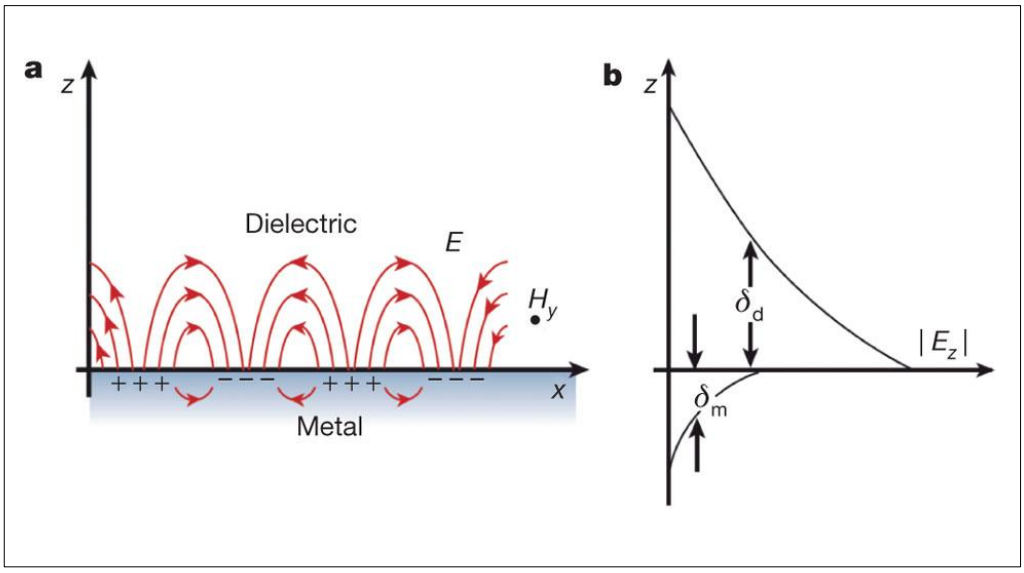

Figure 5: Surface Plasmon Polaritons (SPPs). **a** represents the electromagnetic field E propagating parallel to the incident plane i.e. in x-z plane. Magnetic field H is propagating parallel to the surface i.e. in x-y plane. **b** represents the perpendicular field Ez decays exponentially at an order of δ_d in the dielectric (when δ represents the wavelength of the incident light) and at an order of δ_m in the metal. With $\delta_m \sim 1/3\ \delta_d$ This Figure was taken from [46].

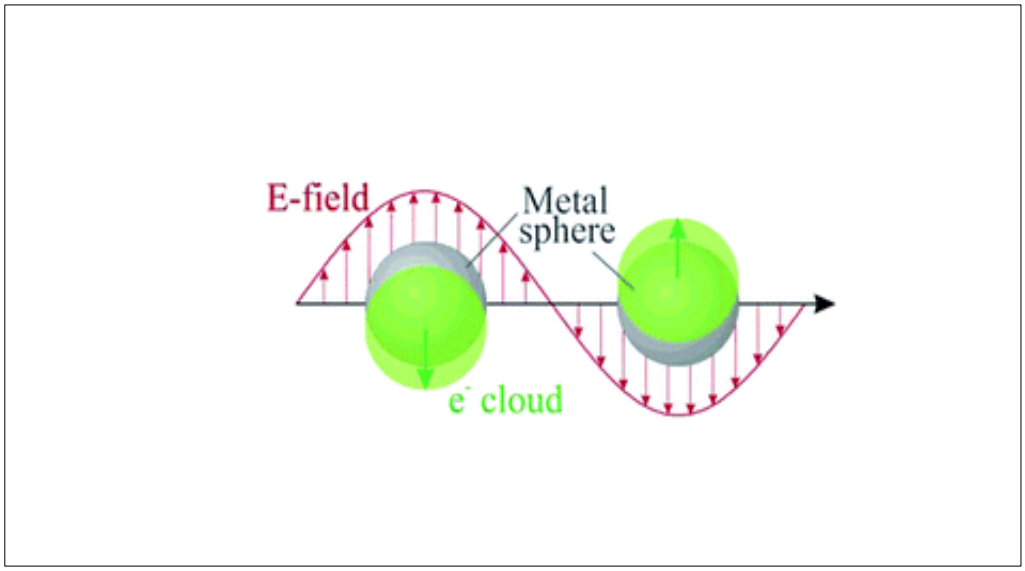

Figure 6: Localised Surface Plasmon Resonance. This Figure was taken from reference [47].

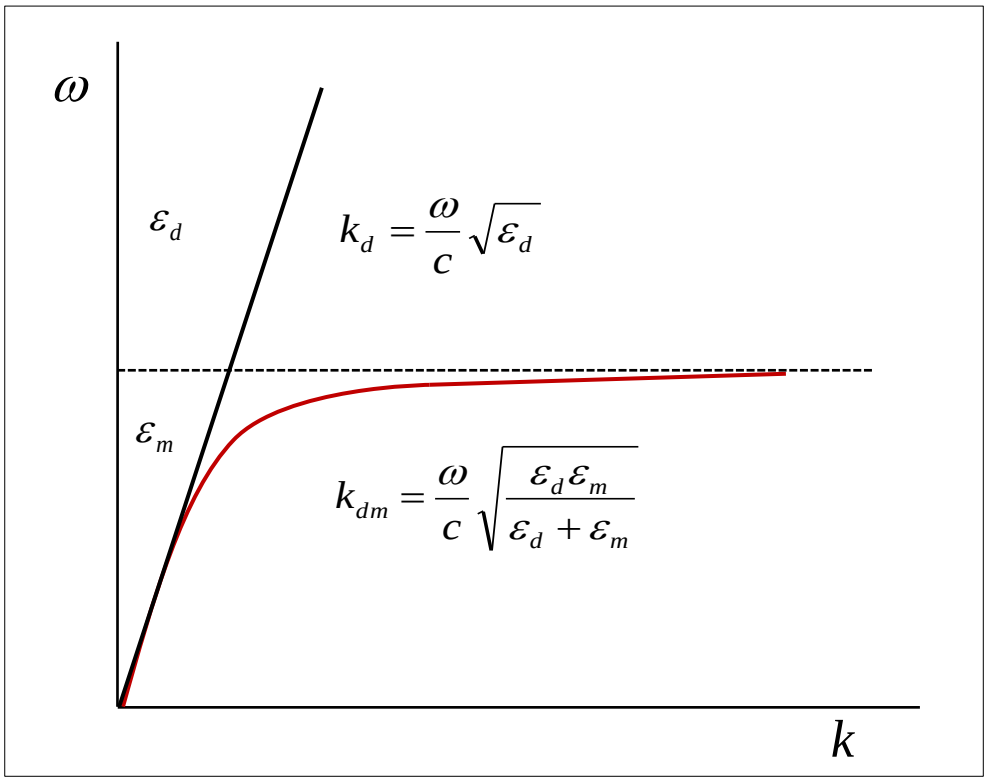

Figure 7: Dispersion plot of the surface Plasmon for continuous thin film. k_d represents the wave vector of the dielectric medium , k_{dm} represents the wave vector of the surface Plasmon, ε_d represents the dielectric constant of the dielectric medium and ε_m represents the dielectric constant of the metal. Black sold line represents the propagation of the wave vector in dielectric medium, red sold line represents the propagation of the wave vector in surface Plasmon and black dashed line represents the metal-dielectric interference.

As mentioned previously, the SPPs from the nanoparticles and the nanostructures are confined by the LSPR which is itself confined by the boundary conditions of the nanoparticles and the nanostructures which vary depending on their size, shape, inter-particle spacing and the surrounding medium [48]. Such confinements coming from the fact that those different boundary conditions imply different plasmon modes. For example, in Figure 8 we show five plasmon modes from the surfaces of different nanoparticles presented by Wang et al [49]. In this Figure, spherical nanoparticles support dipolar mode, and hence SPPs with dipolar radiation is generated. Also, metal nanoshells of different thicknesses support symmetric (Figure 8b) and asymmetric (Figure 8c) plasmon modes and vary with the thickness variation. Likewise, metal nanorods of

different aspect ratios support plasmon mode of field polarization parallel (Figure 8d) or perpendicular (Figure 8e) to the rod. However, for specific engineered nanostructures the plasmon modes are confined by the polarisation state of the incident light and the edge cut of the nanostructures. For example, if the electric wave vector of the incident light is vertically polarised (p-polarised) then it drives the SPR on the surface of the horizontal edges in a manner similar to that shown in chapter 6 Figure1. This also the case for U shape made out of gold, with two assigned edges: A and B, see Figure 9. In this Figure, for plane polarised light, LSPR could be switched *off* or *on* simultaneously at the edges depending on the polarisation state of the incident light whether it is perpendicular (Figure 9a) or parallel (Figure 9b) to A and B. Also, for circularly polarised light, LSPR could be switched *off* or *on* individually at A or B depending on the handedness of the incident CPL whether it is left handed (Figure 9c) or right handed (Figure 9d). On the other hand, LSPR *wavelength* (or LSPR maximum absorption) is confined by the size and shape of the nanoparticles and the nanostructures. In 2011, the Van Duyne group demonstrated a relationship between nanoparticle size and shape and LSPR wavelength. Upon changing the LSPR wavelength of periodic particle arrays via changing nanoparticle in-plane width (Figure 10 inset **a**) and out-of-plane height (Figure 10 inset **b**) they have found that increasing the in-plane width shifts the LSPR wavelength towards lower-energy wavelengths and increasing the out-of-plane height shifts the LSPR wavelength towards higher-energy wavelengths, see Figure 10. On the whole, LSPR confinement for SPPs leads to SPPs coupling within the structural gaps which not only protect the SPPs from rapid decay but also supports much more intense SPP_S fields which could be guided within a specific path depending on the shape of the nanostructures. As such, for specific engineered nanoparticles and nanostructures the field lines of the adjacent SPPs might couple together to generate enhanced SPPs. For example, intense near field oscillations were observed by Chung et al. in the gap area of spherical nanoparticle dimers, see Figure 11a. This research group also observed intense near field oscillations that were developed in the nanogap area for double nanocrescents facing each other, see Figure 11b. Also, Capasso et al, observed intense near field oscillations that were developed in the nanogap area for optical antenna, see Figure 11c. Apparently, gap distance is another factor that affects the SPPs enhancement e.g. for spherical nanoparticles, Chung et al. have demonstrated a maximum

enhancement at a distance gap on the order of the radius of the nanoparticle. In addition, Giessen's group theoretically predicted that SPPs can be enhanced as a result of a near field coupling at the separation gaps between the nanowires of the nanostructures, i.e. chiral nanostructures can confine the SPPs enhancements to a chiral fashion, for example, the right handed gammadion structure (Figure 12**a**) and the left handed helix structure (Figure 12**b**) can enhance the electric energy density $\hat{U}_e$ to 400 and 375, respectively.

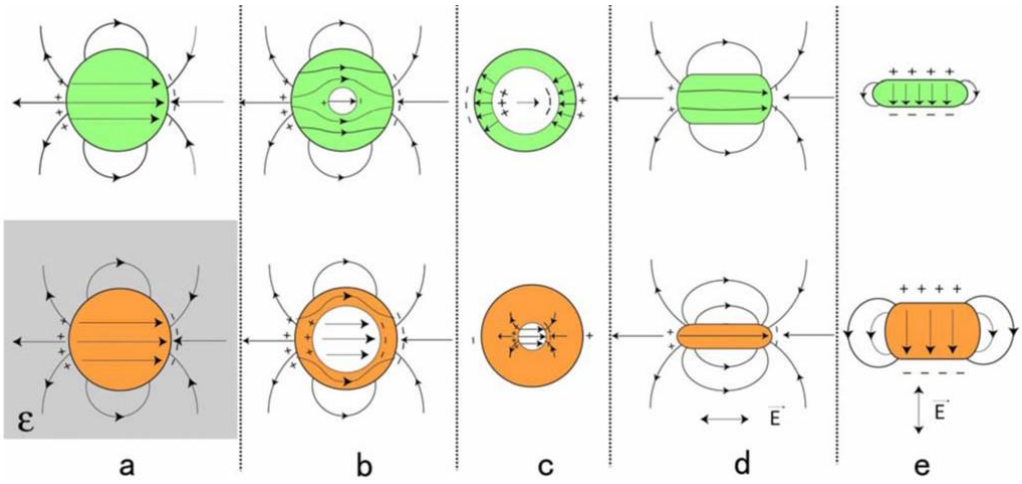

Figure 8: Different field distributions imply different surface plasmon modes. **a** represents dipolar plasmon mode of a metal sphere imbedded in different dielectric media. **b** represents symmetric plasmon mode of a metal nanoshells of different thicknesses. **c** represents asymmetric plasmon mode of a metal nanoshells of different thicknesses. **d** represents metal nanorods of different aspect ratios with plasmon mode of field polarization parallel to the rod. **e** represents metal nanorods of different aspect ratios with plasmon mode of field polarization perpendicular to the rod. This Figure was taken from reference [49].

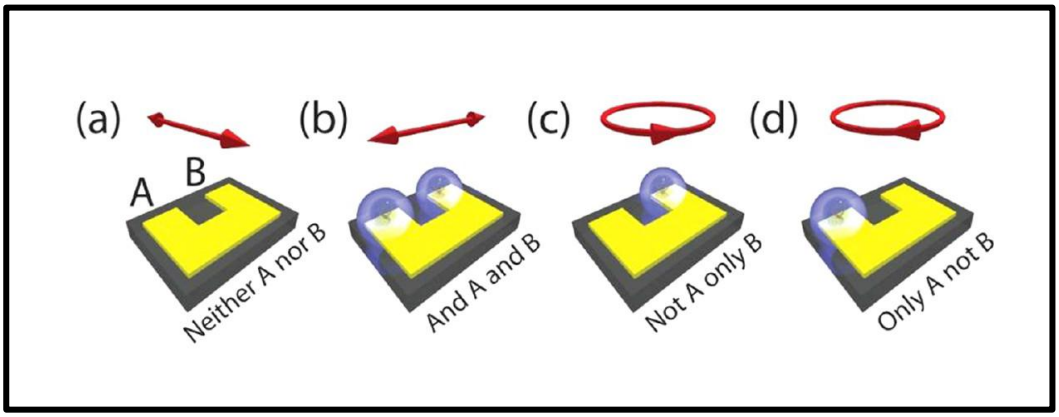

Figure 9: Illustration for SPR modes on U shape made out of gold with two assigned edges: A and B. Red arrows denote the direction of the incident light. Note that for plane polarised light, SPR could be switched *off* or *on* simultaneously at the edges depending on the polarisation state of the incident light whether it is perpendicular (a) or parallel (b) to A and B. Likewise, for circular polarised light, SPR could be switched *off* or *on* individually at A or B depending on the handedness of the incident CPL whether it is left handed (c) or right handed (d). This Figure was taken from reference [41].

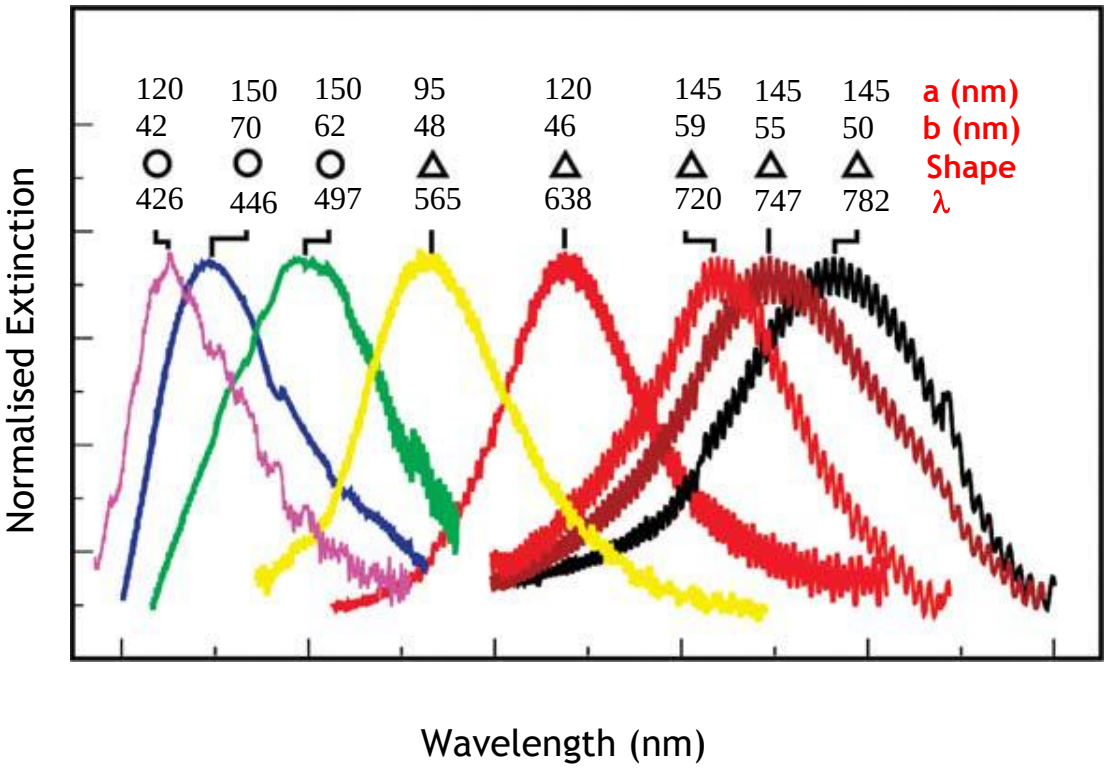

Figure 10: Relationship between nanoparticle size and shape and LSPR wavelength. LSPR wavelength of periodic particle arrays can be changed with changing nanoparticle in-plane width (inset **a**) and out-of-plane height (inset **b**). This Figure was taken from refrence [37].

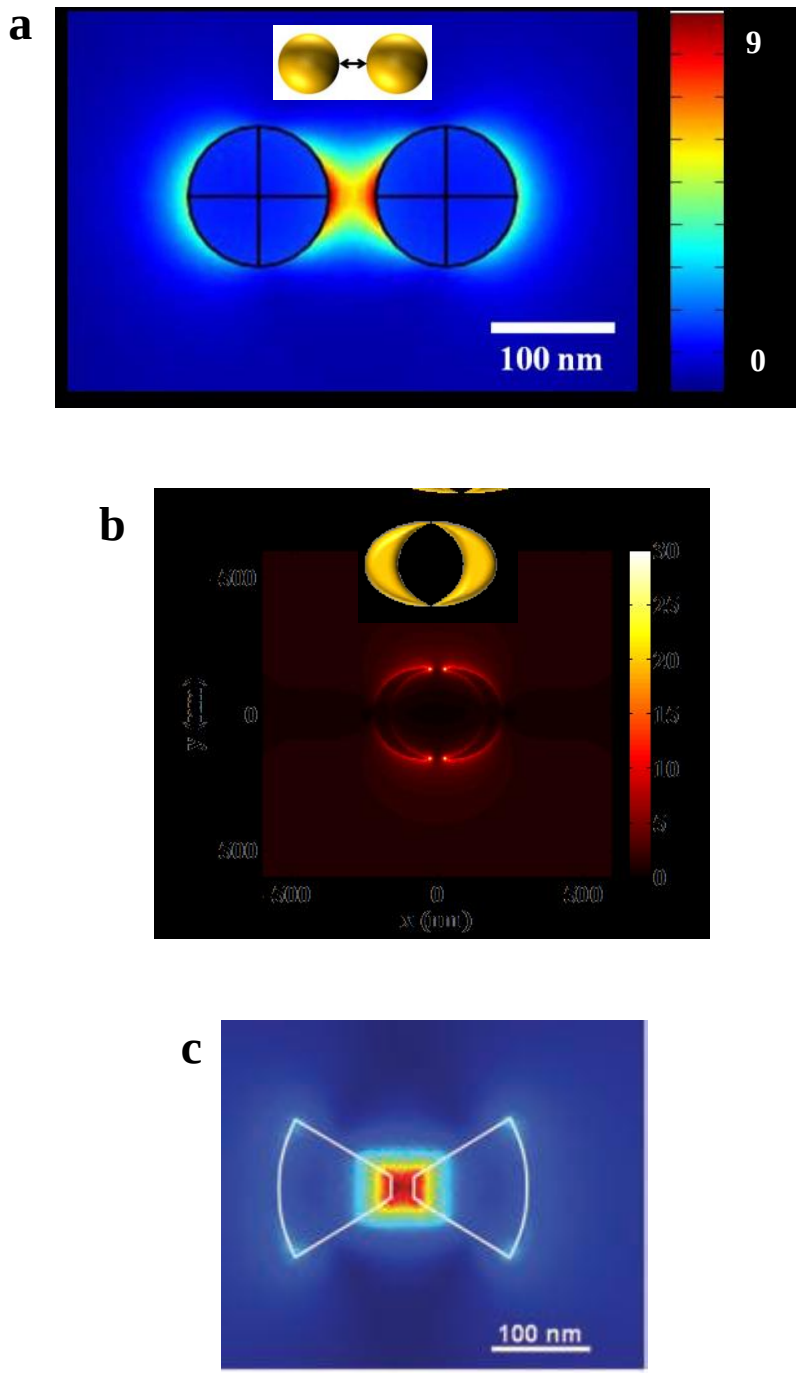

Figure 11: SPPs enhancements are occurred as a result of near field coupling at the separation gaps between nanoparticles. **a** represents an intense near field oscillations in the gap area of spherical nanoparticles dimer. **b** represents an intense near field oscillations in the nanogap area for double nanocrescents facing each other. (a and b were taken from reference [50]. **c** represents an intense near field oscillations in the nanogap area for bowtie optical nanoantenna, see Figure 6c (This Figure was taken from reference [51].

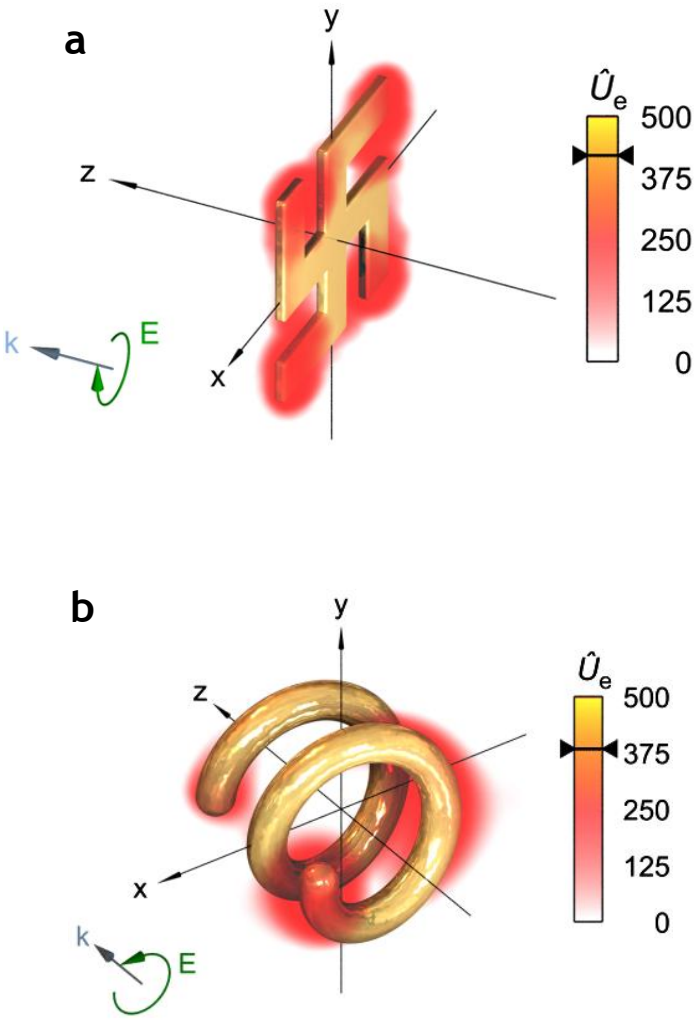

Figure 12: SPPs enhancement occurs as a result of near field coupling at the separation gaps between the nanowires of the nanostructures, e.g. the chiral shapes of the nanostructures confine the SPPs enhancements to a chiral fashion and hence enhance the electric energy density $\hat{U}_e$ in the right handed gammadion structure (**a**) and in the left handed helix structure (**b**). This Figure was taken from reference [52].

In either case (PSPR or LSPR), SPPs are very beneficial fields and have a number of applications especially in biosensing technology. An example for application of PSPR in biosensing technology is SPR spectroscopy `*which measures changes in the refractive index of a monolayer attached to a metal surface*`. SPR spectroscopy is a powerful optical technique for label-free biomolecular interaction detection in real time. In prism-based SPR spectroscopy [majority of SPR instruments are prism-based SPR (Kretschmann configuration)] a linearly polarised (p-polarised) light passes through a prism onto the back side of a central surface chip and then is reflected back to the detector. At a certain incident angle known as the *resonance angle* (defined in Figure 4), light is absorbed by the electrons in the metal film of the central surface chip causing them to resonate and hence surface plasmon resonance arises. As such, an intensity lost in the reflected beam appears as a *dark band* and can be seen as a *dip* in the *SPR reflection intensity curve*. Since the surface plasmon resonances are sensitive to the refractive index of the surrounding environment (because SPPs are sensitive to the refractive index of the surrounding environment) the shape and the location of the SPR dip in the reflection intensity curve can be used to gain information about the surface. In order to take an advantage of this phenomenon, probe molecules are immobilised onto the central surface chip, and hence when a flow of analyte passes over the central surface chip, molecular binding interactions can be monitored between the analyte molecules and the probe molecules. A direct consequence of the molecular binding interactions is that the angular position of the dark band will shift, and hence the SPR dip will shift as well, which means a shift in SPR reflection intensity curve will be observed; indicating molecular interaction, see Figure 13. Monitoring changing in SPR response over time allows monitoring molecular binding interactions in a real time. While analyte is continually delivered to the central surface chip, analyte molecules start to bind to the probe molecules resulting in a rapid increas in SPR response. As the number of molecules binding and dissociating become equal, the SPR response level approaches equilibrium. When no more analyte is introduced into the system the analyte molecules will continue to dissociate resulting in a decrease in SPR response. The association rate constant K_a can be extracted from the behaviour of the binding response and likewise the dissociation rate constant K_d can be extracted from the unbinding response. The ratio between these two constants yields the binding

affinity of the system. An example for application of LSPR in biosensing technology is the Superchiral field induced-CD spectroscopy, which measures changes in the refractive index of dielectric environment surrounding chiral plasominc nanostructures. These changes are induced once the analyte molecules lie within SPPs regions and hence induce shifts (red shift or blue shift depending on the molecular chirality of the analyte molecules) in LSPR wavelengths following the relationship shown in equation 15 chapter3. More details are presented in chapter 3.

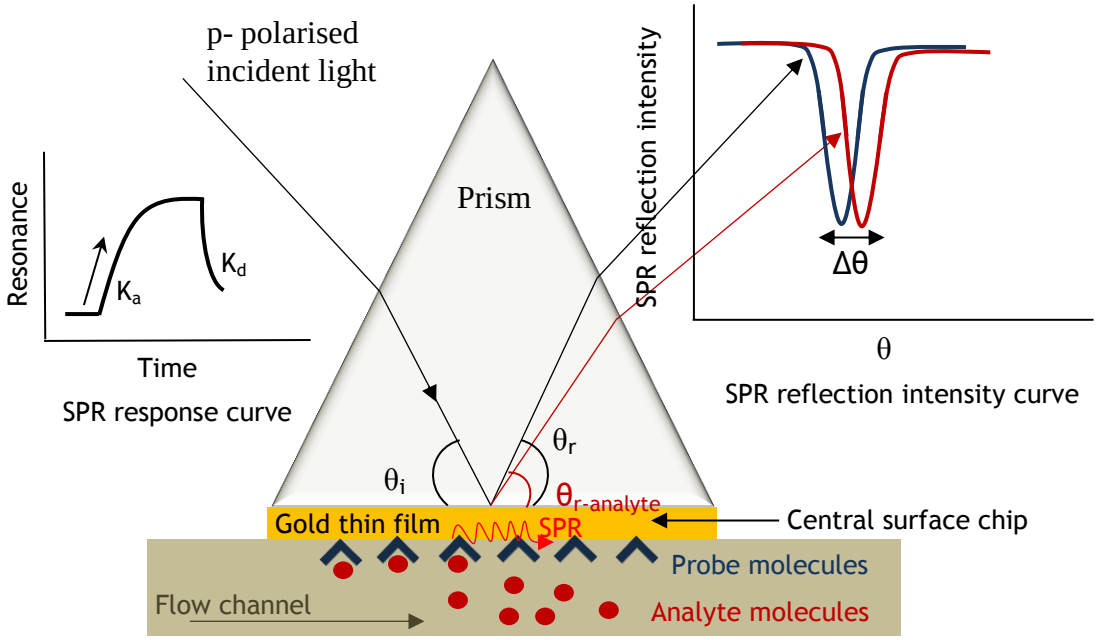

Figure 13: Schematic illustration for SPR spectroscopy. SPR can be excited on a central surface chip when p-polarised light incident by a certain angle called *resonance angle*, denoted by θ_i, which allows light to be absorbed by the gold free electrons. Reflection from central surface chip with immobilised probe molecules is denoted by θ_r and reflection from central surface chip with immobilised probe molecules plus analyte molecules is denoted by by $\theta_{r\text{-analyte}}$. SPR reflection intensity may change from θ_r to $\theta_{r\text{-analyte}}$ by a value of $\Delta\theta$ indicating analyte detection, see SPR reflection intensity curve on right. Location and value of $\Delta\theta$ is sensitive to SPR on the central surface chip which is itself sensitive to the refractive index of central surface chip and hence varies with analyte concentration. Rate of molecular binding interactions between probe molecules (navy angular shape) and analyte molecules (red filled circles) is monitored via SPR response with time, see SPR response curve on left. In SPR response curve, Ka and Kd denote the association and dissociation rate constants, respectively. The ratio of these two constants yields the binding affinity of the system.

2.1.4. Plasmonic metamaterials

As it already mentioned, this chapter describes the nanofabrication of the plasmonic nanostructures i.e. plasmonic metamaterials. Plasmonic metamaterials are materials made out of metals, like gold or silver that have free electrons (conductive electrons) in their outer orbitals i.e. plasmon. Plasmons enable such metals to support plasmonic surfaces. A unique aspect of the plasmonic surfaces is to produce the evanescent fields; which emit photons at the same frequency as of the photons of the incident light. This provides an extra electromagnetic field source for the nearby molecules which is why they glow. This property of the surface plasmon is really useful and is being applied in a number of disciplines; a common example is their usage in biological sensors [38].In general, since the SPPs arise on metal/dielectric interfaces; and because SPPs is oscillating within a fraction of the wavelength, any small disturbance caused by external element, e.g. the adsorption of a biomolecule, could affect the homogeneity of its oscillations, and hence sense particles comparable to the length scale of spectroscopic incident light or even less. However, some circumstances should be concerned here to achieve typical consequences; for example, because the dielectric constant is frequency dependent [37], the resonance condition for gold or silver metal is justified only at visible band with water and at IR spectrum with air. Besides, the dielectric constant of the medium should be less than that for the metal [37,38,42]. Although as circumstances are not difficult to be achieved, still limit the application for a certain metals, certain solutions and certain wavelengths. From other hand, the fact that the metamaterials shapes and structures affect the surface plasmon resonance [53], this might confine researchers to design metamaterials in a way when a triple match: between the incident wavelength of spectroscopic instrument they use (like CD spectrometer), the length scale of the plasmonic surface, and the target proportions (the molecule keen to be sensed) is become possible.

2.2. Theory and background

2.2.1. Electron beam- substrate surface interferences

As mentioned above, electron beam lithography uses a focused electron beam as a means of drawing geometrical features on a matrix of substrate. In principle, when the electronic beam strikes the surface of this matrix, which is represented by the resist film, it is believed that three possibilities might occur depending on the nature of the interaction. These are:

1. The electron beam might be forward scattered. This is when the electrons are deflected by the molecules of the resist as a consequence of elastic collisions. This causes the electron beam to be broadened gradually. The width of the electron beam increases with increasing thickness layer of the resist. It also increases with decreasing energy of the electron beam. Generally, the broadness of the electron beam creates broadened feature sizes. Thus, the width of the electron beam can be a problematic issue. Recently, S.K. Dew and his group simulated the electron beam profile as it strikes the resist layer at energies of 3keV and 10keV. This simulation is shown in Figure 14 below. According to these simulations, the broadening of the electron beam increases with decreasing accelerating voltage. It can be seen that the width of the beam increases towards the base as the thickness of the resist increases. At 60nm thickness the electron beam accelerated with 3 keV approaches a size of 50nm, while the electron beam accelerated with 10 keV approaches a size of 30nm for the same thickness[2 Chapter(2) pp13].

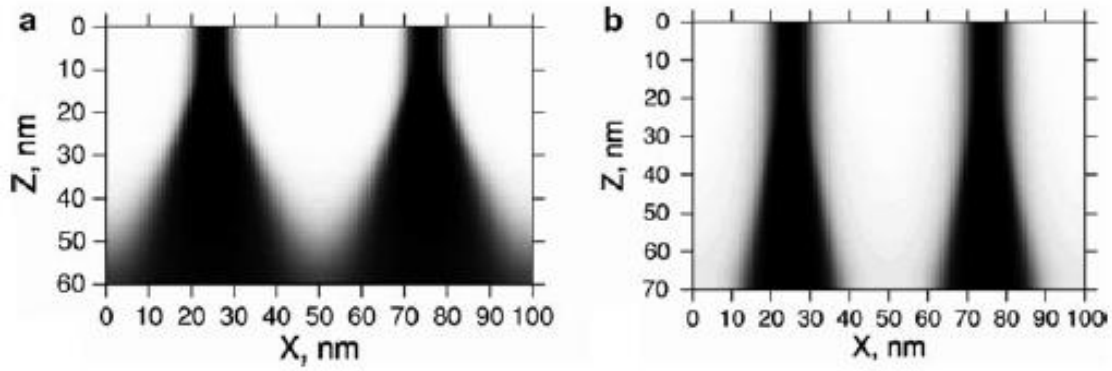

Figure 14: Simulations of two parallel beams of electrons. In **a** and **b**, the electron beam expands with increasing the thickness layer of the resist. The expansion with 3kV accelerating energy (shown in a) is almost a double of the expansion of 10KV one (shown in b). This is accrued as a result of the forward scattering by the molecules of the resist. This Figure was taken from [2 Chapter(2) pp13].

These simulations are in agreement with the view of Rai-Rechoudhury who suggested in 1997 that the electron beam diameter is proportional to the thickness of the resist layer and conversely with the accelerating voltage of the electron beam. This is expressed by the following equation:

$$d_f = 0.9 \, (R_f \, / \, V_b)$$

Where d_f is the effective diameter of the electron beam due to forward scattering, the R_f is the resist thickness and V_b is the electron beam voltage in kilovolt [1 Chapter(2) pp158].

2. More elastic collisions might be due to the electron beam being back scattered by the substrate surface. This arises when the electron beam penetrates through the resist and strikes the molecules of the substrate, like silicon. This causes the electrons to be deflected by relatively large angles and being back scattered through the resist again. In this case, the electrons will be scattered distant from their incident beam. This means the proximal region of the resist will receive a non-zero exposure dose (Figure 15), which causes `the electron beam proximity effect`, a very common problem in nanofabrication. The proximity effect varies depending on two main factors. It depends on both the substrate materials (low molecular weight substrate materials have less effectiveness than high molecular weight substrate materials) and the electron

beam energy. The electron beam launching with high energy causes the electron beam proximity effect to expand microns away from the incident point. This ends up with overexposed and large features [53]. Nevertheless, the research group of Yoshihide Kato believe that increasing the electron beam energy has the advantage of reducing the proximity effect even if the pattern density is changed and hence improves the resolution [54]. In fact, two strategies can be employed to help reduce the proximity effect: a) reduce the thickness of resist layer to, indirectly, restrict the features; b) reduce the electron beam energy to confine the brightness of the electron beam and hence the resolution of the writing process [2 Chapter(2) pp13].

3. In addition to the elastic collisions, the electron beam probably undergoes inelastic collisions with the molecules of the resist. This causes the outer electrons of the resist molecules to be discharged a few nanometers away from their original atoms. This is with a range of energy varied between 2 eV to 50 eV. This leads to the formation of ` Secondary Electrons` (SE) illustrated in Figure 15 below. The SE also contribute to the proximity effect mentioned above. Although their contribution is only a few nanometers, they limit the resolution of the fine detail features [1Chapter2 vpp159, 2 Chapter(2) pp13]. Thought, another issue might contribute to the proximity effect; this is if the secondary electrons are characterised as `fast secondaries`. In such cases, the energy level is much higher than the normal energy levels. It might approach 1000 eV. This affects the proximity effect by a few tenths of a micron. The fast secondaries form only a small fraction of the secondary electrons [1 Chapter2 pp159].

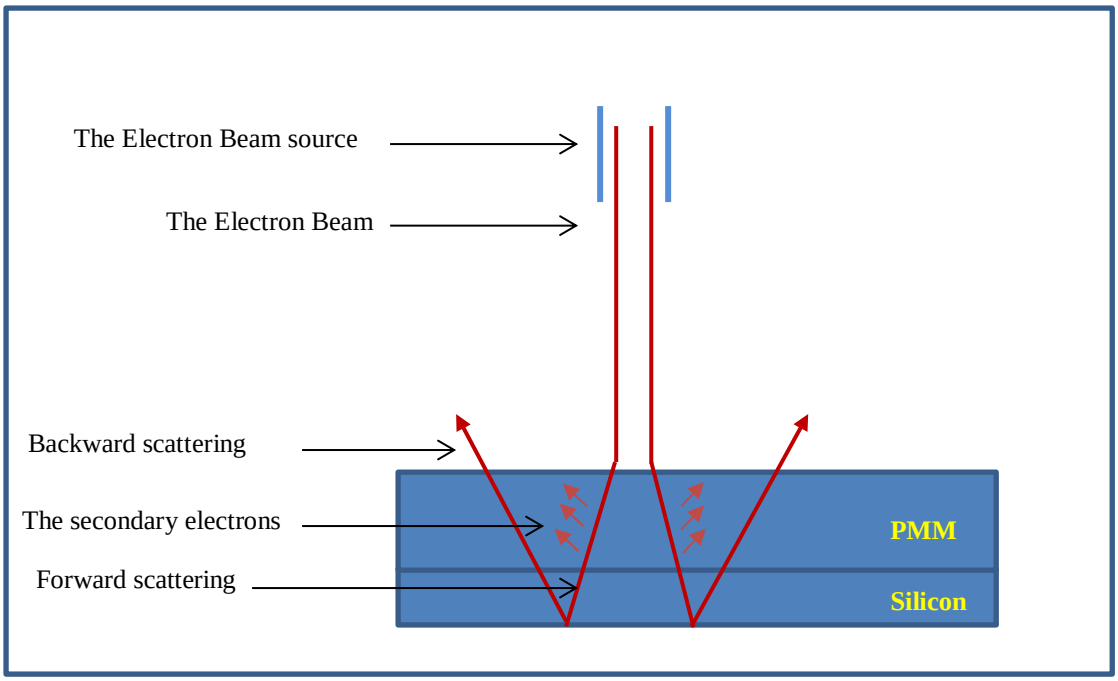

Figure 15: The path of the electron beam striking silicone substrate with PMMA resist on the top. The electron beam is either forward scattered; or elastically releases secondary electrons from PMMA molecules; or backscattered.

2.2.2. Electron beam- PMMA resist interferences

PMMA resist is an organic transparent polymer synthesised by the process of the polymerisation of the monomer methyl methacrylate to form the poly methyl methacrylate PMMA, chemically formulated as $CH_2=C(CH_3)COOCH_3$.

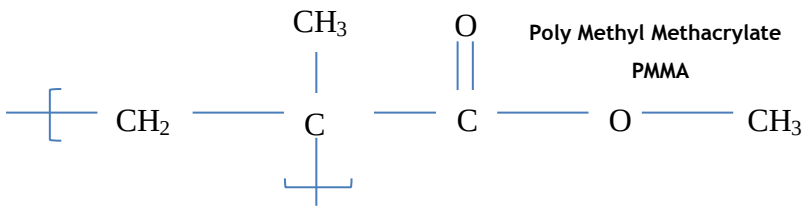

An analogue with ZEP and HSQ, this polymer is used in electron beam lithography as a resist layer. In principle, the writing process is performed upon either positive tone resist or negative tone resist. In positive tone resist, like PMMA and ZEP520, if the electron beam delivers enough energy to ionise the resist molecules, the low solubility of the resist molecules in the developer is

altered to high solubility value. The ionization of the resist molecules aids the polymer chains to break into smaller chains, more soluble than the larger chains. Therefore, in the development process the exposed area of the resist with small fragments chains is removed and the unexposed area with long chains remains (Figure 16 a).

In contrast, negative tone resist consists of small and soluble chains of polymers. Here the electron beam helps the small and highly soluble chains to combine together to form long and low soluble chains. This process called the `cross-linking reaction`. Because of the cross- linking reaction, in negative tone development process the exposed area is retained and the unexposed area is removed (Figure 16b). A common example for negative resist is the HSQ (hydrogen silsesquioxane) [1Chapter(2) pp(205,210),2Chapter(2) pp14, (55-57)]

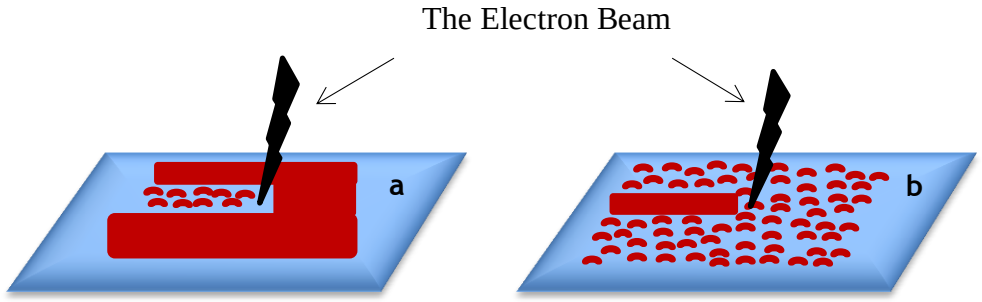

Figure 16: Cartoons of positive tone resist (**a**) and negative tone resist (**b**).

For nanofabrication work of this project a positive tone of PMMA resist has been used. Fundamentally, the PMMA resist consists of long chain polymers, with a mass of 496 and 950kDa. Such long chains require many scissions to be fragmented into small and soluble chains. The fragmentation process is influenced by three main factors, these are: the dose of the exposure, the duration of the exposure and the accelerating voltage of the electron beam. Regarding **the dose exposure domain**, S.K. Dew and his group calculated the

exposure dose of 50, 100 and 150μC/cm^2 on PMMA resist. They believe that at a dose of 50μC/cm^2; the fragments sizes are varied between a single to twenty monomers, which give a maximum contribution of 13%. While in exposure dose of 100μC/cm^2, the fragment sizes are varied between a single to twelve monomers, which give a maximum contribution of 18%. Increasing the dose to150 μC/cm^2, the fragment sizes are varied between a single to nine monomers, with a contribution of 25%. It is clear that increasing the dose value leads to smaller fragment's sizes (Figure 17 a). Apparently, this study was necessary to illustrate the spatial variation of the dose caused by the variation of the scattering; which caused by different fragment sizes. The spatial variation of the dose was suggested by the same group, assuming a spatial dose scattering by fragment size of less than ten monomers, and accelerated by 10keV voltage. This prediction ended up with a 3D exposure scission event shown in Figure 17 b. This theoretical calculation could also apply to other positive and negative tones resist [2 Chapter(2) pp15].

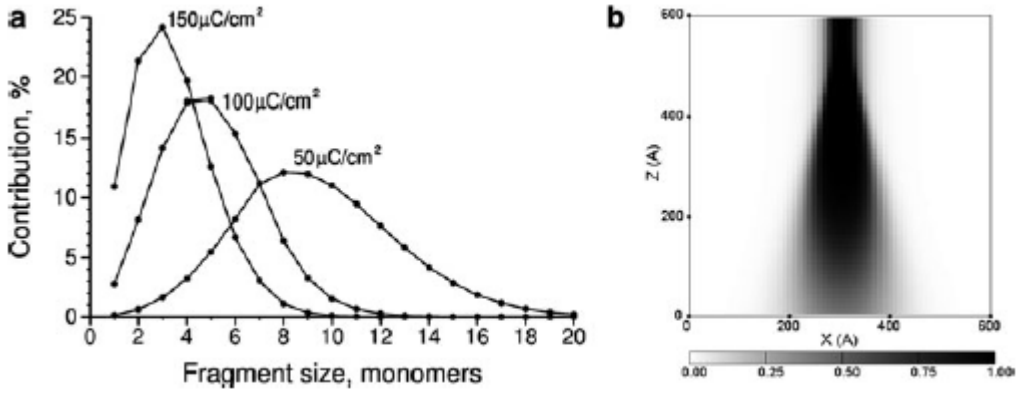

Figure 17: Theoretical simulations of the dose exposure domain on the PMMA resist. **a** shows three doses of 50, 100 and 150μC/cm^2 with their corresponding contributions of the fragments sizes. **b** shows 3D spatial distribution of the dose scattered by less than ten monomer fragments sizes. This Figure was taken from [2 Chapter(2) pp15].

It can be concluded from Figure 17a that the value of the exposure dose plays a key role in the final quality of resolution, and hence the nanofabrication work. The effect of increasing the dose value is shown in Figure 18 below. This Figure shows the cross section profile of 55nm PMMA resist, patterned with a 70nm

grating pitch by accelerating voltage of 30keV. Different doses (line doses) were applied here, these are 2.0 nC/cm, 4.5 nC/cm and 7.0 nC/cm, shown in a, b and c, respectively. An increasing in interlines width with increased dose exposure leads to broadened feature sizes and poorer resolution [2 Chapter(2) pp17].

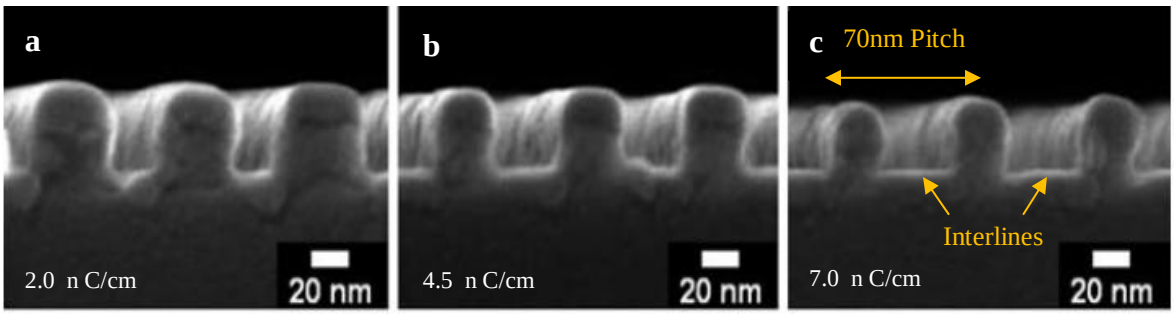

Figure 18: The effect of increasing the dose values on the grating of 70nm pitch on 55nm PMMA resist. The dose (line doses) values of 2 nC/cm, 4.5 nC/cm and 7.0 nC/cm are shown in **a**, **b** and **c**, respectively. These images were adopted from reference [2 Chapter(2) pp17].

The other concern is **the time exposure domain**. Recently, a research group led by Yoshihiko Hirai had demonstrated their theoretical estimation for the scission of the time exposure in molecular detail. They used the Molecular Dynamics (MD) simulations to analyse the atomic-scale region. They assumed a 4nm PMMA film thickness, with 10nm width, on silicon substrate. The exposed line width was 2nm and the PMMA molecular weight was 5000 (Figure 19) below. They believe that the process of fragmentation to small sizes polymer chains is proportional to the exposure time. This is because the fragment sizes in an exposure time of 7 ps were smaller than the fragment sizes of the exposure time of 3 ps. And the fragment sizes of an exposure time of 3 ps were smaller than the fragment size of the exposure time of 1ps [58]. This is shown in the Figure 20 a, b, c and d:

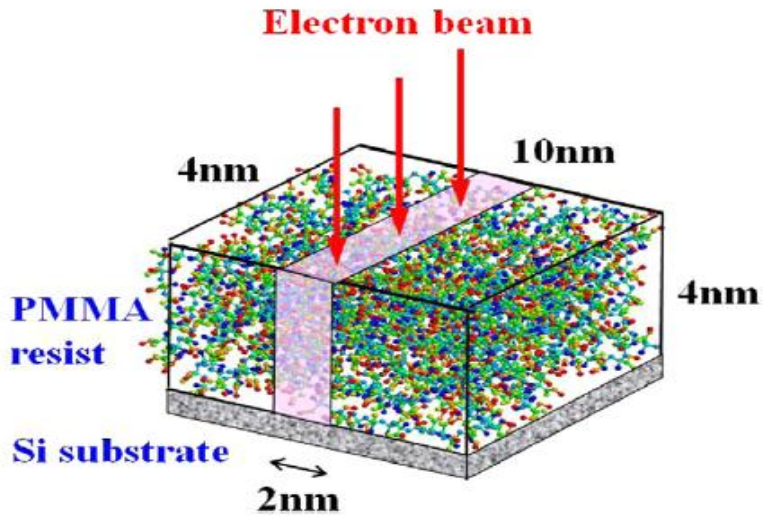

Figure 19: The model of Molecular Dynamic simulations for PMMA resist on silicon substrate. This model was used to conclude the effect of the time domain on the exposure scission, in molecular level system. This Figure was adopted from reference [58].

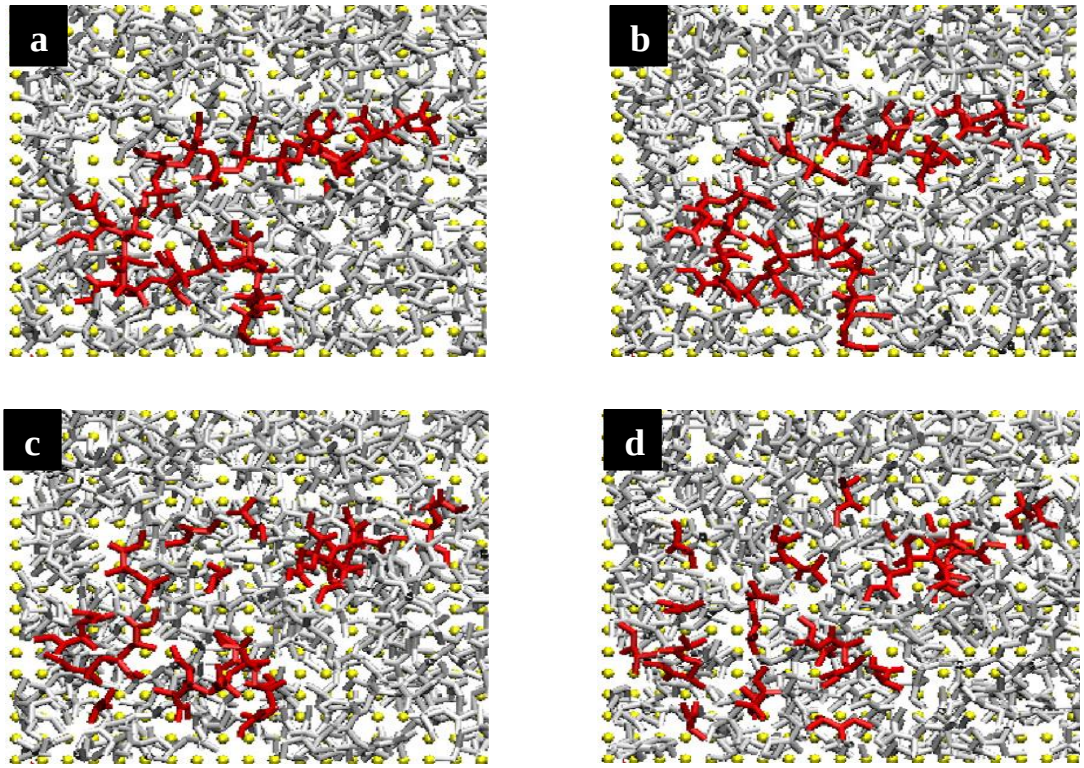

Figure 20: The theoretical estimation of the scission of the time exposure domain in molecular level. The highlighted molecules are the molecules experiencing fragmentation event. **a**, **b**, **c** and **d** show the effect of time exposure at 0 ps, 1ps, 3ps and 7 ps, respectively. This Figure was adopted from reference [58].

The effect of the **accelerating voltage domain** (which represents a key objective of the electron beam interferences with the PMMA resist) represents a further cause for concern in the technique of EBL. It has been found that increasing the accelerating voltage of the electron beam increases the absorption level for the energy by the PMMA resist. This effect was demonstrated in the same study for the model shown in Figure 19 above. Again, the Monte Carlo method was used to simulate the energy distribution absorbed by PMMA resist on silicon substrate. Three values of acceleration voltage were used in this simulation, these are: 1keV, 10keV and 100keV. It has been found that an electron beam with acceleration voltage of 1 KeV has the largest and the broadest distribution level of energy. This is due to electron scattering by the sample molecules. For 10 keV, more energy absorption and less electron beam scattering were observed. Eventually, the best level of absorption with the lowest distribution was achieved by 100 keV (Figure 21). The 100 keV supports the highest resolution of the writing process in electron beam lithography [58]. For our nanofabrication work, a 100 keV was used for all experiments.

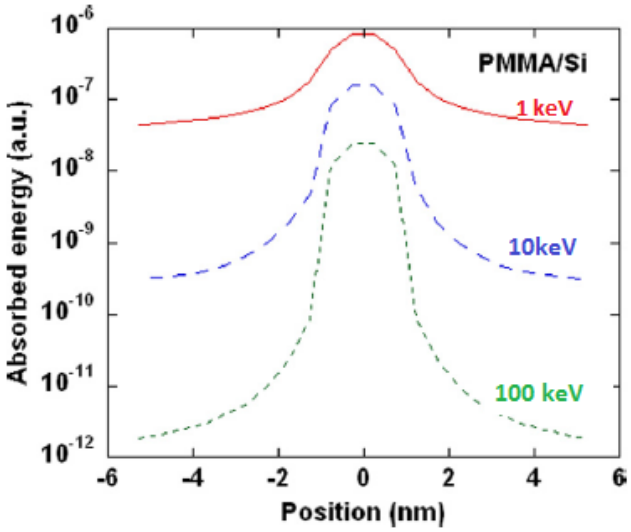

Figure 21: The Monte Carlo simulation for the effect of acceleration voltage domain. Note that by increasing the accelerating voltage; the energy level absorption increases and the energy level distribution decreases. This Figure was adopted from reference [58].

2.2.3. Resist Development

Development is the process of dissolving the small fragments of the resist by a specific solvent for a certain period of time. This is performed by immersing the substrate into a solution of a developer (usually a mixture of organic solvents). The developer dissolves the small fragments of the exposed area for the positive tone resist, or dissolves the non-cross-linked small fragments of the unexposed area for the negative tone resist. When the developer penetrates through the resist matrix it starts to interact with the small fragment of the resist. This interaction leads to the formation of a layer of gel around the fragment. This is shown in Figure 22. Once the fragment is surrounded by the gel layer completely, it starts to detach from its original matrix, and diffuse into the solvent. The developer starts to react with the long polymer chains which ultimately dissolve it.

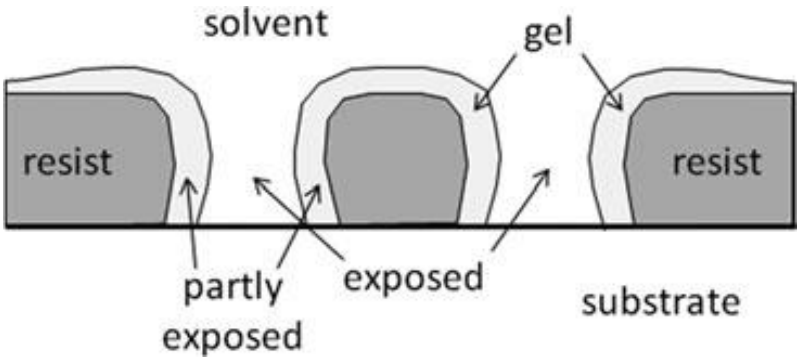

Figure 22: The layer of the gel forming around the small fragments of the resist. This Figure was taken from reference [2 Chapter(2) pp16]

The thickness layer of the gel depends on the fragment size and the strength of the developer. A typical developer for PMMA resist is the 1:3 MIBK (methyl isobutyl ketone) with IPA (isopropyl alcohol) [2 Chapter(2) pp16]. This developer was used for the fabrication work described in this thesis.

Important factors in the developing process are temperature and time dependence. Long incubation times and high temperatures increases the reaction, which leads to low resolution. In contrast, short incubation times and

cold development limit the reaction to yield small fragments only, which is required for high resolution [2 Chapter(2) pp20, 59]. For optimal resolution we have developed our samples at 23C° for 25 second.

Another important concern is the relationship between Exposure dose and the development process. Some research groups have theorised that `*Exposure and development are interrelated as short exposure with long or aggressive development can be equivalent to heavier exposure with short development*`. The determination of the optimal parameters for both exposure and development is a crucial issue in nanofabrication work since it helps to minimise several types of morphological damages, such as pattern collapse or islands formation [2 Chapter(2) pp15]

2.2.4. Forms of the morphological damages

`**Underexposure**` **or** `**underdevelopment**` occurs when the developing process is not sufficient to fully dissolve the resist fragments in the exposed area. This might happen when the time is too short or the developer is not strong enough to dissolve the fragments properly. An example of this problem is shown in Figure 23(a, d). An opposite problematic effect is the `**overexposed**` or `**overdeveloped**` pattern. This is observed when the developing process surpasses the limit of the dissolving process, i.e. excessive clearance. This might happen when the time is too long or the developer is strong enough to dissolve the long chain fragments of the resist. An example of this problem is shown in Figure 23(g, h). In addition, the problem of overexposure or overdevelopment can be observed in other form, such as the `collapsed` which forms when the interline resist walls collapse in patterns with high density features. The high density features consists of a pattern with small interline resist walls and large pitches. An example for collapsed features and the concept of interlines and pitches are shown in Figure 23 (c, f) and 11 (b, e), respectively [2 Chapter(2) pp16].

More morphological damage caused by overexposed or overdeveloped problems can be observed, in particular with gratings of 30nm. This can result in the

formation of `Islands`. This occurs when the `*grating is partly or entirely destroyed by the redistribution of PMMA that tends to form islands at irregular locations. Formation of such globular islands or percolation networks is known to occur in immiscible liquids that undergo a phase transition. Since mixtures of PMMA fragments with most common EBL developers have regimes of limited miscibility, a phase separation can occur*` [60]. Examples of the Islands formation are shown in Figure 23(i, j) [2 Chapter(2) pp19].

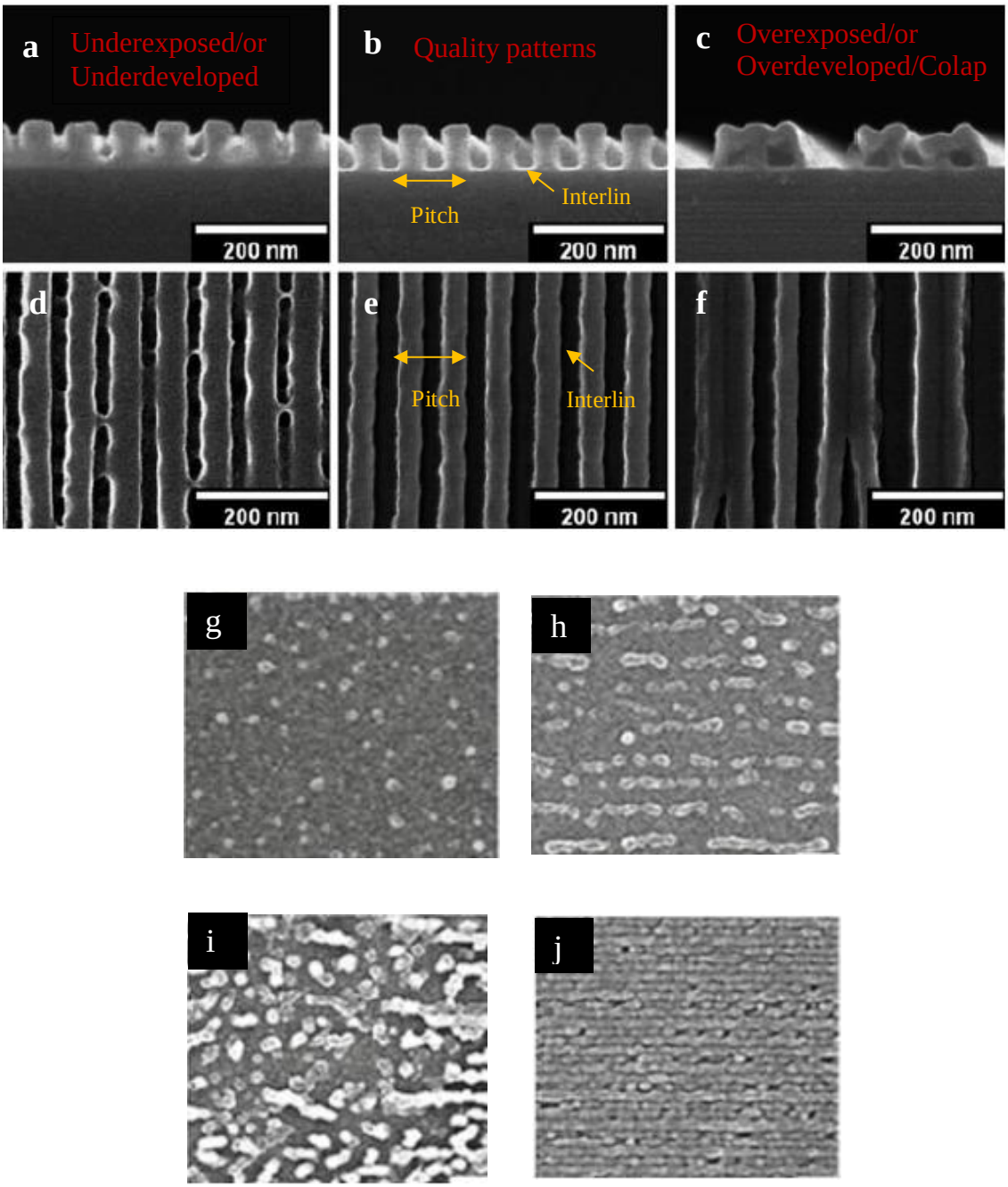

Figure 23: This Figure shows the common morphological damages resulting by the underexposed/or underdeveloped and the overexposed/or overdeveloped problems. The **a** and **d** shows a morphological damages caused by underexposed or underdeveloped problem. The **b** and **e** explain the concepts of the pitch and the concept of interline on a quality pattern. The **c** and **f** show a morphological damages caused by the overexposed/or overdeveloped which lead to the pattern collapse problem. The **g** and **h** show a morphological damages resulting by the overexposed / or overdeveloped problem. The **i** and **j** shows a morphological damages caused by the overexposed/ or overdeveloped which lead to the problem of the Islands formation. Note that the a, b and c are cross section images while the rest are plane images. All images were adopted from reference [2 Chapter(2) pp19] .

It is clear that morphological damage might occur as a result of incorrect choice of exposure dose and the development parameter. This is particularly the case with small features and high density patterns. K.Dew and his group demonstrated the variations of the dose with the variations of the grating periods (pitches), and they were able to optimise these variations to avoid the morphological damages in question [2Chapter (2) pp20], see Figure 24. Figure 24 illustrates common morphological damages resulting from different exposure doses on different periods of gratings. Exposure to low dose results in underexposour damages, while exposure to high dose results in phase separation (micilles) and collapse. Gratings with periods of 20 and 30 nm support phase separation (micilles) while gratings with periods of 40 nm and larger support collapse.

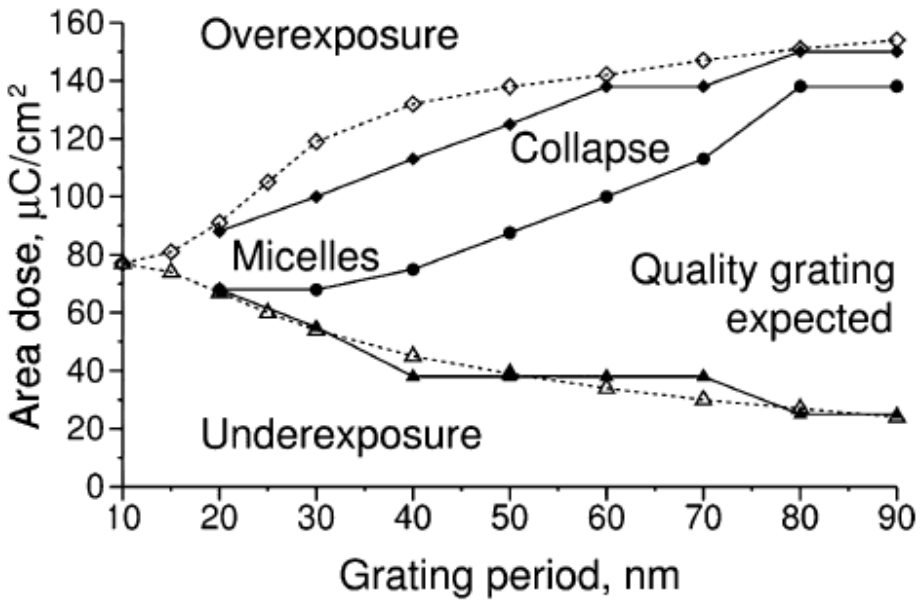

Figure 24: The distribution of the morphological damages resulting by the variation of the dose exposure on different periods of gratings. Filled symbols represent experimental results from Figure 6, open symbols represent the results of theoretical modelling, triangles represent the underexposure damages (insufficient clearance); diamonds represent the overexposure damages (excessive clearance), and circles represent the collapse or phase separation; which lead to micellized patterns. This Figure was taken from [2Chapter (2) pp20].

2.3. Instruments:

2.3.1. VB6 UHR EWF Maschine

The main tool in Electron Beam Lithography is the writing machine which comprises three main parts, namely: the *gun* which generates the electron beam; the *column* which focuses the electronic beam; the *stage* where the substrate is loaded on to write the pattern [61].

In the JWNC the writing machine employed is the *Vistec Vector Beam 6 Ultra High Resolution Extra Wide Field (VB6 UHR EWF)*. Its schematic plot is shown in Figure 25 below. This Figure shows the column and the main chamber. The column consists of a thermal emission field electron beam gun, located on the top. This gun operates with acceleration voltages of 50 keV and 100 keV. The electronic beam is generated with a Gaussian profile system, ranging between 4 nA to 128nA. This is to generate a minimum spot size less than 4nm and maximum spot size greater than 45nm. The column also consists of a cluster of electromagnetic lenses, which shape and focus the beam of electrons coming from the gun. The focusing process is performed by a fully automated alignment system. Underneath the electromagnetic lenses are the blanker plates, where the electron beam passes through to be switched to On/Off depending on the writing position. Since the VB 6 is operated by the vector beam system, the writing is processing in raster lines and the electron beam is switching to On/Off depending on the input data of the location. Finally, the exact location of the writing point on the sample is determined by the deflectors, which are located inside the final lenses of the column.

Following the column is the main chamber. The main chamber contains an electronically controlled movable stage. This is a high precision laser-controlled stage. The stage controllers use the Zeeman Effect to split the line of the He-Ne laser beam. Each splitting frequency is incident on a mirror attached to the stage. This is in X and Y directions. The reflected beam then is detected by high speed electronics to determine the exact location of the stage. Thus the precision of the stage movement is limited by the fraction of the laser wavelength. Therefore, the accuracy of the stage motion in VB6 UHR EWF is

λ/1024 = 0.6 nm [1 Chapter(2) pp172, 61]. The main chamber also contains the sample holder. Where the substrates loaded on, and this is loaded on a multi-substrates load lock inelegant stage, with a piece of ≥ 1 cm. Finally, the main chamber contains the vacuum turbo pumps, which are attached to the back of the main chamber to keep all the system under vacuum [61].

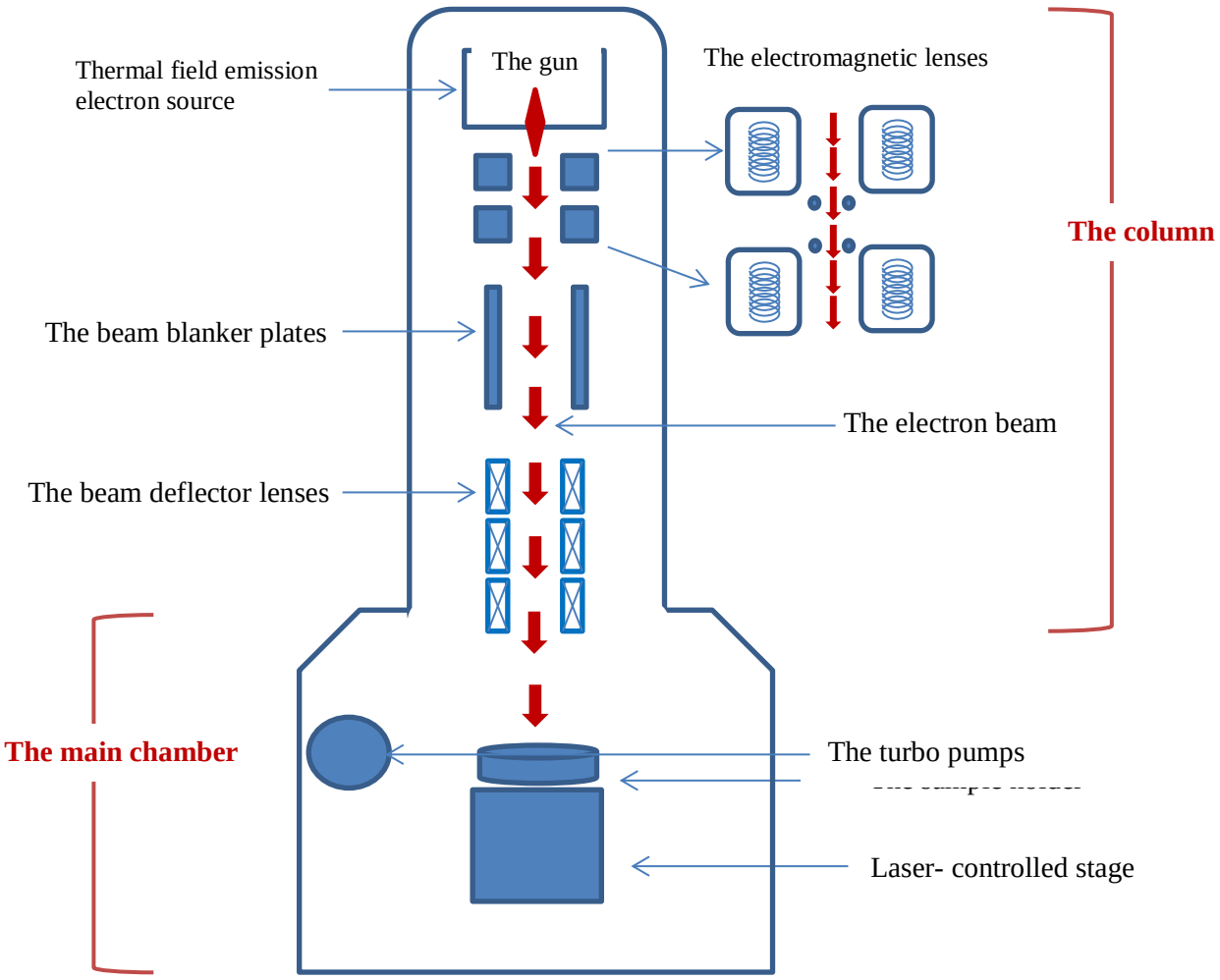

Figure 25: The scheme of the VB6UHR WEF machine. The Figure shows the column and the main chamber. The column consists of the electron beam gun, the electromagnetic lenses, the beam blanker and the beam deflector. The main chamber consists of an electronically controlled movable stage, the sample holder and vacuums turbo pumps. All the system is working under vacuum.

Figure 26 below, shows the VB6 UHR WEF machine in JWNC cleanroom and its controlling unit. Figure 27 shows few images of the sample holder in this

machine, and it also shows the operator examining the samples on the holder to fit their positions. This machine is operated by specialists including engineers and technicians.

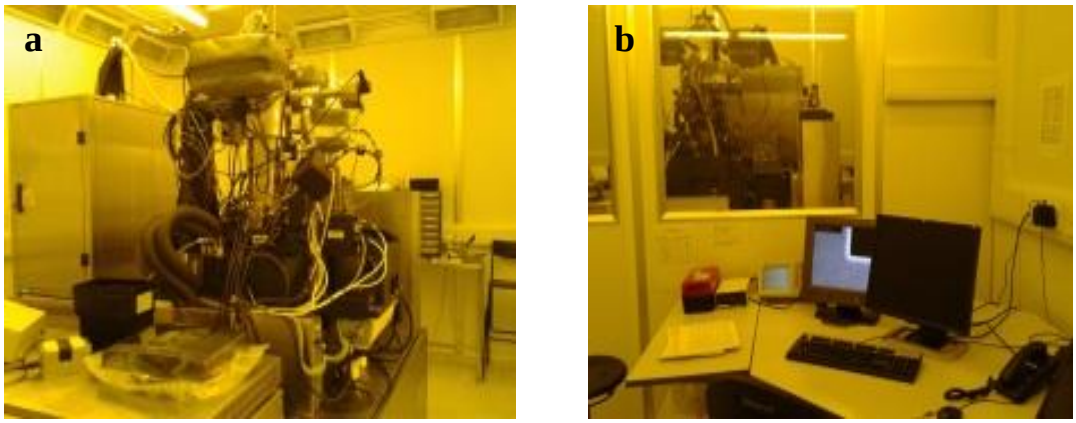

Figure 26: Photograph images of Vestic VB6 UHR EWF machine located in JWNC cleanroom. **a** shows the VB6 machine. **b** shows the controlling unit for the machine in separate room.

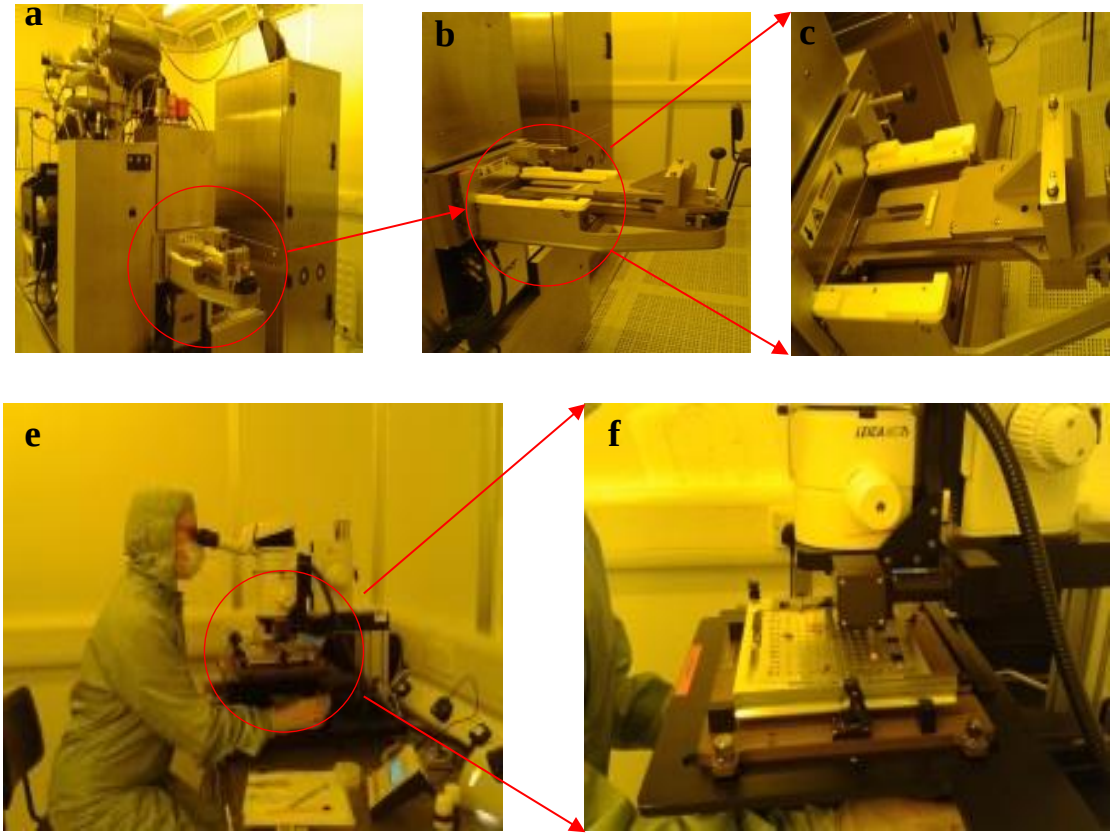

Figure 27: Photograph images of the sample holder in VB6 UHR WEF machine in JWNC cleanroom. **a**, **b** and **c** show the sample holder. **e** and **f** show the operator examining the samples on the holder.

2.3.2. Plassys II MEB550S E-beam Evaporator

This machine is used for the metallisation process. The metallisation process involves coating a surface with a layer of metal. In nanofabrication arena a synonym for metallisation is `evaporation`. This is because the metallisation involves the evaporation of the metallic under vacuum. The process triggers when a coil of tungsten filament gives off a current of electrons. This occurs if the tungsten filament (which is located very close to the metallic crucible) is deployed as a cathode under high potential voltage. The electronic current is then guided and accelerated by a magnetic field towards the crucible of the metallic, which represents the anode (Figure 28). Here the metallic atoms start to transform to gaseous phase as a result of very high heating-power densities. And because it is under vacuum, these atoms are naturally guided towards the substrate surface. There, it will re-condense to solid state in a smooth and uniform film. The process of condensation is referred to as a `deposition` [62].

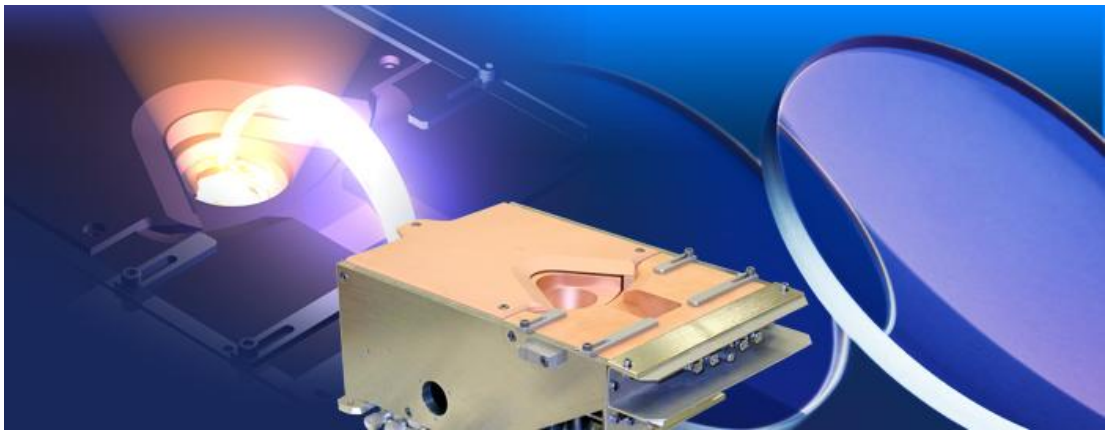

Figure 28: The path of the electronic beam which is guided by the magnetic field inside the main chamber of Plassys II machine. This image was taken from reference [63].

Metallisation conditions are varied depending on the specifics of each deposited metal. Regarding the metals used in this project, we emphasised the details of Al, Au, Ni and Ti, which have been listed in table 2 below [64].

Table 2: Specifications of metals used in this work, like: evaporation guide for the elements`, vacuum level, crucible temperature, crucible type, effusion cell type, E-beam & Plasma choices. All are taken from reference [64].

Element to be Vaporized		**Al (mp 660)**		**Au (mp 1064)**		**Ni (mp 1455)**		**Ti (mp 1660)**	
Recommended Effusion Cell or Evaporator System		Cold Lip		High Temp or Single Filament		High Temp		E-beam or High Temp	
Recommended Crucibles		PBN		Al2O3, PBN,VC		Al2O3, VC, (BeO)		TiC	
Vapor pressure	temperature of crucible	10^{-8}	685	10^{-8}	807	10^{-8}	927	10^{-8}	1067
Vapor pressure	temperature of crucible	10^{-6}	812	10^{-6}	947	10^{-6}	1072	10^{-6}	1235
Vapor pressure	temperature of crucible	10^{-4}	972	10^{-4}	1132	10^{-4}	1262	10^{-4}	1453

Vapore pressure in torr

mp = melting point in degrees Celsius

Temperature of crucible in degrees Celsius

PBN = pyrolytic Boron Nitride.

Low Temp = low temperature effusion cell

High Temp = high temperature effusion cell

E-beam = electron beam. Elements evaporated by E-beam do not use a crucible

VC = Valved effusion cell

The Plassys II MEB550S E-beam Evaporator (shown in Figure 29 below) is used for the automated metallisation process. It operates under vacuum (10^{-4}-10^{-7} mbar) with cryogenic pumping of the two main chambers. The entire system is fully controlled by the computer. Also the machine is equipped with a holder which can be loaded with either four inch wafers or multi pieces of substrates. The holder rotates during the deposition process to achieve uniform thin film. Eight metals can be loaded in 12 cc crucibles located inside the main chamber, these are: Titanium, Nickel, Nickel/Chromium (60:40), Germanium, Gold, Platinum, Molybdenum and Aluminium. The deposition is achieved thermally by means of tungsten filament, which emits 10keV electron beam energy of 10kW power. An individual or multi- layer deposition can be performed in a single run [65, 66].

For present study, single and double layer deposition routine have been used. The single layer deposition routine was used for metals such as Ni which readily binds to the substrate surface. The double layer deposition routine was used for metals which require an adhesion layer to stick to the surface, e.g. a thin layer of Titanium was used to attach Gold.

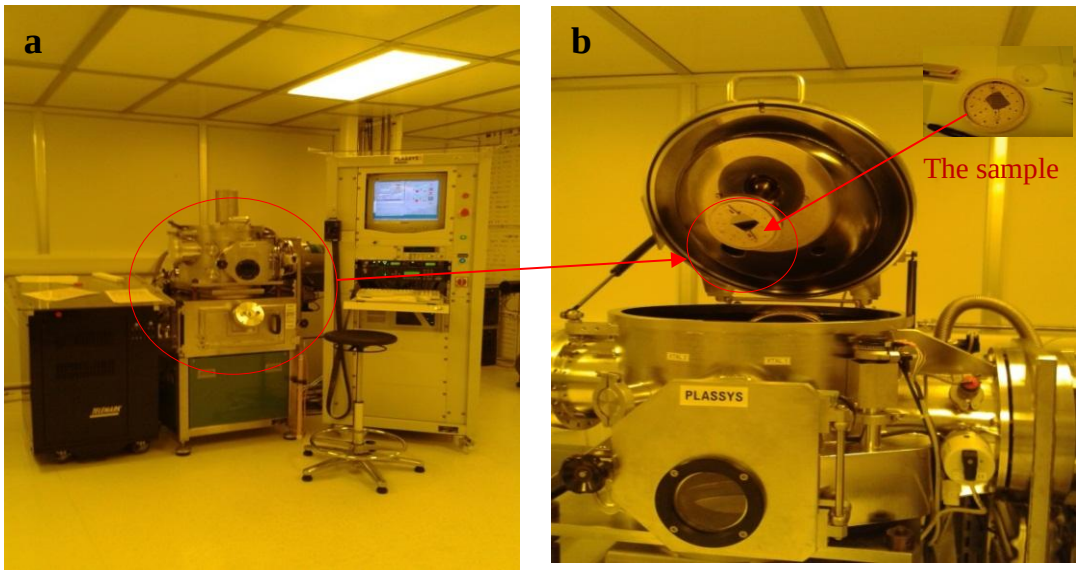

Figure 29: Photograph images of the Plassys II machine located in JWNC cleanroom. **a** shows (from left to right) the power supplier, the main chamber of the machine and the controlling unit. **b** shows the holder with the sample loaded on it.

2.3.3. Scanning Electron Microscope (SEM)

This represents the instrument used to collect images of nano-scale features. Scanning electron microscopy `SEM` is a technique which uses electromagnetic lenses and an electronic beam to illuminate samples under vacuum [32 Chapter(2) pp147, 65Chapter(1) pp2, (67-69)]. By using this technique it is possible to achieve a resolution of 0.05 nm images which is 4000 times better than a resolution achieved by optical microscopy [68]. The central parts of the electron microscope are the column and the main chamber (Figure 30). The column contains the electron beam gun located on the top, and a cluster of electromagnetic lenses to control the electron beam path. This column is joined with the main chamber. The main chamber contains the sample holder, the sample stage and the detectors.

The electromagnetic lenses consist of electrical coils and poles (Figure 30). When electric current passes through the coils, a magnetic field is created around these coils and induced around the poles. By specific arrangement for the electrical coils and the poles, one can create a well-defined magnetic field gap. Thus, when the electron beam passes through this gap it will be affected and hence, shaped [32 Chapter(5) pp(125,126), 68, 69].

The gun emits a beam of electrons when high voltage is applied, under vacuum, between its (cathode and anode) electrodes. This high voltage forces the electrons of the metallic surface of the cathode to leave their atoms. Then, these electrons are accelerated towards the anode and hence directed down the column. Along the column, the electron beam is collimated and electromagnetically shaped by the condenser lenses. This leads the electron beam to strike the surface with a well- defined spot size. The beam is directed to scan the surface of the sample in raster lines by a vector beam system.

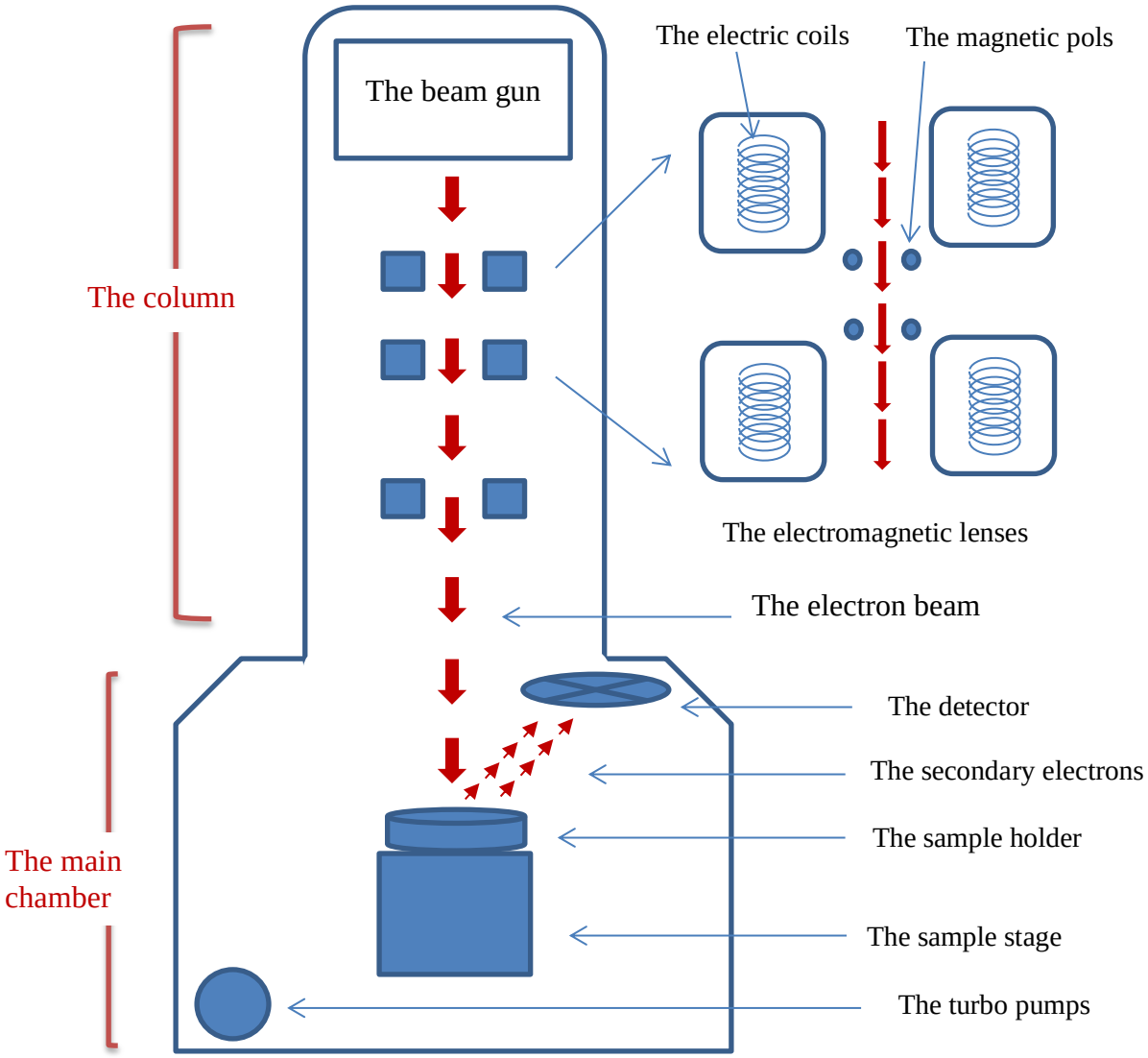

Figure 30: The scheme of the Scanning Electron microscope. Note it is very similar to the scheme of the VB6 writing machine shown in Figure 13. The SEM consists of the column and the main chamber. The column consists of the gun and the electromagnetic lenses. The main chamber contains the sample holder, the stage, the detector and the turbo pumps.

Theoretically, the imaging mechanism in SEM is based on the elastic and non-elastic collisions between the electron beam and the surface. When the electron beam hits the surface of the sample, several probabilities can occur. The electron beam can be back scattered as a result of elastic collision with the nucleus of the surface particles. In this case the electron beam is deflected by large angles to produce the `backscattered beam`. In addition, the electron beam can be deflected by small angles due to the composition and the structure of the sample. This leads to the `phase contrast` in the image. Also it is possible that the back scattered electrons hit the outer electrons of the surface particles in non-elastic scattering event. This causes the release of the `secondary electrons SE` from the atoms of the surface particles. Moreover, it is possible that the electron beam is attenuated by the surface. The level of attenuation reflects the variation of the thickness of the surface. This leads to the mass thickness contrast or most commonly the `amplitude contrast` in the image. Further, it is possible that the electron beam is scattered in specific directions, depending on the crystal structure of the sample. This leads to the `diffraction contrast` in the image. Additionally, the electron beam may force the atoms of the surface particles to emit X-rays with different wavelengths depending on the elemental composition of the sample. This reveals the `characteristic X-ray` spectrum of the sample. Finally, the electron beam might cause the atoms of surface particles to emit photons, this leads to the `cathodoluminescence` microscopy. On the other hand, when the electron beam transmits through the sample, its energy level is varied depending on the structure of this sample. This is because some of the electron beam energy is lost as a result of its interaction with the sample. Thus, the `energy loss` is able to provide important information about the structure of the sample [32Chapter(4) p(93-102), 68].

The different probabilities of the way of the electron beam to be reacted with the surface need to be detected with different types of detectors. Thus, the electron microscope styles varied depending on the type of the detectors that is used. Examples of the detectors that are used in scanning electron microscope are shown in the table 3 below [69].

Table 3: These are styles of some detectors using in scanning electron microscope in JWNC cleanroom. This table provided by the FEI company for the FEI NovaSEM 360 microscope.

Detector name	Tag	Vacuum mode	Detected signal
Everhard -Thornley	ETD	High Vacuum	SE, BSE
Through-lens	TLD	High Vacuum	SE, BSE
Low Vacuum	LVD	Low Vacuum	SE and BSE
Infra-red CCD camera	CCD	Any	Light, infra-red light
Helix	HLX	Low vacuum	SE
Solid-state backscattered electron	BSED	High Vacuum	BSE
Gaseous analytical	GAD	High Vacuum Low Vacuum	BSE
Low Voltage High Contrast Solid State	VCD	High Vacuum Low Vacuum	BSE
Special Low Vacuum (delivered with GAD and vCD)	LVD	Low Vacum	SE
to Multiplier Diode (Scintillation BSE or Cathodo-lumniiscence)	PMD	High Vacuum	BSE, Photons
id State Scanning Transmitted Electron Microscopy Detector	STEM I	High Vacuum Low Vacuum	Transmitted electrons
Energy-dispersive X-ray	EDX	High Vacuum	X-ray photons
Wavelength-dispersive X-ray	WDX	High Vacuum	X-ray photons

An important concern is the resolving power of the electron microscope. The resolving power, or most common the` resolution`, is the smallest distance could be observed between two points. For example, the resolving power of human eyes is 0.2 mm. This means that the smallest distance could be distinguished by human eye is 0.2 mm. The resolving power of the optical light microscope could approach a sub- micron. While the resolving power of the electron microscope could be less than <0.1nm, a resolution which approaches the atomic level. The resolution of an optical microscope is limited by the wavelength of the visible light; i.e. (400- 500) nm. While electrons have much shorter wavelength and so greater resolution. Practically, the resolving power of the electron beam could be controlled by the beam voltage and the electromagnetic lenses. The beam voltage controls the brightness. The electromagnetic lenses control the aperture size and the lens aberrations [68]. Experimentally, we achieved a resolution of few nanometers by the scanning electron microscope in JWNC cleanroom (Figure 31 below). Such resolution was very useful for the laboratory work. It helped to monitor the effect of intense irradiation laser by tracking the golden lumps on the gammadion structures (Figure 32). Also it helped to monitor the Collagen Calf Skin fibrillation process on the quartz and Si-wafer substrates (Figure 33 and Figure 34).

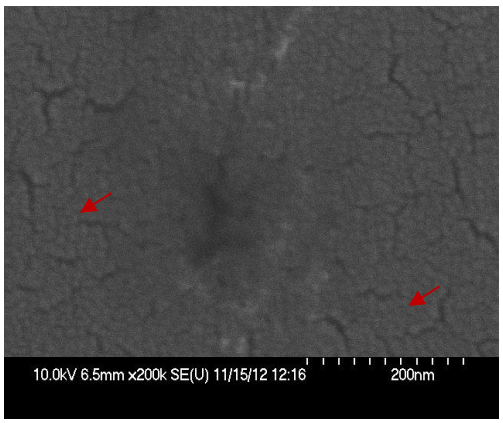

Figure 31: The surface of quartz substrate which shows details of ~2nm

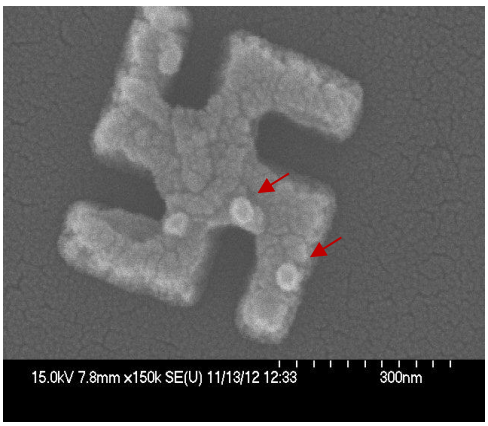

Figure 32: Gammadion was made out of Nickel and fabricated on quartz substrate. Note the gold lumps highlighted by the red arrows.

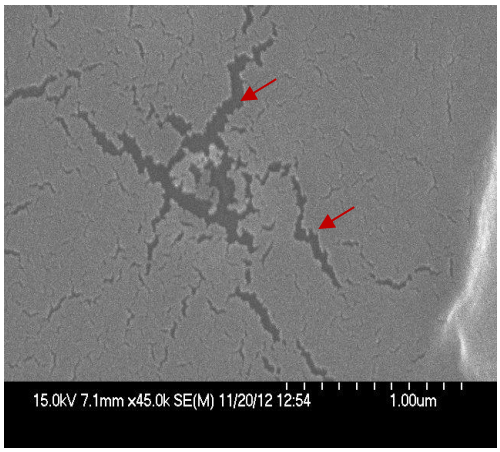

Figure 33: Ribbons of Collagen calf skin type III on quartz substrate (before fibrillation).

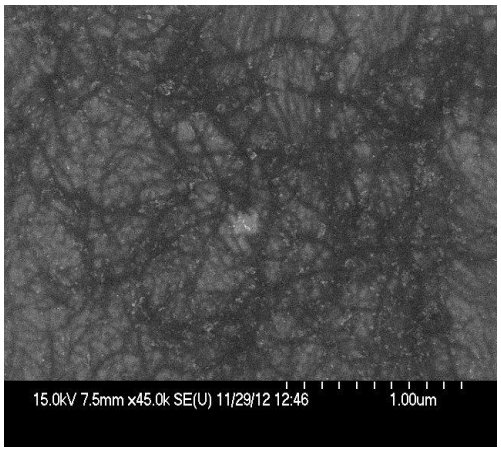

Figure 34: Fibrils of Collagen Calf Skin type III on Si-wafer

A disadvantage of the electron microscope is the difficulty in dealing with the sample once it loaded inside the machine. It is important to mark the sample to facilitate orientation and identification. For the metallic nanofeatures, a Right angle shape was used to orient the sample, shown in Figure 35. For the biological samples we used small dots or lines around the patch of the biological materials, as shown in Figure 36 and Figure 37. The dots and lines around the patch of the sample guided us to the correct targets. In Figure 38 we demonstrated few images which show the area on Si-wafer next to the patch of our sample. Then we compared it with a patch of Collagen Calf Skin in Figure 39.

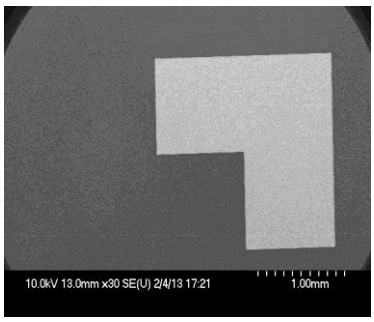

Figure 35: This Figure shows the Corner like shape as a marker emphasising the direction of the metallic features (not shown here) on Si-wafer substrate.

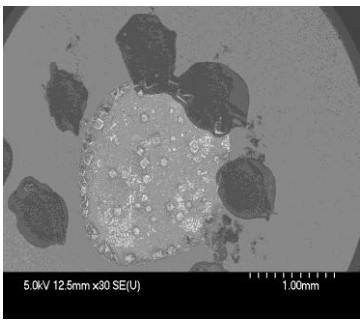

Figure 36: This Figure shows the dots as a marker emphasising a patch of TBS ph7 on Si-wafer substrate.

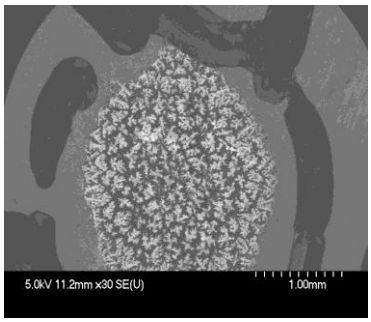

Figure 37: This Figure shows the small lines as a marker emphasising the TRR1 patch on Si-wafer.

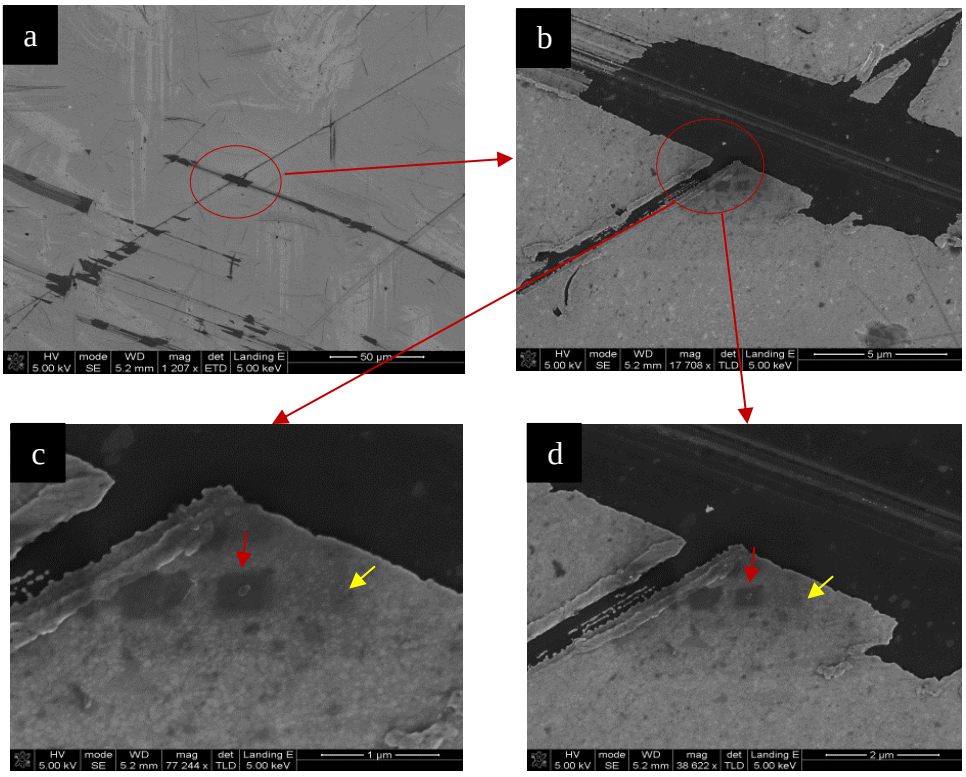

Figure 38: This Figure shows the area of Si-wafer surface next to one of our biological sample. Note the patches emphasised by the red circles in **a** and **b** having features shown in **c** and **d** very similar to Collagen fibrils shown in Figure 27 below. Same colour arrows point to a similar features.

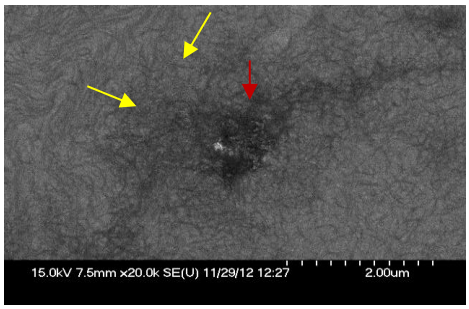

Figure 39: This Figure shows the Collagen Calf Skin type III fibrils on a Si-wafer substrate. The red and yellow arrows pointing to very similar features in Figure 26 above.

The colours in electron microscope traditionalised for obvious looking and nothing to do with the real colour of the sample at all [68]. Despite the fact that coloured images are fashionable, sometimes the uncoloured one supports better and much recognizable features image (see Figure 40). Really, the colouring system in electron microscope is set up to be an optional choice by the user. Whatever colour style one would choose, the basic idea is the same, different colours represent different contrast, i.e. different depths.

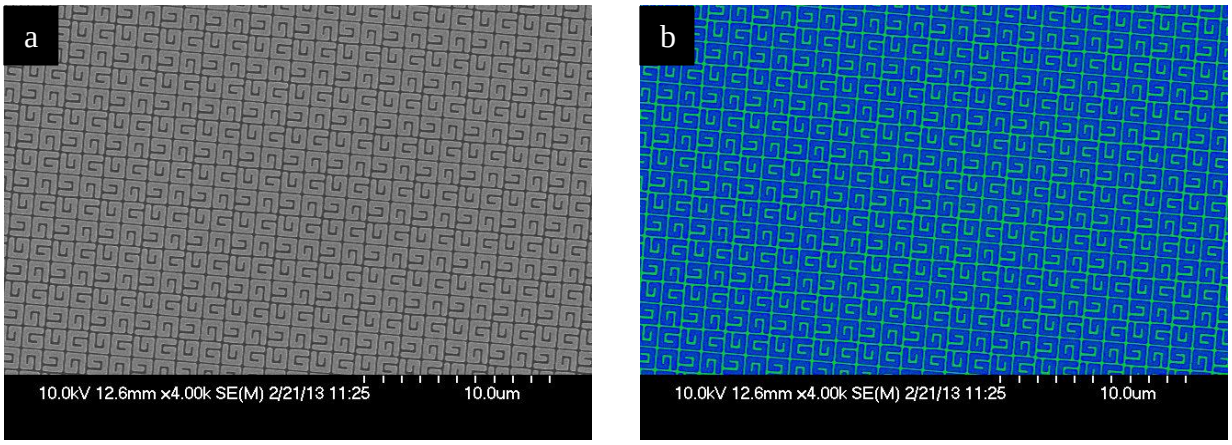

Figure 40: The colour effect on the G`s images. Despite the fact that coloured images are fashionable yet, sometimes the uncoloured image supports better and much recognizable features image, e.g. the G`s features are much recognizable by the uncoloured image in **a** than the coloured image in **b**.

For this project, two types of SEM instruments have been used. The first one is *FEI Nova NanoSEM 630* shown in Figure 41 below. Its electron beam is generated by the gun of Schotty field emitter with up to 100nA. The electron beam is controlled to scan the surface of the sample in raster lines. The main chamber can be loaded with 200mm substrate over a piezo driven stage of (150x150) mm. It can be operated with high and low vacuum. Also, it is capable to support ultra- high resolution of 1nm at 15KeV and 1.8nm at 4KeV at high and low vacuum respectively. Conducting and non-conducting substrate could be used without coating. Several detectors could be used like TLD, ETD, HLX, LVD, VCD, GAD (see table 3). Besides, an integrated camera is fixed in the main chamber. This CCD camera provides the images which displayed to the user by the screen of the computer [69]. The second SEM instrument is *Hitachi S4700*, shown in Figure 42 below. Its electron beam is generated by the gun of cold field emitter with acceleration voltage from 0.5 to 30 keV in 100eV step. The electron beam is controlled to scan the surface of the sample in raster lines. The sample holder

(shown in Figure 30) can be loaded with 150 mm substrate. It is operating with high vacuum. Also, it can support ultra- high resolution of 1.5 nm at 15 KeV. High resolution images could be detected by a cathodoluminescence detector, a backscatter electron detector and an energy dispersive x-ray spectrographic detector, all are supplemented in the microscope. Similarly to FEI Nova NanoSEM 630, the images are displayed to the user by the screen of the computer [70].

Figure 41: FEI NovaSEM 360 electron microscope, located in JWNC cleanroom in Glasgow University.

Figure 42: Hitachi S4700 electron microscope, located in JWNC cleanroom in Glasgow University.

Regarding the sample conditions, different electron microscopes have different requirements for the sample. Basically, the sample in SEM should be dried to avoid any reactions between the electron beam and the liquid particles. The sample should also be electrically conductive, otherwise; the electrons of the electron beam can start to build up sample surface charge which can lead to sample burning, e.g. Figures 43, 44, 45 and 46 illustrate the issue of sample charging. It is possible to use specific detectors to overcome this problem. For example, with our quartz substrates (non-conductive substrates) we used LVD and HLX detectors (see table 3). These detectors are used with *FEI Nova NanoSEM 630* and work under low vacuum. The low vacuum is required since the microscope supports a vapour of water to absorb the charges from the surface.

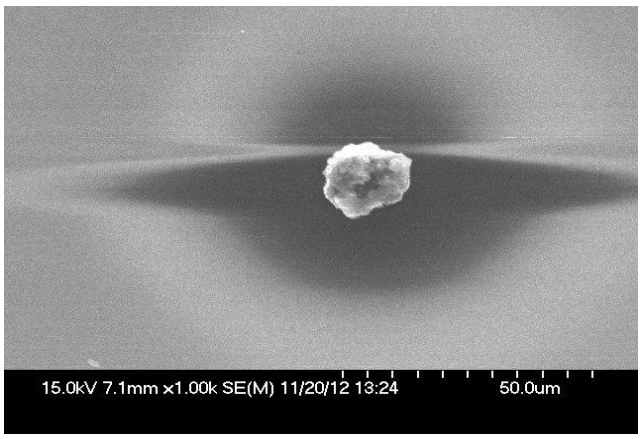

Figure 43: A rare image of Collagen calf skin burning on a quartz substrate. This picture was detected in a real time event, i.e. it recorded the moment of the electron beam striking the collagen particle on uncoated surface of quartz substrate.

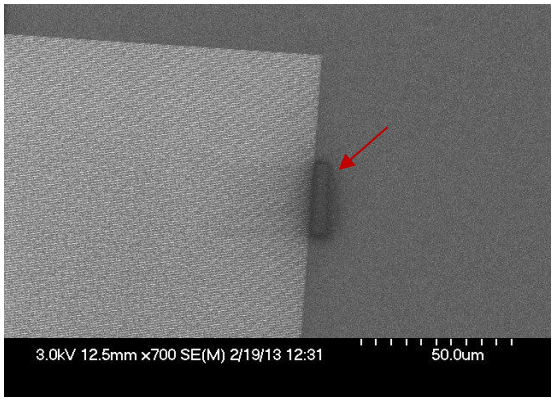

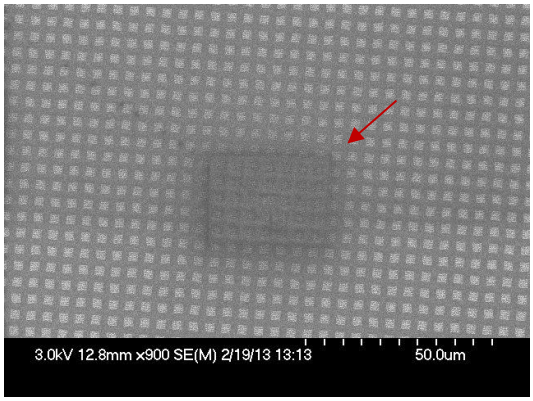

Figure 44: A burned area of PMMA resist on Si-wafer substrate. The tracks of the burned area are pointed by the red arrows.

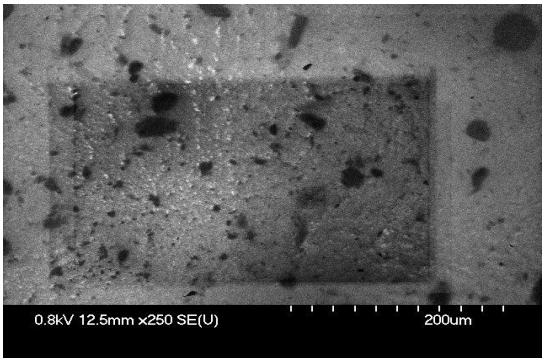

Figure 45: Track of burned area of TRR1 fibrils on Si-wafer substrate.

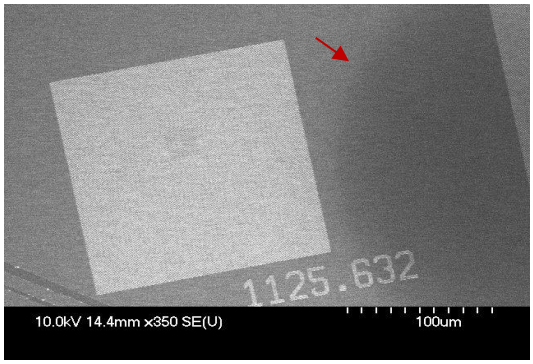

Figure 46: Track of burned area on quartz substrate.

A typical way to achieve good quality images is to sputter the sample with a layer of metal befor using it in SEM; to provide conductive enviroment. This metal could be gold or gold palladium. This method was used with our samples. As such, an `Agar Auto Sputter Coater`, shown in Figure 47 below, was used to coat the samples to absorb charged particles and to support the imaging process.

Figure 47: A photograph of the Agar Auto Sputter Coater in JWNC cleanroom in Glasgow University.

Quartz (non-conductive) and Siwafer (conductive) substrates were mounted with either metalic nanoparticales or biological materials. With transmission spectroscopy such as CD and UV spectroscopy, only quartz substrate was used to avoid intereference with the spectroscopy measurements.

2.4. Pre-nanofabrication work

2.4.1. Pattern Design

Five different designs have been fabricated in this chapter, these are: gammadions, crosses, Right angles, J`s and G`s. All are shown in Figure 48 below. In this Figure, all five designs have been shown with their dimensions and orientations. Although, not all patterns have their features fabricated similarly; this is because dimensions and orientations were subject to experimental requirements. Patterns are deposited in arrays of repeated features; following two or three levels of repetitions; first level refers to the repetitions of the single features, like pattern shown in Figure 49(b,e) which shows array of crosses and gammadions. Second level of repetitions is when a group of two or more features are arranged as individual unit and hence the pattern will be characterised according to the repetitions of these units, e.g. array of G like shapes and J like shapes, see Figure 49(c,d). Third level of repetitions is when patterns in first and/ or second level are repeated as a blocks, like the yellow blocks shown in Figure 49a. Subsequently, a single microchip will consists of (X *x* Y) blocks, when (X, Y) $\geq$ 1, each block consists of 100s x 100s of nanostructures.

Some of these designs are already described theoretically by Euan Hendry from the University of Exeter. As such, numerical simulations were prepared for the Gammadion shapes and for the J shapes. In both, a commercial finite-element software package (HFSS version 11.0) with a mesh size of 4.0 nm was used. We also replicated others designs for our own applications [41]. This was for G like shapes

The L-Edit v14.1 32-bit software was used to design our samples. The patterns were transferred to Vestic-VB6 machine (the writing machine) via multiple tunnelling programs, these are: CATS, Felix, Tank2, Hobbese and Belle. Finally, the patterns have been written in VB6 machine by the software of Layout-beamer.

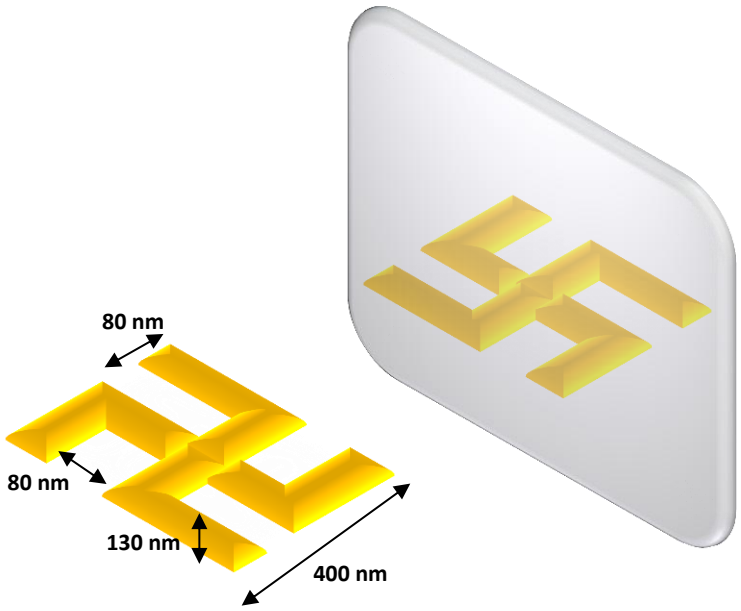

Left (L) handed gammadion **Right(R) handed gammadion**

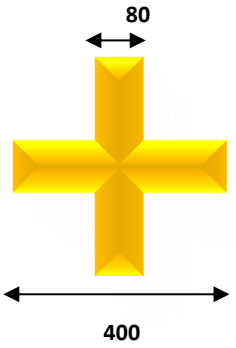

Cross (X)

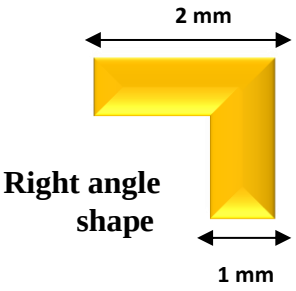

Right angle shape

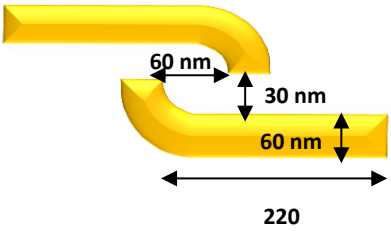

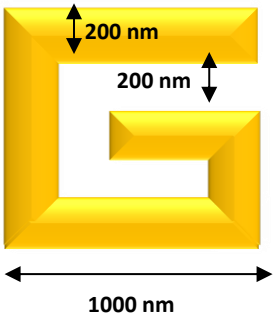

J`s like shapes **G like shape**

Figure 48: Five different designs have been fabricated in this chapter. These are: gammadions like shapes, crosses like shapes, Right angle shape, J like shapes and G like shapes. Dimensions and orientations of each design are subjected to experimental and hence pattern requirements. Dimensions we presented here are default; however in some cases we used exactly the same numbers; otherwise dimensions were varied with comparable range; again depending on the design.

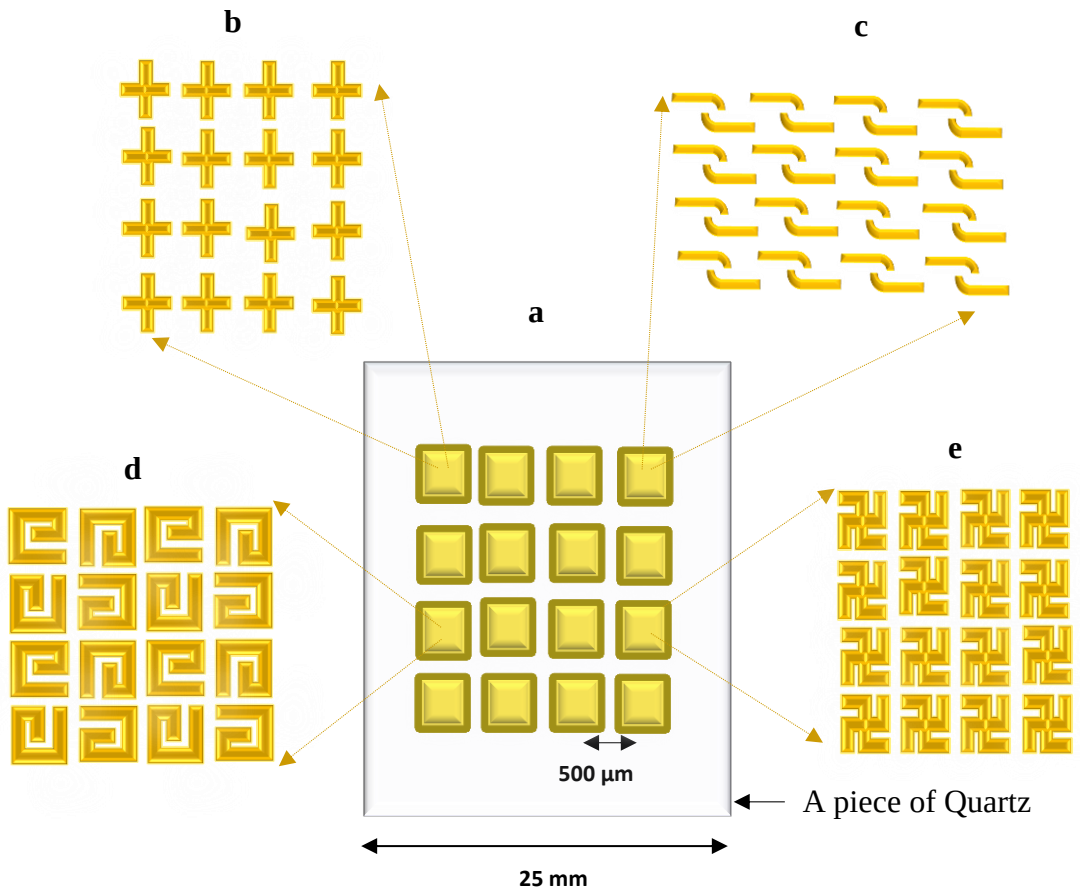

Figure 49: Our microchip is a piece of quartz consists of an array of (100s x 100s) Nano features. Each yellow block could have its own pattern lithographically written (and separately) via VB6 machine. As such, it is possible to fabricate more than 400 different patterns (on basis of (20 x 20) blocks) on (25 x 25) mm quartz substrate with a single job. **a** shows the microchip, **b** shows the crosses, **c** shows the J`s, **d** shows the G`s and **e** shows the gammadions.

We fabricated these designs within three sets of patterns, in addition to a substrate direction mark pattern, these are:

- First set (shown in Figure 50 below):
  - Right handed gammadion shapes.
  - Left handed gammadion shapes.
  - Crosses like shapes, as a control for the gammadions.
  - Racemic shapes: another control which is a combination of two of the gammadions shapes orientated in a way that each shape is a mirror image to the next one.

- Second set (shown in Figure 51 below):
  - Right handed pairs of J letter like shapes.
  - Left handed pairs of J letter like shapes.
  - Racemic shapes: as a control which is a combination of four pairs of J letter like shapes orientated in a way that each pair is a mirror image to the four other surrounding pairs.

- Third set (shown in Figure 52 below):
  - Right handed pairs of G letter like shapes.
  - Left handed pairs of G letter like shapes.
  - Crosses like shapes as a control for the G like shapes.

- The right angle shape (used as orientation marker as described above), shown in Figure 53 below

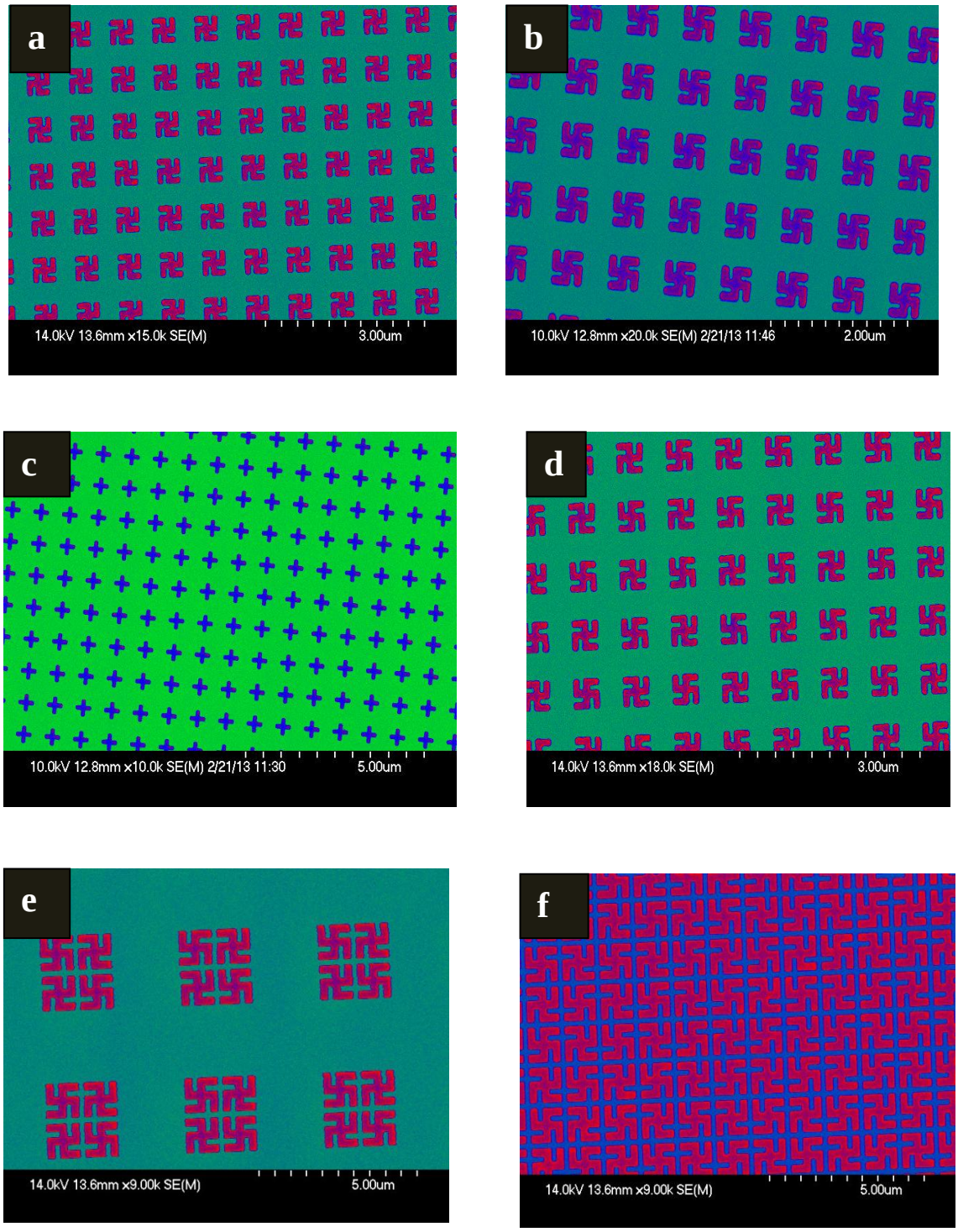

Figure 50: SEM images for the first set of our nanofabricated samples. **a** shows the Left handed of gammadion shapes. **b** shows the Right handed of gammadion like shapes. The **c** shows the Crosses like shapes as a control. **d**, **e** and **f** shows the Racemic shapes; another control which is a combination for four of the gammadion like shapes.

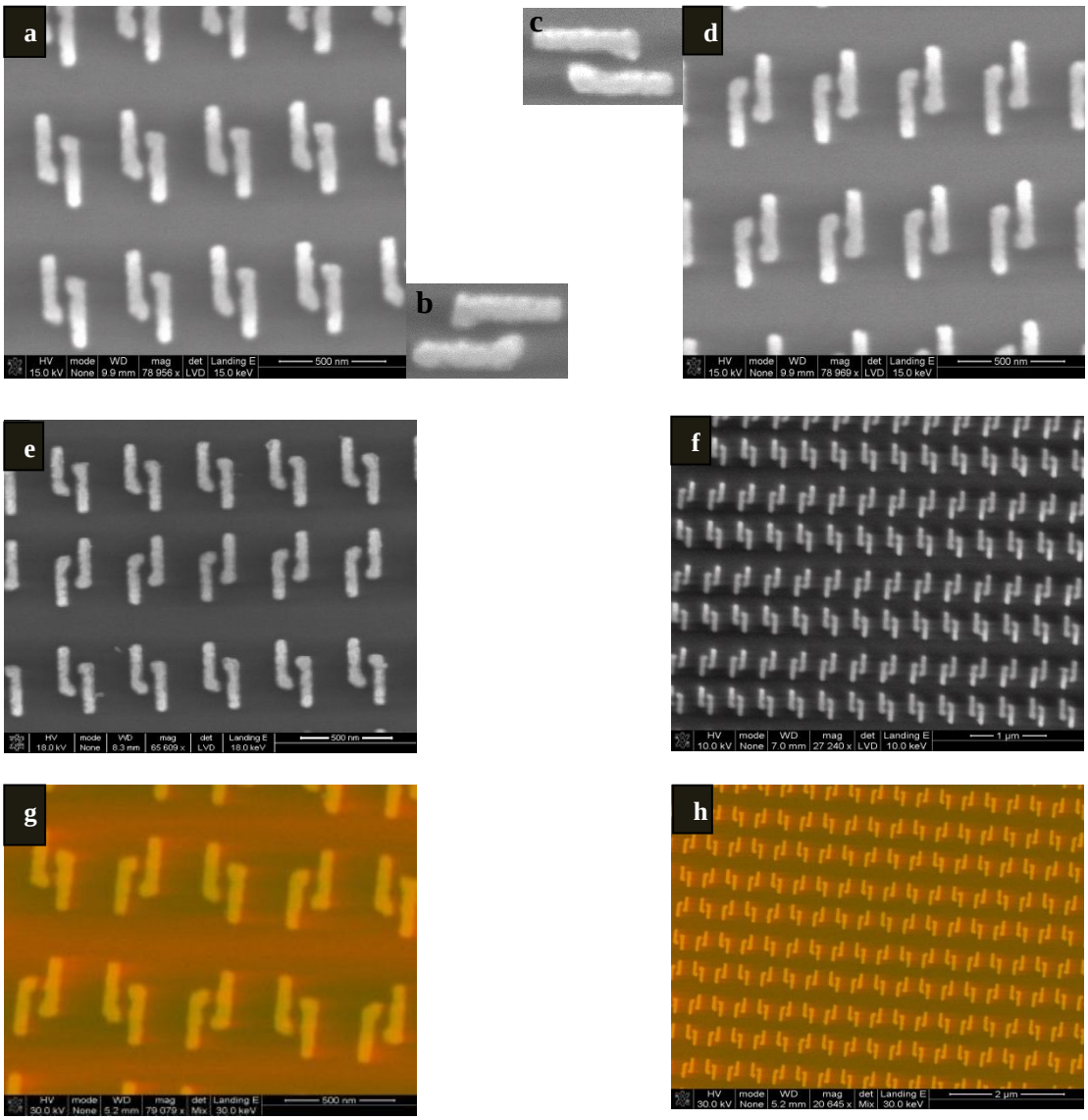

Figure 51: SEM images for the second set of our nanofabricated samples. **a** and **b** show the Left handed pairs of J letter like shapes. **c** and **d** show the Right handed pairs of J letter like shapes. **e, f, g** and **h** show the Racemic shapes as a control samples, which is a combination of four pairs of J letter like shapes orientated in a way that each pair is a mirror image to the four other surrounding pairs.

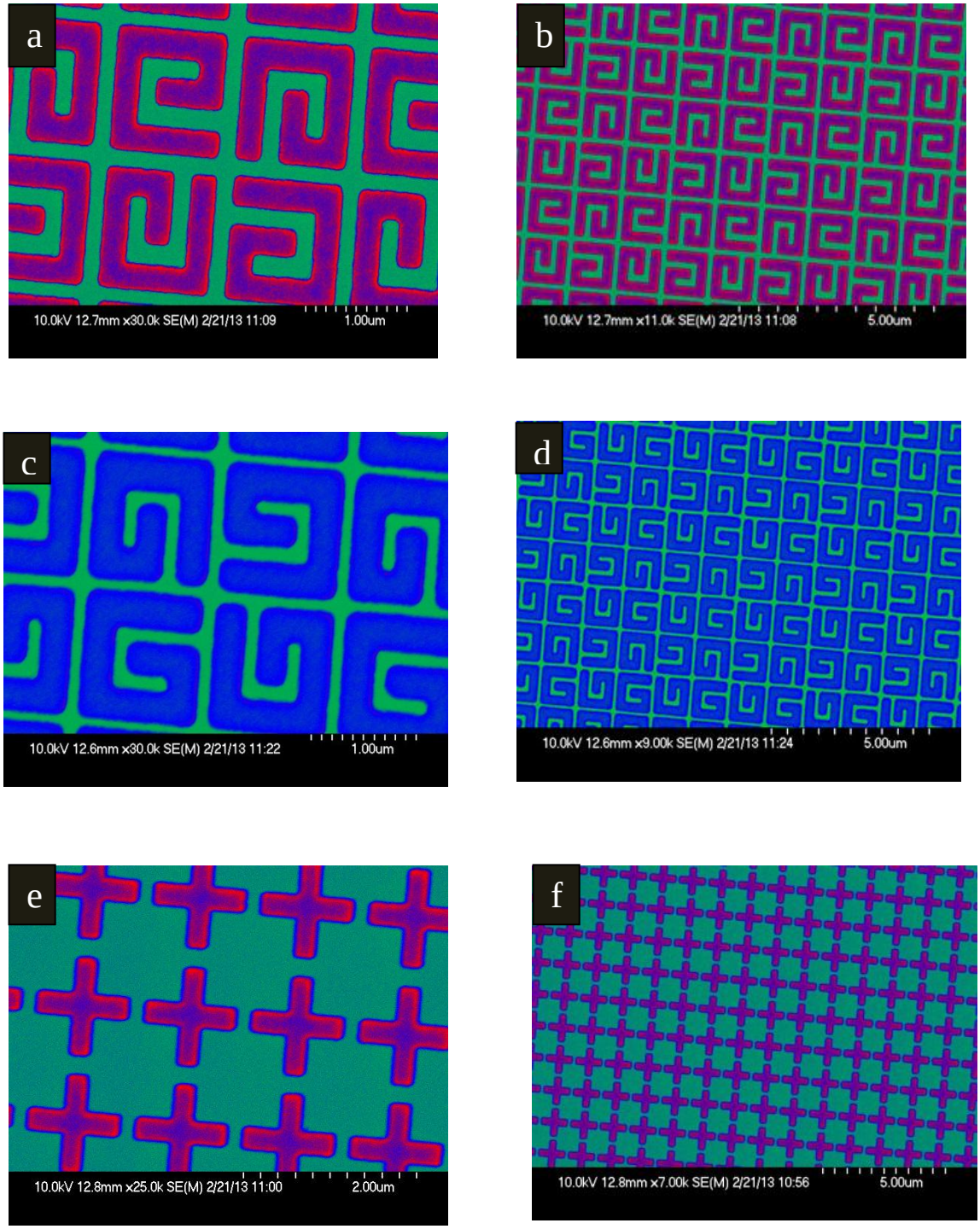

Figure 52: SEM images for the third set of our nanofabricated samples. **a** and **b** show the Right handed pairs of G letter like shapes. **c** and **d** show the Left handed pairs of G letter like shapes. **e** and **f** show the Crosses like shapes as a control. Note: in **a**, **b**, **c** and **d** images it is easy to see the direction of the orientation if you focus you`re sight at the green background.

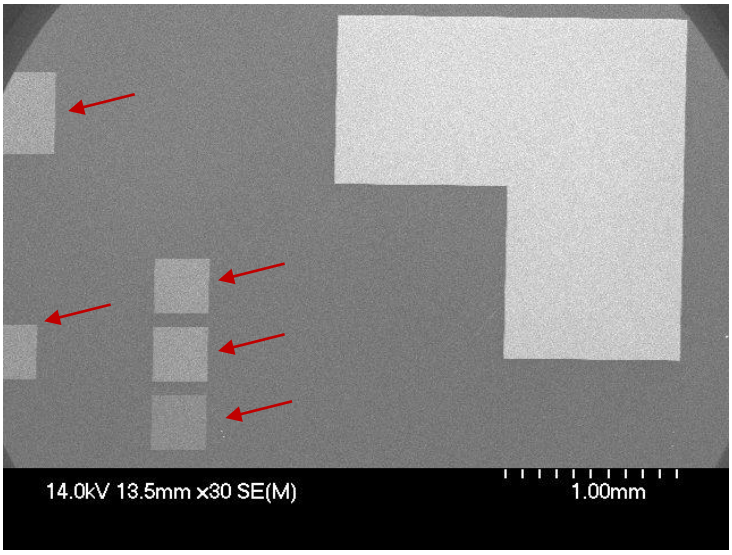

Figure 53: SEM image of the corner like shape. This shape used to determine the exact direction of our nanofabricated samples. Note the red arrows pointing to the squares which contain our nano-features.

2.4.2. Substrates preparations

The substrate was selected according to its type and its dimensions. Two types of substrates have been used in this project. These are:

I. Vitreosil Quartz Plates, all faces and edges polished. Purchased from Newcastle Optical Engineering Limited.

- Dimensions: 15mm x 15mm x 1mm thick.
- Dimensions: 20mm x 20mm x 1mm thick.
- Dimensions: 25mm x 25mm x 0.5mm thick.
- Dimensions: 25mm x 25mm x 1mm thick.

II. 4 inch Mechanical Silicon wafer

This used to be cut in small pieces varied between squares of > (15 x15) mm and polygon of > (35 x 40 x 50) mm.

2.4.3. Cleaning routine

Cleanroom conditions (shown in Figure 54 below) are essential for nanofabrication work. Fully cleaned surfaces can be achieved by using different agents, such as Piranha solution (3:1 H_2SO_4:H_2O_2), Opticlear original, Acetone, Isopropyl alcohol (IPA) , Methanol, distilled water, steam of Nitrogen and sonication bath. Each type of substrate requires specific cleaning recipe compatible with its own surface. For the samples used in this project we have followed the following procedure:

i. Five minutes sonication in acetone bath.
ii. Five minutes sonication in methanol bath.
iii. Five minutes sonication in isopropyl alcohol bath.
iv. Rinsing with distilled water.
v. Dried off with steam of Nitrogen.
vi. Five minutes in 180C oven to be fully dried.

Figure 54: Cleaning room in JWNC building in Glasgow University. **a** shows the cleaning room inside the JWNC cleanroom. **b** and **c** show the sonication bath inside the two cabinet pointed by the red arrows. We used to put our sample inside the beaker and leave it for sonication for 5 minutes with methanol, acetone and IPA baths.

2.5. Nanofabrication parameters

2.5.1. PMMA Resist

An important concern in Electron Beam Lithography is the electron beam resist that is used. The electron beam resists are solutions of polymers which spun over the substrate to form a smooth and uniform film. This is then represents the platform where the patterns supposed to be transferred at. The patterns transferred by exploiting the fact that as polymers considering high sensitivity against the electronic beam. So it is called `Resist film` or mostly used `The Resist`. The sensitivity against the electronic beam means the electronic beam destroys the region of the resist film completely once hitting it (for positive tone resist), or oppositely, the electronic beam helps small and highly soluble chains to combine together via cross-linking reaction (for negative tone resist), see section (2.2.2.).

Researchers have used this unique property of the resists to write high resolution patterns scaled to the nano scope level. The electronic beam strikes a region in the resist film similar to the size of its own spot. Hence, the smaller the spot beam the higher the resolution of the writing achieved. Different resist polymers have different levels of sensitivity against the electronic beam. The selection of different beam sizes and types of resist polymers allows variation in pattern resolution.

Other important considerations affecting the resolution are: the exposure time, the variable resolution unit (VRU), the electronic beam acceleration and the electronic beam power which are controlled by the writing machine. Some of these parameters are variable like the exposure time and VRU but others are fixed by the operators.

The thickness of the resist film and the number of layers of resist also affect the resolution. Five factors which influence thickness include:

- The type of the resist: different resists supports different thicknesses.

- The type of the substrate: Here the thickness of the resist is affected because the roughness of the surface highly affects the spreading of the resist molecules on the substrate`s surface.
- The amount of the polymer solution which refers to the number of droplets deposited on the substrate before spinning.
- The pre-spinning time: the longer the time for the droplet to be kept on the surface before spinning, the non-uniform film is obtained.
- The speed of the spinning: high speed support thin layer film and vice versa.

As has been mentioned, the resist films could be classified in two main types. The first type is the positive tone resists. Here the exposed areas are cleared out, Figure 55a. The second type is the cross link or a negative tone resists. Here the pattered areas remain, Figure 43b. Importantly, Figure 55 clarifies the type of the positive and the negative tones on the PMMA resist. However, this Figure does not represent the actual use of as resist. Normally, each resist is used for a single type. For examples PMMA and ZEP are used as a positive tone resists and is a HSQ negative tone resist.

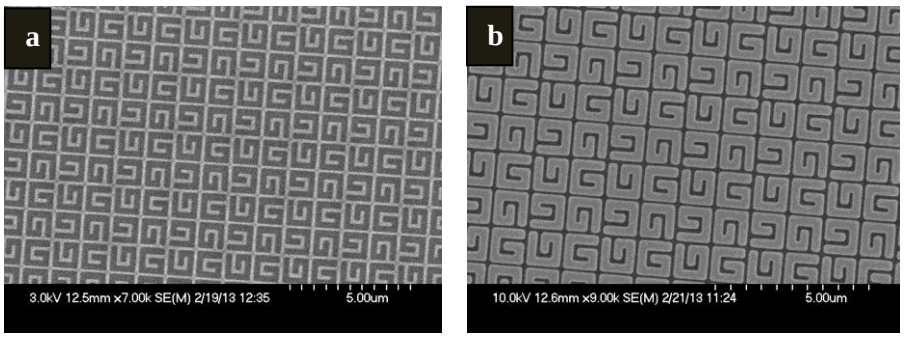

Figure 55: SEM images for the left handed G`s features. These images are shown the - Negative tone (**a**) and the - Positive tone (**b**) senses. **a** represents the PMMA resist patterned with G`s features, without metal deposition. **b** represents the metallic features. Note that these are not a real negative or a real positive tone resists, they are only demonstrating the sense of the negative and the positive tone concepts.

In this project, three types of PMMA resist have been used all the time. These are: 2.5% 2041, 4% 2010 and 8% 2020 .The percentage numbers represent the

amount of the PMMA dissolved in O-xylene. So, the (8% 2010) is more sensitive than the (4% 2010) and this more sensitive than the (2.5% 2041).

We have used a double layer system, first layer, which is attached to the surface, is 4% 2010 (sometimes 8% 2010). The second layer is (2.5% 2041). The reason for using double layer system is to improve the sharpness of the features. When the electronic beam passes through the layers (Figure 56) the first layer (attached to the substrate) will be affected much more than the second layer because it is more sensitive. This leaves the second layer with a narrower channel than the first layer, such that, during the metallisation process the metal will be confined by the narrow channel of the second layer. Consequently, the metal will be deposited on the surface of the substrate without touching any side of the first layer. If the height of the first layer resist is larger than the thickness of the metallic layer, this leaves the metallic layer untouched from above. An optimal lifting off process can be achieved by ensuring that the metallic layer has remained untouched by the resist.

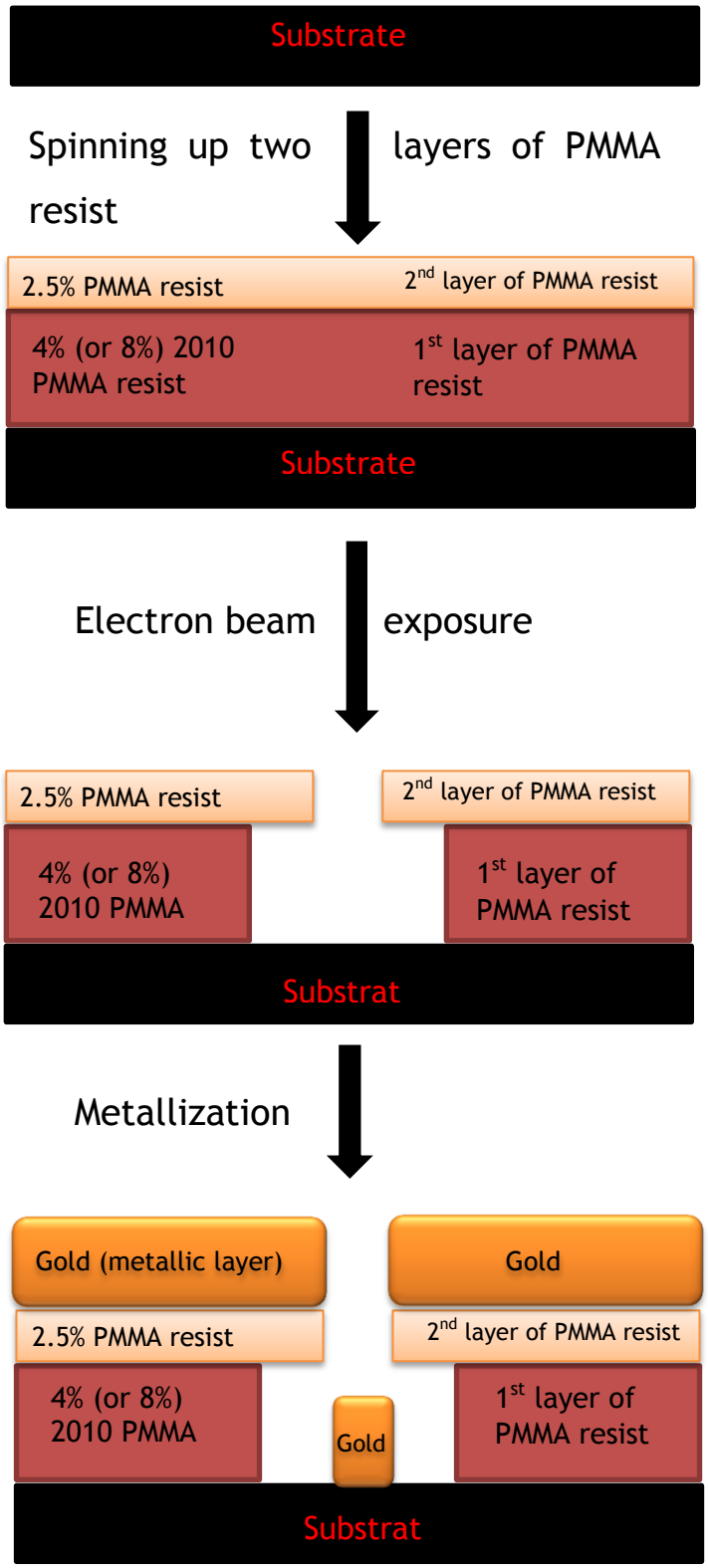

Figure 56: A cartoon of the steps of the PMMA resist deposition, the electron beam exposition and the metallization processes on the top of the substrate surface.

2.5.2. Resist spin coating

In electron beam lithography it is important to control the thickness and the homogeneity of the resist films to optimise the resolution of the lithography. The thickness and the homogeneity of the resist can be controlled by the methodology used to apply the resist films on the surface of the substrate. Resist spin coating, or RSC for short, is one of the most common strategies used to apply the resist film.

Resist spin coating is the practice of spreading materials on the surface of the substrate by specific rotating motors. In electron beam lithography, the Micronetics spinner, shown in Figure 57a, is used for this purpose. The spinning routine is determined by the number of the rotations per minute (rpm). Increasing the value of rpm reduces the thickness of the resist film and vice versa. Table 4 shows a sheet of the theoretical and the actual values for several types of PMMA resist varying with the speed of the spinning and the type of the PMMA resist.

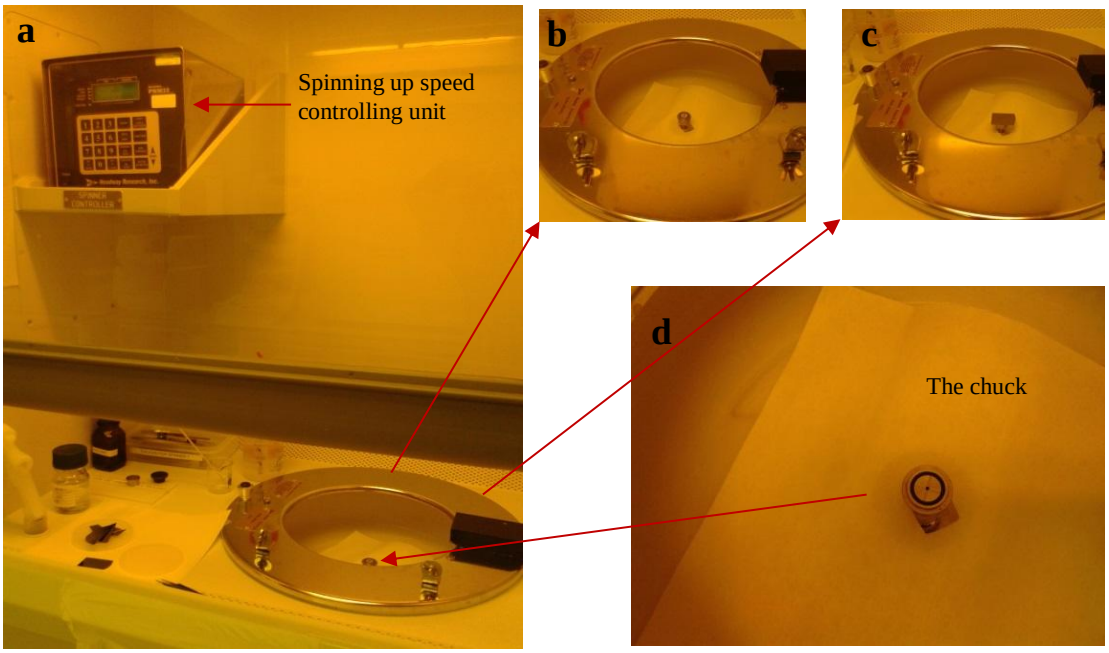

Figure 57: The spinner in spinning up laf- cabinet in JWNC cleanroom. **a** shows the spinning control unit setting the speed of the spinning process. **b** and **c** show the chuck (the sample holder) without and with the sample on the top, respectively. **d** shows the chuck while it was spinning the sample.

Table 4: Theoretical and the actual values for several types of PMMA resist. This is the prevailing table uses in JWNC.

Resist	Spin Speed	Theoretical Thickness	Real thickness measured by JWNC stuff
12% 2010	2k	900 nm	
	3k	750 nm	
	4k	650 nm	
	5k	535 nm	550 nm
8%2010	2k	375 nm	
	3k	302 nm	
	4k	265 nm	
	5k	185 nm	205 nm
4% 2010	2k	186 nm	
	3k	153 nm	
	4k	134 nm	
	5k	110 nm	110 nm
4% 2041	2k	215 nm	
	3k	176 nm	
	4k	152 nm	
	5k	126 nm	115 nm
2.5% 2041	2k	81nm	
	3k	66nm	
	4k	57nm	
	5k	47nm	38 nm

Resist spin coating parameters should be chosen according to the final thickness of the metallic features. As has already been mentioned in 2.6.1, we need to end up with untouched metallic layer. Therefore we have used the following ratio to decide the spinning parameters that suit our samples:

- The thickness of the metallic layer ≅ 2 / 3 The thickness of the 1st PMMA layer
- The thickness of the metallic layer ≅ 3 /1 The thickness of the 2nd PMMA layer

Practically, we have used the 4% 2010 PMMA resist in some cases and 8% 2010 PMMA resist in other cases as the first layer resists. While the 2.5% 2041 for the second layer resist. Following Table 3, we spun 4% 2010 on a quartz substrate at 4500 rpm to deposit the first layer of the PMMA resist. Then, this layer was baked for one hour at 180C°. This yielded a layer of (85 -110) nm thick. Then we spun 2.5% 2041 PMMA resist at 4500 rpm. Again, it was baked at 180C for one

hour. To yield a (25 – 35) nm layer thick. This procedure has been used with the samples of (25 - 100) nm Gold thick, which were mostly used with Quartz substrates.

The same procedure was used for the (120-130) nm Gold thickness but with 8% 2010 PMMA resist instead of 4% 2010 PMMA resist. This was used with Quartz and Silicon wafer substrates. The yield of 8% 2010 was > 150nm.

Thickness measurements of PMMA layer were measured using a DEKTAK machine. This was used in particular when we test the suitable spinning speed. It is not necessarily to check the thickness of the PMMA layer each time since this highly affects the cleanliness of the sample. In most cases, the measurements were very close to the values shown in table 5 below.

During resist spin coating a stream of Nitrogen was passed over the sample before applying the first and the second layers of the resists. This is necessary to keep the surface clean. The number of the resist droplets varied between one to three droplets and the time delay before spinning was kept to a minimum (< 1 sec).

Table 5: Types of PMMA resist, the correspondents spinning speed and the baking conditions we have used in our nanofabrication work.

Metallic thickness in nm	1st layer of the PMMA resist	Speed of spinning in rpm	Baking conditions	2nd layer of the PMMA resist	Speed of spinning in rpm	Baking conditions
25-100	4% 2010	4500	1 hour at 180C	2.5% 2041	4500	1 hour at 180C
120-150	8%2010	4500	1 hour at 180C	2.5% 2041	4500	1 hour at 180C

2.5.3. The Spot size, the VRU and the Dose parameters

These parameters represent the specifications of the electronic beam, and hence, they are essential for electron beam writing:

- The spot size represents the spatial intensity distribution of the electronic beam.
- The VRU is the variable resolution unit which defines the step size of the electronic beam.
- The dose of the beam is the intensity of the beam within a period of time. The intensity of the beam is defined by the number of electrons. And the period of time is defined by the exposure time.

The values of the spot size, the VRU and the dose of the beam depend on the source of the electronic beam, i.e. the type of the writing machine. Different machines provide different profiles for the electronic beam. The parameters used here were optimised for the VB6 instrument we used in JWNC. Figure 58 illustrates the layout of a 25mm x 25mm substrate sample in the writing machine. The patterns are normally written in any area such as (a) or (b) apart from the clamping zone. This area is known as `the field of writing`. According to VB6 UHR EWF, the maximum field of writing is 1310.72 μm.

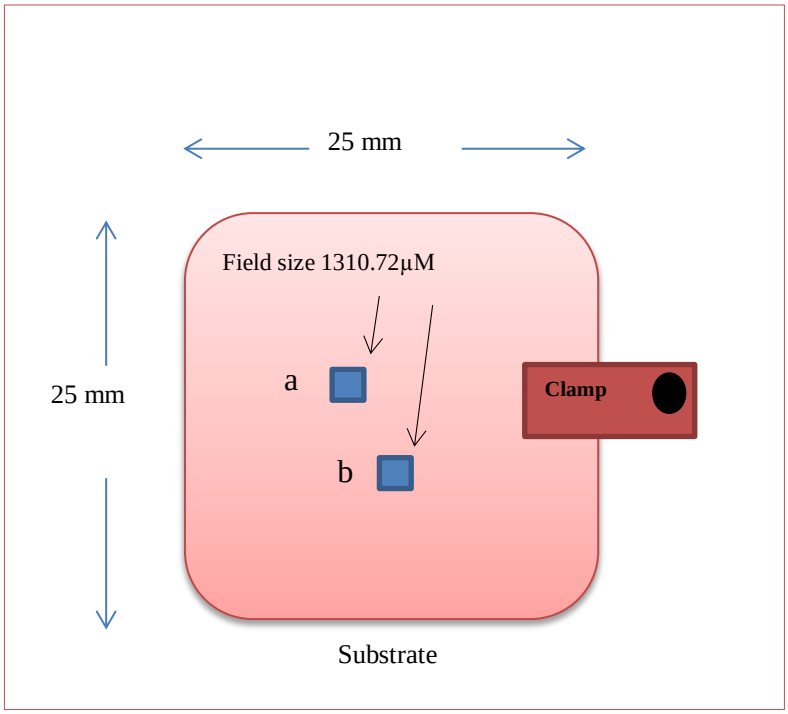

Figure 58: A layout demonstrating the sample underneath the writing machine. It shows the concepts of the field in **a** and **b,** which should be at a maximum size of 1310.72µm. This field represent the position of the writing.

Since VB6 UHR EWF is 20 bit style, each field has a 2^{20} (=1048576) pixel in *x* and *y* directions. This gives a resolution of 1.25 nm.

$$Resolution = \frac{Field\ size}{Pixels}$$
$$= (1310.72\mu m)/1048576$$
$$= 0.00125\mu m$$
$$= 1.25nm$$

The VB6 UHR EWF machine can also write in a resolution of 1nm and 0.5nm however this reduces the field size to 1048.576µm and 524.288µm respectively. Figure 59 shows a magnified writing field.

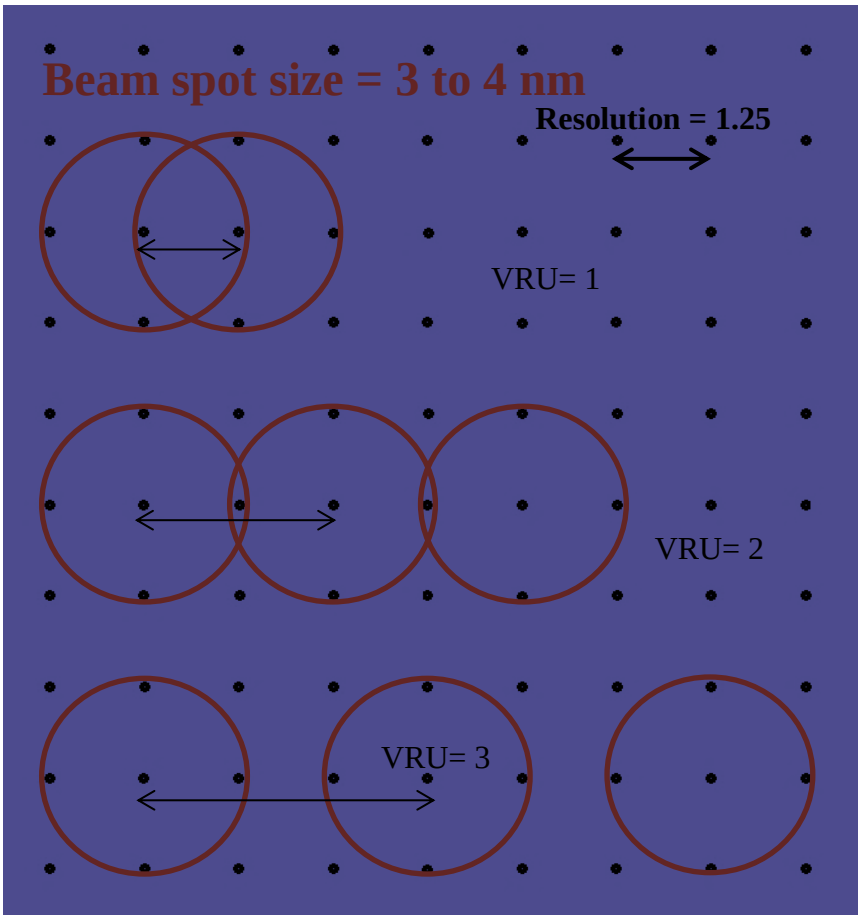

Figure 59: A layout of a virtual grid on the sample surface. It also shows the concepts of the electron beam spot size, the VRU and the effect of increasing or decreasing the VRU values.

Principally, the minimum spot size of the electronic beam in VB6 UHR EWF varies between 3 to 4nm. Therefore in lithography, the electronic beam should be directed to step a distance of 3 to 4nm as well.

The electronic beam should be stepped by one fifth of the minimum wire size of the feature to achieve typical writing.

Typical writing can also be achieved if the electronic beam is moved in an order of the writing field resolution. This means that the beam step size could be changed to step in an integer number of the resolution.

In VB6 UHR EWF, the integer number can vary from (1 to 512). So, at a resolution of 1.25nm, the maximum step size of the electronic beam is 640nm. All of our samples have been fabricated at the resolution of 1.25nm.

From the above, we conclude that:

The spot size ≈ minimum feature size/ 5 ≈ VRU x 1.25nm

In order to explain how to use these expressions practically, we demonstrated a real example that we have done for the gammadions (200nm features) shapes. At the beginning, we would first decide the minimum line (wire) size of the feature we want to fabricate. For example we have a wire of 40nm, so:

- The spot size ≈ 40 / 5
  ≈ 8 nm

Then we looked at the` Dose Clock table`, shown in table 6 below, to decide which spot value we should use.

Table 6: Dose Clock table using in JWNC cleanroom.

Selected spot nA (nano Amper)	Actual spot	Spot size	Aperture
1 nA	1.0 nA	4 nm	40
2 nA	2.1 nA	6nm	40
4 nA	3.9 nA	9 nm	50
8 nA	8.2 nA	12 nm	50
16 nA	16.0 nA	19 nm	70
32 nA	32.0 nA	24 nm	70
64 nA	63.6 nA	33 nm	100
100 nA	131 nA	45 nm	100

For our example, the calculation above has given the spot size of 8nm. So, we selected both the 2nA and the 4nA, since these give 6nm and 9nm respectively.

After that, we used the first and the final sides of the expression 4 to determine the VRU values as following:

- The spot size ≈ VRU x 1.25nm for 2nA
  6 ≈ VRU x 1.25
  VRU ≈ 4.8

- The spot size ≈ VRU x 1.25nm for 4nA
  9 ≈ VRU x 1.25
  VRU ≈ 7.2

Then, we run ` VRU test` for each selected spot to determine the exact value which gives the sharpest feature. So we verified VRU=4, VRU=5, VRU=6, VRU=7, and VRU=8 by the aid of SEM images, see Figure 60, then we decided to use VRU 5 at 2nA (shown in e and d).

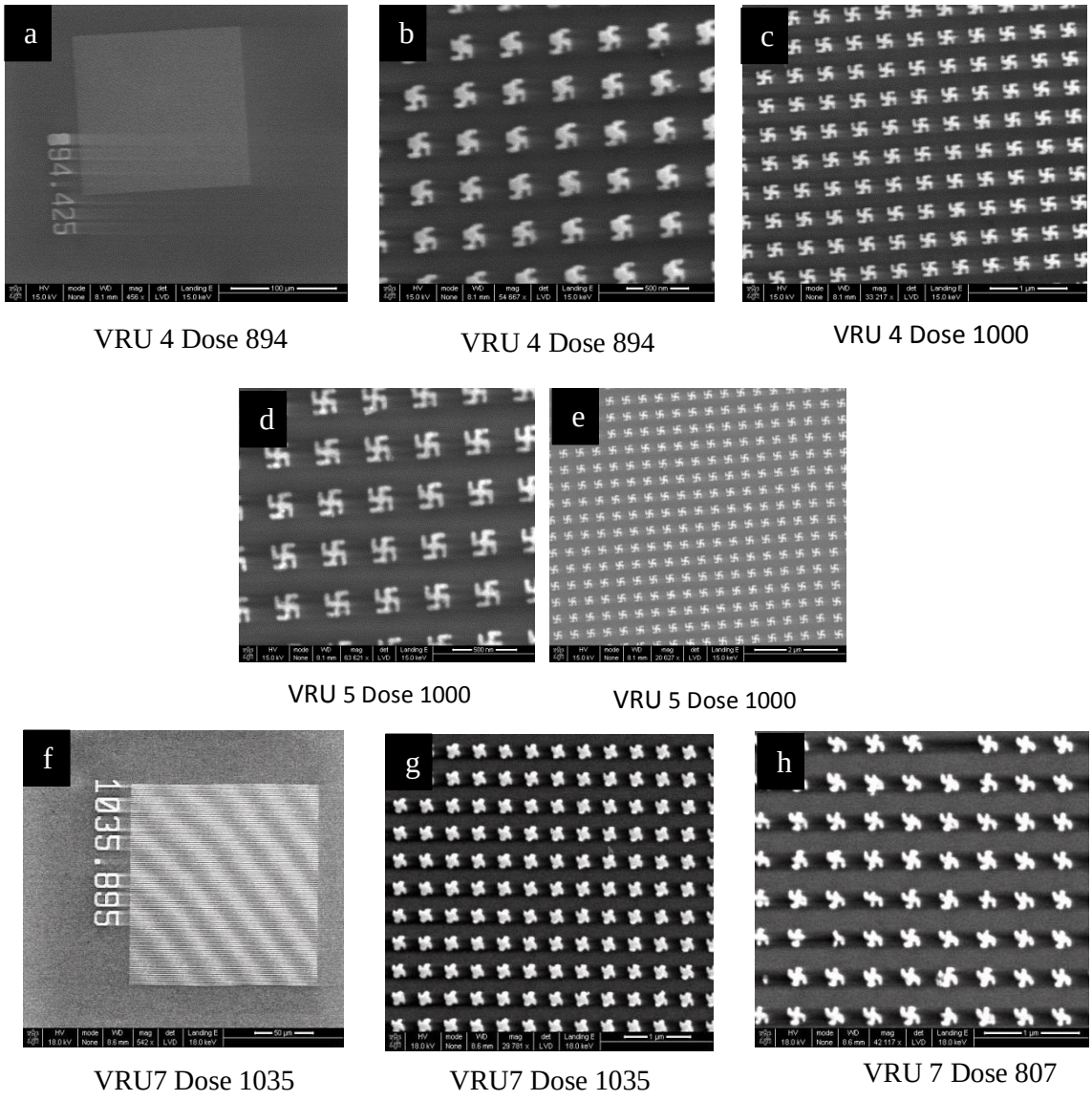

VRU 4 Dose 894 VRU 4 Dose 894 VRU 4 Dose 1000

VRU 5 Dose 1000 VRU 5 Dose 1000

VRU7 Dose 1035 VRU7 Dose 1035 VRU 7 Dose 807

Figure 60: SEM images demonstrating different doses with different VRU values and showing their effect of on the nanofabrication process. For all, the spot size was 2nA . **a**, **b** and **c** show the variations of VRU 4. **d** and **e** show the variation of VRU 5. **f**, **g** and **h** show the variation of VRU 7.

So far, only the values of the beam spot size and the value of the VRU have been determined. We still need the dose value to be determined as well. In general, the dose value could be determined by the `Dose test`. In this test, we can give a range of values extended from 200 to 2500 μC/cm^2 or even to 3000 μC/cm^2, see Figure 61 below. This range is flexible and depends on many variables such as the type of the resist, the thickness of the resist and the feature specifications. For example in Figure 62 we demonstrated the dose test for the J`s shapes. Here we have used a range of 200 to 2500 μC/cm^2.

Moreover, the frequency value of the electronic beam is an important concern that should be taken in account when we chose the exact values of the electronic beam spot size, the VRU and the beam dose. The frequency value depends on the values of the electronic beam spot size, the VRU and the beam dose together. The maximum frequency for the VB6 UHR EWF is 50 MHz. A frequency error accrues mostly in large spot size, small VRU and low dose.

In conclusion, four elements should be considered before the sample is submitted to the writing machine. These are:

- Optimised frequency of the writing machine
- Optimised feature size
- The consideration of low cost
- The consideration of high quality sample

Finally, we demonstrated below (table 7) some values of the beam spot size, the VRU and the dose that we have applied to fabricate the designs of the set no.1, the set no.2, the set no.3 and the right-angled shape.

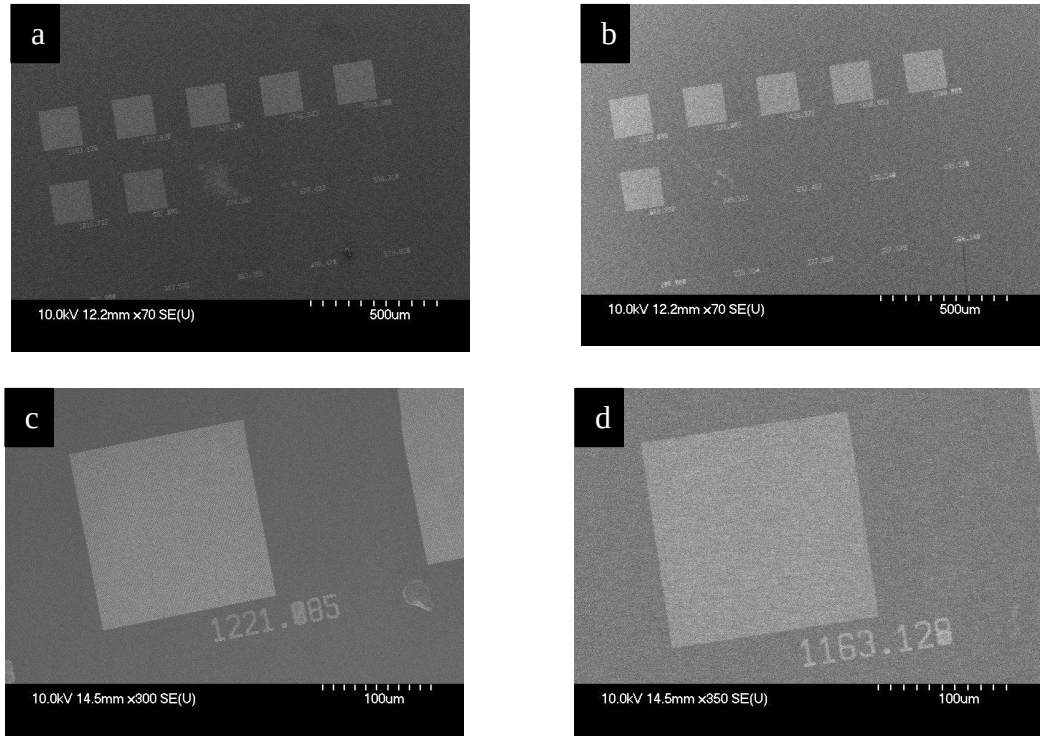

Figure 61: SEM images for the does variations in the dose test routine. **a** and **b** show the full range of a (200 – 2000) dose unit values. **c** and **d** show the dose value written in the exact number next to the corresponding features.

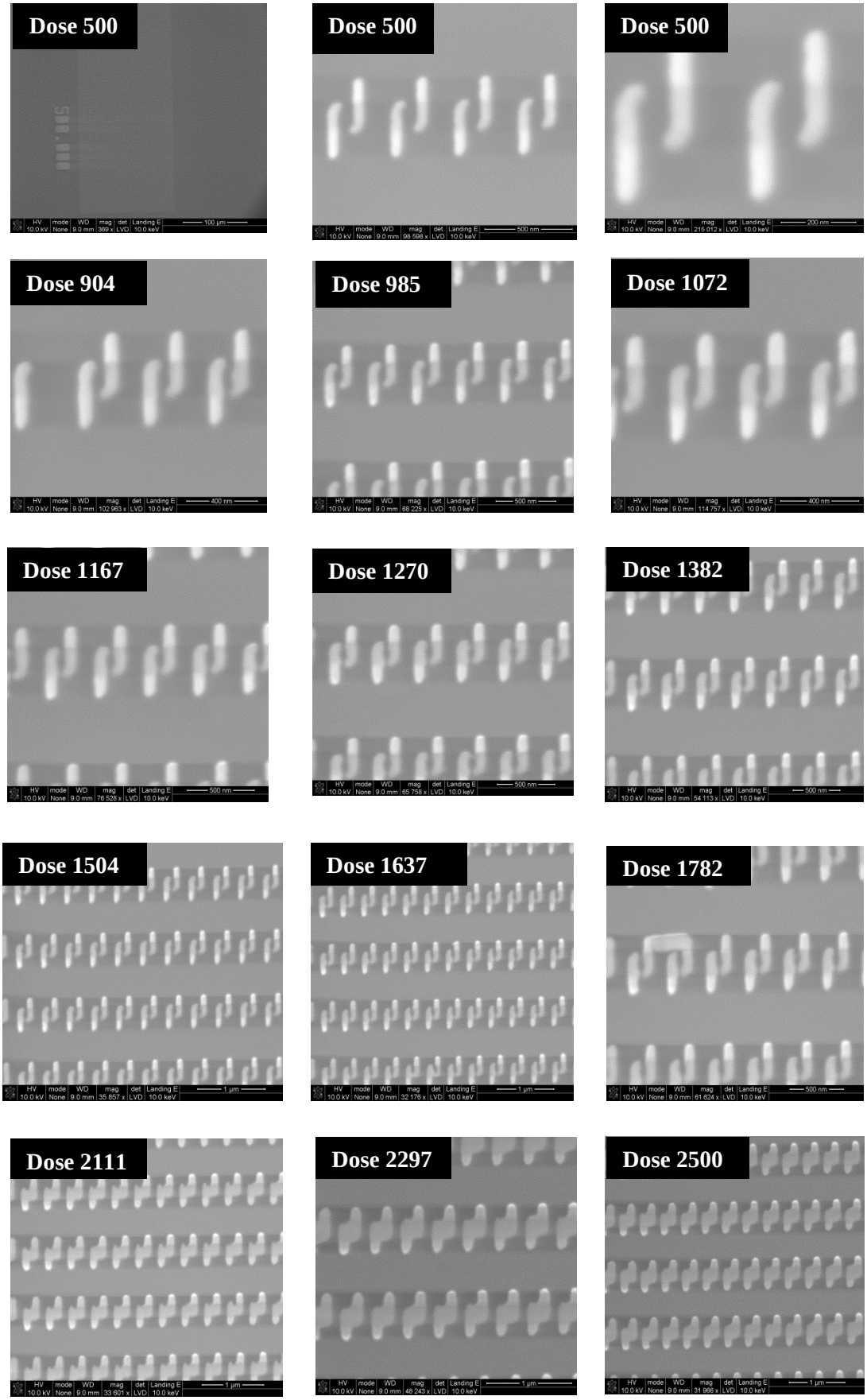

Figure 62: The variation of the dose values of the J`s shapes fabricated on quartz substrate. The dose ranged between (500-2500). Note as the dose value increases the width of the features lines (wires) increases as well. This is expected and it is a normal effect caused by the backscattered electrons.

Table 7: Experimental parameters we have used to fabricate our samples. These values were predicted theoretically first and then we tested practically. Some of these values were deviated a little bit to suit the reality of the sharp features.

The pattern	The size of the feature	Minimum wire size	the Spot size	The VRU	The Dose	The substrate
Gammadion RH	400 nm	80 nm	32 nA	20	1200	quartz
Gammadion LH	400 nm	80 nm	32 nA	20	1200	quartz
Crosses X	400 nm	80 nm	32 nA	20	1200	quartz
Racemic 4	400 nm	80 nm	32 nA	20	1200	quartz
Gammadion RH	200 nm	40 nm	2 nA	5	1015	quartz
Gammadion LH	200 nm	40 nm	2 nA	5	1015	quartz
Crosses X	200 nm	40 nm	2 nA	5	1015	quartz
Gammadion RH	1 µ m	200 nm	32 nA	20	1200	Si wafer
Gammadion LH	1 µ m	200 nm	32 nA	20	1200	Si wafer
Crosses X	1 µ m	200 nm	32 nA	20	1200	Si wafer
Racemic 4	1 µ m	200 nm	32 nA	20	1200	Si wafer
J`s shape CL	320 nm	60 nm	8 nA	10	1200	quartz
J`s shape CR	320 nm	60 nm	8 nA	10	1200	quartz
J`s racemic 2	320 nm	60 nm	8 nA	10	1200	quartz
J`s racemic 4	320 nm	60 nm	8 nA	10	1200	quartz
J`s shape CL	220 nm	60 nm	8 nA	10	1200	quartz
J`s shape CR	220 nm	60 nm	8 nA	10	1200	quartz
J`s racemic 4	220 nm	60 nm	8 nA	10	1200	quartz
G`s RH	1µm	200nm	32 nA	20	1200	Si wafer
G`s LH	1µm	200 nm	32 nA	20	1200	Si wafer
Corner like shape	2 mm	1 µm	128 nA	20	600	Quartz &Si wafer

2.5.4. Pattern writing

The pattern writing is the process of fracturing a well- defined area on the top of a resist film. This is performed under vacuum by an electron beam. The current of the electronic beam is directed to scan a specific area of the resist film such that, the chemicals in the scanned area undergo severe chemical transformations. The scanned area is known as` the exposed area` and the resultant design is known as `the pattern`. Moreover, the writing speed depends on the type of resist we use. And the writing time depends on the type of the resist we use in addition to the size of the design we need. The cost of the writing for each sample is estimated according to the writing time. For our samples, the writing time varied from half an hour to almost five hours. Although, the VB6 writing machine is able to write on rough surfaces. See Figure 36 below. This Figure shows SEM images of cross shapes written on the top of the edge of Si-wafer substrate. However, some defects were recorded with some of our samples. Such defects are out with the operators control; as they are caused by the machine; some of these defects are shown in Figure 64.

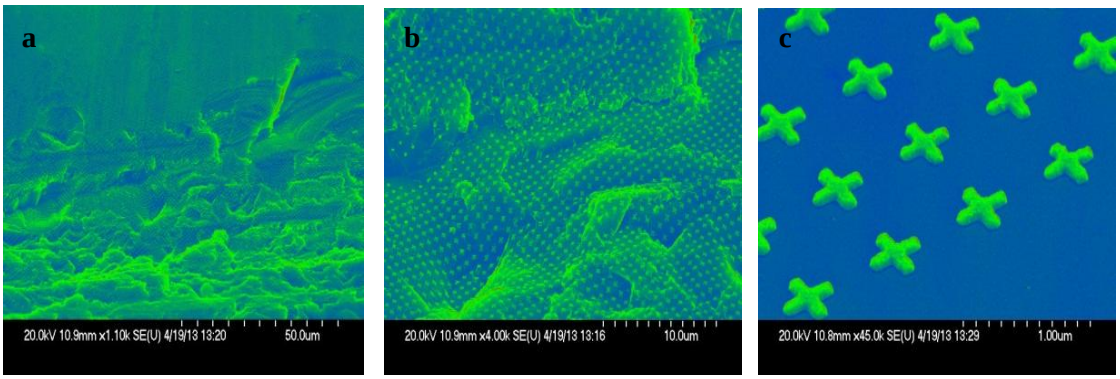

Figure 63: 3D SEM images of crosses shapes written on the top of the edge of Si-wafer substrate reflecting the capability of the VB6 to write efficiently on rough surface. The **a**, **b** and **c** show different zones and different zooming scales.

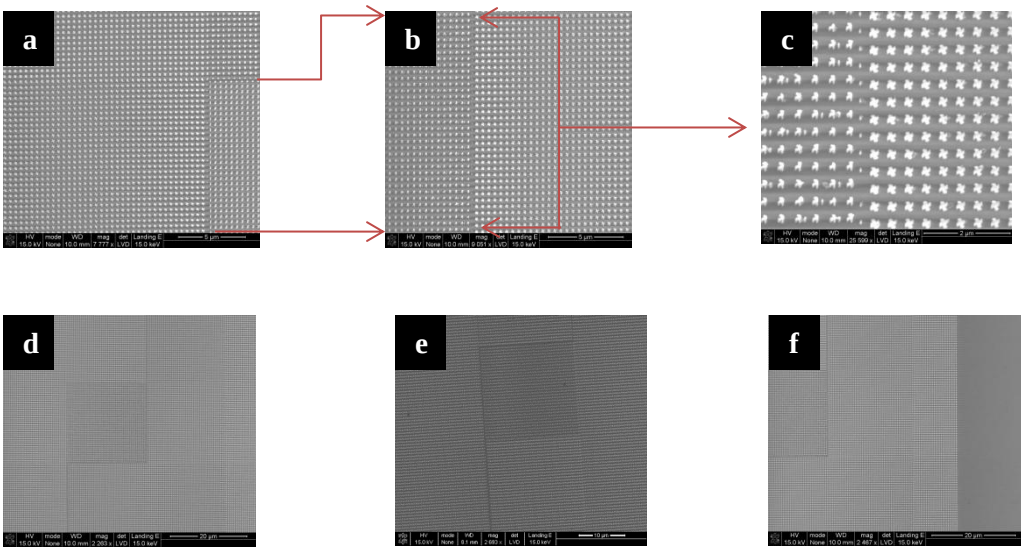

Figure 64: SEM images for some defects caused during the writing process by the VB6UHR EWF machine.

2.5.5. Wet etching

Wet etching is the process of dissolving the metallic layer mounted on the top of the resist film. This metallic layer (such as 20nm Al) is usually used as a conductive layer with non- conductive substrates like quartz or glass. Etching solutions (normally strong acids) attack the layer of the metal to dissociate it. This process can last one to two minutes. The process should be ended once the metal layer disappears completely. Importantly, wet etching solutions do not affect the layer of the resist.

For the samples used here, two types of wet etching solutions have been used. The first solution was a mixture of nitric acid and sulphuric acid. The second solution was a solution of CD-26 developer (aqueous solution of tetramethyl ammonium hydroxide TMAH) [71]. Each solution has been used to etch 20nm Al layer. At the beginning of our nanofabrication work we used the first solution; however it was later found that the CD26 was much more effective, faster and easier to use. The defects observed are shown in the SEM images below (Figure 65). The layer of sulphuric acid was found to adhere to the surface of the resist film which covered the pattern. Further optimisation showed that the CD26 was a superior etching agent.

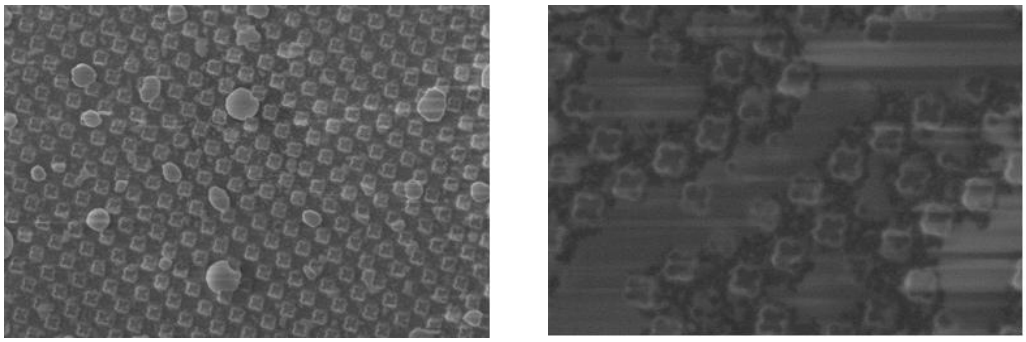

Figure 65: A layer of Sulphuric acid covering the features of the pattern. This was caused by the miss choice for a suitable wet etching solution.

2.5.6. The Development

The developing is the process of revealing the written area of the resist film. This is performed by dissolving the exposed area of the resist by specific organic solvents, see section (2.2.3) above. Such organic solvents are known as developers. The process of developing is affected by two main factors, the chemical agents used and the duration of the development. Figures of 66 and 67 illustrate some SEM images of our samples following development. For samples used here, the solution of MIBK: IPA 3:1 has been used as a developer. The temperature of the solution was maintained at 23 C°. The development time used was 25 seconds. Finally, the sample was cleaned for 30 seconds using a `New Gala Asher` plasma cleaner in JWNC cleanroom.

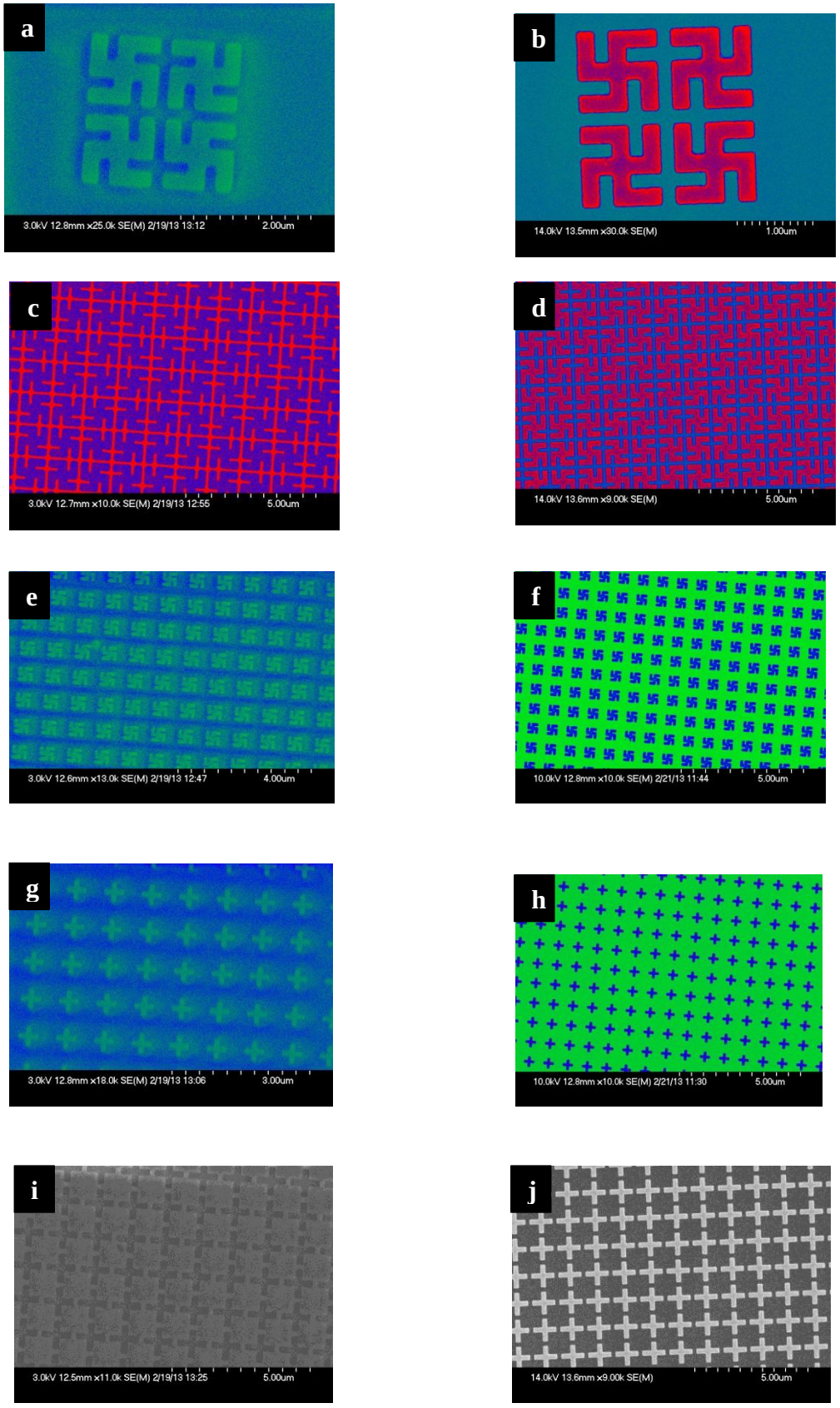

Figure 66: SEM images for the features of our samples patterns after the development (left column) and after the metallisation (Right column) processes. **a**, **c**, **e**, **g** and **i** show the features of the patterns before metallisation process. **b**, **d**, f, **h** and **j** show the features of the patterns after the metallisation process.

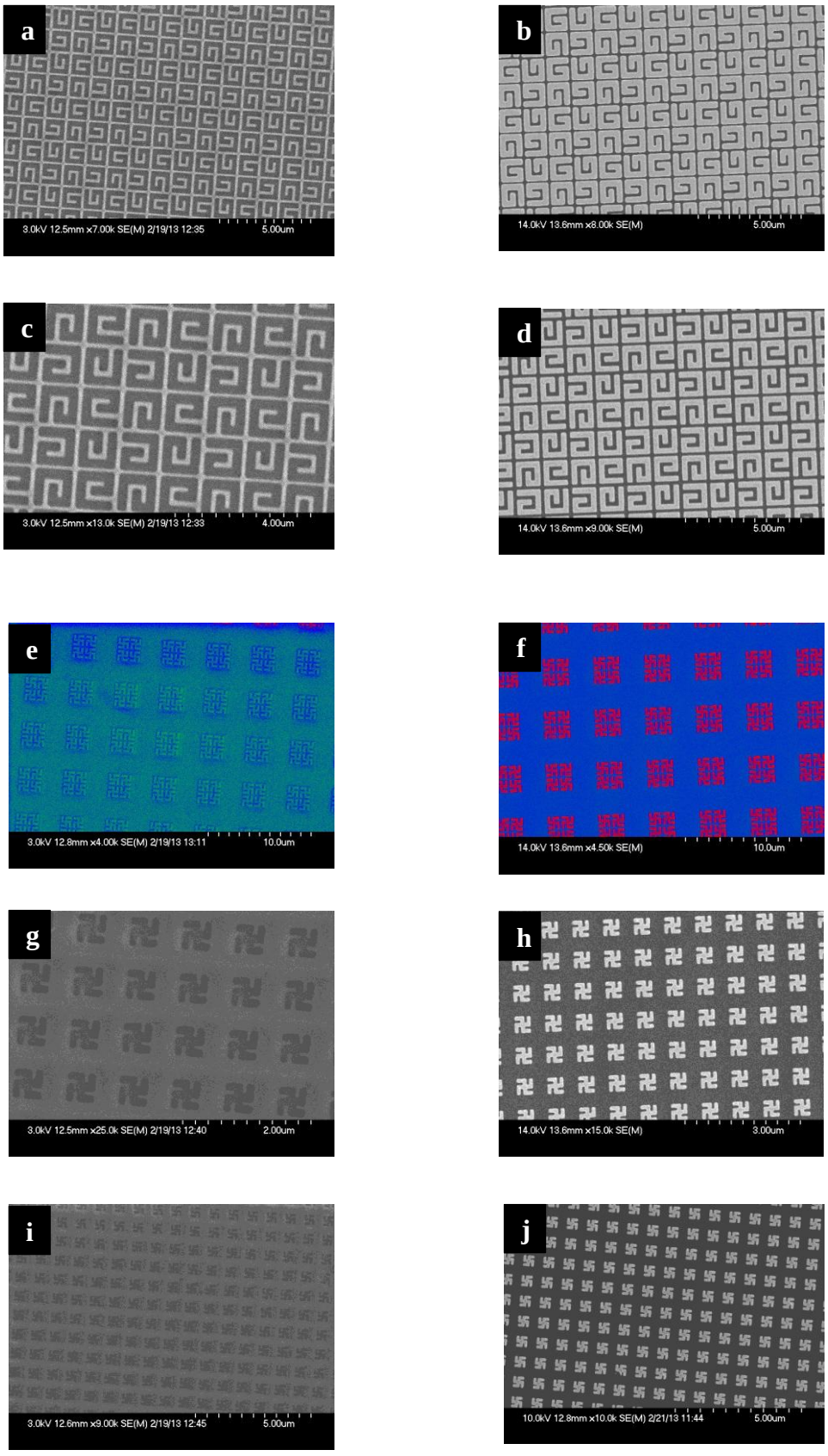

Figure 67: SEM images for the features of our samples patterns after the development (left column) and after the metallisation (Right column) processes. **a**, **c**, **e**, **g** and **i** show the features of the patterns before metallisation process. **b**, **d**, f, **h** and **j** show the features of the patterns after the metallisation process.

2.5.7. Metal deposition

A range of metallic thicknesses (varied between 25 – 150 nm) were used for metal deposition as detailed below:

- Gold (25 - 150) nm as a target metal.
- Silver (25 - 120) nm as a target metal.
- Nickel (25 – 60) nm as a target metal.
- Aluminium (20) nm as a conductive layer.
- Titanium (3 – 10) nm as an adhesive layer.

Gold: In order to deposit Gold on the surface of the substrate it is important to apply an adhesive layer first. This is necessary to bind the golden patterns strongly. Titanium was used as the adhesive layer. We applied 5nm of Titanium to adhere to a range of Gold thicknesses (between 50 – 130 nm). Also we have used a 2nm Titanium layer to hold 25 nm Gold.

Silver: A modified evaporator (this is different from plassysII) was used for silver deposition. 3-aminopropyltriethoxysilane (APTS) was used as a chemical adhesive layer for silver deposition. This was applied manually in a fume cupboard. The sample was immersed in 4% APTS (dissolved in ethanol) for four hours. This allowed adhesion of a 130nm layer of Silver.

Nickel: Nickel has self-adhesive properties and therefore did not require an adhesive for deposition of metal thicknesses less than 30nm.

Aluminium: A 20nm film of Aluminium was used as a charge conductive layer. This layer was deposited on the top of the PMMA resist prior to the writing process to absorb the scattered electrons by the electronic beam during the writing process.

Titanium: Mostly used as an adhesive layer. The range of Titanium thicknesses used was varied between 2 – 10 nm.

2.5.8. Lifting off

Lifting off is the process of removing the un-patterned area of the resist to emphasise the patterned area only on top of the substrate. The process is usually achieved by dissolving the layer of the resist by an organic solvent, such as acetone. See the Figure 68 below.

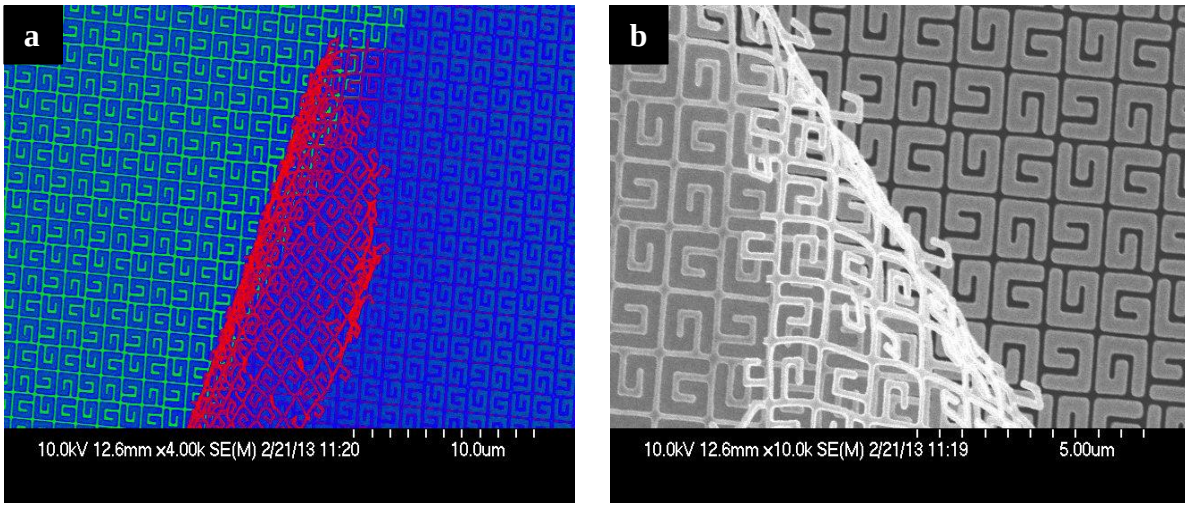

Figure 68: SEM images of the left handed G like shapes clarifying the definition of the lifting off process.

The successful lifting off process is achieved by the careful consideration of parameters such as: the solvent, incubation time, temperature, and sonication time. For our samples, we have used: acetone as the organic solvent; a temperature of 50 ^{o}C; incubation time was varied between 4 to 72 hours. The incubation time was found to be important for a successful lifting off process and had to be determined for each metal and pattern. It was generally found that the patterns with small features and thicker layers required longer incubation times than the patterns with larger features and thinner layers. Table 8 illustrates the time required for each pattern.

Table 8: The periods of time required for the lifting off process for our samples. Note that the period of the time increases with decreasing the sizes of the features.

Set no.	Pattern	Feature size	Time required
1	Gammadion LH	200 nm	3 days
1	Gammadion RH	200 nm	3 days
1	Crosses	200 nm	3 days
1	Gammadion LH	400 nm	2 days
1	Gammadion RH	400 nm	2 days
1	Gammadion racemic	400 nm	2 days
1	Crosses	400 nm	2 days
1	Gammadion LH	1 µ m	4 hours
1	Gammadion RH	1 µ m	4 hours
1	Gammadion racemic	1 µ m	4 hours
1	Crosses	1 µ m	4 hours
2	J`s LH	220 nm	2 days
2	J`s RH	220 nm	2 days
2	J`s racemic	220 nm	2 days
3	G`s LH	1 µ m	4 hours
3	G`s RH	1 µ m	4 hours
3	Crosses	1 µ m	4 hours

Following the incubation step a Pasteur pipette was used to gently flow air bubbles over the sample surface. The samples were then sonicated for 20 seconds. Finally the samples were rinsed with isopropyl alcohol solution and dried with a stream of nitrogen. All the lifting off procedures were performed inside the lifting off cabinet in JWNC cleanroom Figure 69.

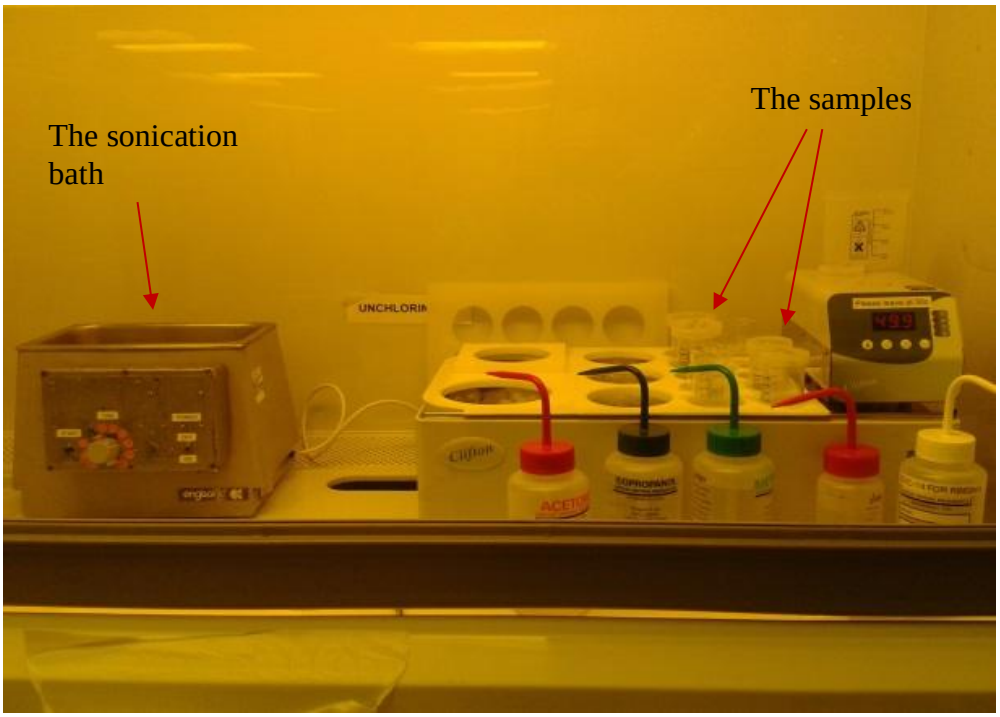

Figure 69: The lifting off process was performed inside a cabinet in JWNC cleanroom in Glasgow University. The red arrows pointing the location of the samples to be kept in during the lifting off process, and the sonication bath usually used to proceed the lifting off process.

Some SEM images illustrating defective samples due to problems with the lifting off process are shown in Figures (70-72). Figure 70 is an example of `over lifting off`, caused by over-incubation. After the layer of the resist dissolved completely, the metallic particles which were associated with the resist moved towards the patterned metallic layer resulting in 'spiky' features. Moreover, incomplete lifting off results from short incubation times where the resist is not given sufficient time to dissolve completely. This results in a patch of metal remaining on the top of the patterns. If the patch is large, entire, or centralised, the sample will be defective as exemplified in Figure 71 below. Another example is the problem of `over sonication time`. This results in loss of features from their patterns as shown in Figure 72.

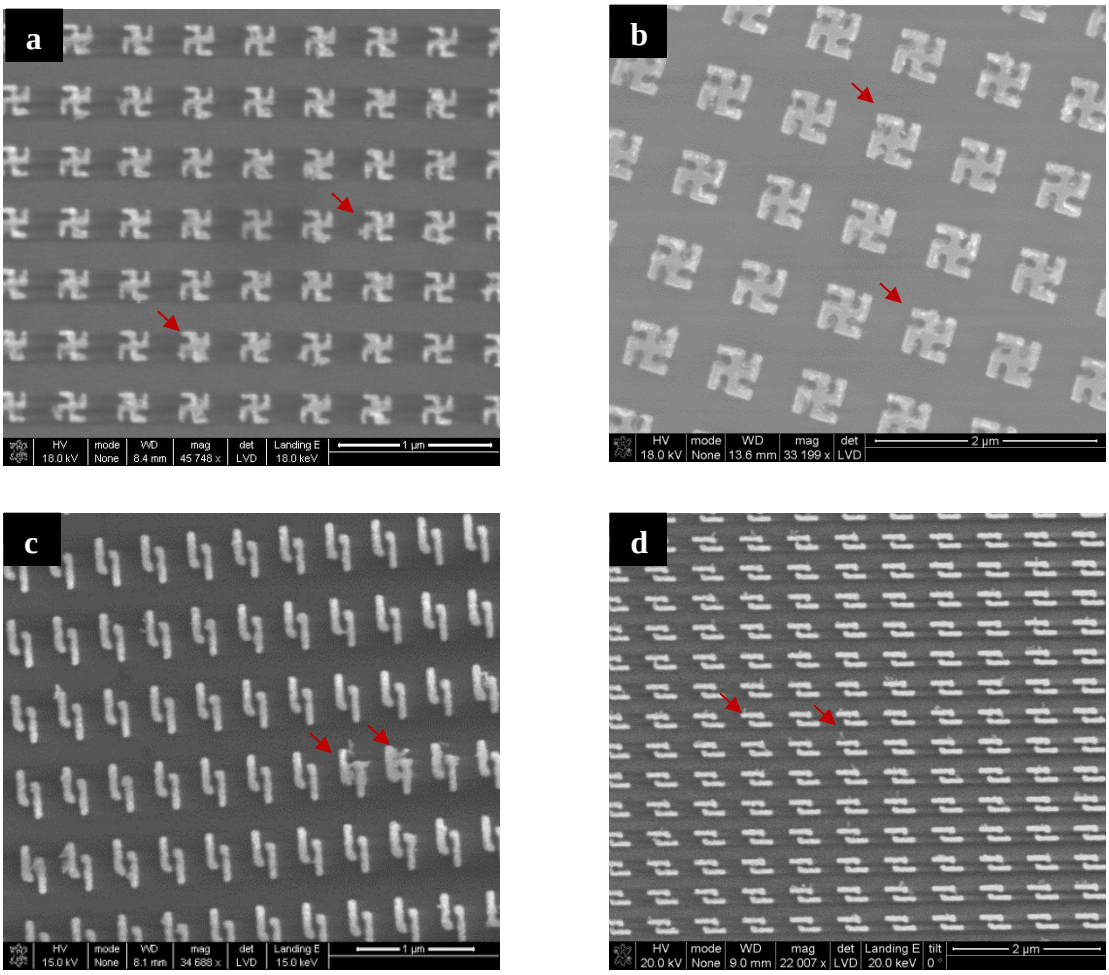

Figure 70: SEM images for over lifting off problem. The red arrows point to the features undergone over lifting off problem.

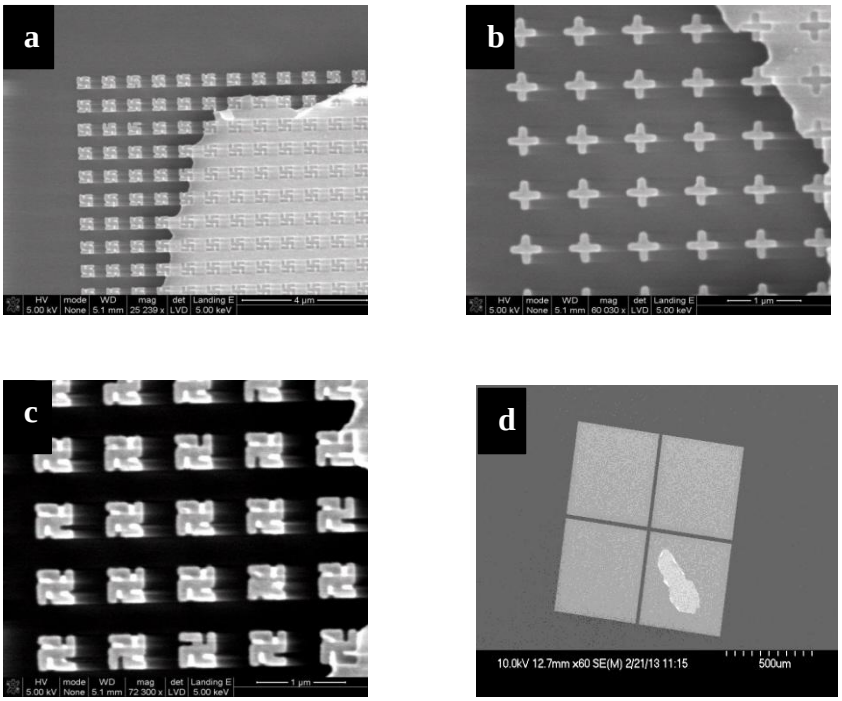

Figure 71: SEM images for incomplete lifting off problem. Note the large patch in **a**, the entire patch in **c** and the centralised patch in **d.** In **b** the sample is less affected.

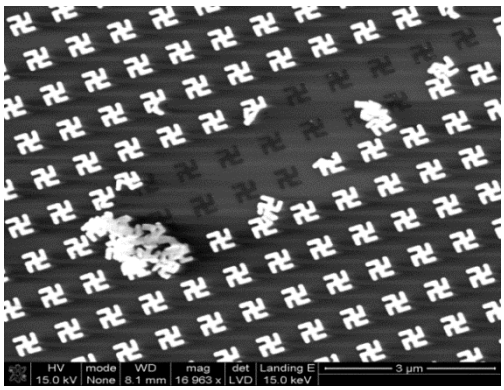

Figure 72: An SEM image demonstrating the problem of the `over sonication time` problem occurring during the lifting off process.

2.6. Sample validation test

Samples were evaluated post fabrication using Scanning Electron Microscopy (SEM) and/or CD spectroscopy. SEM was performed by using either FEI Nova NanoSEM 630 for quartz samples or by using Hitachi 4700 for Si-wafer and coated quartz samples (coated with conductive materials like Gold Palladium layer). Samples were imaged with a number of different scales (between 300nm to 1mm) to check the quality and the integrity of our nanofabricated features. The evaluation by circular dichroism spectroscopy was performed by using aJASCO-J-810CD spectropolarimeter (shown in chapter 4). The CD instrument measures the differential absorption of left and right circularly polarised incident light by chiral molecules (or chiral nanofeatures). CD was useful in that it could detect subtle differences in the chiral patterns which helped to validate the integrity of each sample. Both CD and SEM provided complementary information about pattern integrity. In some cases good CD spectral features were obtained in the absence of sharp SEM images and vice versa. Only samples which gave both good quality CD spectra and SEM images were found to be reliable for optical experiments due to the small differential absorbance measurements being detected when target molecules bound to the chiral nanostructures. Small deviations in pattern integrity could give rise to similar spectral shifts to those used to assess molecule binding to nanosurfaces.

2.6.1. Influence of the nanopattern shape

The CD spectra obtained with the different nanostructures were found to be influenced by chiral shape as illustrated in Figure 73. This Figure shows the pattern of gammadions and `J` shapes where: **a** and **c** represent the SEM images for the left and right handed gammadion shapes, respectively; **d** and **f** represent the SEM images for the left and right handed `J` shapes; **b** and **e** represent the CD spectra for the gammadion shapes and `J` shapes, respectively. Both patterns were fabricated with the same EBL parameters using 5nmTi and 130nm gold on quartz substrate. The different CD spectra produced by the `J `and the gammadion shapes reflect the differential absorbance of the two patterns.

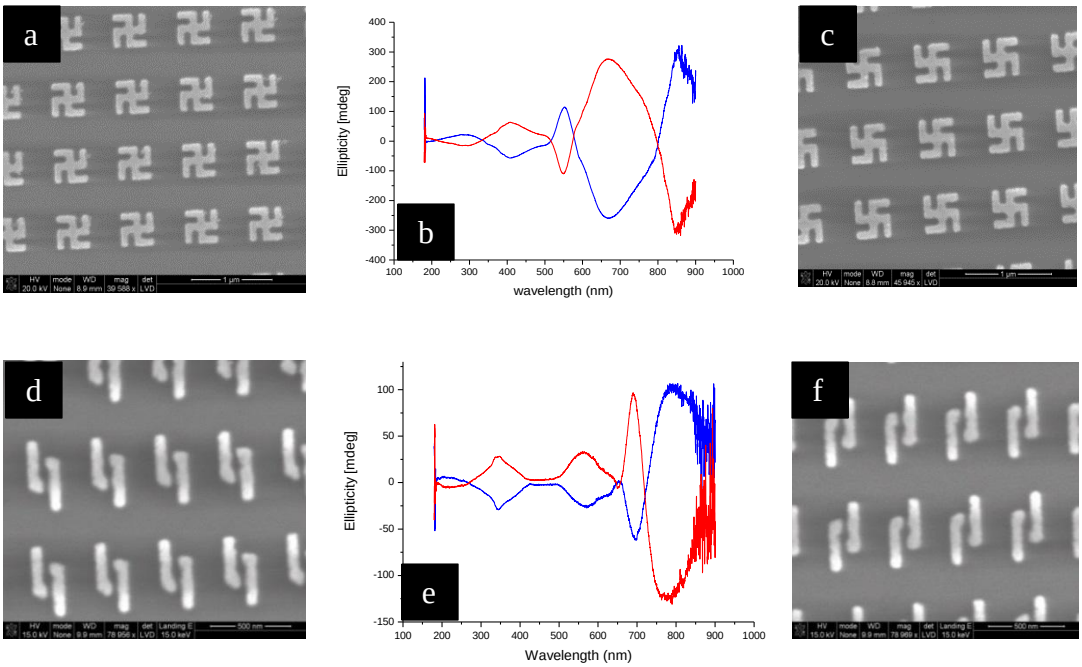

Figure 73: SEM images and the CD spectrum of gammadion shapes and `J` shapes. (**a**, **d**) and (**c**, **f**) represent the left and right orientations for gammadion and `J` shape, respectively. **b** and **c** represent the CD spectrum for the mirror image pairs for the gammadions and `J` shape, respectively. Note the differences in the resonance of the CD spectrum, which correspond the differential absorbance of the two patterns

2.6.2. Influence of the nanopattern chiral orientation

As expected the CD spectra of left and right-handed nanostructures were found to be practically mirror images of each other as shown in Figure 74. This Figure shows two samples of `J` shape patterns: **a** and **c** represent the SEM images of the left and right handed features, respectively; **d** and **e** represent the CD spectra for the left and right handed features, respectively; **b** represents the mirror image CD spectra of the left and right handed nanostructures. Both patterns were fabricated with the same EBL parameters using 5nmTi and 130nm gold on quartz substrate. Slight variations in the integrity of the mirror-image were noticed and can be attributed to slight differences in the uniformity of the patterns produced as a result of slight electron scattering during fabrication and/or during metallisation.

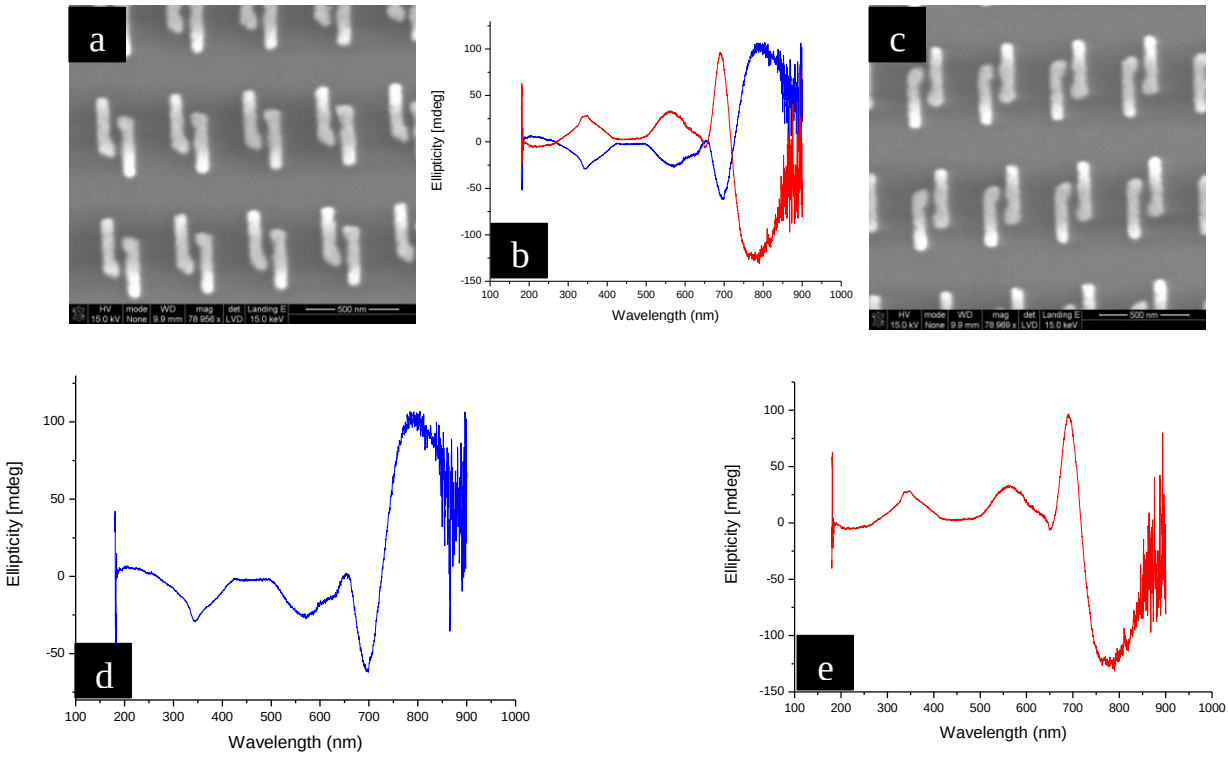

Figure 74: SEM images and the CD spectrums of the `J` shapes. **a** and **c** represent the left and right handed features respectively. **d** and **e** represent the CD spectrum for the features in **a** and **c** respectively. **b** represents the mirror image spectra if **d** and **e** are plotted within the same plot.

2.6.3. Influence of the depth of metallic layer

The depth of the gold layer affected the intensity and shape of the CD spectra obtained as illustrated in Figure 75. CD spectral differences corresponding to the variation of the thickness layer of the gold were observed. For example nanostructures with depths of gold corresponding to 55nm, 110nm and 130nm gave CD intensities of 50mdeg, 100mdeg and 300mdeg, respectively, in the wavelength region 650nm-750nm. These observations were not evident by SEM due to lack of sensitivity to depth when capturing images in this way. Cross sectional SEM images are sensitive to depth however such imaging was not possible as this would have destroyed the nanostructures required for these experiments as exemplified in Figure76. This Figure shows SEM images for the cross section of the left handed gammadion shapes.

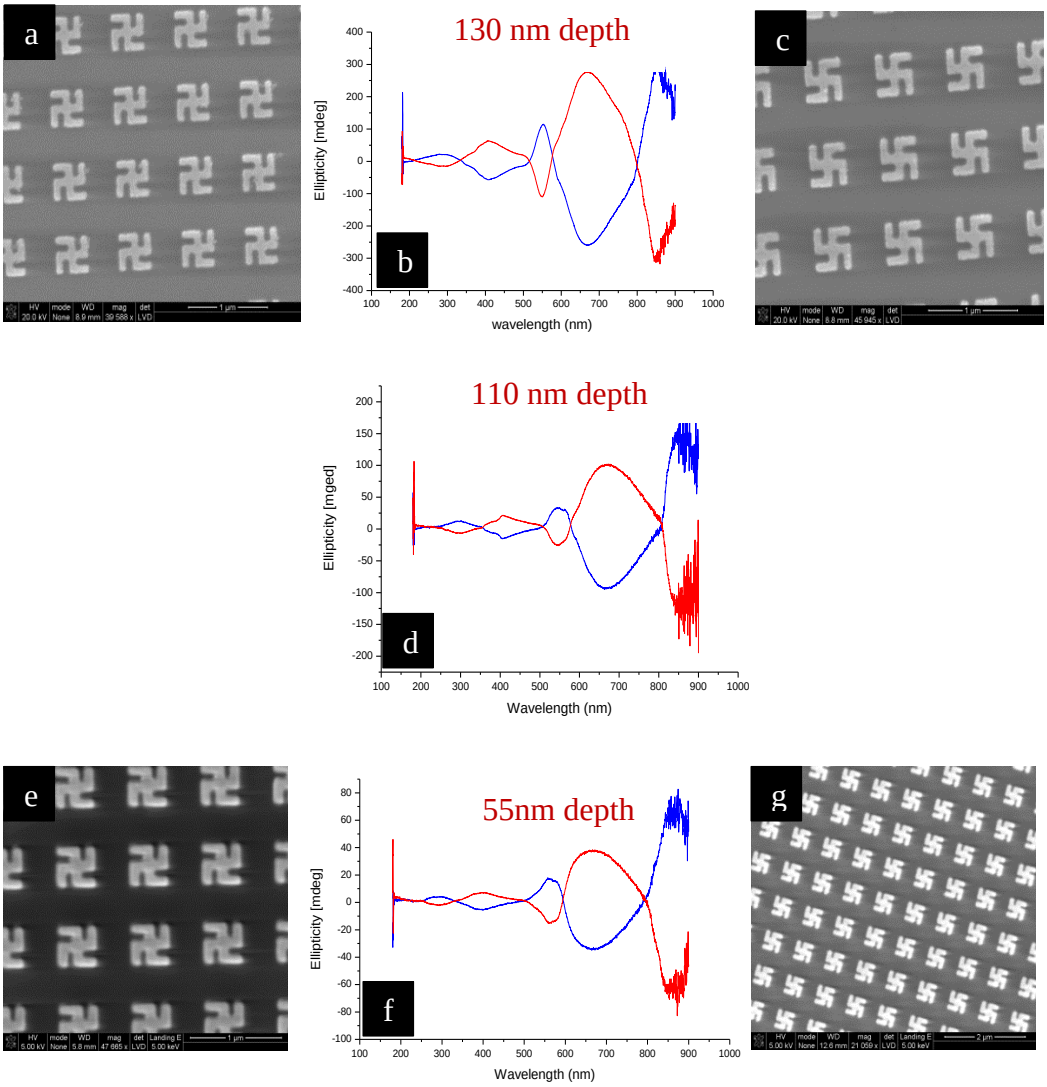

Figure 75: SEM images and the CD spectrums of the gammadion shapes. (**a**, **e)** and (**c**, **g)** represent the left and right handed features, respectively. **b**, **d** and **f** represent the variation of the mirror image CD spectrum correspond to the variation of the thickness layer of gold which is a 130 nm, 110nm and 55nm respectively. Ellipticities are shown with their original scales in b, d and f in order to show resonance details clearly.

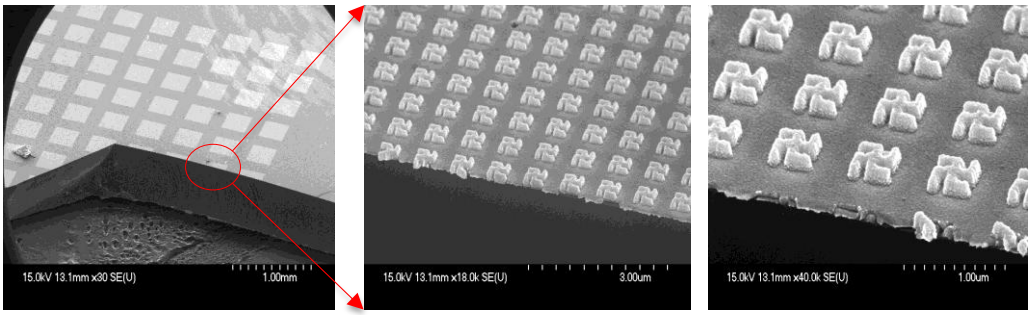

Figure 76: Cross section of 3D SEM images for the left handed gammadion shape features. Although the images are high resolution product, it is incapable to use with our samples. So the cross section routine is inappropriate way to measure the thickness of our samples.

2.6.4. Pattern reproducibility

Sample batch variations were observed which resulted in slight differences in CD spectral contributions. Figure 77 gives an example of the type of batch to batch variations observed by CD spectroscopy. Two sets of CD spectra are shown which represent two sets of right-handed (red lines in **b** and **e**) and left-handed (blue lines in **b** and **e**) gammadions. The spectra of the two right-handed gammadions and the spectra of the two left-handed gammadions do not superimpose. Also slight variations in the integrity of the mirror-image were noticed and can be attributed to slight differences in the uniformity of the patterns (**a**, **c**, **d** and **f**) produced as a result of slight electron scattering during fabrication and/or during metallisation. It was therefore important to characterise each individual chip sample prior to binding analysis. Figure 78 shows some differences in the uniformity of the metallisation process observed with our cross control patterns.

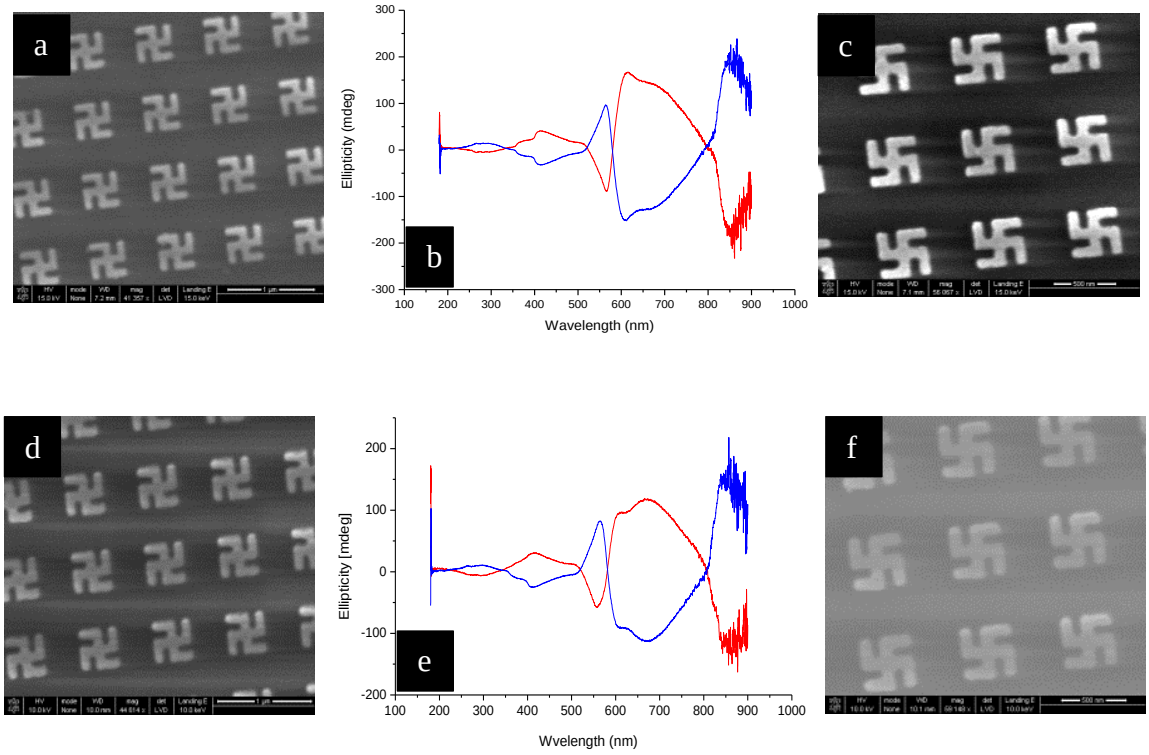

Figure 77: SEM images and the CD spectra of the gammadion shapes. (**a**, **d)** and (**c**, **f)** represent the left and right handed features, respectively. **b** and **e** represent the CD spectrums of the mirror image pairs for two identical samples. Note the effect of slight differences of the nanofeatures (shown in SEM images) on the CD spectra.

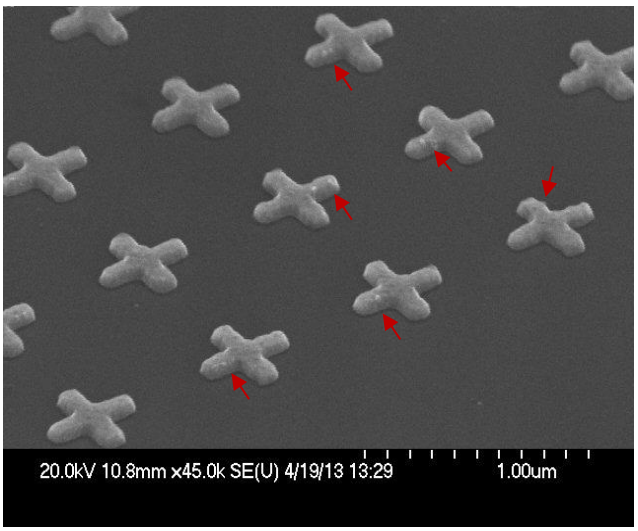

Figure 78: 3D SEM image for the cross shapes. Note the small differences between the features highlighting by the red arrows.

2.6.5. Influence of the nanofeatures size on CD spectra

A correlation between the size of the nanostructures and the CD spectral features was observed. As illustrated in Figure 79. This Figure shows the SEM images and the CD spectra for the gammadion shapes. (**a, c**) and (**d, f**) represent the SEM images for the left and right handed orientation, respectively. **a** and **c** represent the 200nm shapes. **d** and **f** represent the 400nm shapes. Note the nanostructures with 200nm and 400nm gave CD intensities of ~200mdeg and ~300mdeg, respectively, in the wavelength region of 200nm-570nm.

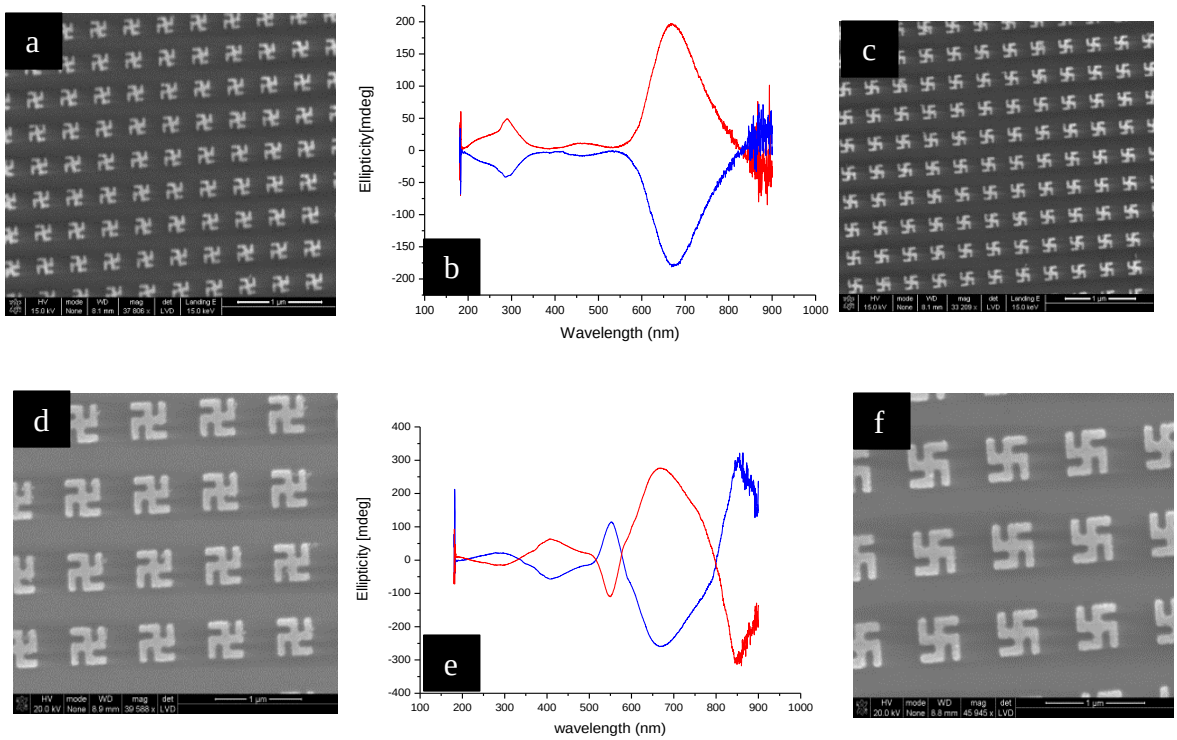

Figure 79: SEM images and the CD spectrums for the gammadion shapes. (**a, c**) and (**d, f**) represent the SEM images for the left and right handed orientations respectively. **a** and **c** are the 200nm shapes. **d** and **f** are the 400nm shapes. Note the differences between the CD spectrums for the two shapes which correspond to the differences of the two sizes.

2.6.6. Complements necessity

During the course of these studies it was found that SEM imaging in addition to CD spectral analysis was important to assess sample integrity. Each technique gave complementary information corresponding to successful fabrication. Figure 80 shows that although the CD spectral features were evident in the expected wavelength regions (Plasmon regions) the SEM images showed that the `J` patterns were in fact distorted with no spaces between the nanostructure pairs. Further investigations showed that the CD spectrum of the sample with merged pairs were different from those with spacing between the `J` pairs. Figure 80 **a** and **b** represent the SEM images for the normal and the merged features, respectively; **c** represents the CD spectra for the mirror image pairs of the normal and merged features.

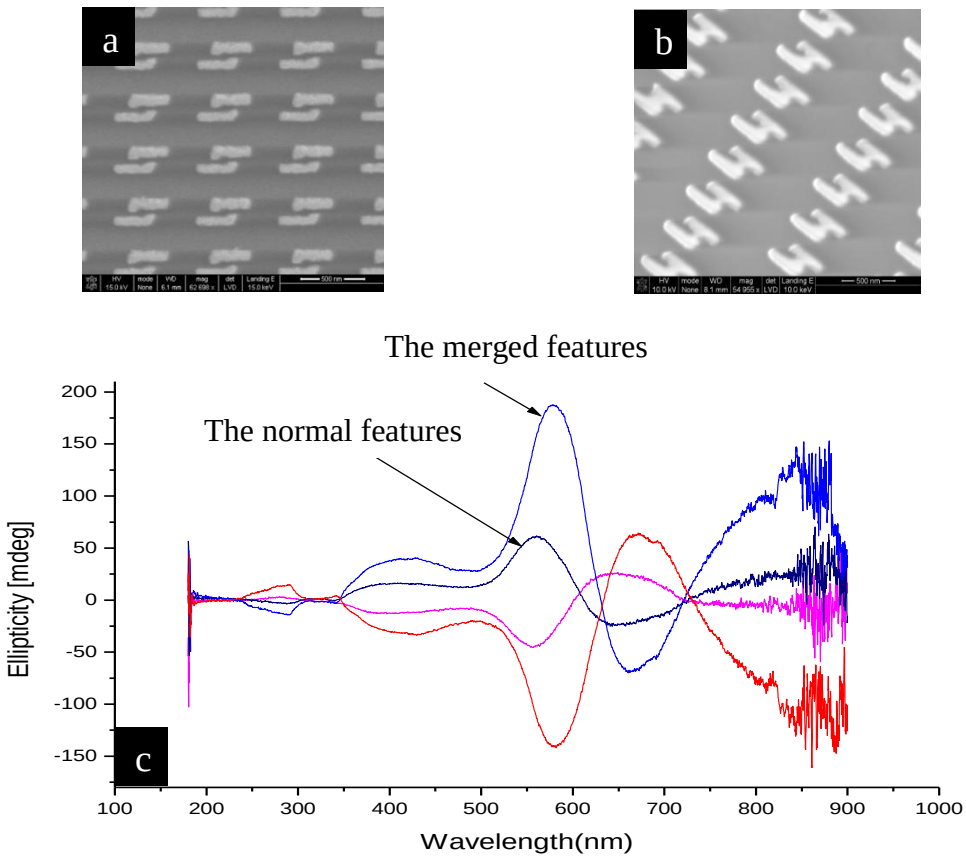

Figure 80: SEM images and the CD spectrums of the 'J' shapes. **a** represents the SEM image for the normal features. **b** represents the SEM image for the merged (stuck) features. **c** represents the CD spectrums for the mirror image pairs of the normal and stuck features. Note the resonance for the stuck features look decent and reliable but in fact it is just artefact caused by the merged features.

2.7. Summary

Nanofabrication work has been optimised to develop a new biosensing platform using a combination of CD spectroscopy and SEM microscopy. It has been found that Gold is the optimal metal which can be used to manufacture these effective nano-electronic biosensing platforms. Gold nanopatterns produce biosensors with the unique properties: high sensitivity; reliability; stability; durability (i.e. can be used more than once); which give reproducible results. It is anticipated that such electronic biosensors can be developed to produce highly sensitive 3-D platforms which can be used for multiple applications.

2.8. References

1. Rai-Choudhury P., "Handbook of microlithography, micromachining and microfabrication", *The Society of Photo-Optical Instrumentation Engineers*, Vol.1,1997, printed book
2. Stepanova M., Dew S., "Nanofabrication / techniques and principles", *Springer Wien New York*, c2012. Chapter2, e-book.
3. Zhao X., Xia Y. and Whitesides G., *J.Mater.Chem*., 1997, Vol.7, pp (1069-1074).
4. Cumming D., Thoms S., Weaver J. M. R. and Beaumont S., *Microelectronic Engineering*, 1996, Vol.30, pp (423-425).
5. Maile B., Henschel W., Kurz H., Rienks B., Polman R. and Kaars P., *Japanese Journal of Applied Physics*, 2000, vol.39, pp(6836-6842).
6. Grigorescu A. E., Van der Krogt M. C., Hagen C. W. and Kruit P., *Microelectronic Engineering*, 2007, Vol. 84, pp (822-824).
7. Grigorescu A. E., Van der Krogt M. C. and Hagen C. W., *Proc.SPIE*, 2007, Vol. 6519, pp (822-824).
8. Yamazaki K. and Namatsu H., *Japanese Journal of Applied Physics*, 2004, Vol 43, pp (3767- 3771).
9. Selinidis K., Thompson E., Schmid G., Stacey N., Perez J., Maltabes J., Resnick D., Yeo J., Kim H. and Eynon B., *Proc. SPIE*, 2008, Vol.7028, pp (70 280R (1-10)).
10. Broers A. N., Hoole A. C. F., Ryan J. M., *Microelectronic Engineering*, 1996 Vol.32, pp (131-142).
11. Zhang W., Potts A., Bagnall D. M. and Davidson B. R., *Thin Solid Films*, 2007, Vol.515, pp (3714-3717).

12. Groves T. R., Pickard D., Rafferty B., Crosland N., Adam D. and Schubert G., *Microelectronic Engineering*, vol.(61–62), 2002, pp (285–293).
13. Egerton R. F., "Physical Principles of Electron Microscopy", *Springer Science+Business Media, Inc.* 2005, e-book.
14. Rai-Choudhury P., "Handbook of microlithography, micromachining and microfabrication", *The Society of Photo-Optical Instrumentation Engineers*., 1997, Vol.2., printed book
15. Hahmann P. and Fortagne O., *Microelectronic Engineering*, 2009, Vol.86, pp (438-441).
16. Molhave K., Madsen D. N., Boggild P., *Ultramicroscopy*, 2005, Vol.102, pp(215-219).
17. Grigorescu A. E., Van der Krogt M. C. and Hagen C. W., *Qinghuang Lin Proc. of SPIE*, 2007, Vol.6519, pp (A (1-12)).
18. Saleem M. R., Stenberg P. A., Khan M. B., Khan Z. H., Honkanen S. and Turunen J., *Proc. of SPIE*, 2012, Vol.8249, pp (G(1-7)).
19. Ma S., Con C., Yavuz K. and Cui B., *Nanoscale Research Letters*, 2011, Vol.6, pp (1-6).
20. Soanes C. and Stevenson A., "Concise Oxford English Dictionary", *Oxford University Press*, 11th Edition, 2008.
21. Collins English Dictionary, *HarperCollins Publishers Limited*, 2006.
22. Cai W., *Physics*, 2013, Vol.6, pp (1-3).
23. Vaselago V. G., *Usp*, 1968, Vol.10, pp (509-514).
24. Engheta N. and Ziolkowski R. W., "Metamaterials: Physics and Engineering Explorations", *Institute of Electrical and Electronic Engineering, Inc. Press, John Wiley & Sons*, 2006, printed book.
25. Jindal S. and Sharma J., *International Journal of Computer Applications*, 2012, Vol.54, pp (48-54).
26. Frierson W. and Shvets G., "Negative Index Metamaterials for particle Acceleration and Radiation Generation", *University of Texas, Honors Thesis in Physics*, 2010.
27. Pendry J. B., Holden J., Robbins D. J. and Stewart W. J., *Institute of Electrical and Electronic Engineering Transactions on Microwave Theory and Techniques*, 1999, Vol.47, pp(2075-2084).
28. Chen H. T., Padilla W. J., Averitt R. D., Gossard A. C., Highstrete C., Lee M., Ohara J. F. and Taylor A. J., *Terahertz Science and Technology*, 2008, Vol.1, pp(42-50).
29. Capolino F., "Applications of Metamaterials", *CRC Press, Tylor & Francis Group*, 2009, printed book.
30. Kuttge M., Vasseur E. J. R., Koenderink A. F., Lezec H. J., Atwater H. A., Garcia de Abajo F. J. and Polman A., *Physical Review B*, 2009, Vol.79, pp (113405(1-4)).
31. Wang B., Zhou J., Koschny T., Kafesaki M. and Soukoulis C. M., *Journal Of Optics A: Pure And Applied Optics*, 2009, Vol.11, pp (114003(1-10)).
32. Wang B., Zhou J., Koschny T. and Soukoulis C. M., *Optics Express*, 2008, Vol.16, pp(16058-16063).
33. Lapine M., Powell D., Gorkunov M., Shadrivov I., Marqués R. and Kivshar Y., *Applied Physics Letters*, 2009, Vol.95, pp (084105(1-3)).

34. Alici K. B. and Özbay E., *Phys. Stat. Sol.b*, 2007, Vol.244, pp (1192-1196).
35. DeRose C. T., Kekatpure R. D., Trotter D. C., Starbuck A., Wendt J. R., Yaacobi A., Watts M. R., Chettiar U., Engheta N. and Davids P. S., *Optix Express*, 2013, Vol.21, pp (5198-5208).
36. Engheta N., *Science*, 2007, Vol.317, pp (1698-1702).
37. Kosuda K. M., Bingham J. M., Wustholz K. L. and Van Duyne R. P., *Comprehensive Nanoscience and Technology*, 2011, Vol.3, pp (263-301).
38. Hendry E., Carpy T., Johnston J., Popland M., Mikhaylovskiy R. V., Lapthorn A. J., Kelly S. M., Barron L. D., Gadegaard N. and Kadodwala M., *Nature Nanotechnology*, 2010, Vol.5, pp (783-787).
39. This image could be found at this website (cited in 2014): http://www.aph.kit.edu/wegener/img/vis-neg-refractive-index.jpg
40. Sambles R., *NATURE*, 2005, Vol 438, pp(1-7)
41. Valev V. K., Langmuir, American Chemical Society, 2012, Vol.28, pp (15454-15471).
42. Willets K. A. and Van Duyne R. P., *Annu. Rev. Phys.Chem*, 2007, Vol.58, pp (267-297).
43. Gupta B. D. and Verma R. K., Journal of Sensors, 2009, PP (1-12) 979761
44. Zeng s., Baillargeat D., Ho H. and Yong K. Chem. Soc. Rev., 2014, Vol. 43, pp(3426—3452)
45. Schasfoort B. M. and Tudos A.J. "Handbook of Surface Plasmon Resonance", *The Royal Society of Chemistry*, 2008.
46. Benson O., *Nature*, 2011, Vol 480, pp(193-196).
47. Zhou X, Liu G., Yu J. and Fan W., *J. Mater. Chem.*, 2012 vol 22, pp(21337-21354).
48. Li X. D., Chen T. P., Liu Y. and Leong K. C., *OPTICS EXPRESS*, 2014,| Vol. 22, pp(5124-5132).
49. Wang F. and Ron Shen Y., PHYSICAL REVIEW LETTERS, 2006, Vol.97, pp (206806 (1-4)).
50. Chung T., Lee S., Song E., Chun H. and Lee B., *Sensors*, 2011, Vol.*11*, pp(10907-10929).
51. Capasso F., Yu N., Cubukcu E. and Smythe E. *OPN May*, 2009, pp(22-27).
52. Scha¨ferling M., Dregely D., Hentschel M. and Giessen H., *PHYSICAL REVIEW X*, Vol. 2, 2012, pp(031010(1-9)).
53. Hunber H. , *Microelectronic Engineering / Elsevier*, 1992, vol.18, pp (275-293).
54. Takigawa T., Kawabuchi K., Yoshimi M. and Kato Y., *Microelectronic Engineering/ North-Holland*, 1983, Vol.1, pp (121-142).
55. Rommel M., Nilsson B., Jedrasik P., Bonanni V., Dmitriev A., Weis J., *Microelectron. Eng.*, 2013, Vl. 110, pp (123-125).
56. Yang H., Jin A., Luo Q., Li J., Gu C. and Cui Z., *Microelectronic Engineering*, 2008, Vol.85, pp (814-817).
57. Yang J., Anant V. and Berggren K., *American Vacuum Society B*, 2006, Vol. 24, pp (3157-3161).
58. Yasuda M., Sakai H., Takai R., Kawata H. and Hirai Y., *Microelectron. Eng*., 2013, Vol.112, pp (287-290).
59. Yan M., Lee J., Ofuonye B., Choi S., Jang J. H. and Adesida I., *J. Vac. Sci. Technol. B*, 2010, Vol. 28, pp (1-5).

60. Hasko D. G., Yasin S. and Mumtaz A., *J. Vac. Sci. Technol. B*, 2000, Vol.18, pp (3441-3444).
61. Docherty K. E., *Glasgow University, PhD thesis*, 2010.
62. Rahate A., *Paintindia Pvt, Ltd*, 2010, Vol.60, pp (111-116).

63. Find this image at (cited in 2013): http://www.temescal.net/images/anim/poptopguns.png
64. This table is available to view on the web (cited in 2013): http://www.oxford-vacuum.com/background/thin_film/reference_data.pdf
65. This publication is available to view on the web (cited in 2013): http://www.kelvinnanotechnology.com/equipment/metallisation/plassys_meb550s_1.html
66. This publication is available to view on the web (cited in 2013): http://www.first.ethz.ch/infrastructure/equipment/pvdm
67. Schatten H., " Scanning Electron Microscopy for the Life Sciences", *Cambridge University Press*, 2013, e- book.
68. An Introduction to Electron Microscopy, *FEI company*, 2013.
69. Dufek M., *FEI Company*, 2007, 1st Edition.
70. This information is available to view on the web (cited in 2013): www.jwnc.eng.gla.ac.uk

71. Yang J. K., Anant V. and Berggren K.K., American Vacuum Society B, 2006, Vol.24, pp (3157- 3161).

Chapter 3: Super Chiral Fields to Sense Biomolecules on Gold Chiral plasmonic nanostructures via CD spectroscopy and scanning microscopy

Abstract

Super chiral fields have been generated by exposing 400nm chiral nanostructures with circularly polarised light (CPL) over the wavelength range180-900nm. When chiral biomolecules were adsorbed onto these lithographically sculptured nanostructures a dissymmetry in left and Right CPL absorption was observed. This dissymmetry has been utilised to detect and characterise a range of biomolecules up to several microns in size. The study involved secondary and higher order protein structures, which is important in biomedical sensing and pathogenic detection, e.g. to detect early signs of amyloidal diseases, such as Alzheimer's disease and Parkinson's disease. Three techniques, CD spectroscopy, SEM and AFM microscopy have been used for this purpose.

3.1. Introduction

3.1.1. Chirality and biomolecule sensing

Determinations of optical properties are usually performed using chiroptical spectroscopies like CD, ORD, ROA etc., which are all based on the interaction between the chiral structure of the biomolecule and the electromagnetic field of the incident light [1,2chap.1 pp2]. The microscopic origin of these optical properties originates from the non-locality of the light –matter interaction, which leads to the electromagnetic field of the incident light experiencing the spatial extension of the molecule and hence probe its spatial organisation which is sensitive to the molecule handedness [3]. Fundamentally, while the electromagnetic field of the incident light experiencing the spatial extent of the molecular; the electrons of the chiral molecules will be affected; and therefore induces electromagnetic fields which interact with the electromagnetic fields of the incident light, and

hence illustrating why these molecules respond to the electromagnetic fields of the incident light [4].

3.1.2. CD spectroscopy

CD spectroscopy can be used to characterise the low resolution structures of chiral biomolecules such as proteins and DNA. It has been used to characterise the optical activity of the surface plasmon resonances associated with colloidal nanoparticles or with metamaterials [5-7]. In principle, CD spectroscopy detects the chiral molecule's differential absorption of left and right circularly polarised light. Achiral molecules exhibit no differential absorption [8-10]. Conventional CD spectroscopy can detect biomolecules in microgram quantities as a minimum amount. However, the use of chiral gold metamaterials i.e. plasmonic nanostructures has been found to improve sensitivity by detecting picogram quantities of adsorbed biomolecules [6]. The rationale behind this study is to design highly sensitive biosensors which can detect picogram quantities of biomolecule. Such biosensors are gold metamaterials lithographically structured in the shape of 400nm left and right handed gammadions (see chapter 2). The idea is to improve the capabilities of the CD spectroscopic measurements by using a sculpted electromagnetic field, referred to as the *Superchiral Field*, which is usually generated when plasmonic nanostructures interact with the circularly polarised incident light of the CD spectrometer (this is explained with more details in section 2 of this chapter). The measurements described in this chapter are based on the fundamental discovery of previously published work which described the potential of the Superchiral field to allow the ultrasensitive detection of the secondary structural properties of different proteins [6]. Our new studies have involved the characterisation of biomolecular secondary (and higher order) structures which are out with the limits of detection using conventional methodology. In addition, scanning electron microscopy (SEM) and atomic force microscopy (AFM) were used to support the spectroscopic data.

3.2. Theory and background

In this section we present some theoretical aspects which we believe will help the understanding of our experimental work and hence help to follow our discussions. We first discus aspects of Circular Dichroism (CD) and optical rotation (OR) using a set of images that are based on appropriate mathematical functions from reference [11]. We then discus aspects of the Superchiral field, which are generated by our nanostructures. We finally discus how Superchiral field could be effectively used to sense biological molecules.

3.2.1. Circular Dichroism (CD) and Optical Rotation (OR)

It is possible for circularly polarised light, whether it oscillates in a sense of left or right handedness, to be absorbed by the materials of its propagation medium and therefore its magnitude could be reduced; with its circular polarisation state remains unchanged, see Figure 1**a**. In this Figure, we show how the intensity of circularly polarised light could be reduced upon passing through a light-absorbing medium. We also show the front sides of the intersecting planes which show the evolutions of the electric field vectors before (Figure1**b**) and after (Figure1**c**) entering the optical medium. Despite the fact that the evolution of the electric field vectors in **c** was reduced because of the absorption, yet, both evolutions remain circular. Having this fact means, if a combination of left and right CPL propagate simultaneously, and one of them was selectively absorbed by the materials of the propagation medium; the resultant field vector will be characterised by an elliptical evolution instead of circular, and hence a phenomenon known as *circular dichroism*, or most commonly CD, will occur, see Figure 2. In this Figure, we show a schematic of two circular electric field waves (contrarily orientated to each other) propagating simultaneously and demonstrating how the resultant plane polarised light (blue line) could be altered from circularly to elliptically polarised light (EPL) upon passing through a medium that selectively absorbs the left CPL (left CPL is used here as an example, so right CPL should has similar concepts). The degree of ellipticity depends on the strength of the absorption, which of course depends on the

absorbant. In **a** one can observe how the intensity of the left CPL (green line) could be reduced as a result of the absorption by the material of the medium, with the intensity of the right CPL remains unchanged (red line). Also, we present the front sides of the intersecting planes to show the evolutions of the plane polarised light before (**b**) and after (**c**) entering the optical medium [11, 12].

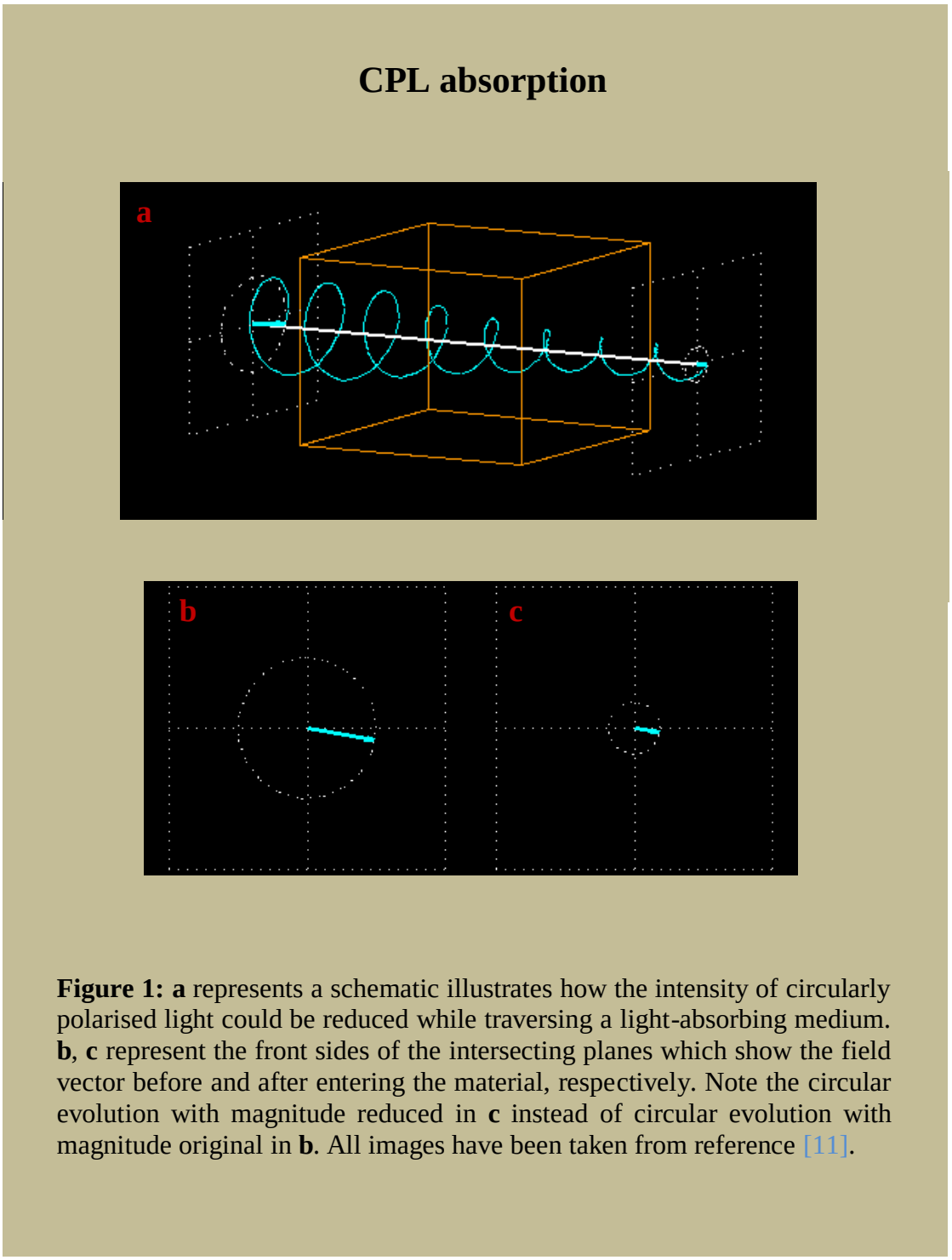

Figure 1: a represents a schematic illustrates how the intensity of circularly polarised light could be reduced while traversing a light-absorbing medium. **b**, **c** represent the front sides of the intersecting planes which show the field vector before and after entering the material, respectively. Note the circular evolution with magnitude reduced in **c** instead of circular evolution with magnitude original in **b**. All images have been taken from reference [11].

Circular Dichroism CD

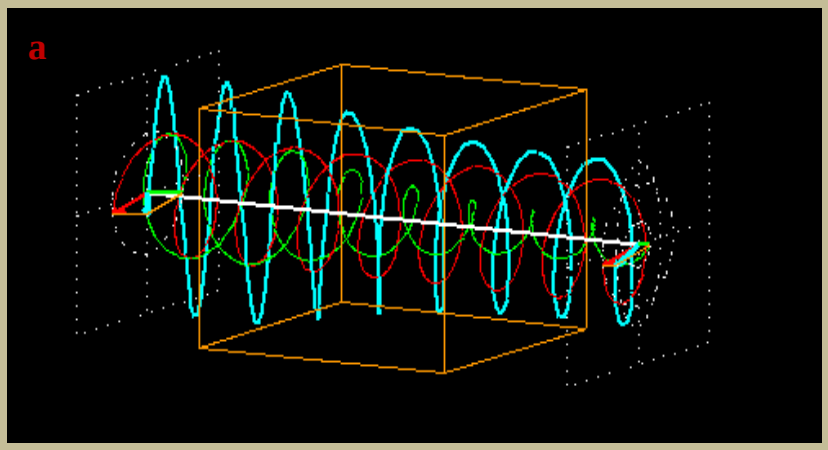

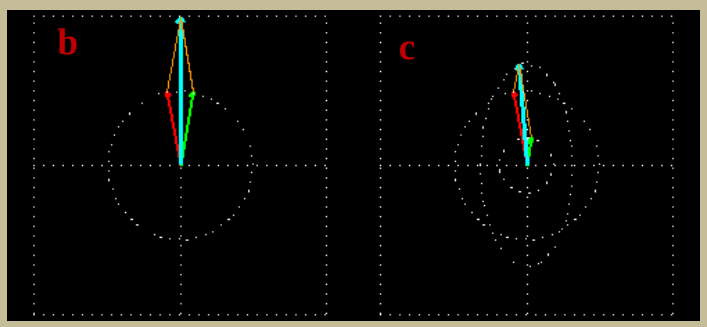

Figure 2: A schematic of two circular electric waves propagate simultaneously to show how the resultant plane polarised light (blue line) could be modified from circular to elliptical (CD phenomenon) upon traversing a left CPL-absorbing medium. **a** represents a schematic illustrates how the intensity of left circularly polarised light (green line) could be reduced as a result of absorption by the medium, with right circularly polarised light remain unchanged (red line), this is while traversing a left CPL-absorbing medium. **b**, **c** represent the front sides of the intersecting planes which show the plane polarised light before and after entering the material, respectively. Note how the circular evolution had changed from circular in **b** to elliptical in **c**. All images have been taken from reference [11].

Practically, researchers use this principle to determine the optical activity of chiral molecules via CD spectroscopy. They determine the dependence of the ellipticity (which represents the y-axis in CD spectrum) on the variations of the wavelength of the incident CPL (which represents the x-axis in CD spectrum). This ellipticity, given by θ, is defined as the ratio between the minor and the major axis of the resultant ellipse (i.e. tangent ratio) [8]. In Figure 3 we present schematic descriptions for the CD phenomenon. In **a** we show a cross section of the left CPL and right CPL evolutions propagating with two different intensities referred to as I_L and I_R, respectively. Should we have left CPL to be absorbed selectively by the chiral molecules one would expect to have $I_R > I_L$. In **b** we show a cross section of the resultant evolution coming from the left and right circular evolutions that are shown in **a**. In **c** we show the cross section of the same resultant to illustrate how the ellipticity depends on θ. Having all that means θ could be expressed by the following equation:

$$\theta = \frac{I_L - I_R}{I_L + I_R} \qquad \ldots\ldots\ldots\

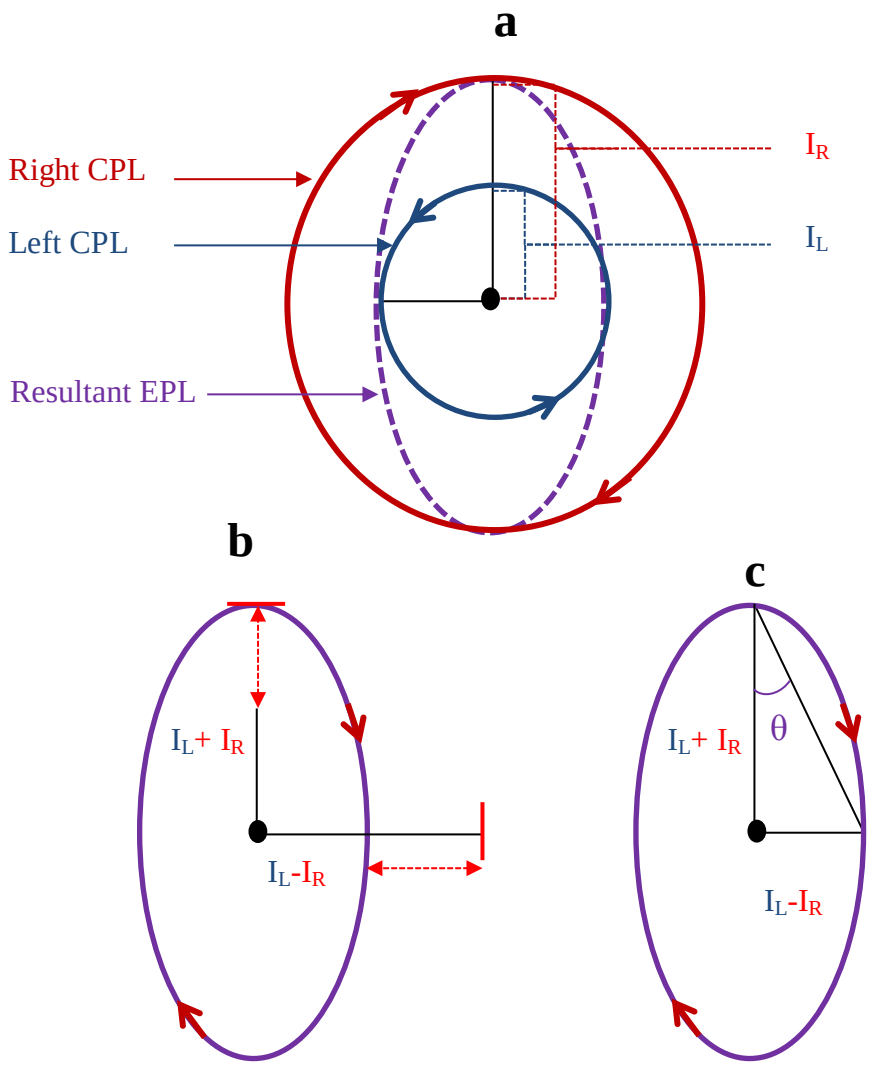

Figure 3: Schematic descriptions for the CD phenomenon. **a** represents a cross section of left CPL and right CPL propagating with two different intensities ($I_R > I_L$). **b** represents a cross section of the resultant evolution (shaped in ellipse) of the two circular evolutions shown in **a**. **c** represents cross section of the resultant evolution which illustrates the dependency of the ellipticity on θ. This represents the ratio between the minor axis of the ellipse to its major axis (i.e. the tangent ratio).

Another principle tells us that, it is possible for circular polarised light, whether it oscillates in a sense of left or right handedness, to be refracted by the materials of its propagation medium, and therefore its speed will be reduced with its magnitude and its circular polarisation state remain unchanged, see Figure 4**a**. In this Figure, we show how the intensity of circularly polarised light could be conserved but slow down speed (indicating by the reducing pitches) upon passing through non-absorbing medium. We also show the front sides of the intersecting planes which show the evolutions of the electric field vectors before (Figure 4**b**) and after (Figure 4**c**) entering the optical medium. Once again, this means that if a combination of left and right CPL propagate simultaneously and one of them was selectively refracted by the materials of the propagation medium, the resultant field vector will be characterised by new circular evolution with a plane of polarisation rotated instead of old circular evolution with a plane of polarisation in original position, and hence a phenomenon known as *optical rotation*, or most commonly OR (i.e *Circular Birefringence*) will occur, see Figure 5. In this Figure, we show a schematic of two circular electric field waves (contrarily orientated to each other) propagating simultaneously and demonstrating how the resultant plane polarised light (blue line) could be rotated with its circular oscillations reserved upon passing through a medium whose selectively refract the left CPL (again left CPL is used here as an example so right CPL should has similar concepts). The degree of the rotation depends on the refractive index which depends on the material of the propagation medium. In **a** one can observe how the speed of left CPL (green line) could be reduced as a result of the refraction by the material of the medium, with the speed of right CPL remains unchanged (red line). We also present the front sides of the intersecting planes to show the evolution of the plane polarised light before (**b**) and after (**c**) entering the optical medium [11,12].

CPL Refraction

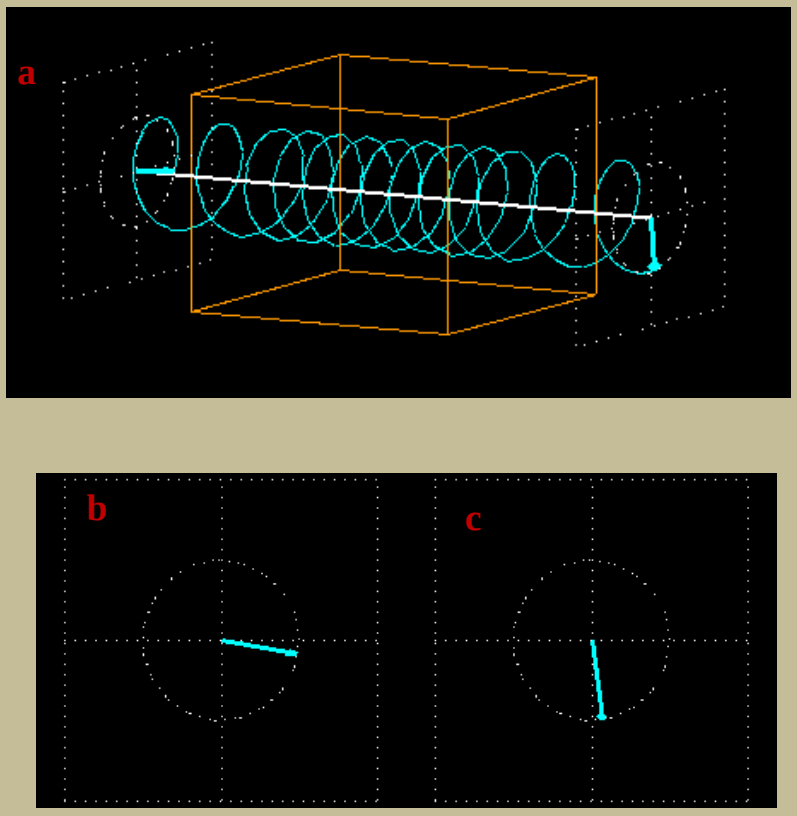

Figure 4: a represents a schematic illustrates how the intensity of circularly polarised light could be retained while slowly (note the reducing pitches) traversing a non-absorbing medium. **b**, **c** represent the front sides of the intersecting planes which show the field vector before and after entering the material, respectively. All images have been taken from reference [11].

Optical Rotation OR (or Circular Birefringence)

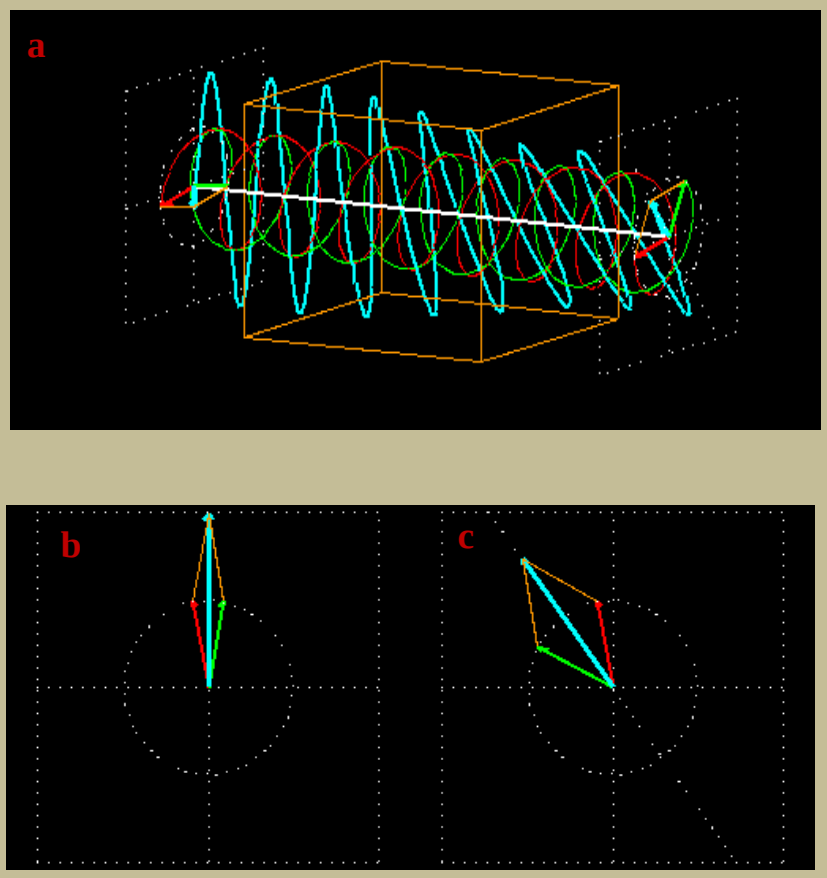

Figure 5: A schematic of two circular electric waves propagate simultaneously to show how the resultant plane polarised light (blue line) could be rotated with its circular oscillations reserved (circular birefringence i.e. OR phenomenon), this is upon traversing a left CPL- highly refracting medium. **a** represents a schematic illustrates how the speed of left circularly polarised light (green line) could be reduced by the medium, with right circularly polarised light remain unchanged (red line). **b**, **c** represent the front sides of the intersecting planes which show the plane polarised light before (original) and after (rotated) entering the material, respectively. All images have been taken from reference [11].

Practically, researchers use this principle to determine the optical activity of chiral molecules via ORD spectroscopy, in which they determine the dependency of the optical rotation OR (which represents the y-axis in ORD spectrum) on the variations of the wavelength of the incident light (which represents the x-axis in ORD spectrum).

In real life, the existence of chiral biological materials might cause CD, or OR, or most likely, both phenomena to be occurred simultaneously. This means if a combination of left and right CPL simultaneously propagate across a medium of chiral biological materials, and one of them was selectively refracted and absorbed by the materials of the propagation medium, the resultant field vector will be characterised by an elliptical and rotated evolution instead of the circular one, and hence both phenomena of CD and OR will occur, see Figure 6. In this Figure, we present a schematic of two circular electric field waves (contrarily orientated to each other) propagating simultaneously and demonstrating how the resultant plane polarised light (blue line) could be altered from circularly to rotated and elliptically polarised light upon passing through and experiencing a medium of chiral biological molecules whose selectively absorb and refract the left CPL (again, left CPL is used here as an example so right CPL should has similar concepts), and hence both phenomena CD and OR will occur. The degree of the ellipticity and the degree of the rotation depend on the strength of the absorption and refractive index, respectively, and these depend on the materials of the propagation medium, which represented here by the chiral biological molecules. In **a** one can observe how the intensity and the speed of left CPL (green line) could be reduced as a result of the absorption and the refraction by the material of the medium, with the intensity and the speed of right CPL remains unchanged (red line). We also show the front sides of the intersecting planes to show the evolution of the plane polarised light before (**b**) and after (**c**) entering the optical medium (i.e. the chiral biological molecules) [11,12].

Optical Rotation + Circular Dichroism

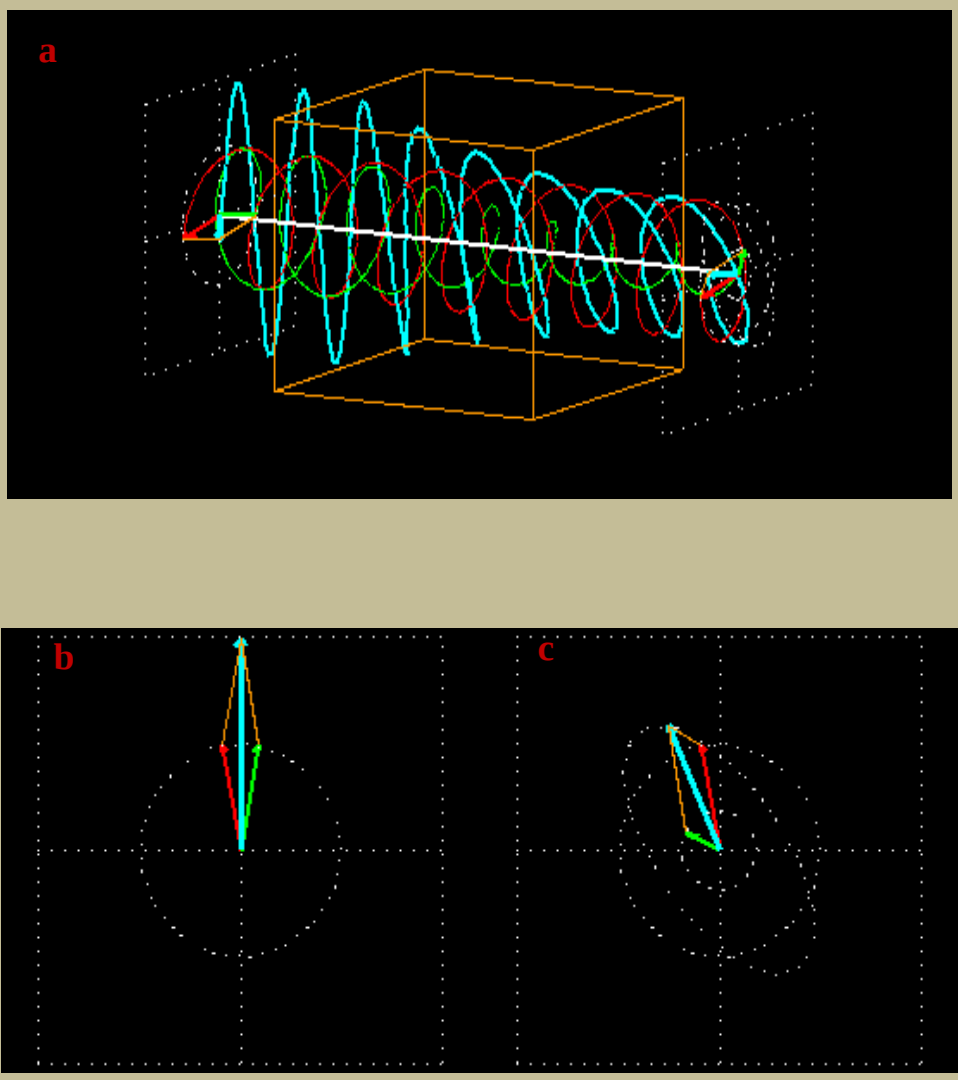

Figure 6: a represents a schematic of two circular electric waves propagate simultaneously to show how the resultant plane polarised light (blue line) could be rotated at the same time of its circular oscillations modified to elliptical (two phenomena CD and OR occur simultaneously), this is while traversing a left CPL- absorbing and refracting medium. **b**, **c** represent the front sides of the intersecting planes which show the plane polarised light vectors before (original) and after (rotated and modified to elliptical) entering the material, respectively. All images have been taken from reference [11].

In principle, Circular Dichroism (CD), Optical Rotatory Dispersion (ORD), Absorption (A) and refractive index (η) are related to each other as follows: CD and ORD characterize Optical Activity (OA). CD is an absorption based- quantity and ORD is a refractive index based-quantity. As such, `*The relationship between a CD spectrum and its corresponding ORD spectrum parallels the relationship between the absorption spectrum of a material and its index of refraction*`. When a chiral molecule absorbs circularly polarised light differentially (Circular Dichroism) there is also a different refractive index for the right and left circularly polarised light components which results in rotation of the plane of polarisation of the light. This rotation is dependent on wavelength (Optical rotatory dispersion). The relationship between CD and ORD can be expressed using the *Kramers-Kronig Transform* (This is the relationship to transform between the real part (e.g. refractive index) and the imaginary part (e.g. absorption) of any response function for the interaction of radiation with matter). For CD and ORD spectra, Kramers-Kronig Transform can be expressed by the following expressions [1[ch3 pp84-85]]:

$$\Theta(\bar{\nu}) = -\frac{2\bar{\nu}}{\pi}\mathscr{P}\int_0^\infty \frac{\Phi(\bar{\xi})}{\bar{\xi}^2 - \bar{\nu}^2}d\bar{\xi} \qquad \text{.....} \qquad 2$$

$$\Phi(\bar{\nu}) = \frac{2}{\pi}\mathscr{P}\int_0^\infty \frac{\bar{\xi}\Theta(\bar{\xi})}{\bar{\xi}^2 - \bar{\nu}^2}d\bar{\xi} \qquad \text{.....} \qquad 3$$

Where $\bar{\xi}$ represents the integration variable which has the same units as wave numbers (cm^{-1}), $\bar{\nu}$ is the wave number = $1/\lambda$, $\mathscr{P}$ represents the Cauchy principle value assigned for improper integration using complex variables, $\Theta(\bar{\nu})$ represents the molar ellipticity in degrees mol^{-1} L cm^{-1} and $\Phi(\bar{\nu})$ represents the molar rotation in degrees mol^{-1} L cm^{-1}.

Generally speaking, researchers use CD spectroscopy or ORD spectroscopy separately to characterise chiral biological materials. However, via chiral plasmonic nanostructures, it is possible to use CD spectroscopy alone to

characterise the chiral biological materials via their general optical activities. This is because our nanostructures were designed to have its own optical properties which come from its own chiral plasmon resonances (i.e. its own LSPR) and therefore our nanostructures could be characterised via their own CD spectrum. This is an essential property which could be used as an effective tool to reveal the optical properties (optical rotation in particular) of the biomolecules adsorbed on the surface of these nanostructures. This is not possible to be achieved with conventional CD technique or even upon adsorption on the surface of the metallic nanoparticles, especially, if the biomolecule are found in an order of picogram level. Once the biomolecules are adsorbed on the surface of the nanostructures, the supramolecular structure of these biomolecules will strongly influence the chiral plasmon resonances (LSPR) of the nanostructures; and therefore; shift its wavelengths (i.e. λ of LSPR) backward or forward; depending on the biomolecules handedness.

3.2.2. Theoretical aspects of the Superchiral Field

Dark states and forbidden transitions for typical molecules (i.e. molecules with size of 0.2-1 nm) play an important role in intermolecular forces and chemical reactions. Having dark states and forbidden transitions is because `*Molecules have a host of states that are only weakly coupled to, or simply invisible to, far-field radiation*` [14]. This means visible light (400-700 nm) is unseen by such molecules due to a mismatch between the plane waves of the visible light and the structural details of the molecules. Dark states and forbidden transitions exist because `*An arbitrary bounded distribution of charges and currents (e.g. a molecule) may be expanded as a series of multipoles, where the electric (or magnetic) field of the nth multipole falls off as* $1/r^{n+2}$*. A point charge corresponds to a multipole of order n = 0, a dipole to n=1, a quadrupole to n = 2, and so on. Coupling of the nth multipole of molecule A to the mth multipole of molecule B yields an interaction energy that falls off as* $(1/R_{AB})^{m+n+1}$ `[14]. This implies domination by dipole-dipole modes with large intermolecular spacing and domination by quadrupole and higher modes with small intermolecular spacing (i.e. when intermolecular spacing becomes comparable

to molecular size). An accurate solution to overcome this mismatch problem is to have the length scale of the incident light and the length scale of the molecules comparable with each other. As such, others suggested reducing the length scale of incident circular polarised light CPL incident on chiral molecules via reshaping its spatial distribution to be further twisted. Reshaping here involves rendering the incident CPL to elliptical polarised light EPL with a smaller pitch length scale to yield a modified light referred to as `*superchiral light*`. Reshaping CPL to superchiral light may be achieved via constructive interferences between the incident CPL (e.g. Left CPL) and its counter-propagating mirror image CPL (i.e. right CPL); with the counter-propagating mirror image CPL being reflected from a semi reflected mirror facing the incident CPL. Here, both lights should propagate at the same frequency and the same phase with slightly different amplitude. This leads to the generation of what is known as `*superchiral standing waves*`, also known as `*optical standing waves*`. Figure 7 shows a computer simulation presented by Raymond et al. [15] for a general configuration of constructive and destructive interferences of two CPL waves, regardless of their handedness. Constructive waves are produced when troughs or crests coincide (bright areas in Figure 7); otherwise the two waves result in destructive interference (dark areas in Figure 7). Cohen et al. hypothesise if small molecules are localised at the nodes of optical standing waves then (via enhancing their rate of excitation) the chiral asymmetry of these molecules could be dramatically enhanced.

Figure 7: Computer simulations illustrates interference pattern of two expanding CPL waves. Bright areas denote constructive interferences and dark areas denote destructive interferences. This Figure was taken from reference [15].

Superchiral light was theoretically predicted in 2010 by the Cohen group who went on to present experimental evidence for their hypothesis in 2011 using the enantiomers of *binaphthylene-perylene-biscarboxyl-diimide dimer* [13]. In their experiments they demonstrated that incident CPL of 543 nm interfered with the mirror image CPL that was reflected from an aluminium mirror (reflectivity R=0.72). It has been suggested by the same group that if a molecule is replaced by a metallic or magnetic nanostructure it is possible then to generate electric and magnetic fields with enormous field gradients that have a magnitude and direction which differs from their original one, i.e. `*using nanostructures to reshape the electric and magnetic fields and thereby to bring molecular dark states to light*`. As such, and following Cohen group hypothesis: `*One might expect near field of plasmonic effects to be necessary to generate highly twisted fields*`[13], we have generated our superchiral fields via our chiral nanostructures instead of the semi reflected mirror, and hence the counter-propagating component is represented here by the chiral SPPs instead of mirror image CPL. Our work in this chapter is complementary to the work of the Kadodwala group [6] who produced experimental evidence for superchiral light generation from chiral plasmonic nanostructures. To quantify superchiral light, it is essential first to define a quantity called `Optical Chirality` or C, which describes the geometrical picture of the chiral fields. In principle, superchiral

light is considered as the mathematical illustration of the optical chirality. Optical chirality was mathematically defined, in 1964, by Lipkin expression:

$$C \equiv \frac{\varepsilon_o}{2} \mathrm{E} \cdot \nabla \times \mathrm{E} + \frac{1}{2\mu_o} \mathrm{B} \cdot \nabla \times \mathrm{B} \qquad \ldots\ldots\ldots\ldots\ldots\ldots\ 4$$

Here, C represents the amount of chirality, E and ε_o is the electric field and electric permittivity, respectively, while B and μ_o is the magnetic field and permeability, respectively.

However, optical chirality was physically defined, using the same expression, in 2010, by Cohen et al. as follows: chiral fields are actually field lines wrapping around a central axis with a component parallel to this axis. Chiral fields were considered as a dimensionless time-even pseudoscalar quantity [In general, quantities of energy (scalar), momentum (vector) and angular momentum (pseudovector) are three essential quantities which characterise the EM field, however none of them characterises the chirality of this field, so it was necessary to have the fourth component which completes this quadrant][10].

Another expression for optical chirality is given by equation 5:

$$C \equiv \frac{c}{\omega} \frac{\langle \mathrm{E} \cdot \nabla \times \mathrm{E} \rangle}{\langle |E^2| \rangle} \qquad \ldots\ldots\ldots\ldots\ldots\ldots\ 5$$

This expression was given by Cohen group in 2009. At that time Cohen et al. referred to this quantity as *electromagnetic field chirality*, denoted by η, however in 2010 and afterward they used the term *optical chirality*, denoted by C. Equation 5 illustrates that optical chirality `*which measures the local density of handedness, or twistiness, of the electromagnetic field*` is the ratio between electric dipole—magnetic dipole interference (numerator) and electric dipole absorption (or emission) (denominator). It follows that if one would have increasing optical chirality (C), then the numerator needs to be increased also,

which means the interferences between the incident light and the matter need to be increased, and hence mismatch problems need to be overcome. For this, the Cohen group suggested either changing the size of the molecule or tuning the chirality of the EM field. Tuning the chirality of the EM field is the best option since molecule size is constant. Tuning the chirality of the EM field was achieved via generating bespoke superchiral light. Generally speaking, for plane polarised light optical chirality (C) equals to zero, otherwise, optical chirality (C) approaches +1 for the right handed circularly polarized light and -1 for the left handed circularly polarized light, i.e. C_{CPL} = ± 1, see scheme in Figure 8.

Yet, in Figure 9, enhanced optical chirality (denoted by $\hat{C}$) exceeds these values to approach ~100. Figure 9, which illustrates theoretical simulations of optical chirality (helicity) of circular polarised light, shows that optical chirality of conventional CPL may equal 1 (Purple) and optical chirality of superchiral light could be enhanced to reach 100 (blue). This Figure also shows the distribution of electric field intensity in superchiral light (Red).

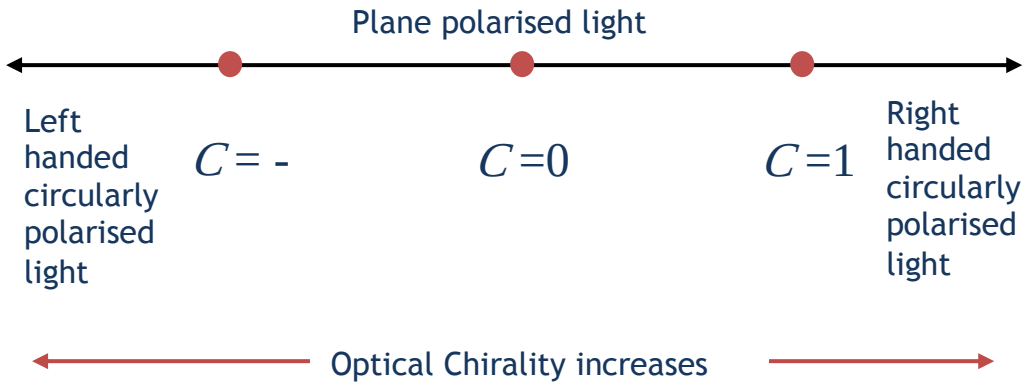

Figure 8: Optical chirality (C) illustration for plane polarised light, right CPL and left CPL. Note that optical chirality equals to zero for plane polarised light, however, it approaches +1 for the right handed circularly polarized light and -1 for the left handed circularly polarized light.

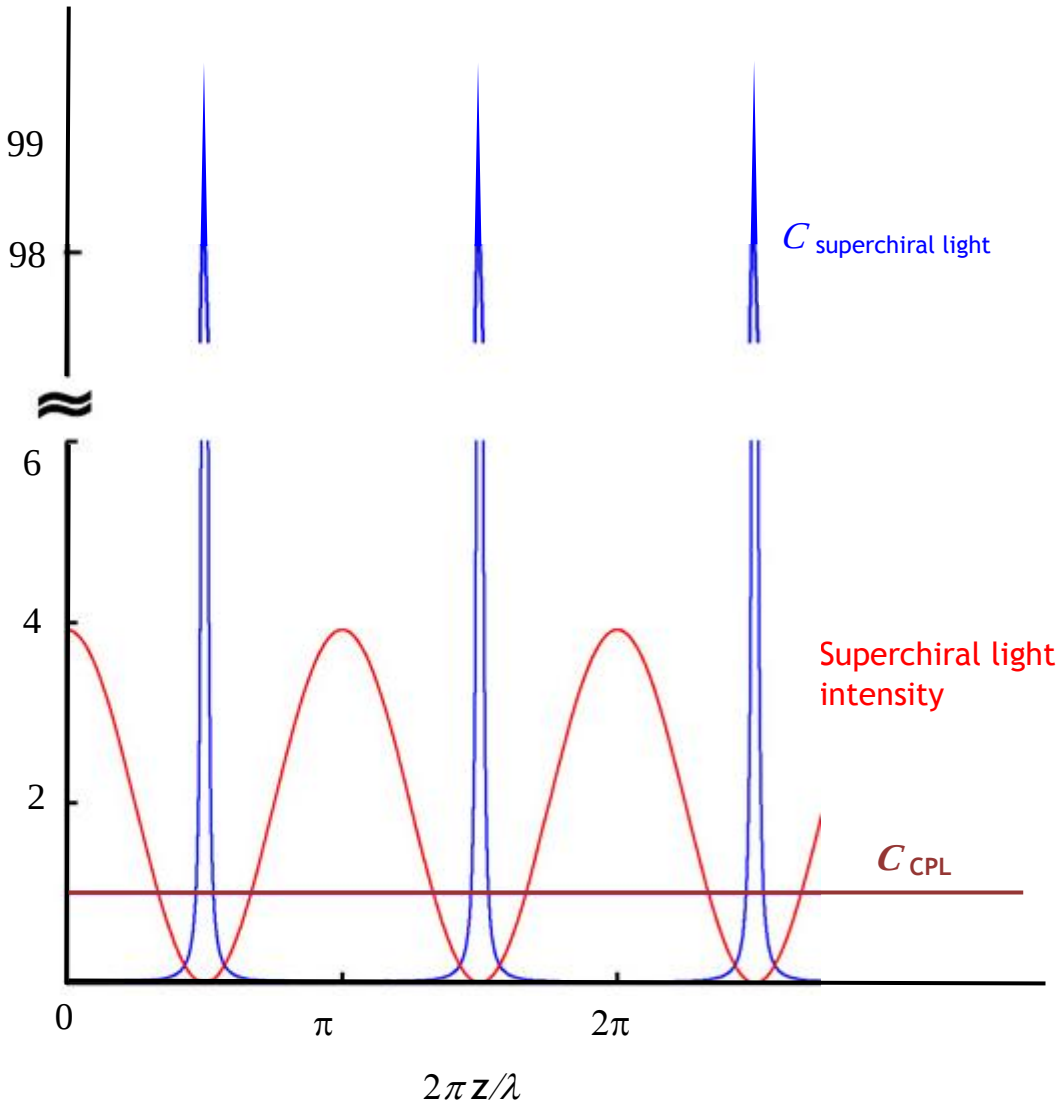

Figure 9: Optical chirality (helicity) of electromagnetic field. Purple track represents optical chirality of conventional CPL (C_{CPL} = 1). Red track represents distribution of electric field intensity in superchiral light. Blue track represents optical chirality of superchiral light. This plot was taken from reference [14] and it was set for a racemic mixture of chiral molecules kept near a node of a superhelical field, hence, one enantiomer will be excited with higher probability than the other.

Generally speaking, *Helicity*, *Chirality* and *Ellipticity* are three quantities that characterise the handedness of the electromagnetic field, yet they are different. *Electromagnetic helicity* characterises the polarisation state within a single plane (i.e. a two dimensional property). *Electromagnetic chirality* characterises the polarisation state in three dimensions [14]. *Ellipticity* characterises the differential absorption between left CPL and right CPL (see Figure 2 and Figure 3) `*but this is actually the result of conversion to units of traditional usage rather than an actual measurement of the degree of ellipticity imposed by a chiral sample on an incident linearly polarized light beam*` [1].

Optical chirality is related to the rate of excitation A (absorption or emission) via the relationship:

$$\mathrm{A} \propto \alpha\omega U_e - \beta C \qquad \ldots\ldots 6$$

where $$U_e = \frac{\varepsilon_o}{4}|E|^2 \qquad \ldots\ldots 7$$

α is a molecular electric polarizability and β is a molecular electric-magnetic dipole polarizability, with β being sensitive to the chirality of the molecule. ω and U_e are the angular frequency and the time-averaged local electric energy density of the surrounding field, respectively. Mathematically, optical chirality (C) is sensitive to the chirality of the molecule since the rate of excitation (A) is sensitive to this quantity via β (equation3). This agrees with the fact that `*circularly polarized light (CPL) is a chiral object, so its interactions with matter are sensitive to molecular chirality*` [14].

Chiral asymmetry, also known as enanatioselectivity, of the chiral molecules is quantified by what is known as `$g$ factor`, which is connected with the rate of excitation via equation:

$$g \propto -\frac{2\left(A^{+}-A^{-}\right)}{A^{+}+A^{-}} \qquad \ldots\ldots\ldots\

$$\hat{C}\pm = \frac{C^{\pm}}{\left|C_{cpl}^{\pm}\right|} \quad \text{..... 10}$$

$$\hat{U}_e = \frac{\varepsilon_o}{2}\left[E_1^2 + E_2^2 - 2E_1E_2\cos(kz)\right] \quad \text{..... 11}$$

$$g^* \propto -\frac{C^+ - C^-}{U_e{}^+ + U_e{}^-} \quad \text{..... 12}$$

$$\hat{g}^* = \frac{g^*}{g_{CPL}} \quad \text{..... 13}$$

$$g' = \frac{g_{superchiralfield}}{g_{CPL}} \quad \text{..... 14}$$

Where $\hat{C}$ represents the local enhancement of the optical chirality, $C^{\pm}$ represents optical chirality for CPL with the presence of the nanostructures, $\hat{U}_e$ represents electric energy density enhancement, E_1 is the electric fields amplitude for incident CPL, E_2 is the electric fields amplitude for counter-propogating mirror image CPL, g* represents the enantioselectivity in the presence of the nanostructures and $\hat{g}^*$ represents the enhancement of g* in comparison to g obtained for incident CPL. g` represents the enantioselectivity in the presence of the chiral molecules. Hence, quantities of equations 10, 12 and 13 are associated with the superchiral field from chiral plasmonic nanostructues *without* the presence of the chiral molecules, while quantities of equations 11 and 14 are general formula associated with the superchiral field and chiral molecules *with* and *without* the presence of the chiral nanostructures.

Enantioselectivity enhancement was theoretically illustrated by Cohen et al in 2010, see Figure 10. In this Figure, E_1 is the electric field amplitude of incident

CPL and E_2 is the electric field amplitude for counter-propagating mirror image CPL. E_1 is slightly greater than E_2. At nodes, E_1= E_2 = zero, as such, optical chirality (C) and electric energy density (U_e) approach zero as well. Crucially, U_e approaches zero faster than C and therefore the ratio C/U_e dramatically grows, hence, enantioselectivity (g) may reach 100 at the nodes of the superchiral standing waves. More examples for different parameters enhancements are presented in table 1. Values of this table were taken from different references and hence from different experimental setting, importantly, the principles for all are the same. i.e. superchiral field were generated either by the aid of semi reflected mirror, such as the case with the first example or by the aid of chiral plasmonic nanostructures.

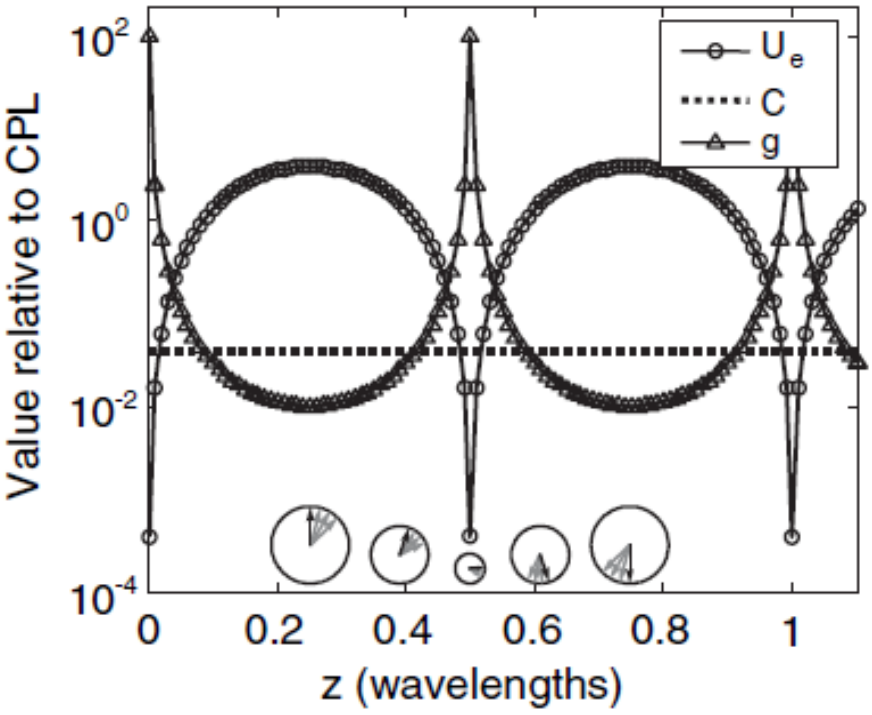

Figure 10: Intensity interferences of incident CPL and its counter-propagating mirror image CPL with electric fields amplitude for the former (E_1) is slightly bigger than the electric field amplitude for the later (E_2). Black arrows that are shown in the bottom denote the electric field vectors at the real time, grey arrows denote the electric field vectors for the earlier times. Circles denote energy density (U_e), dashed line denotes optical chirality (C) and triangles denote enntioselectivity factor (g). This Figure was taken from reference [10].

Table 1: Optical chirality parameters calculated by [6,10,13,14,16]. The chiral objects are illustrated in subsequent Figures (as noted in column 2 of the table).

Chiral object	Figure no.	Wavelength of incident CPL (nm)	Type of excitation	Optical chirality parameters			
				C^	$U^{\wedge}_e$	g`	g^*
Biperylene - derivative	5a	543	Fluorescent emission	-	-	11	-
Tryptophan on gammadions	5b	800	Absorption	-	-	10^6	-
Right handed-gammadion	6	2010	Absorption	20	400	-	-
Left handed - helix	7	2030	Absorption	20	375	-	7
Left handed-nanospiral	8a	1840	Absorption	40	-	-	-
Left handed-chiral plasmonic oligomer	8b	900	Absorption	100	-	-	-

In table 1, it has been found that superchiral light that is generated from a surface of semi reflected aluminium mirror is able to excite fluorescent transitions of binaphthylene-perylene-biscarboxyl-diimide dimer (see its molecular structure in Figure 11a) to enhance enantioselectivity (g`) ~ 11 times larger than conventional g_{cpl} [13]. Also, it has been found that superchiral light that is generated from a surface of 400nm gammadions (fabricated using 100 nm gold thickness with 80nm wire width) is able to excite electronic transitions of tryptophan (see its molecular structure in Figure 11b) to enhance enantioselectivity (g`) by one million times compared with conventional g_{CPL}

[6]. In Figure 12, theoretical simulations predicted that superchiral light that is generated from a surface of right handed 400nm gammadions (made out of 20 nm gold thick with 80nm wire width) is able to excite electronic transitions to enhance optical chirality $\hat{C}$ by a factor of 20 in the areas with red or blue shadows (see colour scheme bar) and also to enhance electric energy density $\hat{U}_e$ to 400 (energy units) in the areas with red shadows (see colour scheme bar) [16]. As Figure 13 illustrates, other theoretical simulations have predicted that superchiral light that is generated from a surface of left handed helix (with a diameter of 400nm and made out of gold with a wire width of 80nm) is able to excite electronic transitions to enhance: 1. Optical chirality $\hat{C}$ by a factor of 20 in the areas with red or blue shadows (see colour scheme bar) 2. Electric energy density $\hat{U}_e$ to 375 (energy units) in the areas with red shadows (see colour scheme bar) and 3. Enentioselectivity $\hat{g}^*$ by a factor of 7 in the areas with red shadows (see colour scheme bar). In Figure 14a it can be seen that theoretical simulations which predicted that superchiral light that is generated from a surface of left handed nanospiral (made out of 20nm gold thick with a wire width of 80nm) is able to excite electronic transitions to enhance optical chirality $\hat{C}$ by a factor of 40 in the areas with red or blue shadows (see colour scheme bar) and by a factor of 100 in the areas with red shadows (see colour scheme bar) [16]. Figure 14b illustrates theoretical simulations which predicted that superchiral light that is generated from a surface of left handed-chiral plasmonic oligomer (this is a bilayer structure consisting of three gold desks; each desk is a 50nm in diameter and made out of 40nm gold thick) is able to excite electronic transitions to enhance optical chirality $\hat{C}$ by a factor of 100 in the areas with red shadows [16].

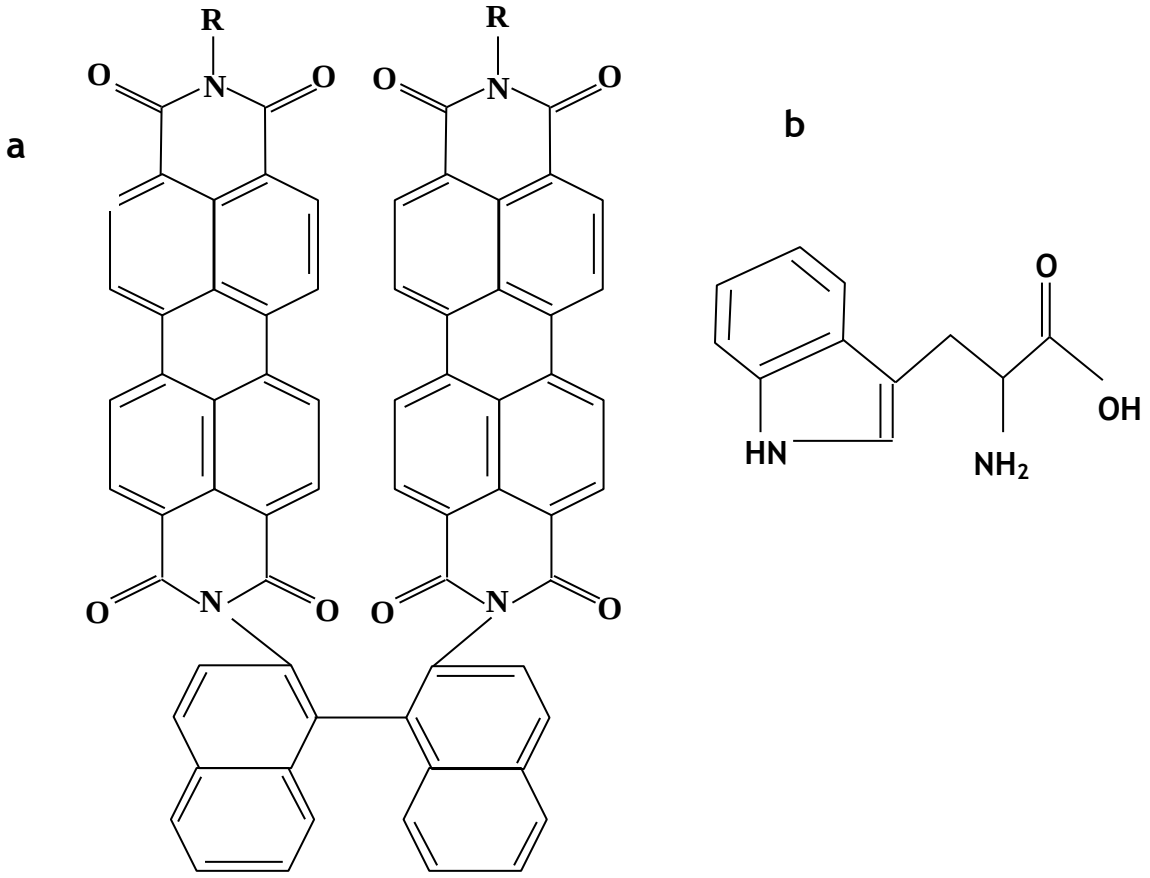

Figure 11: a. chemical structure of binaphthylene-perylene-biscarboxyl-diimide dimer. Enantioselectivity strength (g`) in the presence of this molecule was enhanced ~ 11 times, this is via fluorescent transitions which were excited by superchiral light generated from a surface of semi reflated Al mirror [13]. **b.** Chemical structure of tryptophan. Here enantioselectivity strength (g`) in the presence of this molecule was enhanced ~ 10^6 times, this is via electronic transitions which were excited by superchiral light generated from a surface of 400nm gammadion nanostructures [6].

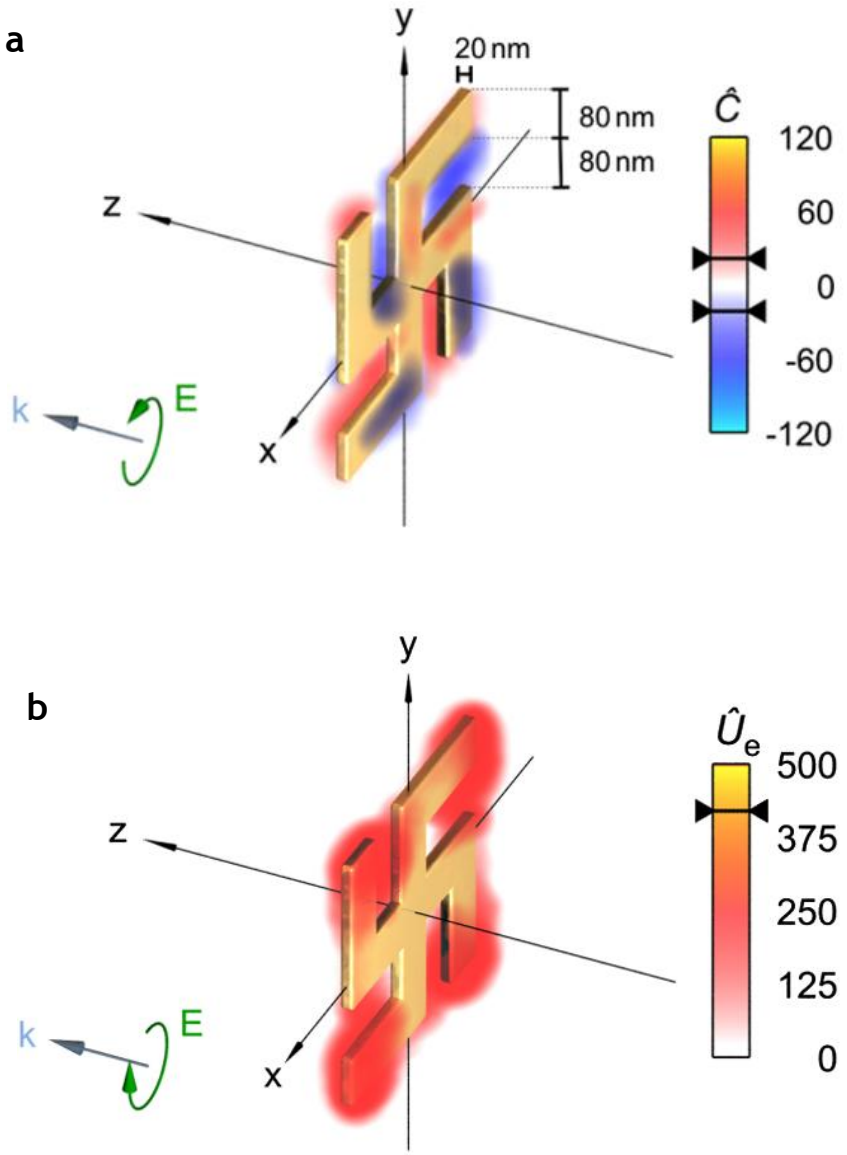

Figure 12: Theoretical simulations of optical chirality enhancement $\hat{C}$ and electric energy density enhancement $\hat{U}_e$ for right handed 400nm gammadion made out of 20nm gold thick and 80nm wire width. Handedness of incident CPL is denoted by the green semi-circle line. **a** shows that $\hat{C}$ could be enhanced by a factor of 20 in the areas with red or blue shadows (this could be concluded from colour scheme bar). **b** shows that $\hat{U}_e$ could be enhanced to 400 in the areas with red shadows (again, this could be concluded from colour scheme bar). These Figures were taken from reference [16].

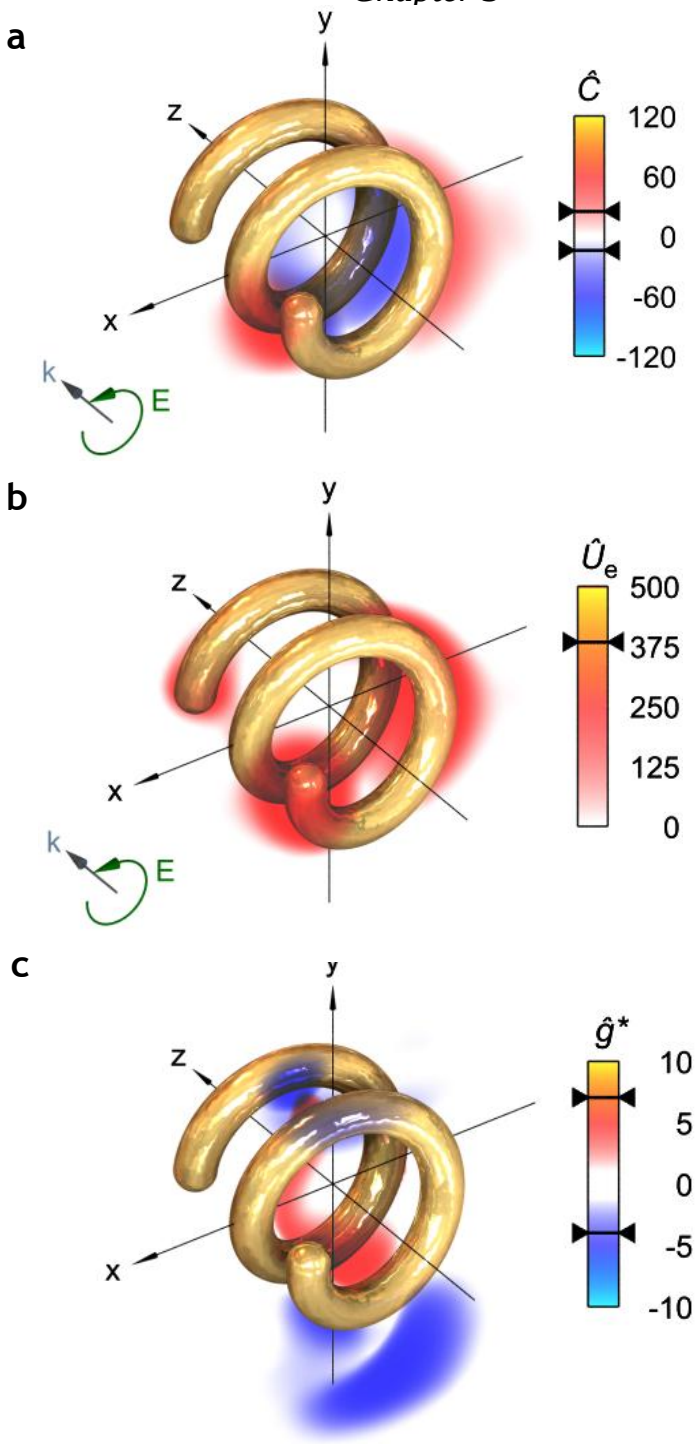

Figure 13: Theoretical simulations of optical chirality enhancement $\hat{C}$, electric energy density enhancement $\hat{U}_e$ and enanatioselectivity enhancement $\hat{g}^*$ for left handed helix with a diameter of 400nm and made out of gold with a wire width of 80nm. Handedness of incident CPL is denoted by the green semi-circle line. **a** shows that $\hat{C}$ could be enhanced in a factor of 20 in the areas with red or blue shadows (this could be concluded from colour scheme bar). **b** shows that $\hat{U}_e$ could be enhanced to approach 375 in the areas with red shadows (again, this could be concluded from colour scheme bar). **c** shows that $\hat{g}^*$ could be enhanced in a factor of 7 in the areas with red shadows (once again, this could be concluded from colour scheme bar). These Figures were taken from reference [16].

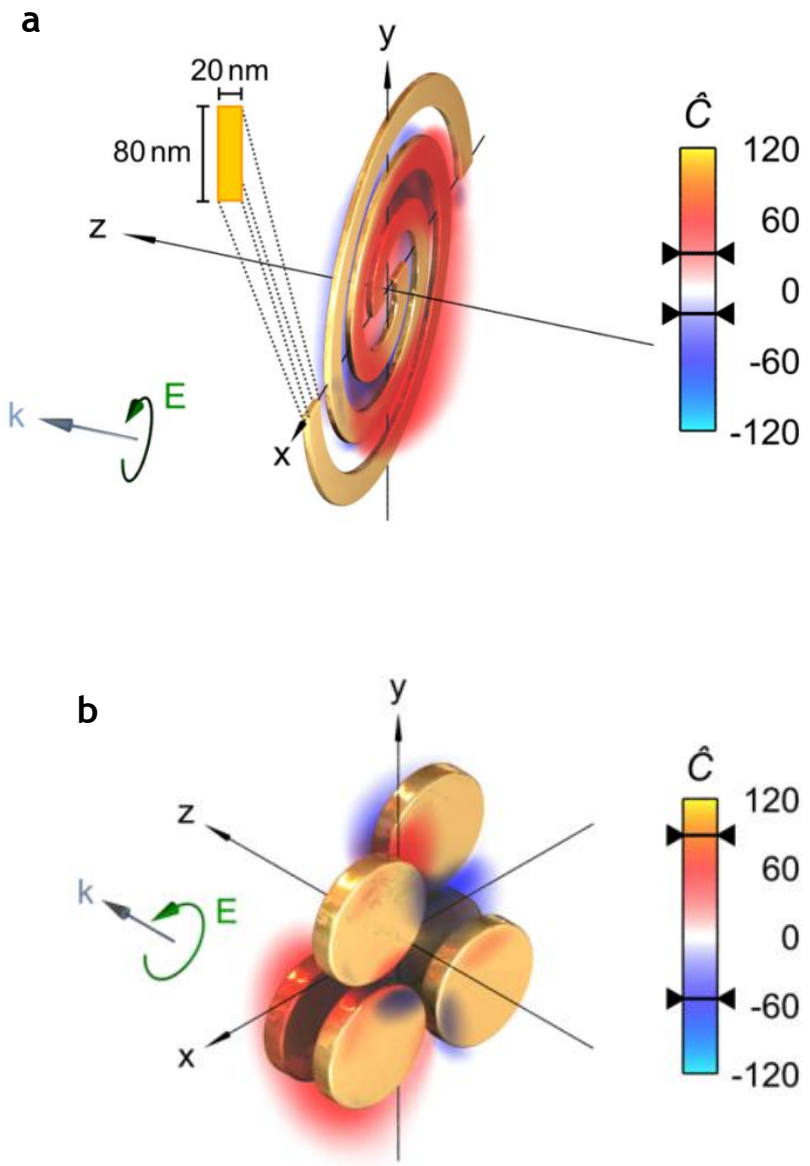

Figure 14: Theoretical simulations of optical chirality enhancement $\hat{C}$ for left handed nanospiral (made out of 20nm gold thick with a wire width of 80nm) and left handed-chiral plasmonic oligomer (this is a bilayer structure consists of three gold desks; each desk is a 50nm in diameter and made out of 40nm gold thick). Handedness of incident CPL is denoted by the green semi-circle line. **a** shows that $\hat{C}$ for nanospiral structure could be enhanced in a factor of 40 in the areas with red shadows (this could be concluded from colour scheme bar). **b** shows that $\hat{C}$ could be enhanced in a factor of 100 for chiral plasmonic oligomer in the areas with red shadows (again, this could be concluded from colour scheme bar). These Figures were taken from reference [16].

3.2.3. Superchiral Field to sense biological molecules

From the electromagnetic model shown in Figure 2 in chapter 6, it can be observed that intense electric fields (areas shown with red colour) originated near specific regions of the nanostructure; with a magnitude dependent upon the wavelength of the incident Circularly Polarised Light. These intense electric fields are raised as a result of the combinations between the electric fields of the incident light and the electric fields of the evanescent fields. As already mentioned, the latter refers to the electric fields oscillating in the vicinity of the excited conductive electrons (i.e. LSPR) of the nanostructure [17]. In principle, the evanescent fields are very sensitive to the surrounding dielectric environment, and more specifically, the refractive index of the surrounding environment, and hence, any perturbation in the surrounding environment could be detectable (see chapter 2). Regarding our work in this chapter, the evanescent fields of our chiral nanostructures are considered to be influenced by two factors: first, the chiral shape of the nanostructures since this confines the orientations of the LSPR; and second, the wavelength of the CPL since this affects the oscillations of the LSPR.

In principle, Superchiral fields could be twisted either in left or right handed direction because the interaction between the LSPR and the CPL selectively twist either the left or right component of the CPL. This means the left and the right handed component of the CPL will be differentially absorbed depending on the wavelength of the CPL which leads to CD spectral features which correspond to a number of asymmetry resonance modes of the chiral nanostructures. These features do not appear in the CD spectrum of the control achiral nanostructures.

Unlike conventional CD spectroscopy, sensing biomolecules with Superchiral fields is a million times more sensitive than sensing biomolecules with normal CPL [6]. Therefore, once the chiral molecules are adsorbed on the surface of the nanostructures, especially within the intense electric field regions, they affect the electromagnetic interaction in this area; through the interaction between the induced electric field of its free electrons movements and the electric field of the Superchiral field. This induces an observable dissymmetry in one /or all

of the six asymmetric resonance modes that are practically observed (namely resonance modes I, II, III, 1, 2, 3), see Figure 15. Such observable dissymmetry could be determined by estimating the CPL wavelength shift according to the following equation [4,6,10,13]:

$$\Delta\lambda = m\Delta\eta\left[1-\exp\left(-2d/l_d\right)\right] \quad \ldots\ldots\ldots\ldots\ldots \quad 15$$

Where:

m = a constant value which is sensitive to the chirality of the nanostructure.
d = Thickness of the molecular layer
l_d = spatial evanescent decay of the local fields
$\Delta\eta$ = changes in refractive index
$\Delta\lambda$ = Dielectric-induced wavelength shift in CPL as a result of changes in LSPR modes of the nanostructure.

From this equation, it is clear that the dissymmetry determination is sensitive to changes in the refractive indices (η) of the surrounding environment; which is highly affected by the dielectric (ε) of this environment (since refractive indices is relating directly to the dielectric constant by the relationship of $\varepsilon = \eta^2$). In principle, optical properties are used to be described by such quantities and are related to each other by the following equations [2 ch2 pp55, 18ch2 pp227]:

$v = (\varepsilon\varepsilon_o \mu\mu_o)^{-1/2}$ 16

$c = (\varepsilon_o \mu_o)^{-1/2}$ 17

$v = c/\eta$ 18

$\eta = (\varepsilon \mu)^{1/2}$ 19

v is the wave velocity of the medium.
c is the wave velocity of the free space.
η is the refractive index of the medium.
ε is the dielectric constant.
ε_o is the permittivity of the free space.
μ is the magnetic permeability.
μ_o is the permeability of the free space.

Practically, the CPL wavelength shift could be estimated by collecting the CD spectrum before and after applying the biomolecule on the nanostructures. The estimation on left $\Delta\lambda_{LH}$ and Right $\Delta\lambda_{RH}$ handed nanostructures could be determined separately. The overall change could be determined by the following equation:

$$\Delta\Delta\lambda = \Delta\lambda_{LH} - \Delta\lambda_{RH} \quad \text{..... 20}$$

3.3. Experimental work

This section includes the sample preparation and materials deposition. The experimental work was performed by using our nanostructures to sense different biological molecules following the strategy shown in Figure 15 below. The nanostructured samples were cleaned using SDS (sodium dodecyl sulphate) solution, ethanol and distilled water in addition to plasma cleaning. Plasma cleaning averaged between five minutes to half an hour, depending on the avidity sample binding. CD spectra for cleaned nanostructured sample were obtained prior to the material deposition to check the integrity of the nanostructures, see Figure (15, **b** and **d**) below and to obtain a control spectrum in the absence of adsorbents. This was performed by collecting the CD spectra for either an open or a sandwich cell sample. The open sample, shown in Figure (15**c**) corresponds to gammadion with nothing on its surface. The CD spectra obtained for the open samples are shown for both the left (blue) and right (red) chiral nanostructure gamma set (15**b)**. The sandwich cell sample, shown in Figure (15**e**), illustrates sealed quartz plates containing the sample in solution. This solution is either the blank solution (distilled water or buffer) or the analyte. Once again, the CD spectra obtained for the sandwich cell is shown for the left (blue) and right (red) gamma set (15**d)**.

In general, high molecular weight materials with thiol group are known to be strongly adsorbed by the gold surface of the nanostructures. With such materials the open sample model (shown in 15**c**) was used to perform the CD measurements. In this model the analyte was deposited on the surface of the

gammadion and allowed to dry off naturally for a period of time which was varied between half an hour to overnight, depending on the solvent. Following the binding of analyte the gammadions were rinsed with distilled water or buffer solution to remove any non-adsorbed molecules. The samples were then dried over a stream of air prior to recording the CD spectra. On the other hand, with small molecules which may have no thiol group, we used the sandwich cell model (shown in 15**e**) to perform the CD measurements. Similarly to the open cell model, we used to leave a certain amount of the analyte on the surface of the sample to dry off naturally, again, for a period of time which was varied between half an hour to overnight, depending on the analyte solvent. Then, we used to leave a certain amount of the solvent, like water or buffer, for about half an hour to help the molecules to come off again. Finally, we sealed the sample with another piece of quartz as a sandwich cell to be ready for the CD measurements.

In previous work [6] researchers measured the dissymmetry shifts $\Delta\lambda$ of the resonance in the areas of I, II and III which are shown in Figure 15 **d** below. Since the nanostructured samples used in this work were fabricated with sharper features and with ~30nm thicker gold layer, resonances exhibiting spectral features of the type 1, 2,and 3 (Figure 15d) were achieved.

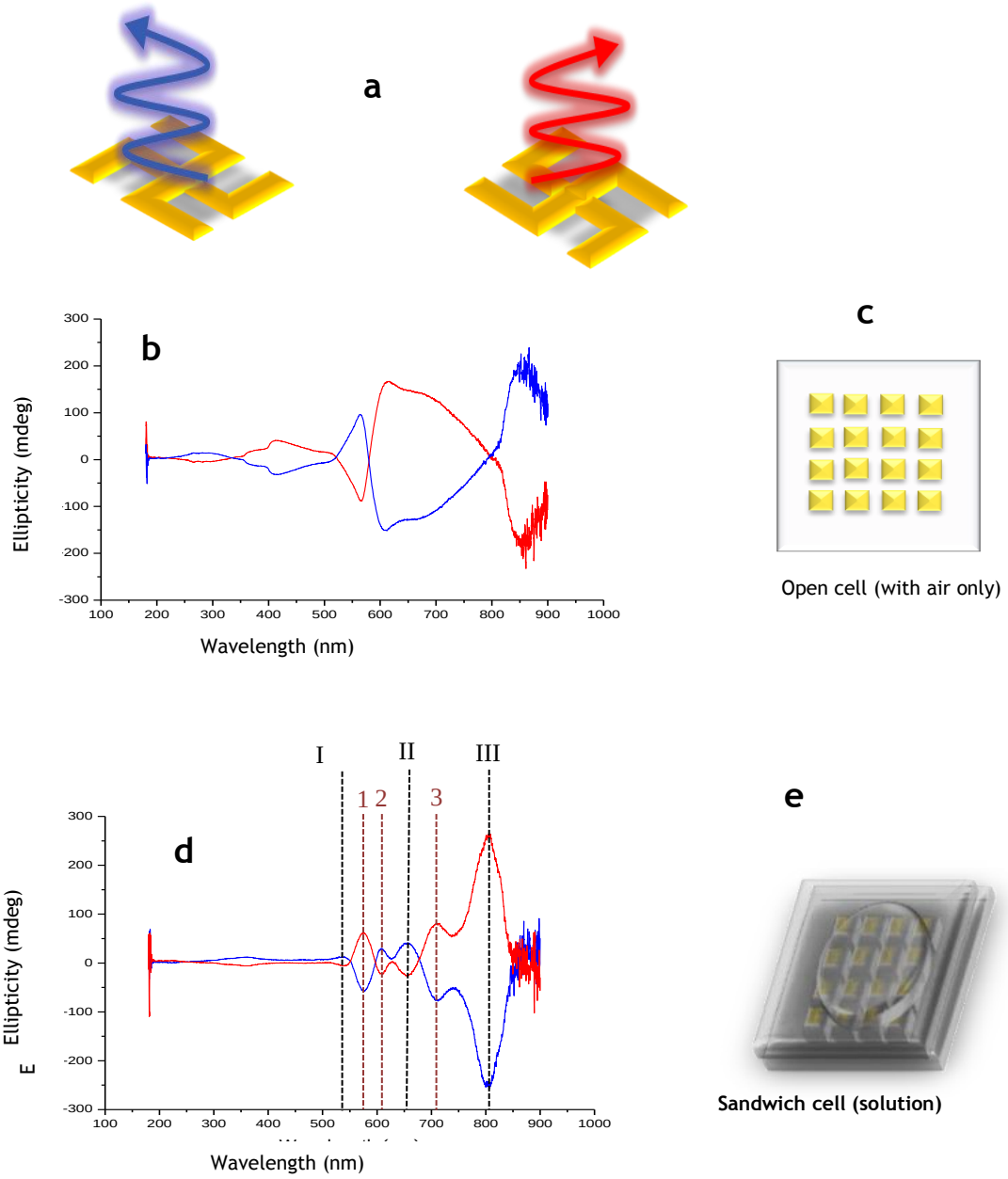

Figure 15: CD spectra of left (L) and right (R) handed gammadion shapes, dimensioned in 400 nm, with 130 nm gold thick layers. The Figure demonstrates two ways to use these nanostructures in CD measurements, which is either with air only (open cell **c**), or with solution (sandwich cell model **e**). **a** represents the gammadions with left CPL(blue) and Right CPL(red) interacting with their surfaces. **b** represents CD spectra from open model for the gammadions, with blue for left handed and red for right handed features. Similarly,**d** represents the sandwich cell model. Note how the resonance of the asymmetries is changing when it is used in solution rather than air. This is due to the difference in refractive index between air and the solution environment. Also, note the old resonance areas which we referred to as I, II and III; in accordance with previous work [6], and note the addition of our own new resonance areas which are referred to as resonance areas 1, 2 and 3.

3.4. Results and Disscusions

3.4.1. Sensitivity to proteins with α-helical and β-sheet secondary structures

Three proteins with α-helical secondary structures and two proteins with ß-sheet secondary structure have been found to be distinguishable upon adsorption on the surface of our nanostructures. BSA (Bovine serum albumin), Heamoglobin and Cytochrome C are known to have α-helical secondary structure. ß-Lactoglobulin and concanavalin A are known to have ß-sheet as a secondary structure [6]. In order to set the stage for the results presented on those proteins, it is essential first to describe the hierarchy of protein structure and then, determine the effect of protein orientation in the chiral field. In principle, proteins are polypeptide chains made out of combinations of 20 different amino acids. These 20 amino acids are known to combine differently to yield proteins with unique sequences which are encoded by an organism's DNA. The linear sequence of amino acids which are joined together through the formation of peptide bonds in a condensation reaction is described as the ***primary structure*** of a protein, see Figure 16a. As a result of peptide bond torsion angles (these are tetrahedral angles known as: Ψ which represents the rotation angle about the C_α-C bond and Φ which represents the rotation angle about C_α-N bond, see Figure 17b) and hydrogen bonding along the polypeptide backbone (shown in dashed red in Figure 16b and 16c and in shadow blue in 16d), portions of protein begin to coil and fold around a common axis in unique formations to give a higher level of protein structure which is described as ***secondary structure***. Secondary structure is represented by three kinds of conformational folds namely: α -helix, β-sheet and random coil, see Figure 16 (b and c) and Figure 17b. Intermolecular interactions between side chains of the amino acids and interactions with the surrounding solvent cause a protein to fold into a compact globular shape, with many of the hydrophobic amino acids becoming buried within the protein away from the surrounding solvent. The resulting compact globular protein is described as the ***tertiary structure*** of the protein, see Figure 16a. At this stage monomeric proteins have reached their optimal structure; however proteins which contain more than one polypeptide chain can form a higher order structure known as ***quaternary structure*** following the assembly of

their other subunits, see Figure 16a. Different types of non-covalent interactions may stabilise the tertiary and quaternary structures, these include *electrostatic interactions* such as *ion pair* or *salt bridge* (e.g. some amino acids contain an extra carboxyl group interact with other amino acids which contain an extra amine group), also, *hydrogen bonds* and *Van der Waals*, in addition, hydrophobic interactions and Chemical Cross-links (e.g. disulfide bonds within and between polypeptide chains) [19,20].

Generally speaking, the 20 amino acids are classified according to the properties of their side chains; hence, they are classified as: ***polar*** (when side chains have partial positive and negative charges and are attracted to water), ***hydrophobic*** (when side chains are like hydrocarbons and tend to avoid water.) and ***charged*** (when the protein contains either more acidic amino acids or more basic amino acids, giving an overall net charge) see Table 2 below.

Table 2: A list of charged, polar and hydrophobic amino acids.

Charged	**Polar**	**Hydrophobic**
Arginine - Arg - **R**	Glutamine - Gln - **Q**	Alanine - Ala - **A**
Lysine - Lys - **K**	Asparagine - Asn - **N**	Isoleucine - Ile - **I**
Aspartic acid - Asp - **D**	Histidine - His - **H**	Leucine - Leu - **L**
Glutamic acid - Glu - **E**	Serine - Ser - **S**	Phenylalanine - Phe - **F**
	Threonine - Thr - **T**	Valine - Val - **V**
	Tyrosine - Tyr - **Y**	Proline - Pro - **P**
	Cysteine - Cys - **C**	Glycine - Gly - **G**
	Methionine - Met - **M**	
	Tryptophan - Trp - **W**	

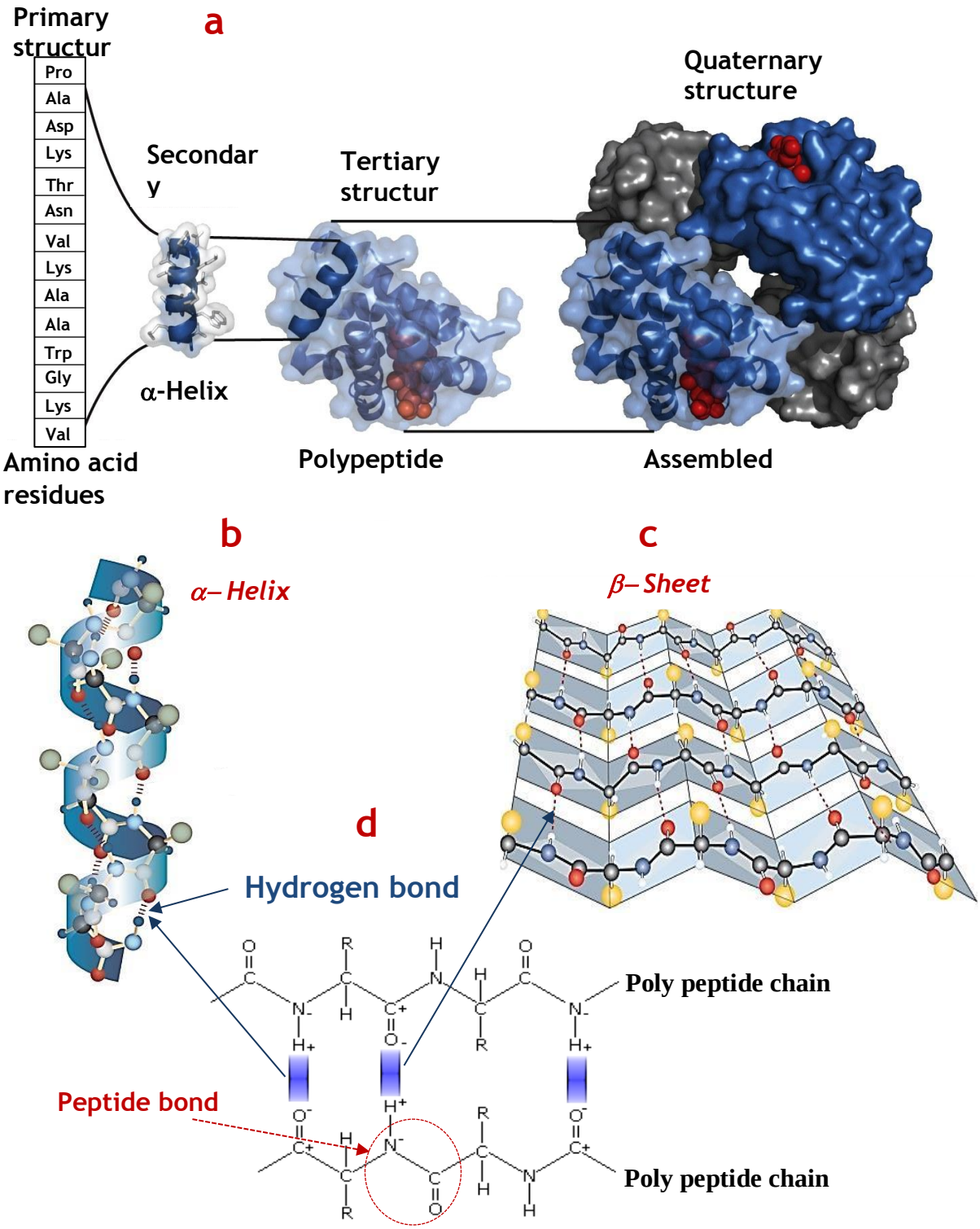

Figure 16: Different levels of protein structure. **a** illustrates the hierarchy of protein structure. ***Primary structure:*** the sequence of amino acids in a polypeptide chain, ***Secondary structure*****:** the arrangements of the poly peptide chain into α- helix and/or β-sheet and random coil. ***Tertiary structure*****:** the distinct three dimensional shape of polypeptide chain. ***Quaternary structures:*** the arrangements of multiple poly peptide subunits. This Figure was taken from [21]. **b** illustrates α-helix secondary structure which is naturally folded and stabilised via hydrogen bonds (black dashed line). **c**. illustrates β-sheet secondary structure which is also naturally folded and stabilised via hydrogen bonds (red dashed line). **d** Illustrates hydrogen bonds (shown in shadow blue) and peptide bond (shown in red dashed line). Figures a and b were taken from [22]. Figure d was taken from [23].

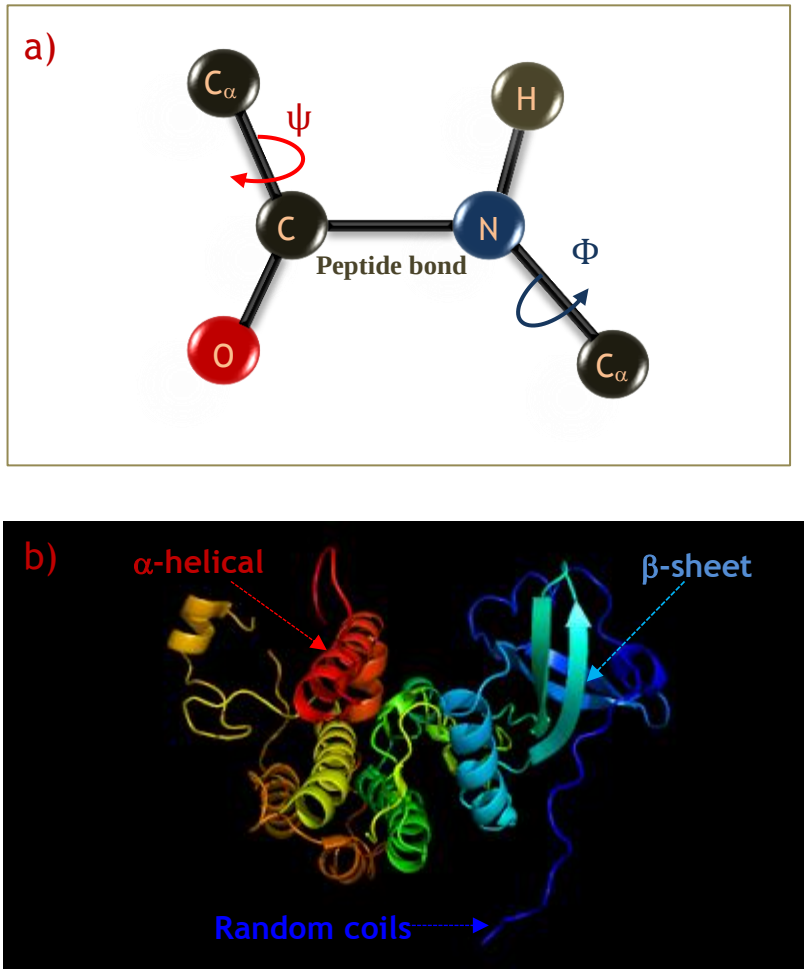

Figure 17: a Illustration of peptide bond torsion angles, such as: Ψ which represents the rotation angle around the C_α-C bond and Φ which represents the rotation angle around C_α-N bond. **b** Illustration of three kinds of protein`s secondary structures, these are, α-helical (red, yellow, orange, green and cyan), β-sheet (cyan and blue) and random coils (blue, red, yellow, orange, green and cyan). Figure **b** was taken from reference [24].

As it has mentioned, in order to set the stage for the results presented on our proteins, it is essential to determine the effect of protein orientation in the chiral field. In fact, the effect of adsorption onto metal surfaces on protein conformation and orientation is an interesting area of study. Two possible orientations have been considered, and described as ` *not the most general configurations, however, experimentally it is the most convenient one*`, these are: well-defined orientation with an axis fixed perpendicular to the surface or; random orientation in the plane parallel to the surface. Molecules with α-helical

structure were assumed to adopt a well-defined orientation perpendicular to the surface, hence, such molecules were considered to be *isotropic* due to broad spatial distribution along the surface normal, see Figure 18 (top). Molecules with β-sheet structure were assumed to adopt a random orientation in the plane parallel to the surface, and therefore, such molecules were considered to be *anisotropic* due to the limit spatial distributions along the surface normal, see Figure 18 (bottom).

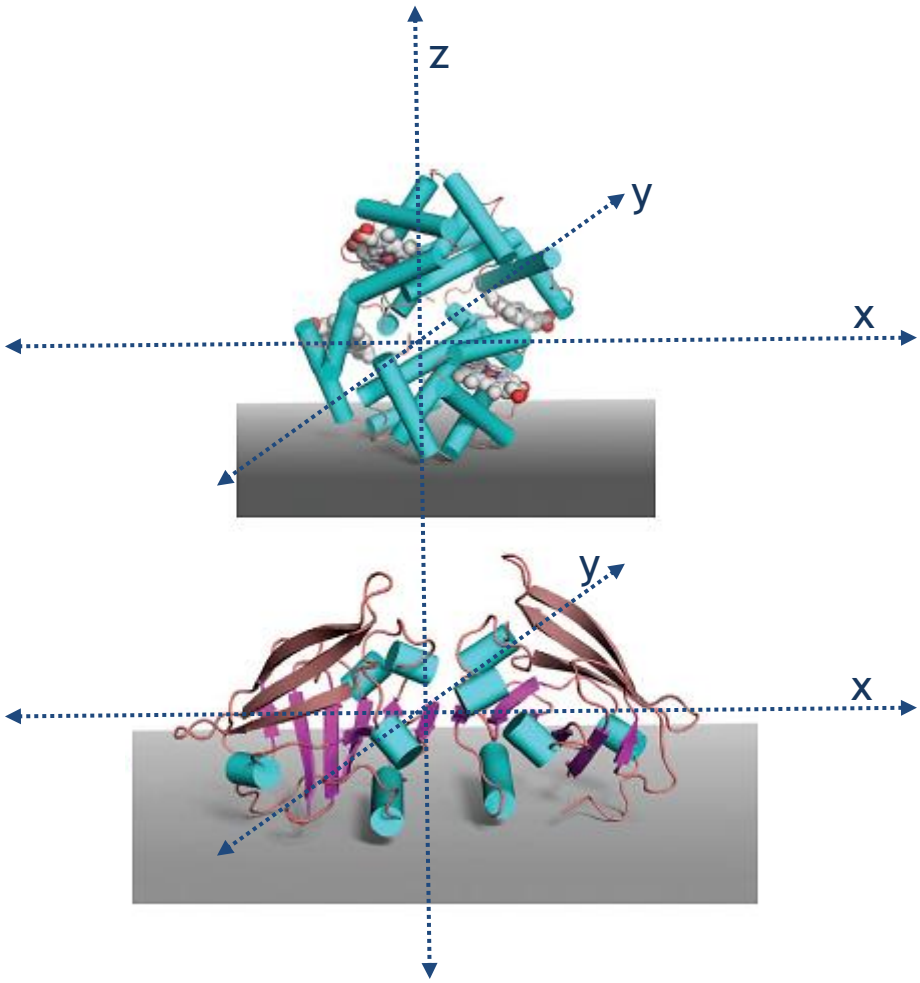

Figure 18: Illustration of protein orientations which assumed to be adopted upon protein adsorption on metal surface. Haemoglobin (top) adopts a well-defined orientation with an axis fixed normal to the surface. β-lactoglobulin (bottom) adopts random orientation in the plane parallel to the surface. From population of α-helix (cyan cylinders) and β-sheet (magenta and brown ribbons) one can conclude an isotropic nature associated with haemoglobin (top) and an anisotropic nature associated with β-lactoglobulin (bottom). The z axis is normal to the surface and run through the centre of the molecule, x and y axes are parallel to the surface. This Figure was taken from reference [6].

In principle, intense near fields (steep gradient field) can induce electric dipole-magnetic dipole (dipolar) excitations from isotropic surfaces (such as molecules with α-helical structure), also, such intense near fields can induce electric dipole-magnetic dipole in addition to electric dipole-electric quadrupole (quadrupolar) excitations from anisotropic surfaces (such as β-sheet structure). Such effects result in chiroptical phenomena. This means, chiroptical phenomena can be induced via dipolar excitation from isotropic surfaces or via dipolar plus quadrupolar excitations from anisotropic surfaces. Having that and considering chiroptical enhancement, others expect the dissymmetry factor *g* to be enhanced via quadrupolar excitations from anisotropic surfaces rather than isotropic surfaces; simply because quadrupolar contribution from isotropic surfaces is averaged to zero. Indeed, it has been found that adsorbed tryptophan and β-lactoglobulin (molecules with β-sheets structure) resulted in a large enhancement in the optical activity in visible region, which was not evident in molecules containing predominantly α-helical structure such as myoglobin, haemoglobin and BSA [6]. As it will be presented in this section, we observed similar enhancement (in the UV region) from ß-Lactoglobulin and Concanavalin A (molecules with β-sheets structure), but not from BSA (Bovine serum albumin), haemoglobin and cytochrome C (proteins with α-helical structure).

The ability to distinguish between proteins with α-helical secondary structure and ß-sheet secondary structure was reported previously using CD measurements of the Plasmon modes corresponding to spectral regions I, II and III [6]. Here, we have similarly been able to distinguish between α-helical and ß-sheet structures in the 200-400nm region (UV region) which complements the work described by Hendry *et al* [6]. It was noticed that the asymmetry in CD spectra of the left handed gammadions and the right-handed gammadions along the x-axis of CD spectra for proteins with ß-sheet secondary structure is different from those for the proteins with α-helical secondary structure. Figure 19 shows the CD spectra obtained for left and right-handed gammadions in the absence of protein. These spectra show several nodes that are located in the areas of n1, n2, n3, n4 and n5. Figure 20 (a magnification of (200-500) nm region shown in Figure 19) shows CD spectra for three proteins with α-helical secondary structure (shown with maroon and magenta lines), these are: BSA, Haemoglobin and Cytochrome C.

Also shown are the CD spectra for two proteins with ß -sheet secondary structure (shown with red and blue lines), these are: β-lactoglobulin and Concanavalin A. All spectra were collected following adsorption of the proteins onto the substrates of the left handed gammadions (blue and magenta) and Right handed gammadions (red and maroon). These proteins were deposited on a layer by layer basis. A fixed volume of a 0.1mg/ml solution of protein was deposited on the chip (open sample) and allowed to dry with moderate shaking in a 37^{o}C incubator. Following each layer deposition a CD spectrum was measured for both left and right-handed gammadions. Protein concentrations were judged to be approximately equal on both left and right-handed nanostructures by using the far UV spectral intensities observed (which were not influenced by plasmonic excitations. From solvent (50% Ethanol + 50% Distilled Water) density of 0.91384 g/cm^3 we estimated the average molecular surface density (the mass of proteins per cm^2) for each sample to have: 7.7 μg/cm^2 for BSA, 13.5 μg/cm^2 for Hemoglobin, 31 μg/cm^2 for Cytochrome C, 34.5 μg/cm^2 for β-Lactoglobulin and 29.4 μg/cm^2 for concanavalin A. Provided that these amounts of proteins were spread on the surface of an area of (1x1)cm^2 one might estimate the approximate film thickness of these proteins as: 84nm for BSA, 148nm for Hemoglobin, 339 nm for Cytochrome C, 378nm for β-Lactoglobulin and 323nm for Concanavalin A. Clearly, the amounts of the proteins were varied because their molecular weights are varied. Although we have deposited at least six layers on each sample however, for the results shown in Figure 20 only the pairs of layers whose matched similar proteins amount on the left and the Right handed gammadions have been chosen.

Figure 20 illustrates asymmetries along the x-axis in the 200-400nm region; indicated by navy arrows. Now, via comparison between Figure 19 and Figure 20 one might observes that the areas pointed with navy arrows in Figure 20 represent the red shifts of the nodes n1 and n2 in Figure 19. In fact, nodes of n3, n4 and n5 also could be seen that they are red shifted (see Figure 21 (a-e)). This is expected consequences of environments having their refractive indices changed (increased). This behaviour have been further confirmed from the spectra we shown in Figure 21 (a-e). In this Figure, spectra with red colours represent CD spectra for the plain substrate (without proteins) and spectra with black colours represent CD spectra for the substrate with proteins. Here, one

might observes ~ constant red shift with layer after layer deposition. Clearly, all proteins in question behaved almost similarly. However, areas of n2 for proteins with ß -sheet secondary structure (i.e β-lactoglobulin and Concanavalin A) were not only red shifted but they were negatively induced asymmetrical alteration as well (note regions pointed by the navy arrows). It is our opinion to illustrate this observation as following:

From Figure 19, it is clear that n2 had zero CD signal, i.e. the left CPL and the Right CPL do not exhibit differential absorbance. However, following adsorption of the beta sheet proteins (β-lactoglobulin and Concanavalin A) differential absorbance was observed (Figure 20b and 20d) at n2. Zhu H. *et al* [16] demonstrated that when gold nanoparticles were irradiated with electromagnetic light oscillating within the UV wavelength region a phenomenon called `*interband excitation of electrons*` could be observed which includes excitation of electrons from 5d orbitals to 6sp orbitals. Also they demonstrated that, if the gold nanoparticles were irradiated with electromagnetic light oscillating within visible wavelengths then a phenomenon of `*interband migration*` could be observed involving the excitation of 6sp electrons to higher energy levels. It has been demonstrated that these energetic electrons could have a life time of 0.5-1 ps, which is long enough to excite the electrons of the molecules that are adsorbed on the surface of the nanoparticles, and hence trigger photochemical reactions like those they used for solar cells [25]. A similar excitation mechanism may be evident following adsorption of proteins onto gold gammadion surfaces. This may involve the energetic electrons of the interband excitation (since interband excitation occurs in the UV area where n2 is located) to excite the electrons of ß -sheet proteins; which in turn leads to differential absorption of the left and the Right CPL resulting in the observation of a CD signal. An alternative explanation, as proposed by Hendry *et al* [6] is that proteins with ß -sheet secondary structure have stronger effect on the LSPR than proteins with α-helical secondary structure due to the former having a more anisotropic structure (explained above).

In the work of Hendry *et al* [6] the large dissymmetry shift of ß -lactoglubulin and tryptophan (protein with beta secondary structure and amino acid with flat geometry, respectively) in modes II and III were attributed to electronic

transitions of the molecular system of these species. Such electronic transitions were enhanced by the LSPR (of the gold nanostructures upon which these molecules were adsorbed) through near field coupling. In our case however, we believe that the electromagnetic field enhancements were due to a different phenomenon. First, because it was not from LSPR enhancement (since LSPR resonance is off in this area), instead it was from 5d to 6sp interband excitations (as suggested above). Second, it is still not clear whether it was via near field coupling or it was via far field radiative. Though, in chapter 4 we have shown that chirality could be induced via far field radiative because the thickness of the fmn layer was > 900 nm which is ~ 8 times far-off from near field decay. For β-lactoglobulin and ConcanavalinA we have an estimated molecular layer thickness > 300 nm which is ~ 2 times far-off the near field decay; which makes us thinking to roll out the probability of the near field coupling. With such findings, one may suggests if this is a sort of chirality induction (?) first because achiral nodes turned to chiral nodes and second because it is probably occurred via far field radiative. One may also suggests if this is a sort of chirality enhancement via far field radiative? In fact, these are unanswered questions and highly demanded to be addressed via our future works.

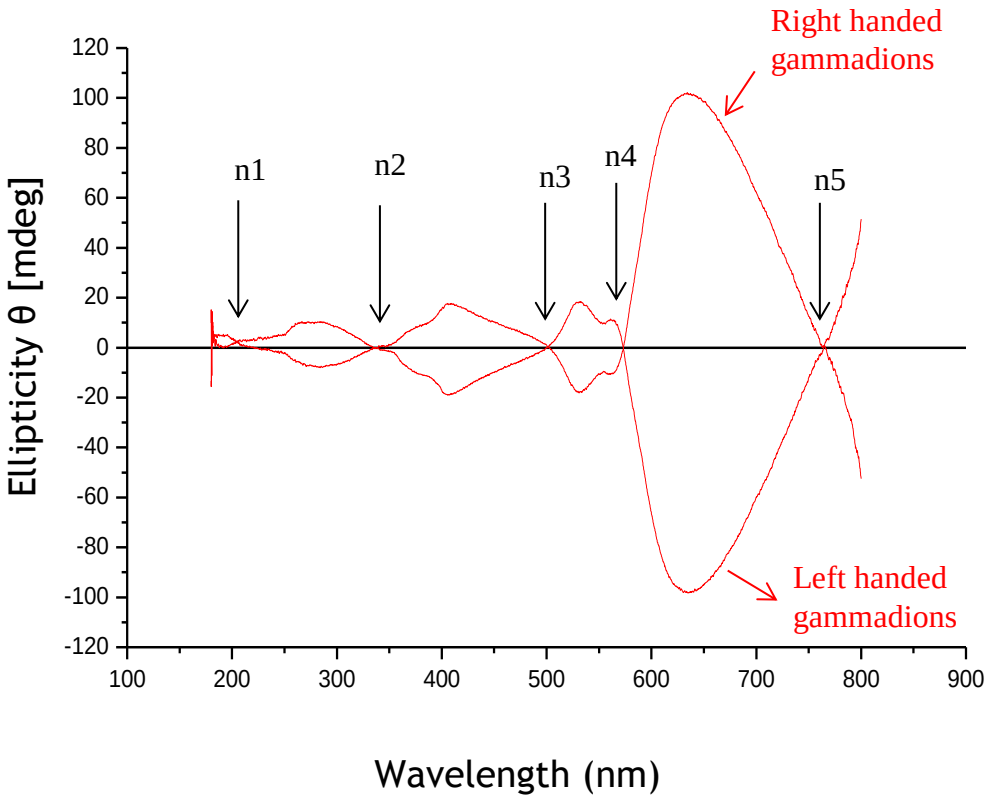

Figure 19: CD spectra for open cell substrate of left and Right handed gammadions. Note nodes areas which are numbered as n1, n2, n3, n4 and n5.

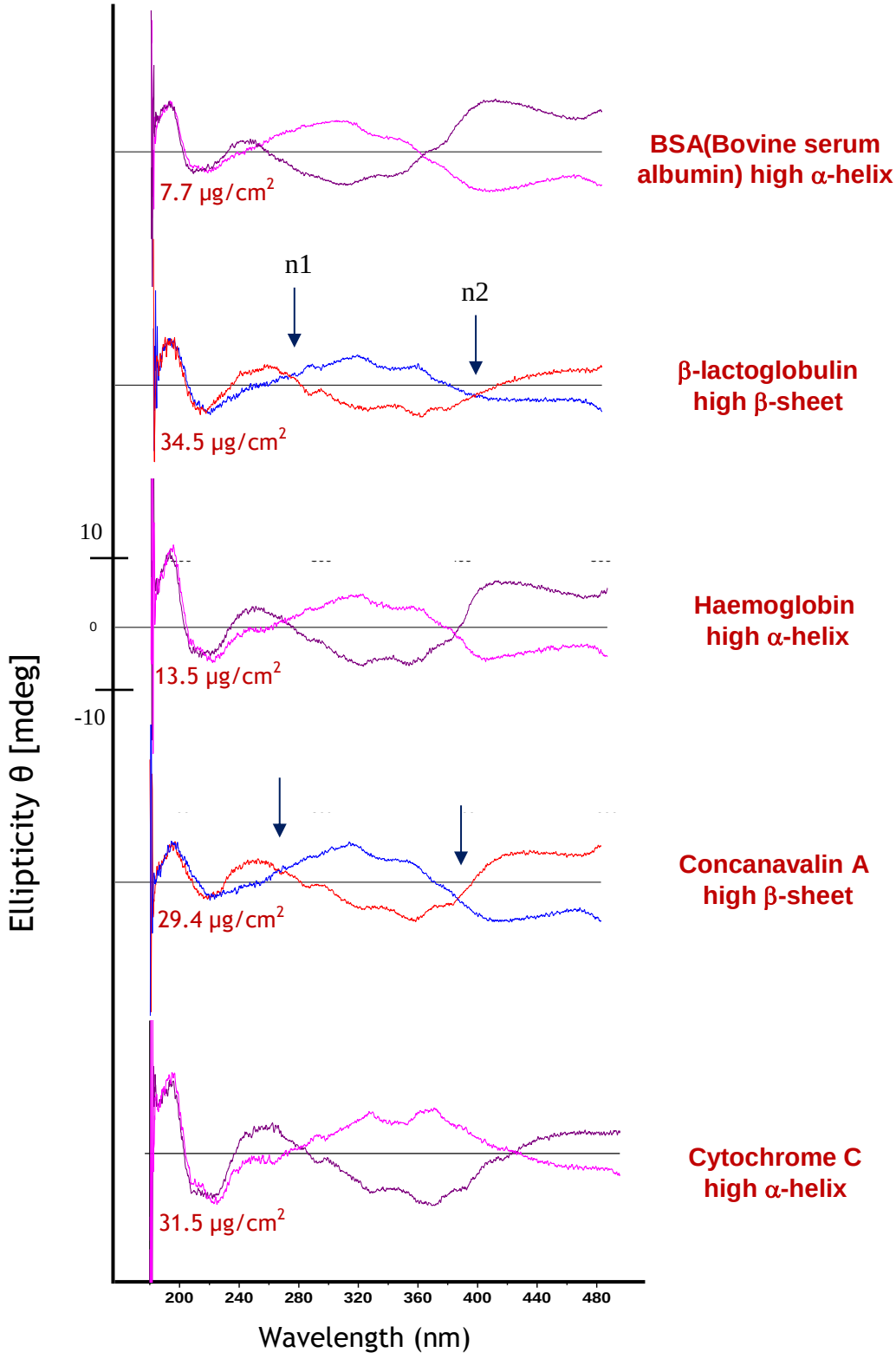

Figure 20: CD spectra for three proteins with α- helical secondary structure (shown with maroon and magenta lines) and two proteins with β-sheet secondary structure (shown with red and blue lines). Note that this is a magnification of (200-500) nm region shown in Figure 8. CD spectra were collected after these proteins were applied on the left handed gammadions (blue and magenta) and Right handed gammadions (red and maroon). Note the asymmetry along the x-axis (200-400) nm area; in particular, regions pointed by the navy arrows.

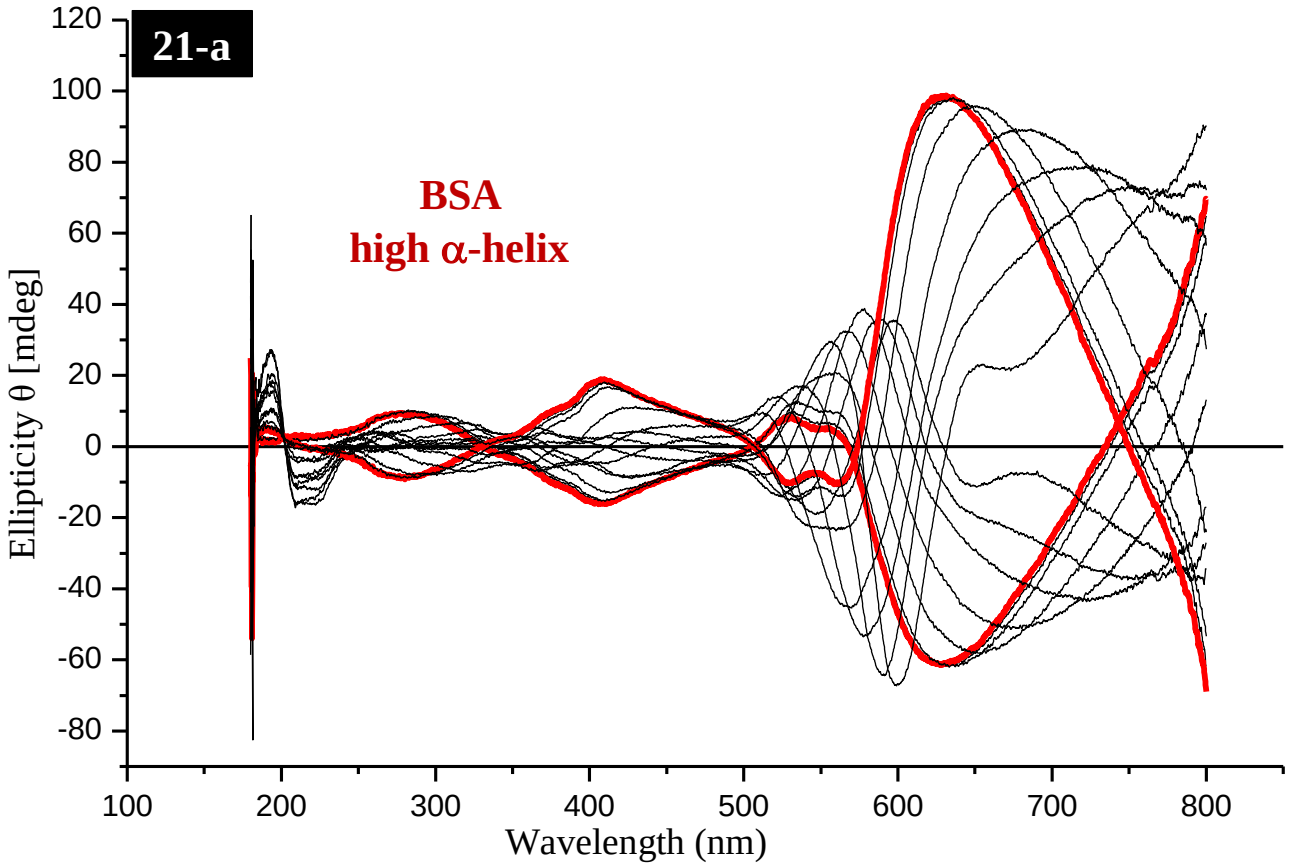
21-a
BSA
high α-helix
Ellipticity θ [mdeg]
Wavelength (nm)

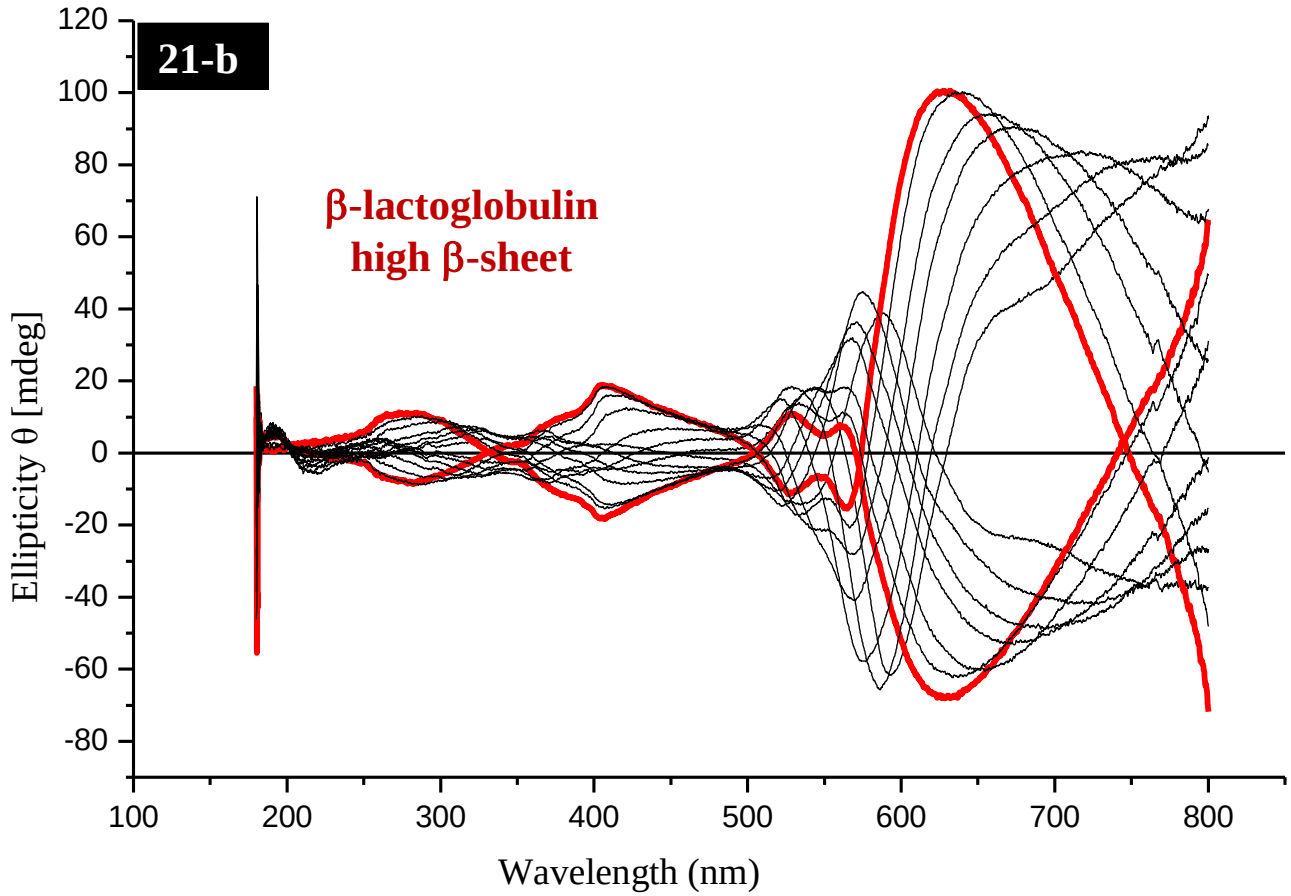
21-b
β-lactoglobulin
high β-sheet
Ellipticity θ [mdeg]
Wavelength (nm)

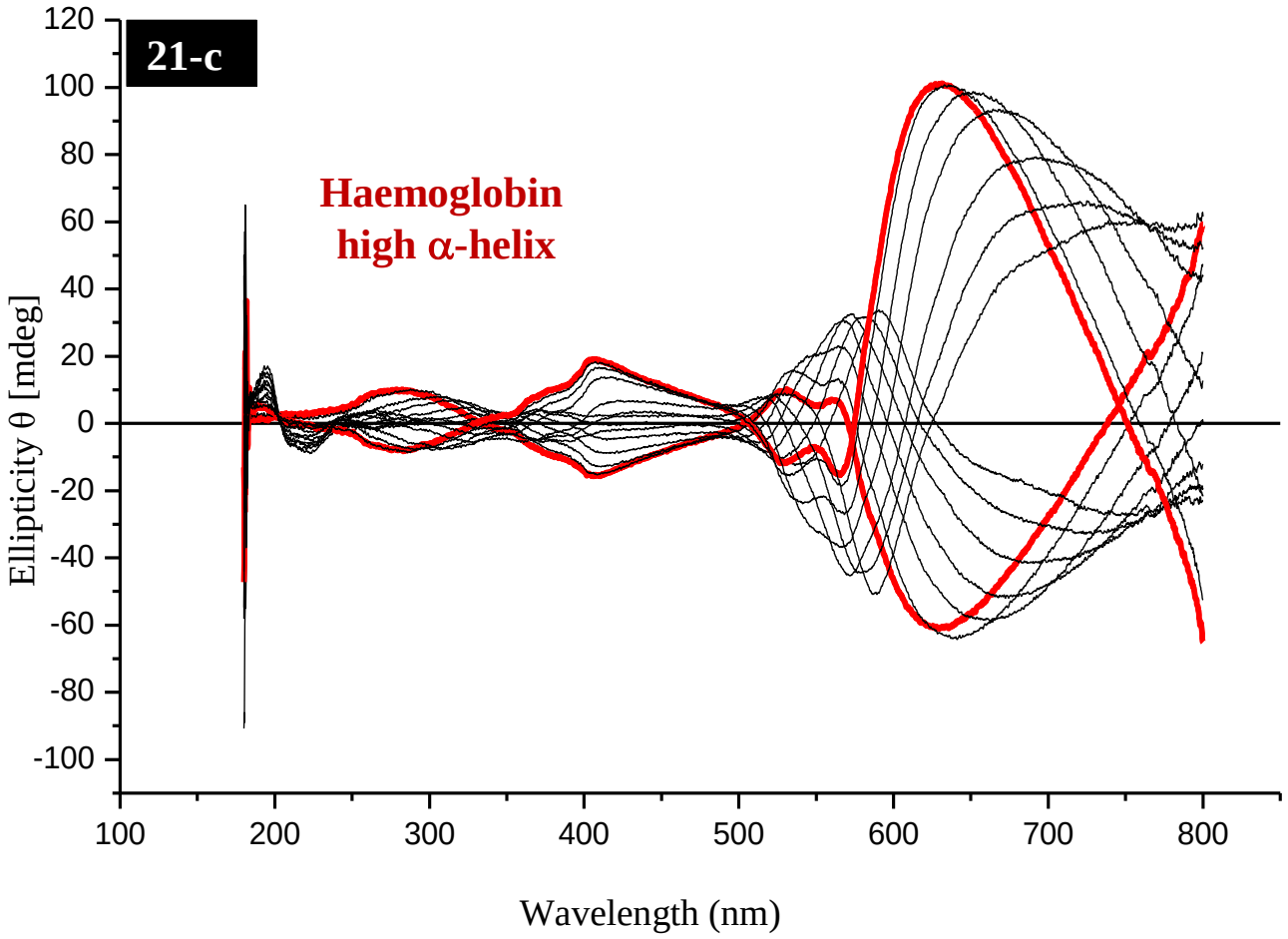
21-c
Haemoglobin
high α-helix
Ellipticity θ [mdeg]
120
100
80
60
40
20
0
-20
-40
-60
-80
-100
100
200
300
400
500
600
700
800
Wavelength (nm)

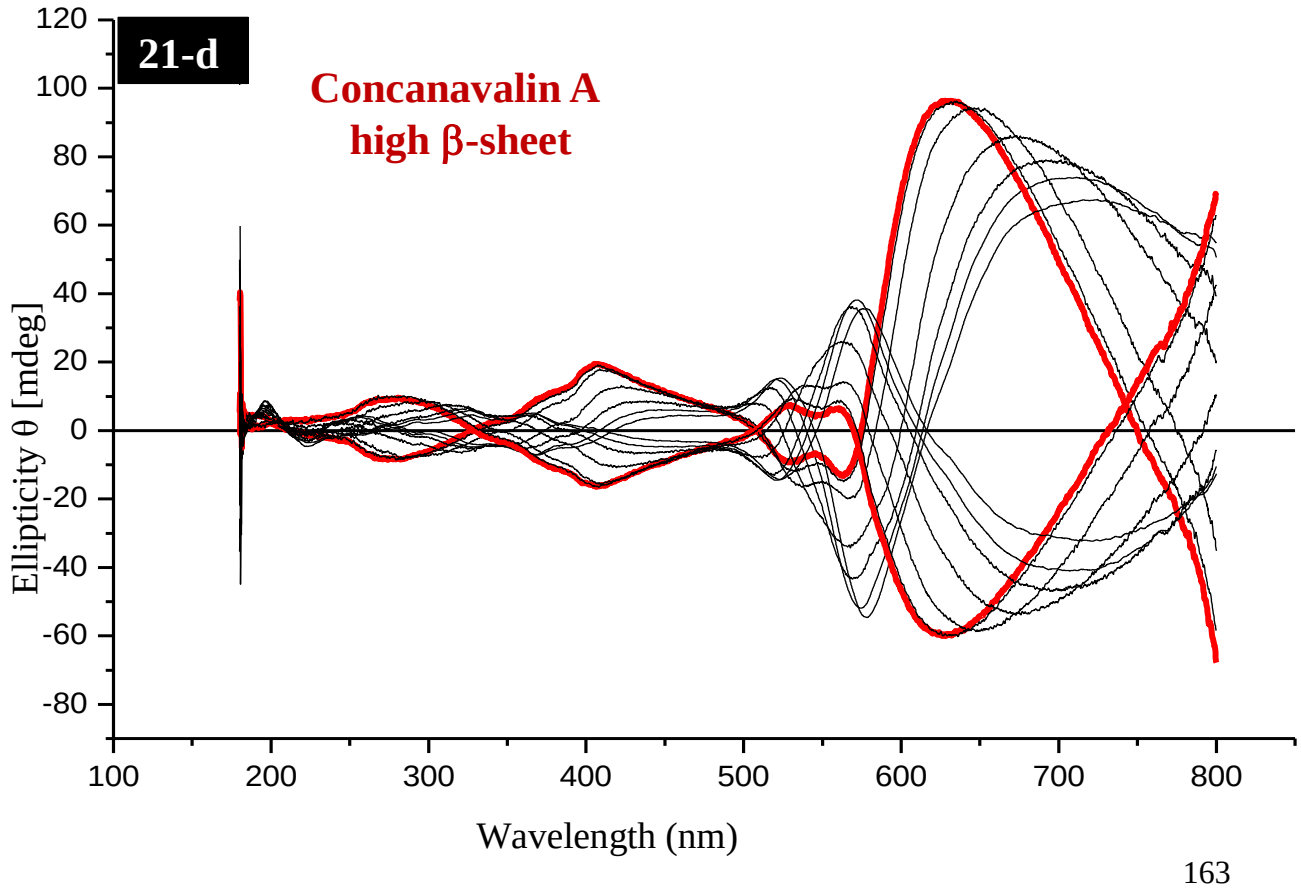
21-d
Concanavalin A
high β-sheet
Ellipticity θ [mdeg]
120
100
80
60
40
20
0
-20
-40
-60
-80
100
200
300
400
500
600
700
800
Wavelength (nm)

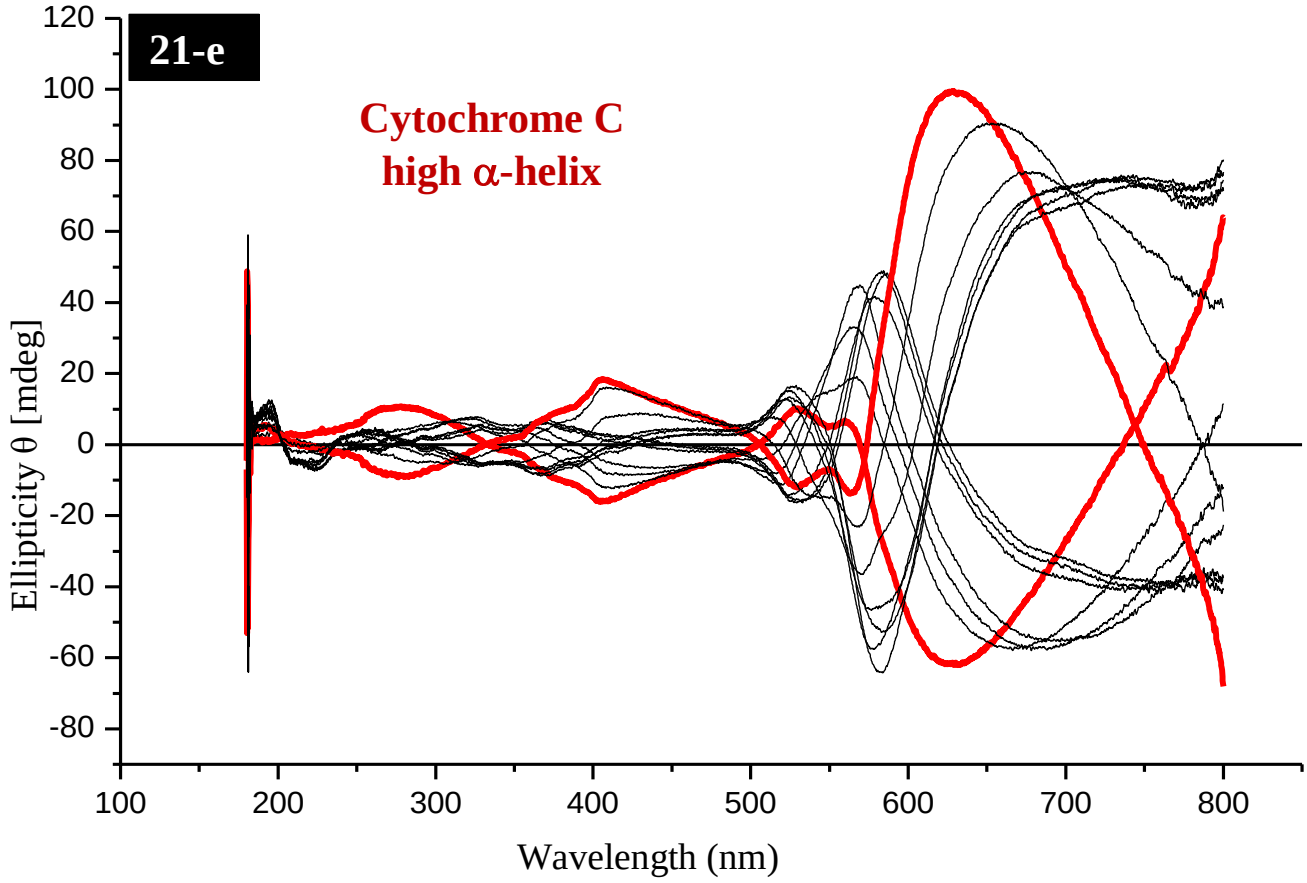

Figure 21 (a-e): CD spectra for three proteins with α-secondary (**21-a**, **21-c** and **21-e**) structures and two proteins with β- secondary (**21-b** and **21-d**) structures. Red lines represent CD spectra for the open cell substrates. Black lines represent CD spectra for the substrates after the proteins deposition layer by layer. Note the increasing red shifts with increasing number of layers.

3.4.2. Sensitivity to proteins with high order structure level (quaternary structure)

Two proteins Insulin and α-Synuclein were allowed to form fibrillar structures to investigate whether their different quaternary structures could be detected by deposition on gold patterned nanostructures. Both of these fibrils have ß secondary structure [26-28] and they are indistinguishable by conventional far UV CD spectroscopy (Figure 22 **c**). Following adsorption onto the surface of the gold nanostructures they showed discernible differences in their CD spectra. Figure 22**a** and **b** represent the CD spectra collected for the gold patterned nanostructures in the absence and presence of adsorbed Insulin and α-Synuclein fibrils, respectively. The solid red and the solid blue lines denote the CD spectra collected for blank samples of the right and left handed gammadions, respectively. The red dash and the blue dash lines denote the CD spectra collected for the samples with fibrils adsorbed on the surface of the right and left handed gammadions, respectively. Figure 22**c** represents conventional CD spectra collected for the solutions of Insulin and α-Synuclein fibrils. A large dissymmetry was observed for the α-Synuclein fibrils between 525-575nm (illustrated by the magenta circle) which was evaluated by the magnitude of $\Delta\Delta\lambda$. In principle, the magnitude of $\Delta\lambda$ varies according to the differences in the refractive indices of the environment; which in turn leads to differential CPL absorption. This chiral detection differs according to the morphology of the adsorbed biomolecules. Therefore, in Figure 22 one would observe small shift for insulin fibrils despite the fact that both of insulin and α-Synuclein fibrils have ß secondary structure. We attribute this behaviour to the fact that their ß -sheets are twisted to form fibrils; so the technique is sensitive to their morphology this time. Figure 23 illustrates these differences in overall morphology using atomic force microscope images.

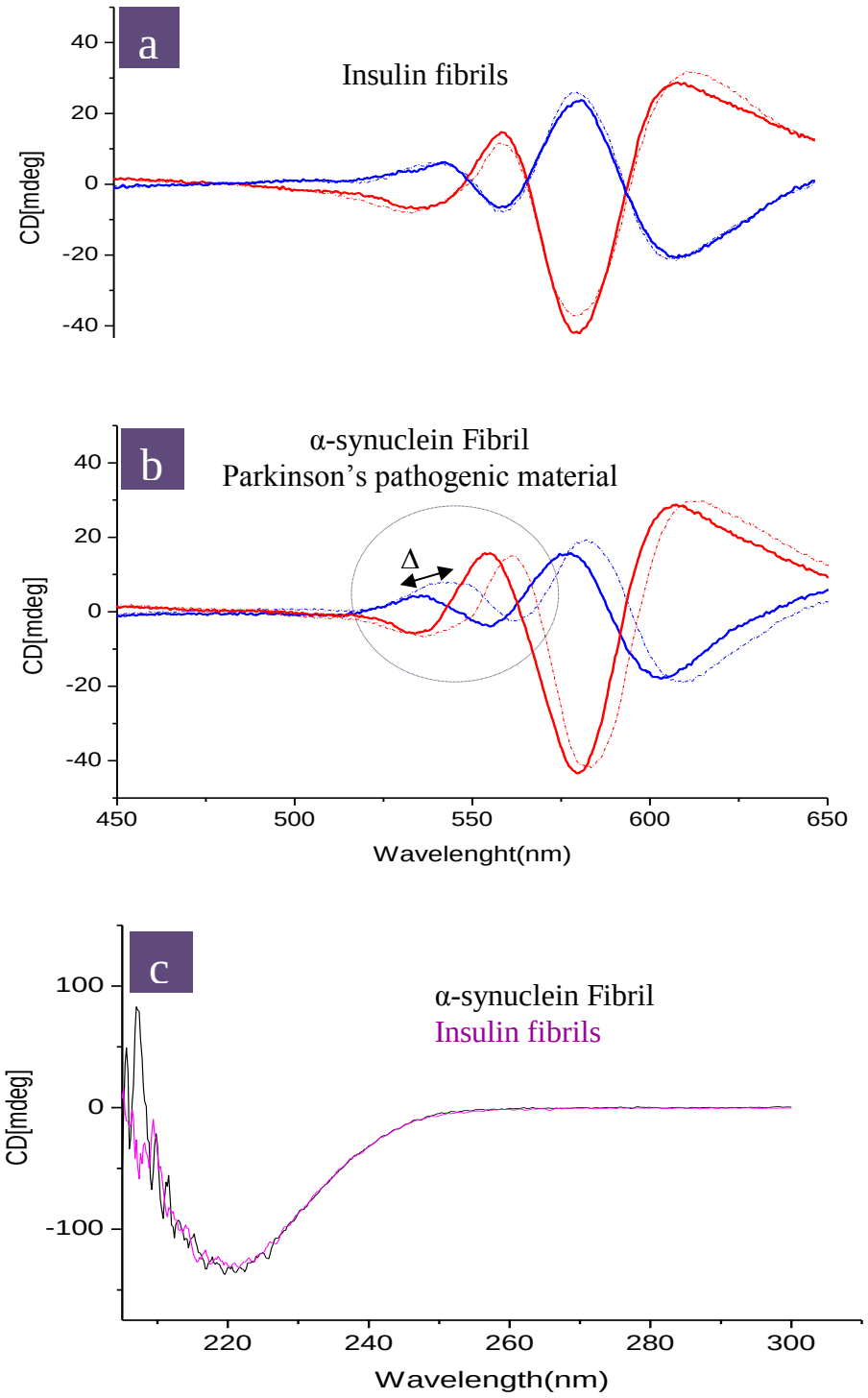

Figure 22: CD spectra comparison for Insulin and α-synuclein fibrils. **a** and **b** represent CD spectra for left (blue) and right (red) handed gammadions showing CD resonances before (solid lines) and after (dashed line) applying Insulin fibrils (**a**) and α-synuclein fibrils (**b**). These fibrils were indistinguishable by normal far UV CD spectropolarimetry (**c**), Note the dissymmetry shift in region 525-575 nm, (dashed circles), for α-synuclein fibril which is clearly more marked than the dissymmetry shift for the insulin fibrils in similar region.

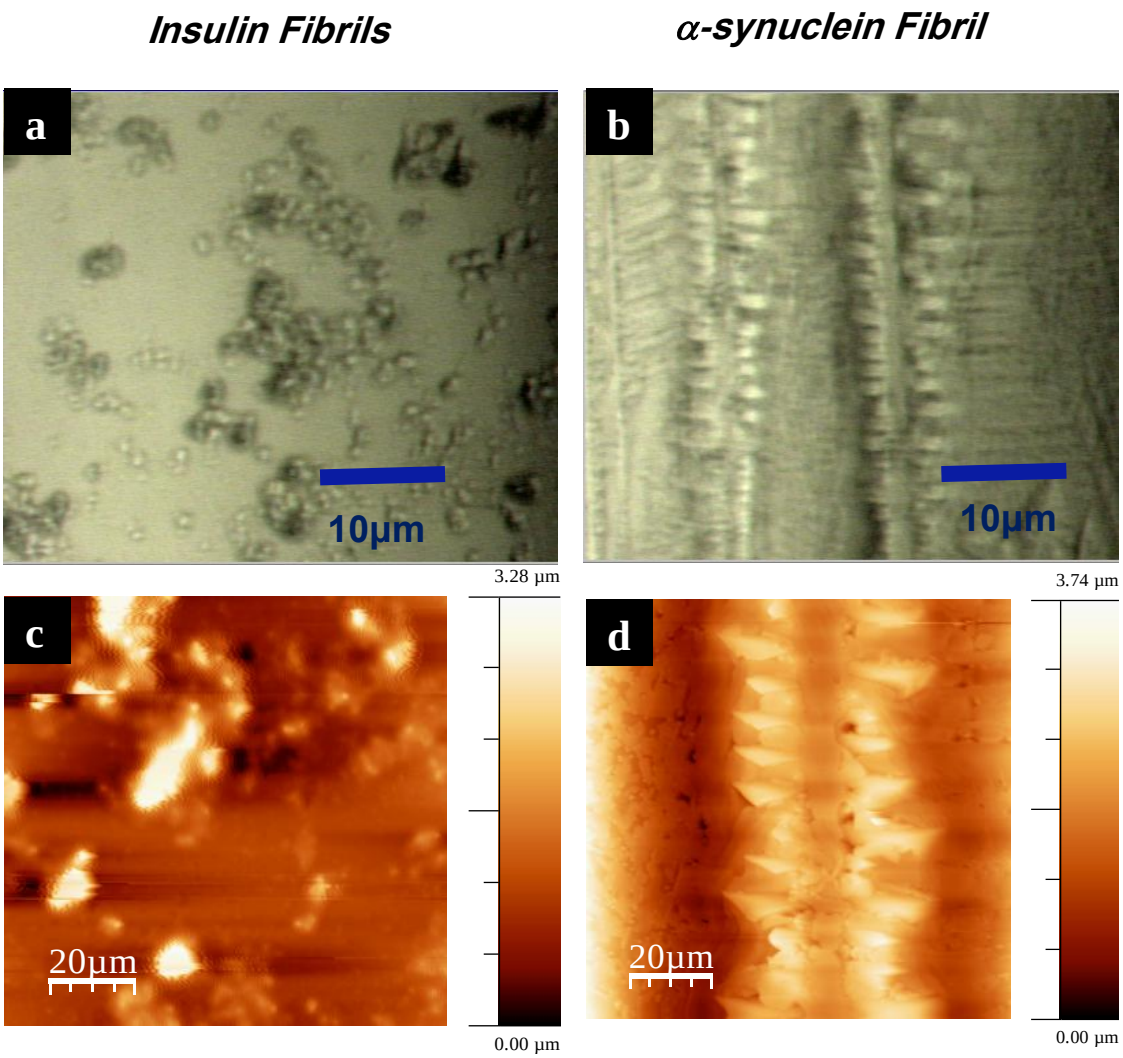

Figure 23: Four AFM images for Insulin and α-synuclein fibrils. In **a** and **b** we present two images optically collected (not by the AFM tip) for Insulin and α-synuclein fibrils, respectively. In **c** and **d** we present atomic force (with AFM tip) images for Insulin and α-synuclein fibrils respectively. Note the clear differences in the fibrils morphology for both proteins which may explain the larger dissymmetry shift of α-synuclein fibrils shown in **Figure 22**.

3.4.3. Sensitivity to different stages of fibrils growth

Proteins (*in vivo* or *in vitro*) are sensitive to changes in amino acid sequence, pH, temperature, pressure, salt concentration, etc. They can easily misfold due to sequence mutations, disease and changes in their surrounding environment. Protein misfolding (or non-native protein conformations) can influence a protein`s secondary structure conformation such that a protein containing predominantly $\alpha$-helical or random coil structure can be converted to form proteins with predominantly $\beta$-pleated sheet structures referred to as *Cross-$\beta$ structures*. These are *`sheets which run parallel to the axis of the fibril, with their component β -strands perpendicular to this axis`*, see Figure 24a. Several cross-β sheets pack together and then twist around a common helical axis to develop yet higher organised structures referred to as *protofilaments*, see Figure 24b. At least two protofilaments twist together to form a very early stage fibril, which in turn, start to twist with another fibril to enter a series of intermediate stages such as: oligomers, rings-like oligomers and globulomers which eventually develop into premature fibrils known as *protofibrils*. These in turn, develop into *amyloid-like fibrils*. Finally, when amyloid fibrils come together they accumulate as insoluble *β-amyloid plaques (*Figure 25) or *spherulites* [29]. In Figure 26 we present a schematic illustration for the hierarchy of amyloid fibril development. Generally speaking, amyloids are pathological proteins characterised as highly organised fibrillar aggregates with cross-β structures. The formation of amyloid fibrils by these pathological proteins remains poorly understood at the molecular level, despite extensive characterisation using different techniques (such as: X-ray Crystallography, Solid-State NMR spectroscopy, Fourier Transform Infrared spectroscopy FTIR, CD spectroscopy, TEM microscopy, SEM microscopy and AFM microscopy) to analyse the structural components of amyloid fibrils. The handedness of an amyloid`s different structural levels, such as β-sheets, protofilaments and fibrils have been described as either left handed or right handed [30,31]. Importantly, amyloids and proteins which display amyloid-like properties play important roles in the development of a group of different diseases collectively known as *Amyloidoses*. Amyloidoses can be developed when the secondary structures of normally soluble proteins are misfolded and misassembled leading to the accumulation of

insoluble amyloid proteins as extracellular amyloid deposits or intracellular inclusions on organs or tissues. In 2006 Chiti and Dobson assigned an association of 40 human diseases with Amyloidoses; which can be classified into three categories. **First** *neurodegenerative diseases*, when amyloidosis is develops in the brain e.g. Alzheimer's disease; which is caused by the aggregation of Amyloid β peptide (Aβ) see Figure 24, also, Parkinson's disease and Dementia which both are caused by the aggregating of α-Synuclein. **Second** *nonneuropathic localized amyloidoses*, when amyloidosis develops in a single type of tissue but not in brain e.g. AL amyloidosis which is caused by the aggregating of immunoglobulin light chains or fragments, also, AA amyloidosis which is caused by the aggregating of fragments of serum amyloid A protein, as well, Familial Mediterranean fever which is caused by the aggregating of fragments of serum amyloid A protein, see table 3. **Third**, *nonneuropathic systemic amyloidoses* when amyloidosis is developed in multiple tissue e.g. Injection-localised amyloidosis which is caused by the aggregating of insulin, also, pulmonary alveolar proteinosis which is caused by the aggregating of lung surfactant protein, as well, Inclusion-body myositis which is caused by the aggregating of Amyloid β peptide and Cutaneous lichen amyloidosis which is caused by the aggregating of Keratins. Nevertheless, nonpathological amyloid structure is found to have a beneficial function in living system, especially if it is regulated and allowed to take place under highly controlled conditions, e.g. Curlin fibrils, which share structural similarities to amyloid fibrils, are known to be a functional fibrils that are used by *Escherichia coli* to support inert surfaces and mediate binding to host proteins; more examples include fungi, insects and mammals are found in reference [29,32]. Also, since amyloid fibrils are extremely stable and resistant to degradation, nonpathological amyloid structure is found to have a beneficial function in bionanotechnology, e.g. amyloid-like assemblies of fusion proteins were used to form nanotubular scaffolding for bionanotechnological applications, likewise, nanowires of 100nm gold and 20nm silver have been fabricated by assembling protein peptides to form amyloid-like nanotubes [32] again more examples are found in reference [32]. In table 3, general amyloids fibrils classifications with some examples are presented.

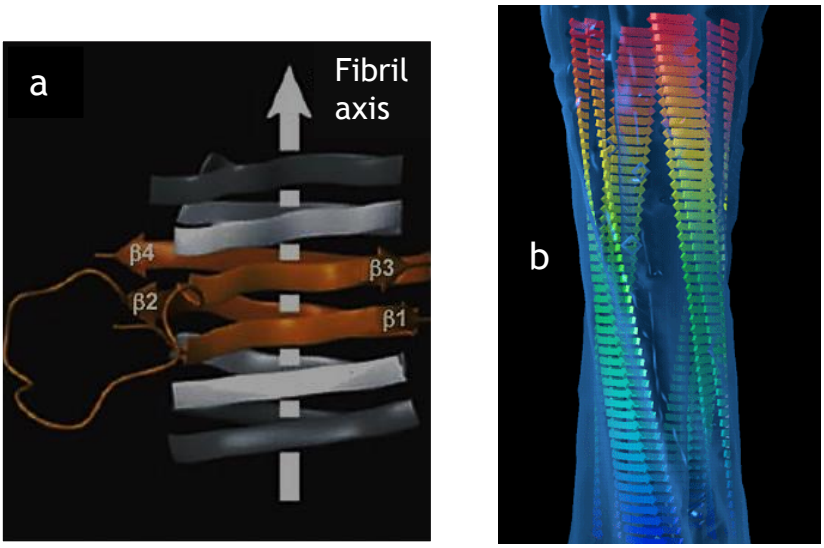

Figure 24: Cross-β structure. **a** illustrates β strands along fibril axis. **b** illustrates how Cross-β sheets twist together to develop the protofilaments in amyloid fibrils. These Figures were taken from reference [29].

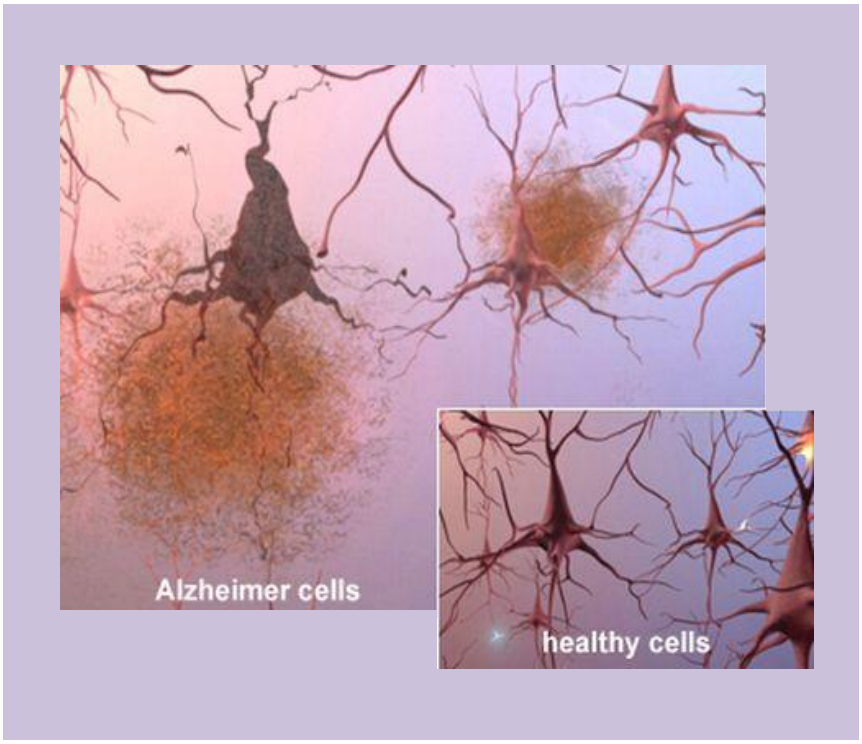

Figure 25: An aggregating of amyloid β peptide in brain results in neurodegenerative disease such as Alzheimer's disease. This Figure was taken from reference [33].

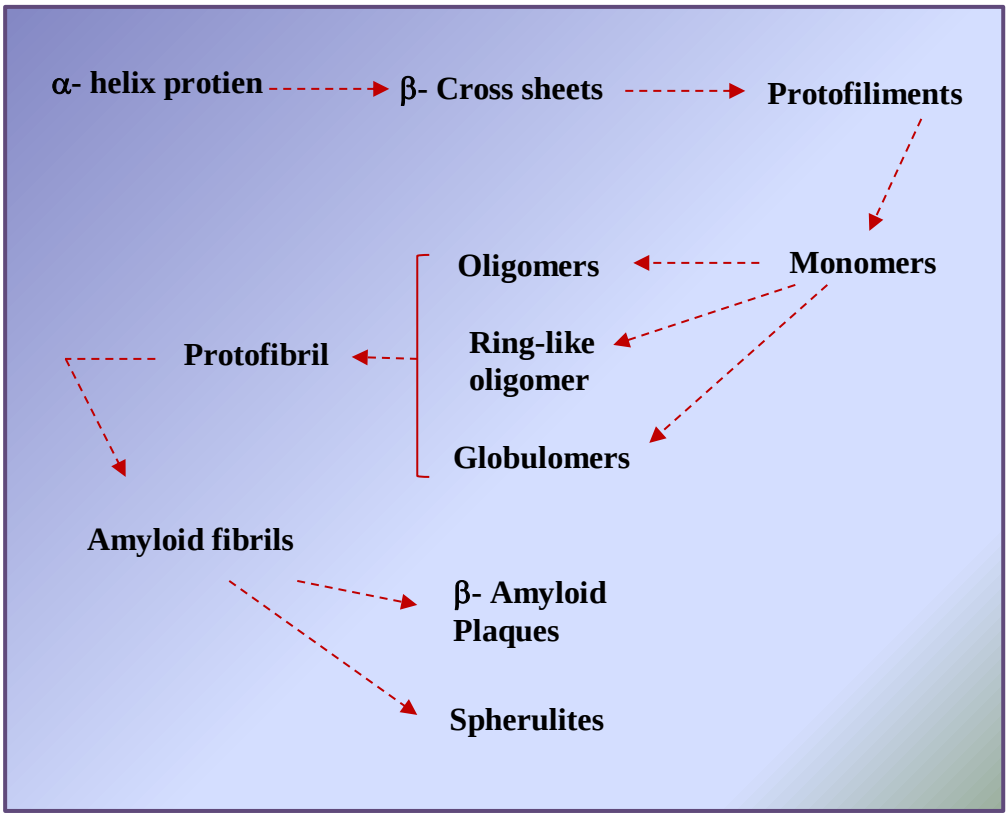

Figure 26: Schematic illustration for the hierarchy of amyloid fibrils developments.

Table 3: Amyloid fibrils classification with some examples that were presented by references [29, 32].

Amyloid fibrils classification	**Amyloid fibrils type**	**Found in**	**Example**	**Caused by**
Amyloidoses	Neurodegenerati-ve diseases	Brain	Alzheimer's disease	Amyloid β peptide (Aβ)
=	=	Brain	Parkinson's disease and Dementia	α-Synuclein
=	Nonneuropathic localized amyloidoses,	A single type of tissue but not in brain	AL amyloidosis	immunoglobulin light chains or fragments,
=	=	=	AA amyloidosis	serum amyloid A protein
=	=	=	Familial Mediterranean fever	serum amyloid A protein
=	Nonneuropathic systemic amyloidoses	Multiple tissue	Injection-localized amyloidosis	insulin
=	=	=	Pulmonary alveolar proteinosis	lung surfactant protein
=	=	=	Inclusion-body myositis	Amyloid β peptide
=	=	=	Cutaneous lichen amyloidosis	Keratins
Nonpathological amyloid structure	–	In living system	Escherichia coli to support inert surfaces and mediate binding to host proteins	Curlin fibrils
Nonpathological amyloid structure in bionanotechnolo-gy	–	In non-living system	Nanotubular scaffolding for bionanotechnological applications	Amyloid‐like assemblies of fusion proteins
=	–	=	Amyloid‐like nanotubes	Nanowires of 100nm gold and 20nm silver

In Figure 27 (a-c) we present AFM images for Insulin which shows the spherical beads and in Figure 27 (d-f) we present AFM images for Insulin which shows the spherical beads with the formation of chains. Figure 27 (g, h) shows AFM images for α-synuclein which shows the annular species [27,34]. As it has mentioned, all these are intermediate stages preceding higher order assemblies, i.e. Fibrils. Figure 27i is an example of a single AFM image for α-synuclein showing the early stage of these fibrils. In fact, fibrils can assemble into much higher ordered species ranging from small twisted fibrils (Figure 28a and b) to Insulin spherulites Figure 28 (c-f), or into tree branch-like, structures as shown for α-synuclein (Figure 28 g and h).

It has been demonstrated that the growth stages of α-synuclein fibrils formation, can be detected by the observation of CD spectral changes (in the wavelength range 525-575nm) upon adsorption onto gold chiral nanostructures. Scanning microscopy (AFM and SEM) was used to verify morphological changes. The growth of α-synuclein fibrils was monitored over the time period of a few days to ~6 weeks (incubation at 37^{o} and pH7). The related spectra are shown in Figure 29 and Figure 30 below. In these Figures the four CD spectra correspond to four different time periods: 3days, 5days, 18days and 6 weeks. Figure 29 represents the conventional CD spectra for the fibrils measured in their buffer solutions. Figure 30 represents the CD spectra for the fibrils adsorbed onto the surface of the chiral gold nanostructures. In each Figure a shift in λ with increasing of time was observed (Figure 29, 30) for 3 and 5 days. Once the fibrils had formed (18 day - 6weeks), which was indicated by λ=220nm and scanning microscopy no further changes were observed by conventional CD (Figure 29). In Figure 30 however, clear differences could be observed between 18 days to 6 weeks representing further stages in fibril assembly. Yet, these stages in fibril assembly have not been investigated here.

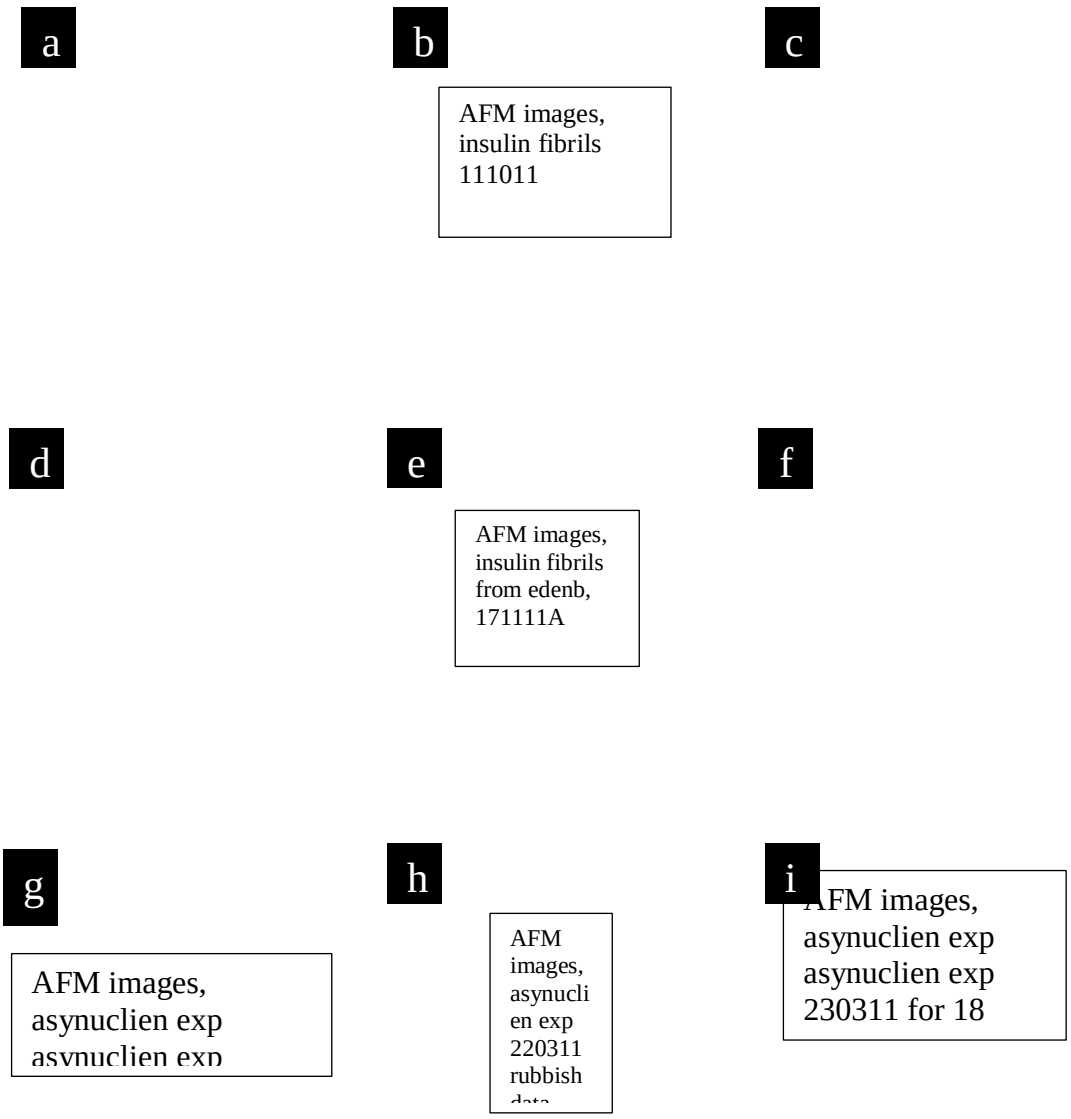

Figure 27: AFM images illustrate different protofibrillar species for Insulin and α-synuclein. (**a-c**) represent Insulin spherical beads. (**d-f**) represent Insulin spherical beads assembling into linear and curly chains. (**g, h**) represent α-synuclein annular (ring) species. **i** represents early-stage α-synuclein fibrils.

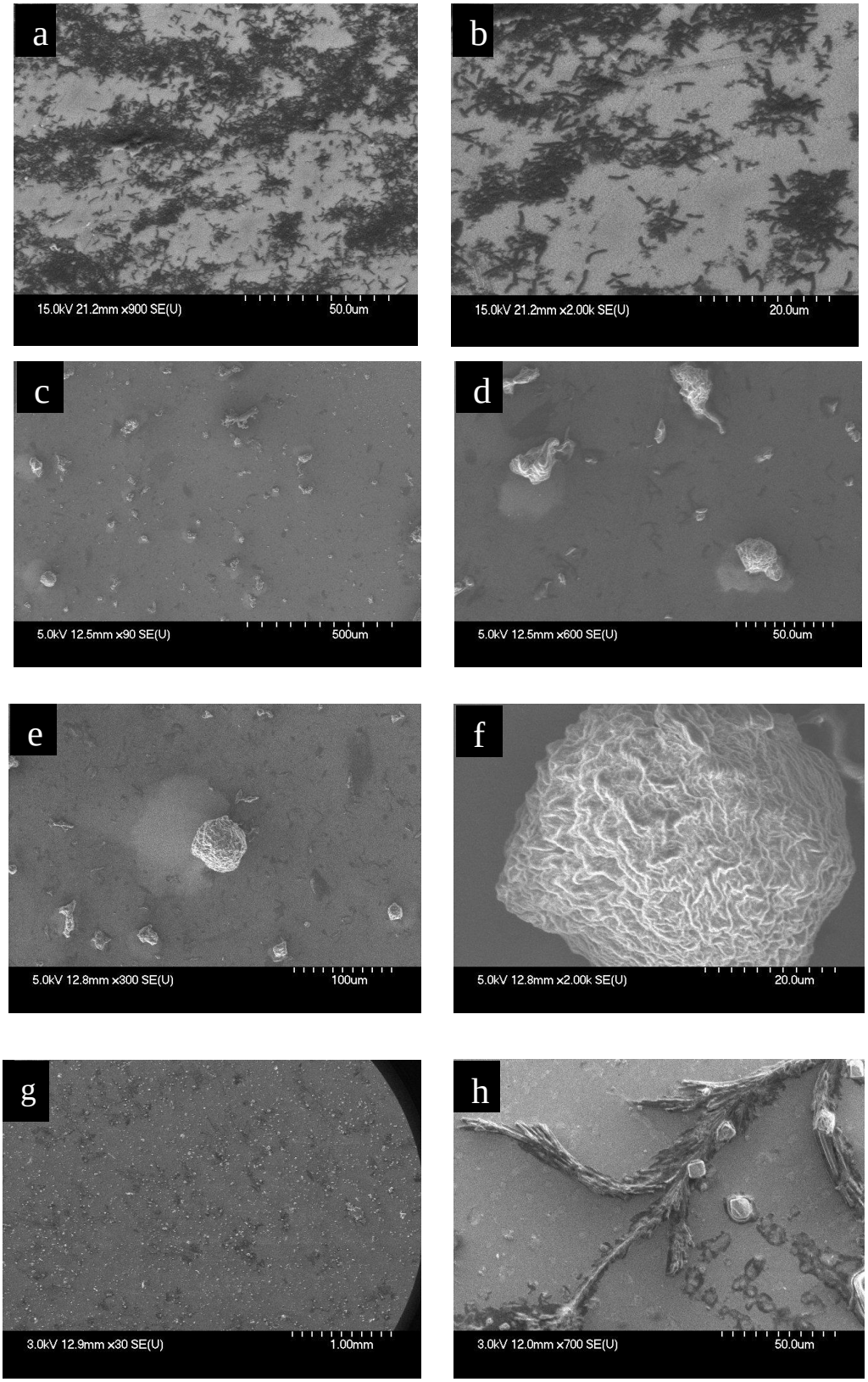

Figure 28: SEM images for Insulin and α-synuclein fibrils illustrate different stages of their fibrils maturity. **a, b** represent Insulin fibrils developed to small chunky twisted fibrils. (**c-f**) represent Insulin fibrils developed to spherulites. (**g, h**) represent α-synuclein fibrils developed to tree branch-like .

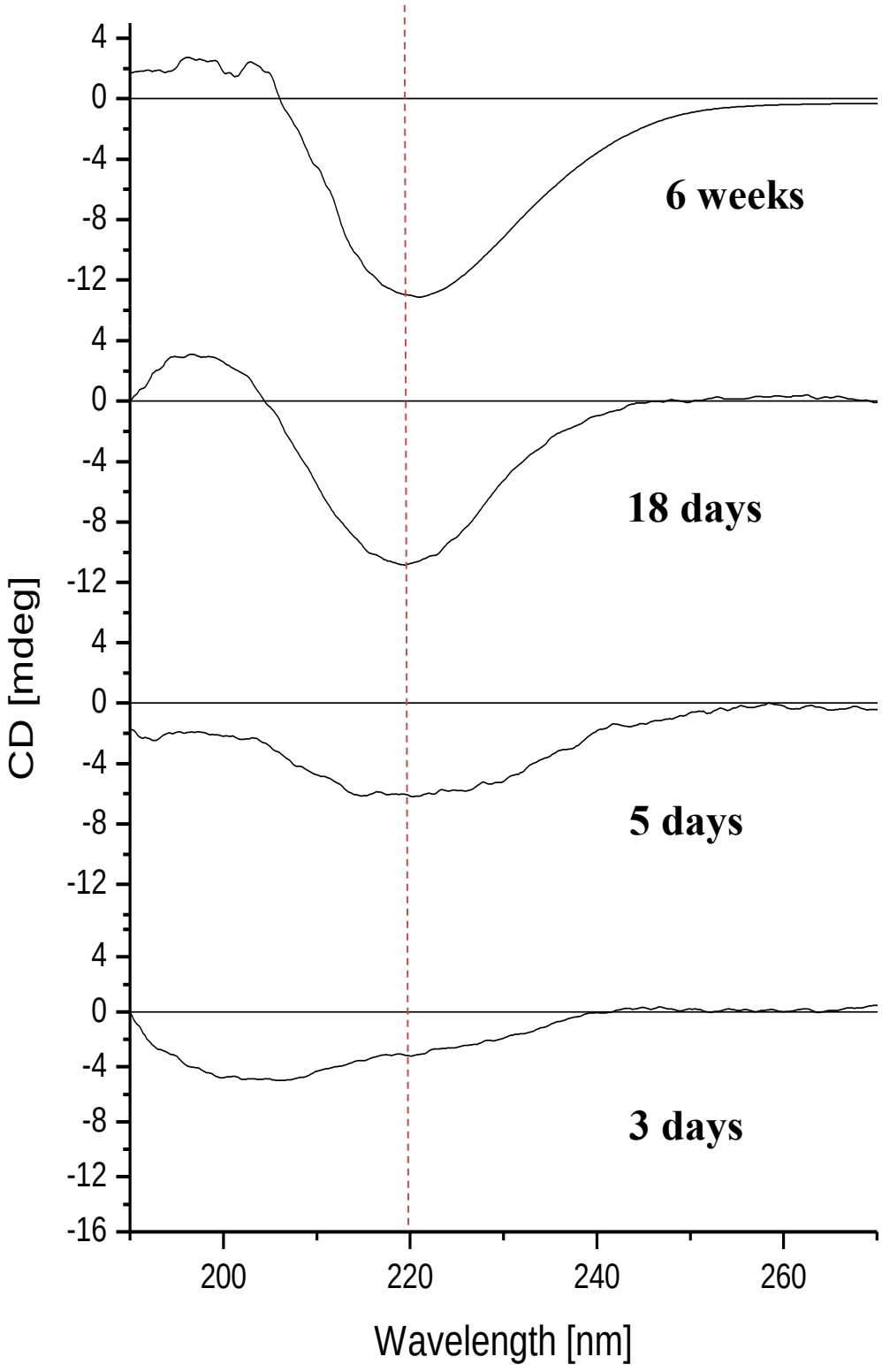

Figure 29: Conventional CD spectra showing the progress of α-synuclein fibrillation over a period of time namely 3 days till several weeks. Note the early stages prior to fibrillation e.g. 3 and 5 days and how the fibrillation seems to be completed after two weeks indicated by the 220nm absorption. However, the maturity (whether it is single or aggregated) of the fibrillation is not clear.

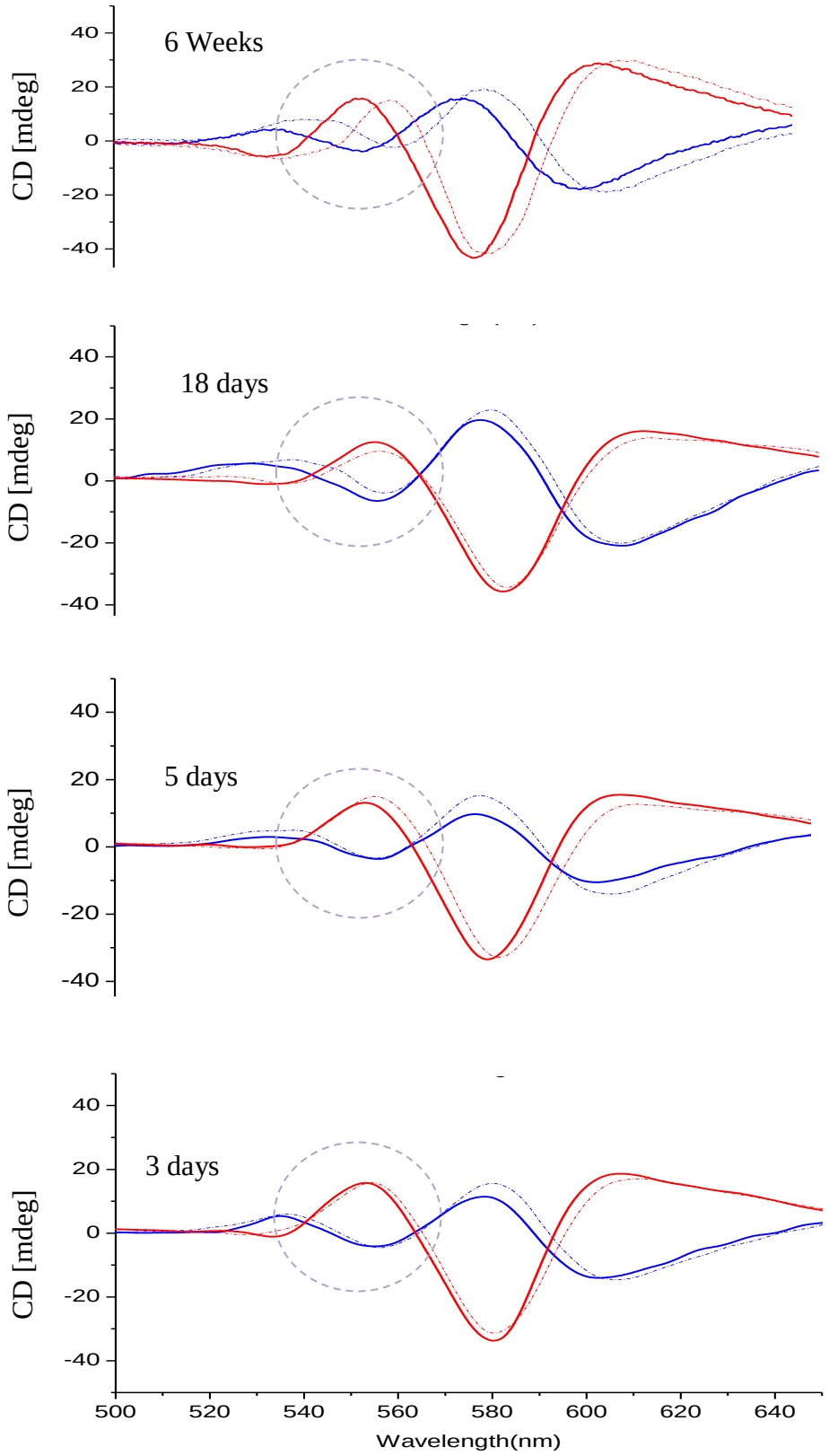

Figure 30: CD spectra for α-synuclein fibrils showing the progress of its fibrillation over a period of time namely 3 days till several weeks. The CD spectra for left (blue) and Right (red) handed gammadions are showing CD resonances before (solid lines) and after (dashed line) applying α-synuclein fibrils. Note the increasing of the dissymmetry shifts in the region between 525-575nm, (dashed circles), indicating spectral changes.

3.4.4 Adsorption of insulin and a-synuclein on the surface of our nanostructures

Bovine serum insulin is a protein hormone consisting of two polypeptide chains; A and B. The A chain consists of 21 residues with two helical segments; A2-A8 and A13-A20. The B chain consists of 30 residues with: extended structures at B1-B8 and B24-B28, as well, α-helical segment at B9-B19, in addition, β-turn at B20-B23, see Figure 31(top) [35, 36, 37]. α-Synuclein fibril is a protein consisting of 140 residues; with a single chain which consists of two broken α-helical regions and a flexible and disordered C-terminal tail, see Figure 31 (bottom) [37,38]. For insulin and α-synuclein, polar and charged amino acids are expected to be exposed at the surface of the fibril; conversely, hydrophobic amino acids are expected to be repelled from water and hence hidden away from the surface. From table 2, cysteine is a polar amino acid; therefore it is expected to be exposed to the surface of the fibrils; hence facilitating thiol binding between these fibrils and the surface of our nanostructures. In aqueous solutions, it has been established that `*fibril disulfide bonds remain intact with the same molecular conformation as in native insulin, even after an extensive conversion of the α-helical structure to a fibrillar β-sheet*` [39]. Yet, upon insulin adsorption on our gold nanostructures it is not clear whether this view is still effective; because another study showed that upon adsorption of methanethiol and dimethyl disulphide on Au(III) surface, the `*dissociation is clearly favoured for the disulfide with subsequent formation of strongly bound thiolates*` [40]. Besides, it is not clear how mature our fibrils are; different morphologies could expose fewer or larger amounts of cysteine. On the other hand, α-synuclien fibrils have no cysteine associated with its primary sequences, and therefore, α-synuclien fibrils binding to the surface of the nanostructures cannot be attributed to thiol bond. Clearly, how these proteins are adsorbed onto and oriented on the gold nanostructure surfaces cannot be characterised at this stage, however, this is an issue we hope to address in our future work.

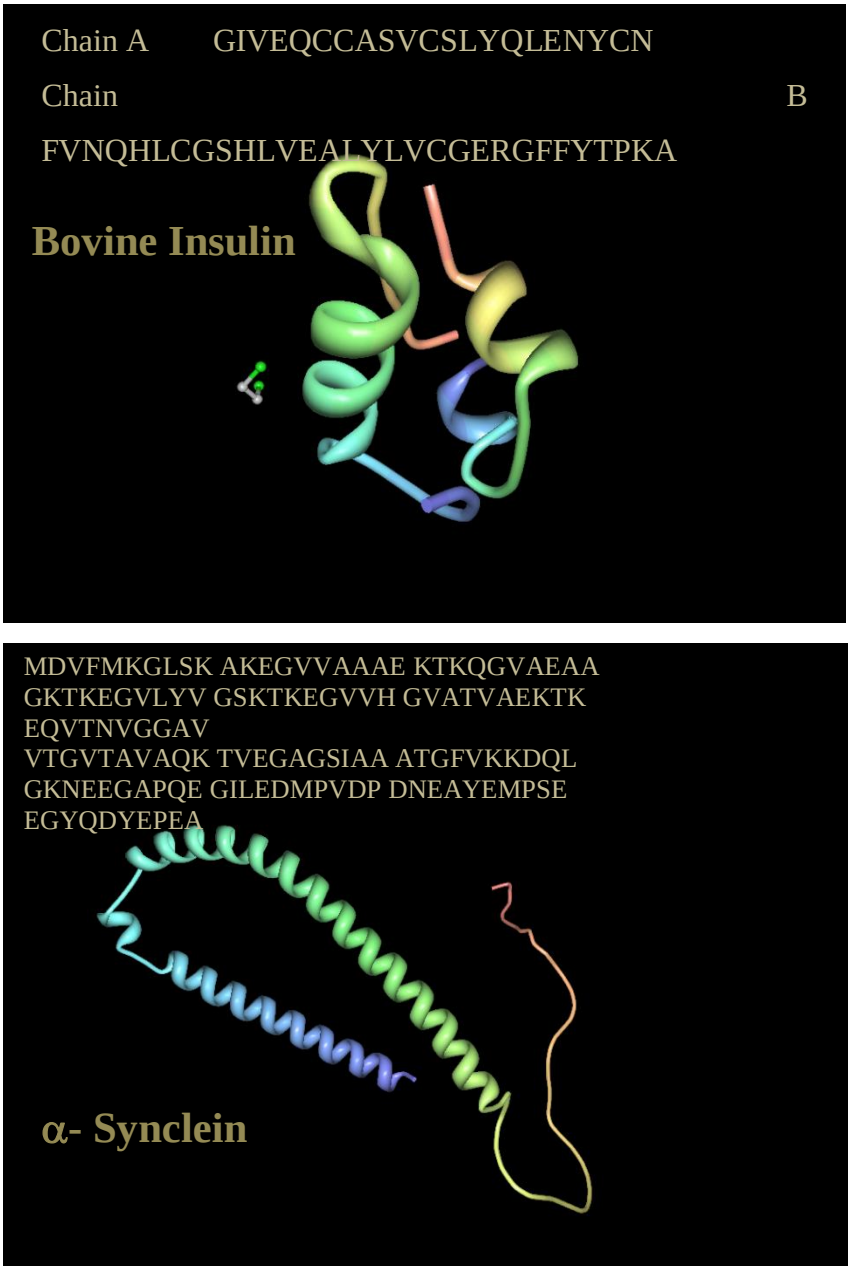

Figure 31: Illustration of Bovine Insulin hormone (top) and α-Synuclien protein (bottom) 3D structures. In set we show the amino acid sequences denoted by the common code of each amino acid (shown in table 2). 3D structures were taken from reference [37]. Amino acid sequences for bovine insulin hormone were taken from reference [36,37]. Amino acid sequences for α-Synuclien were taken from reference [37,38].

3.5. Conclusions

In conclusion, we have found that gold nanostructures can be used to make sensitive biosensors based on the generation of Superchiral fields. Also, this work demonstrates new applications of metamaterials in ultrasensitive spectroscopy/bio-detection, based on the combination of natural and induced chirality. Our strategy for bio-sensing is capable of distinguishing between proteins with α-helical and β-sheet secondary structures. Also, it can distinguish between two proteins with high order structure level (quaternary structure). In addition, it is capable to sense different stages of fibrils growth.

3.6. References

1. Nafie L. A., "Vibrational Optical Activity Principles and Applications", *Jhon Wiley& Sons Ltd*., 2011.
2. Barron L. D., "Molecular Light Scattering and Optical Activity", *Cambridge University press, Cambidge*, 2004, 2nd edition, printed book.
3. Hache F., Mesnil H. and Schanne-Klein M. C., *Journal of Chemical Physics*, 2001, Vol.115**,** pp (6707- 6715).
4. Verbiest T., Kauranen M., Persoons A., Ikonen M., Kurkela J. and Lemmetyinens H., *Journal of the American Chemical Society*, 1994, Vol.116**,** pp (9203-9205).
5. Kosuda K. M., Bingham J. M., Wustholz K. L. and Van Duyne R. P., *Comprehensive Nanoscience and Technology* , 2011, Vol.3, pp (263-301).
6. Hendry E., Carpy T., Johnston J., Popland M., Mikhaylovskiy R. V., Lapthorn A. J., Kelly S. M., Barron L. D., Gadegaard N. and Kadodwala M., Nature Nanotechnology, 2010, Vol.5, pp (783-787).
7. Willets K. A. and Van Duyne R. P., *Annu. Rev. Phys.Chem*, 2007, Vol.58, pp (267-297).
8. Kelly S. M., Jess T. J., Price N. C., *Biochimica et Biophysica Acta*, 2005, Vol.1751, pp (119-139).
9. Corrêa D. H. and Ramos C. H., *African J. of Biochemistry Research*, 2009, Vol.3 pp (164-173).
10. Tang Y. and Cohen A. E., *Phys. Rev. Lett.*, 2010, Vol.104, pp (163901-163904).
11. This images could be found at the following website: http://www.enzim.hu/~szia/cddemo/edemo0.htm (cited in 2013).
12. Valev V. K., Baumberg J. J., Sibilia C. and Verbie T., *Advanced Materials*. **2013**, Vol.25, pp (2517-2534).
13. Tang Y. and Cohen A. E., *Science*, 2011, Vol.332, pp (333-336).
14. Yang N., Tang Y., Cohenb A. E., *Nano Today* , 2009, Vo.4, pp (269—279).
15. Lee R. L., Fraser A. B., ` THE RAINBOW BRIDGE`, Penn State Press and SPIE Press (Bellingham, WA), 2001.
16. Scha¨ferling M., Dregely D., Hentschel M. and Giessen H., PHYSICAL REVIEW X, 2012, Vol. 2, pp(031010(1-9)).
17. Valev V. K., *Langmuir, American Chemical Society*, 2012, Vol.28, pp (15454-15471).
18. Bohren C. F. and Huffman D. R., "Absorption and Scattering of Light by Small Particles", *Wiley-VCH Verlag GmbH & Co.KGaA, Weinheim*, 2004, printed book.
19. Matthews B. W., `Hydrophobic Interactions in Proteins`, *John Wiley & Sons, Ltd*., 2001.
20. PROTEINS:THREE-DIMENSIONAL STRUCTURE. This could be found at this website (cited in 2014): http://csb.stanford.edu/class/public/readings/Molecular_Architecture_I_Lecture2/Voet_and_Voet_BOOK_00_Chapter6_Protein_Structure.pdf
21. Nelson D. L. and Cox M. M., `Principles of Biochemistry`, *Lehninger*, 5th edition 2008, pp92.
22. Ball D. W., Hill J. W. and Scott R. J., "The Basics of General, Organic, and Biological Chemistry v. 1.0", *Flat World Knowledge, Inc.*, 2013.

23. This image could be found in this website (cited in 2014): http://textilesfr.co.uk/technical/terminology
24. This image could be found in this website (cited in 2014): http://mapkapk2.blogspot.co.uk
25. Sarina S., Waclawik E. R. and Zhu H., *The Royal Society of Chemistry*, 2013, Vol.15, pp (1814-1833).
26. Bouchard M., Zurdo J., Nettleton E. J., Dobson C.M. and Robinson C., *Protein Scince*, 2000, Vol.9, pp (1960-1967).
27. Vilar M., Chou H., Luhrs T., Maji S. K., Riek-Loher D., Verel R., Manning G., Stahlberg H. and Riek R., *PNAS*, 2008, Vol.105, pp (8637-8642).
28. Lee J., Hong C., Lee S., Yang J., Park Y., Lee D., Hyeon T., Jung S., Paik S., *PLOS ONE*, 2012, Vol.7, pp (1-9).
29. Fabrizio Chiti1 and Christopher M. Dobson, *Annu. Rev. Biochem.*, 2006, Vol.75, pp (333-366).
30. Jime´nez J., Nettleton E. J., Bouchard M., Robinson C. V., Dobson C. M. and Saibil H. R., PNAS, 2002, Vol.99, pp (9196–9201).
31. Usov I., Adamcik J. and Mezzenga R., acsnano , 2013, Vol. 7 , pp(10465–10474)
32. Rambaran R. N. and Serpell L. C., Prion, 2008, Vol.2, pp(112-117).
33. This image was taken from this website (cited in 2014): http://coloradodementia.org/2012/01/25/marwan-sabbagh-md-on-the-pathology-of-alzheimers/
34. Caughey B. and Lansbury P. T., *Annu. Rev. Neurosci*., 2003, Vol.26, pp (267-298).
35. Bouchard M., Zurdo J., Nettletone E. J., Dobson C. M.and Robinson C. V., Protein Science/ Cambridge University Press, 2000, Vol.9, pp(1960–1967).
36. Friedrichsen T., `Genetics and Evolution`,OpenStax-CNX, E-book Available for free at Connexions http://cnx.org/content/col11595/1.1, 2013. (sited in 2014).
37. Protein Data Bank PDB.
38. Ritchie C. M. and Thomas P. J., Health, 2012, Vol.4, pp (1167-1177).
39. Kurouski D., Washington J., Ozbil M., Prabhakar R., Shekhtman A. and Lednev I. K. PLoS ONE , 2012, Vol. 7, pp(1-12).
40. Gronbeck H., Curioni A. and Andreoni W., J. Am. Chem. Soc. 2000, Vol.122, pp(3839-3842).

Chapter 4: Induced chirality through electromagnetic coupling between chiral molecular layers and plasmonic nanostructures

Abstract

In this chapter we demonstrate the induction of chirality via Flavin Mononucleotide (FMN or Vitamin B2) on an achiral plasmonic surface consisting of gold nanostructures. The induction of chirality has been achieved via electromagnetic radiative coupling between the electromagnetic fields in the biomolecule and the electromagnetic fields resonating on the surface of the gold metamaterials. Our investigations are based on a simple electromagnetic model consisting of a plasmonic object embedded into a chiral molecular medium. The model is validated through several experimental findings. Our investigations were based on the far field fundamentals, which has not been considered before. It follows the fact that the optical properties of the plasmonic particles could be influenced by molecular materials through near field effectiveness. Our study has shown a thousand times bigger effect than that for the near field efficiency; simply because the far field decay spans across hundreds of nanometers, which is ~ three orders of magnitude bigger than near field decay.

4.1. Introduction

As was already mentioned in chapter 3, chiral molecules of different handedness interact differently with left or right circularly polarised incident light. Therefore they possess a property called `*Natural optical activity*`, which is a general property of chiral molecules that is associated with electromagnetic radiation [1 chap.3 pp76]. In principle, the environment of the chiral molecules is known as the `chiral medium`. As a medium, it is capable of differentiating between left and right handed electromagnetic fields. A chiral medium can be described as an `*isotropic chiral medium*`, in which all of its molecules are

handed (chiral), e.g. a solution of any biomolecule like protein, sugar, FMN etc. Chiral medium can also be described as a `*structurally chiral medium*`, in which all of its molecules are positioned in a way to exhibit helicoidally orientation order, e.g. achiral nematic liquid crystal [2[chap.4 pp125], 3] (more examples are shown in chapter 1). In fact, it is possible to convey the natural optical activity of chiral molecules to achiral plasmonic surfaces via electromagnetic *near-field* coupling. This is true when well-orientated single layer of chiral molecules are adsorbed on the surface of achiral plasmonic nanoparticles [4, 5]. In this chapter, we will describe that it is possible to convey natural optical activity of chiral molecules to achiral plasmonic surfaces via electromagnetic *far-field* coupling instead of the near-field one. Again, this is true, but this time, when homogenous multi-layers of chiral molecules are adsorbed on the surface of plasmonic nanostructures [6]. Having that implies the possibility to artificially modify the optical activity on achiral plasmonic surfaces, wherein certain metals, such as gold and silver nanoparticles or/and nanoatructures, have the ability to produce evanescent fields once they have electromagnetic fields irradiated their surfaces (see chapter 2) [7, 8, 9]. In the visible region of the electromagnetic spectrum, the wavelength of the light is larger than the average size of the nanoparticles and/or the nanostructures. Thus, following the electromagnetic exposure, the electron density of the plasmonic surface (i.e. the free electrons of d orbitals for gold and silver nanoparticles) will be polarised and start to oscillate with the frequency of the electromagnetic light. This generates standing resonance conditions, referred to as `standing waves`, which represent the evanescent fields oscillations [10]. The evanescent field will be chiral, if the evanescent field oscillates on the surface of chiral architected metamaterials [11-14] or it will be achiral, if the evanescent field oscillates on the surface of the gold and silver nanoparticles [15].

Potentially, having such optical modifications implies beneficial from the combinations between the physical engineering of the metamaterials and the molecular properties of the surrounding dielectric medium. Indeed, it is a new discovery with new interesting fundamentals which we aim to discuss in this chapter. The main hypothesis here is to increase the sensitivity of the plasmonic surfaces of the nanostructure to aid the detection of chiral biomolecules in the

visible area instead of UV area [3]. Also, to prepare a chiral environment via achiral metmaterials, which highly reduce fabrication costs [16, 17]. On the other hand, theoretical estimations were applied in order to support experimental findings. This was via a simple electromagnetic model consisting of a plasmonic object embedded into a chiral molecular medium.

In this chapter, investigations have been covered by four main sections. At the beginning, in section 2, we demonstrate a few theoretical models which we believe might help the reader to follow the rest of this work. Also, in the same section, we demonstrate our theoretical model which was proposed and fully calculated by the Gorovov group at the University of Ohio in the USA. In section 3 we demonstrate the method we have used to perform our experimental work. We then continue, in section 4, with a demonstration of our results. These involve two types of spectroscopy measurements: the extinction and the circular dichroism (CD) spectra in addition to SEM and AFM scanning microscopy. In section 5 we present our conclusions.

4.2. Theory and background

4.2.1. Theoretical model

The theoretical model used here uses a classical description of electromagnetic dynamics. In that, the sources of the fields of a particular system are defined by Maxwell`s equations [18[chap.7 pp208], 19[pp54]]:

$$\begin{pmatrix} \nabla \times E = -\delta B/\delta t \\ \nabla \times H = J + \delta D/\delta t \\ \nabla . D = \rho \\ \nabla . B = 0 \end{pmatrix} \quad \ldots\ldots\ldots\ldots\ldots\ldots\ldots\ldots\ldots\ldots \quad 1$$

Where:

E is the electric field intensity in (volts/meter).

D is the electric flux density (coulombs/meter^2)

H is the magnetic field intensity (ampere/meter)

B is the magnetic flux density in (weber/meter^2 or tesla)

J is the electric current density (ampere/meter^2)

ρ is the charge density(coulomb/meter^3)

When the medium is isotropic, the fields are related by:

$D = \varepsilon\varepsilon_\circ E$ $B = \mu\mu_\circ H$ ..... 2 [19 ppp4]

Here the **ε** and **μ** are the dielectric constant and magnetic permeability of the medium. The $\varepsilon_\circ$ and $\mu_\circ$ are the electric permittivity and the magnetic permeability constants of free space.

Yet electromagnetic dynamics for the optically active fields are slightly different; hence they follow the following formula of the Maxwell`s equations [6 supporting information files]:

$$\left.\begin{aligned} \nabla \times E &= -(1/C_o)(\delta B/\delta t) \\ \nabla \times H &= (1/C_o)(\delta D/\delta t) \\ \nabla . D &= 0 \\ \nabla . B &= 0 \end{aligned}\right\} \quad \ldots\ldots\ldots\ldots\ldots\ldots\ldots \quad 3$$

Here $c_o = \lambda\ \omega_o / 2\pi$

Where: c_o is the speed of light in free space, λ is the wave length of light and ω_o is the angular frequency for the free space.

Thus, the relations between D & E, and B & H from the classical equations are not compatible anymore. The following relations should be used instead [20]:

$$D = \varepsilon E + \alpha\varepsilon \nabla \times E \quad \ldots\ldots\ldots\

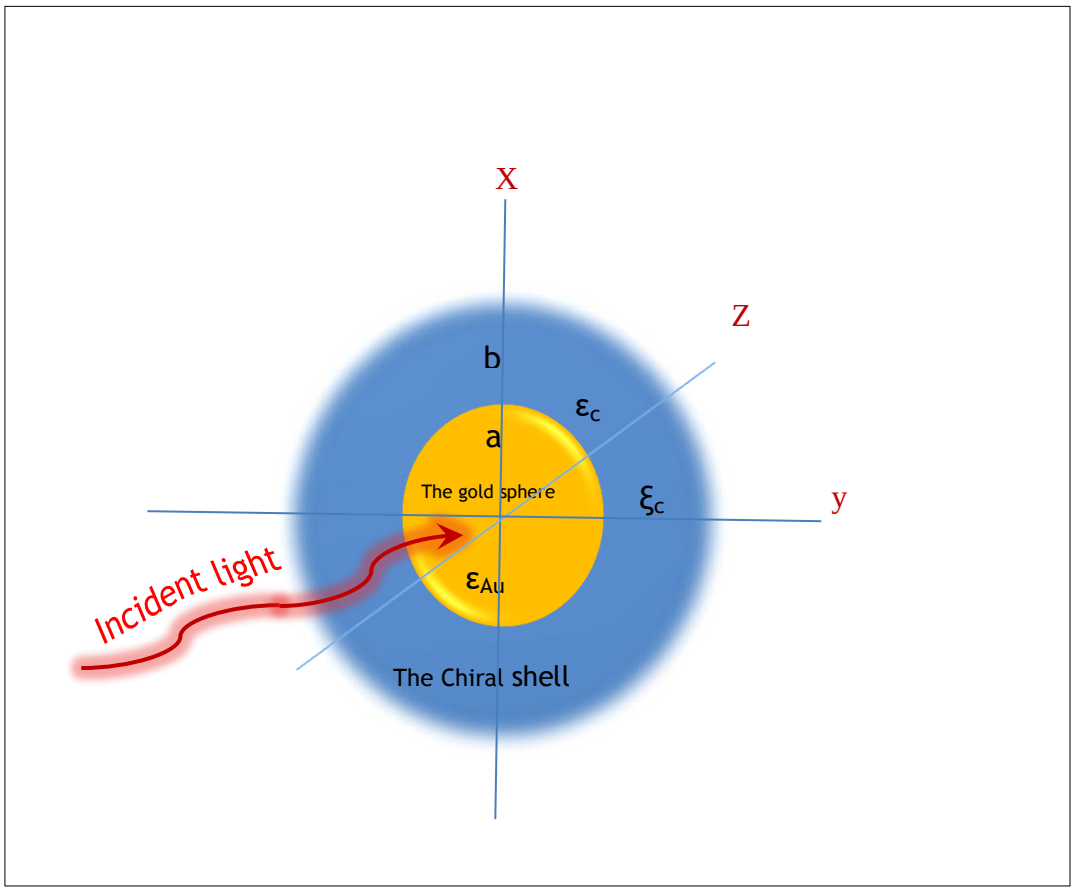

Figure 1: Theoretical model of a chiral plasmonic system consists of a gold metal sphere and a chiral molecular shell. The incident light strikes the surface from the z direction. The ε_c and the ε_{Au} represent the dielectric function for the chiral molecular shell and the gold sphere respectively. The ξ_c represents the chiral property parameter for the chiral molecular layer.

Three standard solutions of Mie theory were applied for three distinct environments. These are: the outside space, the shell and the plasmonic golden sphere. Also, the electromagnetic boundary conditions were applied between the different interferences [6].The boundary conditions verify the electromagnetic field quantities associated with the interface of two different media, one or both is a dielectric [18 chap.3 pp 91].

The electromagnetic coupling between the molecular layer and the gold nanoparticles can be estimated by the circular dichroism response shown in the following equation:

$$CD = (N_A/0.23)\,(C_{ext,+} - C_{ext,-}) \times 10^{-4} \quad \ldots\ldots\ldots\ldots\ldots\ldots\ldots\ldots \quad 6$$

CD represents the extinction response

N_A represents Avogadro number

$C_{ext,+}$ represents the extinction cross sections for right handed circularly polarised incident light.

$C_{ext,-}$ represents the extinction cross sections for left handed circularly polarised incident beams

The CD measurements are usually accompanied with anisotropic factor calculations. The anisotropic factor, symbolic g, characterises the strength of the CD response, this is shown in the following equations:

$$g = (A_+ - A_-) / \bar{A} \quad \ldots\ldots\ldots\ldots\ldots\ldots\ldots\ldots\ldots\ldots\ldots\ldots \quad 7$$

$$A_+ = \log (I_o / I_{\text{transmitted},+}) \quad \ldots\ldots\ldots\ldots\ldots\ldots\ldots\ldots\ldots\ldots\ldots \quad 8$$

$$A_- = \log (I_o / I_{\text{transmitted},-}) \quad \ldots\ldots\ldots\ldots\ldots\ldots\ldots\ldots\ldots\ldots\ldots \quad 9$$

$$\bar{A} = (A_+ + A_-)/2 \quad \ldots\ldots\ldots\ldots\ldots\ldots\ldots\ldots\ldots\ldots\ldots\ldots\ldots\ldots \quad 10$$

A_+ represents the extinction for right circularly polarised light

A_- represents the extinction for left circularly polarised light

$\bar{A}$ represents the average extinction

Basically, when electromagnetic waves traverse a specific medium, they are attenuated exponentially from I_o to $I_{transmitted}$ along a distance of h. Attenuation is occurring because the medium is either absorbing or scattering the electromagnetic waves. Absorption and scattering occur simultaneously; but in different proportions depending on the physical nature of the medium. In principle, attenuation is given by what is known as `Extinction spectrum`, which is a combination of the absorption and scattering spectra of the medium, and it is expressed by equations:

$$I_{transmitted} / I_o = \exp(-\alpha_{ext}) \quad \ldots\ldots\ldots\ldots\ldots\ldots\ldots\ldots\ldots\ldots\ldots\ldots\ldots\ldots\ldots \quad 11$$

$$\alpha_{ext} = n (C_{abs} + C_{sca}) \quad \ldots\ldots\ldots\ldots\ldots\ldots\ldots\ldots\ldots\ldots\ldots\ldots\ldots\ldots \quad 12$$

Where n is the number of particles per unit volume, C_{abs} and C_{sca} are the absorption and scattering cross sections, respectively. Despite the fact that both processes occur simultaneously, one of them dominates; depending on the nature and the homogeneity of the environment of the medium [22chap.11 pp287].

On the other hand, the appearance of the CD peak in spherical core shell model is relatively affected by the chirality parameter of the molecular layer (ξc), in particular the frequency dependence one, this is expressed as:

$$CD_{peak} \propto |\xi c| \approx \xi c(\omega) \quad \text{.....} \quad 13$$

The frequency dependent chirality parameter can be expressed as:

$$\xi c(\omega) = Re[\xi c(\omega)] + Im[\xi c(\omega)] \quad \text{.....} \quad 14$$

Where Re[ξc(ω)] and Im[ξc(ω)] represent the real and the imaginary elements respectively.

For the existence of a chiral molecule in a plasmonic environment, the following expression can be used:

$$\xi c(\omega) = Re\,[\xi c(\omega_{molecule}) + \xi c(\omega_{plasmon})] + Im[\xi c(\omega_{molecule}) + \xi c(\omega_{plasmon})] \quad \text{.....} \quad 15$$

a b c d

According to this equation, the absence of a plasmonic environment will result in CD from the molecular contribution only. In general, this contribution is weak, e.g. for FMN; the chirality parameter |ξc| is ~10^{-3} at λ = 380 nm. Therefore, CD

peak almost entirely originates from the imaginary part of the dielectric function, and hence CD ~ Imξc(ω). However, in hybrid structure, and near the plasmon area i.e. (500-700) nm, the molecular CD is modified. This is because the plasmonic field strongly perturbs the electromagnetic fields of the chiral molecules (this will be explained later). In fact, having a, b, c and d contributions to be considered separately implies better understanding for the chirality observed within plasmonic frequency. At the plasmonic frequency i.e. (500-700) nm, and considering the real parts of equation 15, **a** is relatively **strong** (since FMN does not absorb light at (500-700) nm and hence, FMN scattering ≠0), however **b** is weak (since plasmon scattering ~ 0). Now considering the imaginary parts in the same equation, **c** is relatively weak (since FMN absorption ~ 0), but **d** is **strong** (since plasmon absorption ≠0). Having these considerations implies that, the chirality parameter ξc(ω) is a result of **a** and **d** contributions, which represent the real part and the imaginary part of the chiral parameter, respectively. Following the principles of Cotton Effect ((absorption + ORD = CD)(described in chapter 5)) and taking in account that `*absorption originates from the imaginary component of the dielectric function*` [7], in addition to the non-zero ORD response for FMN at the plasmonic frequency, indicating by the observed CD peak in plasmonic resonance, it is no way other than assuming that the plasmon resonance itself become chiral, i.e. ($Im[\xi c(\omega)_{plasmon}] \neq 0$)(i.e. **d**); since $Im[\xi c(\omega)_{plasmon}]$ is the only absorbance parameter in the plasmonic area. In Figure (2) below we show the theoretical extinction spectra of the estimated model shown in Figure (1) above. The radius of the gold sphere is R_{Au} = a= 100nm and the radius of the chiral shell is R_{shell} = b = 120, 140 and 200nm. **a** shows the absorption spectra of the gold nanoparticle at ~650nm and the absorption spectra of the chiral shell at ~380nm. Both are very close to the experimental spectra shown in Figure 13b and Figure14a.

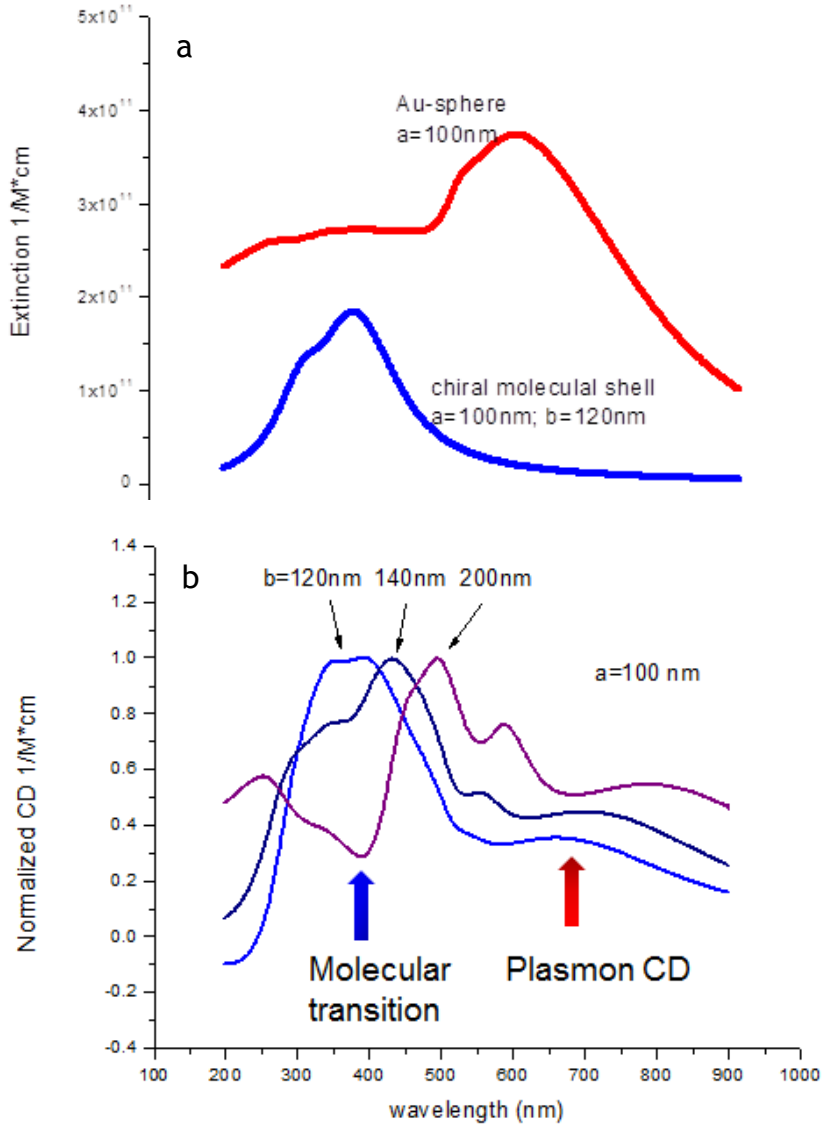

Figure 2: The estimated extinction spectra for the core –shell model shown in Figure 1 above. **a** represents the absorption spectrum of the sphere of gold nanoparticle and the chiral shell with 100nm and 120nm respectively. **b** represents the CD spectra of the same model in chiral radiance shell of 120nm, 140nm and 200nm. Note the plasmon –induced tail at the longer wavelength ~700nm. The complex structure in ~380nm is due to the interference between the plasmonic and the electromagnetic structure. This Figure was taken from reference [6].

4.2.2. Mechanisms

It is believed that chirality might appear on the surface of the nanostructures due to the adsorption of the chiral molecules on their surfaces. This is because adsorption modifies the surface properties and leaves the adsorbance with a distortion state, which optically activates the surface of the nanoparticles [3]. It is also believed that the chirality might appear as a result of electromagnetic interferences from three distinct sources. These are: the electromagnetic field of the incident light, the electromagnetic field of the nanoparticles and the electromagnetic field of the chiral molecules [23]. Thus, three mechanisms, based on several theoretical proposals, have been proposed to illustrate the influence of the chirality (i.e. dynamics of chirality induction) on the nanoparticles surfaces. Yet, without solid experimental evidence, it is impossible to verify a particular mechanism for a particular species [23]. The bespoke mechanisms are:

1. The chirality induction may occur because of coupling, or rather: the `hybridisation`, between the electron wave functions of the chiral molecules and the plasmon of the nanoparticles e.g. chiral system around Au cluster (see Figure6c in chapter 1). This leads to the chiral molecule being `*orbitally hybridised with the electronic state of the nanoparticles in a non-radiative and a covalently binding dynamic*` [24] .Which in turn, leads the electronic state of the nanoparticle surface resonating in a chiral fashion and hence the chirality can be induced [8, (23 – 26)].

2. Another possible mechanism illustrates the chirality induction is the `plasmon-plasmon` interaction. This is a radiative coupling. Herein, an interaction between the chiral plasmonic field of a chiral nanostructures and the achiral plasmonic field of achiral nanostructures is taking place. Thus, optically active building blocks of superstructures are constructed from chiral and non-chiral plasmonic nanostructures [23, 24, 27].

3. An additional mechanism is the dynamic Coulomb interference between a chiral molecule and a plasmonic metal nanoparticle. This is known as a `molecule -plasmon Coulomb interaction`, which is also a sort of a radiative coupling. It occurs as a result of the dipolar (of the chiral molecule) and multipolar (of the nanoparticles) interaction [23,24, (28-30)] .This usually takes place in two electromagnetic field scales. It is either a near-field, which refers to as the dipole- dipole (or multipole) coupling [4, 24, 29, 30]. Or it is a far-field electromagnetic field coupling [6, 23, 28]. The near regime requires a very small distance (d< 10nm) between the objects; this is because the coupling strength between electromagnetic fields decreases rapidly with $1/d^3$. An example of this case is a well-orientated single layer of a chiral molecule surrounding a spherical gold or silver nanoparticle [3,5,6,23,24,31,32[chap.9 pp408]]. Whilst the far-field electromagnetic coupling regime requires a large distance (d>100nm) between the objects, a distance comparable to the wave length of the light; this is because the coupling strength between the electromagnetic fields decreases with 1/d [6, 26, 31, 32[chap.9 pp408,411,412,414]].

As such, it is possible that the mechanism of `molecule -plasmon Coulomb interaction`, which we follow in this project, to be considered as a far-field interaction and is therefore characterised as a long range interaction. Thus, in comparison with the near-field regime; the induction of the chirality supported by the far-field regime is a three order of magnitude more effective in inducing CD in the absorption resonance than the induction of the chirality supported by the near- field one [6]. Another point, unlike the near-field mechanism which is based on a single layer molecular system, the far-field mechanism is based on collective interactions of chiral moleculuar systems, which are used to induce chirality on the surface of the plasmonic nanostructures. The chirality here is influenced as a result of the collective effects coming from the interference of a large number of chiral molecules with plasmonic metal nanoparticles and it is enlarged by three orders with respect to the near-field event [28].

4.2.3. Resonance bands considerations

The electric field of the chiral molecules and the evanescent field of the nanostructures may, or may not, oscillate at the same region of the electromagnetic spectrum. Generally speaking, the electric fields for the majority of biomolecules, such as proteins, amino acids, sugars and DNA, resonance strongly in the near UV region, and very weakly in the visible region [23,24,31,33]. However, the evanescent fields for the well-defined nanostructures made out of gold or silver; have plasmon resonances in the Vis-NIR region [6,8,10,23,31,34,35]. As such, it is necessary to select a definite material for a definite mechanism. For example, in chapter 3, we demonstrate a further application for the hybridisation mechanism (1st mechanism above); in which the chirality induction was emphasised through the chirality enhancement, caused by the adsorption of the biomolecules on the surfaces of well-defined nanostructures. Therefore, we used a biomolecule resonating at the same approximate frequency as the plasmonic structure. But the case of the work presented in this chapter, is quite different. Here, we demonstrate an application of the far-field dynamic Coulomb interference (3rd mechanism above), in which chirality is induced through the chirality shifting from the near UV region (i.e. chiral bands region for Flavin mononucleotide (FMN)) to the Vis-NIR region (i.e. plasmon bands region of our nanostructure) to spot CD coming via the chirality induction effect only.

4.3. Experimental work

For this chapter, micro-chips with metamaterials made out of gold, shaped as crosses and deposited on a (25 x 25 x 0.5) mm vitrosile quartz substrate were used, see Figure 3 below. The samples were made by electron beam lithography technique in Glasgow University (see chapter 2). The individual cross had dimensioned of 400nm with 80nm wire width, fabricated in 55nm, 100nm and 130nm gold thickness; with 5nm Ti as an adhesion layer. Each individual cross was surrounded by another four identical crosses with 400nm separation

distances. This gives a single square lattice consisting of (400 x 400) crosses with a periodicity of 800nm. The single micro-chip consists of (20 x 20) single square lattices, to cover a total area of (6.4 x 6.4) mm. (details for all EBL processes are found in chapter 2).

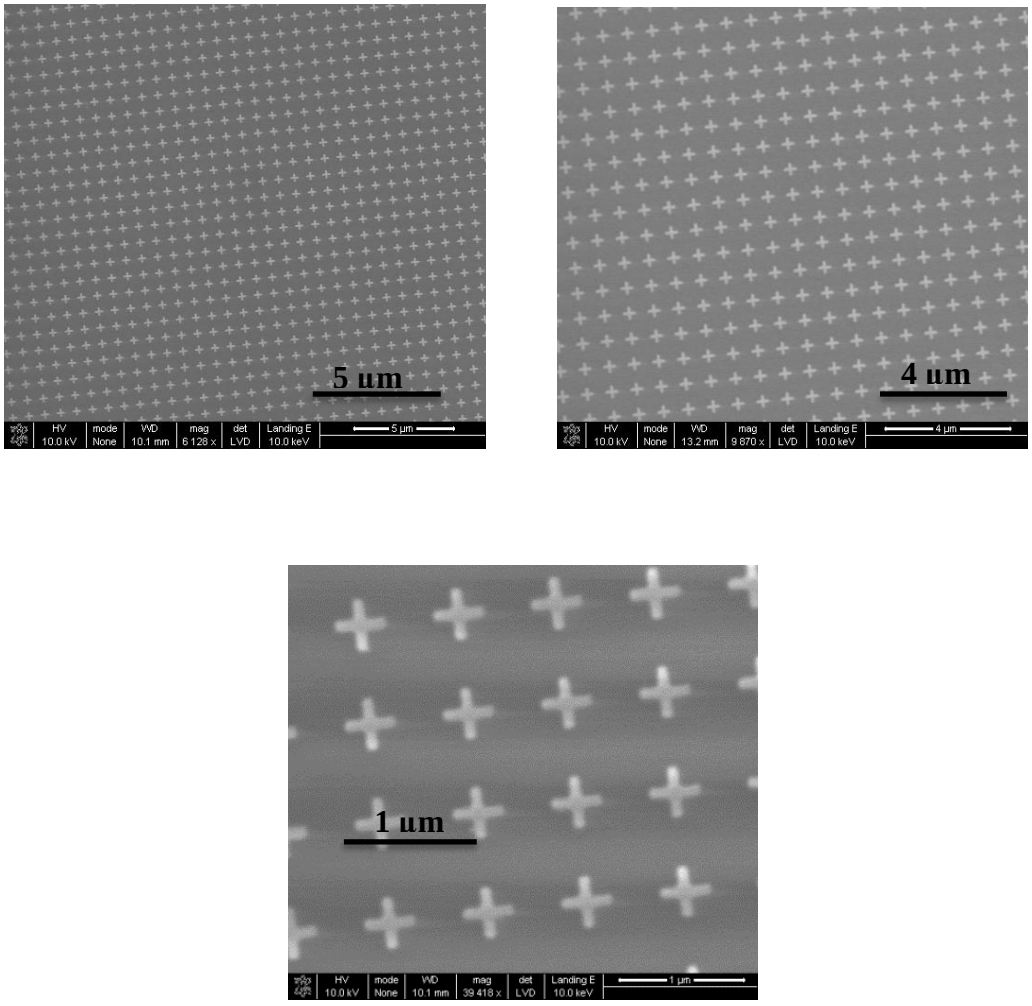

Figure 3: SEM images of an array of gold crosses deposited on a quartz substrate. Each single cross is a 400nm with 80nm wire width. Three different scopes are shown here with their scale bars.

For the chiral molecular layer, we have used the Flavin mononucleotide (FMN) biomolecule. FMN is a biomolecule which shows a strong chiroptical signal in the near UV region. It is also known as Riboflavin monophosphaste. It is characterised as a fluorescent agent and it has a high degree of natural fluorescence when excited by UV light. Thus it can be used for detection and determination purposes [36]. Its chemical structure is shown in Figure 4 below.

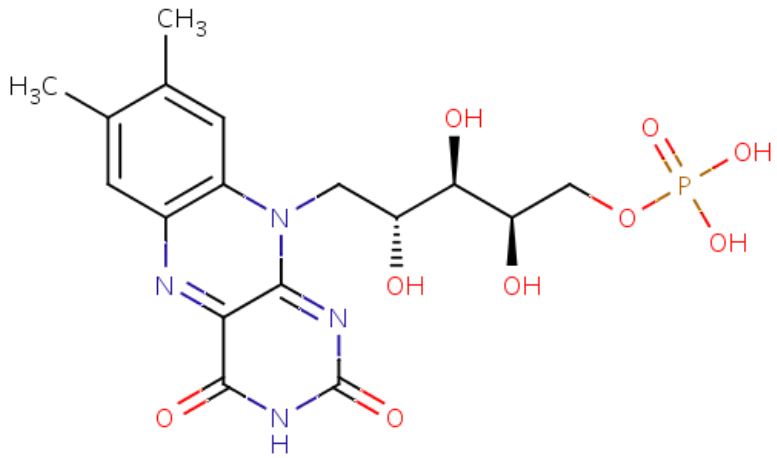

Figure 4: Chemical structure of FMN or the Riboflavin monophosphste. This image is taken from the reference [37]

To deposit a thin film of FMN onto the substrate, we evaporated this film from an aqueous solution of 2.2 mM FMN, similarly to the method used by Sugawara group [38]. Also we replicate Sugawara group strategy to parameterize the FMN film thickness on the surface of the substrate. They used the average molecular surface density (the mass of the FMN per cm^2) which scales with the film thickness on the surface [38]. Thicker films were produced by increasing the volume of the FMN solutions. In addition, the morphology and the heterogeneity of the film were monitored via Atomic Force Microscopy (AFM), see Figure (5) below. This Figure shows AFM images for 70 μl droplet of 1mg/ml FMN deposited on 100nm gold crosses fabricated on quartz substrate. **a** shows a picture of the AFM tip scanning an area of (40x40)μm^2 of FMN on quartz which was evaporated from aqueous solution. **b** shows the real time scanning trace of the sample shown in **a**. The homogeneity of the FMN film could be concluded from the homogeneity of its trace spectrum. Further confirmation for a continuous and homogenous FMN film is presented in Figure (6 (a-d)) below, which shows an AFM

image with a peak of trough roughness of less than 50nm.In this Figure, **a** represents an AFM image of a drop cast FMN film with a surface density of 70 $\mu g / cm^2$ deposited on the surface of the gold crosses. **b**, **c**, and **d** represent the thickness profile of the green, blue and red lines of the **a**, respectively.

We convert the surface density to film thickness by measuring the film thickness with AFM assuming an FMN density of ~ 0.8 g/cm^3. Thus, for 70 $\mu g/cm^2$ film thickness we have got a film thickness of 912 ± 53 nm which is very close to 875nm thickness derived from the estimated FMN density, see Figure (7) below. This Figure illustrates an AFM image and a profile of 70 $\mu g /cm^2$ FMN layer on quartz substrate. **a** represents an AFM image of FMN film, formed by a deposition of FMN droplet next to the abrupt edge. This to allow a well- defined step to be produced in the FMN film, hence, the thickness of the film could be determined precisely. **b** shows the profile of the red line in the image **a**. Clearly, the thickest region of the FMN is the region next to the abrupt area, but this is rapidly tailed off to produce a uniform film with a thickness of 912 ± 53nm.

The optical properties of the samples were investigated through conventional extinction spectroscopy measurements. This involves the absorption and CD measurements for linearly and circularly polarised transmitted light, respectively. Both styles of these measurements were performed simultaneously by JASCO J-810 CD spectrometer in Glasgow University, see Figure (8) below. As it is already mentioned in chapter 3, CD spectrometer detects the differential in absorption of the left and right circularly polarized transmitted light, which occurs when chiral object interacts differently with either. Interestingly, achiral molecules show no resonances at all, which means that any CD signal should be attributed to the presence of the chiral structures [11,15,39]. Most modern circular dichroism instruments, of which the CD-Jasco 810 spectrometer is one, operate on the same principles. Briefly, CD-spectrometer consists of five main elements: *Light source*, *monochrometer*, *sample holder*, *dynamic quarter-wave plate* and the *detector*. Here the instrument control and data processing are handled via `Spectra Manager™ Software` running on the Windows 95 or NT multitasking PC platform. In the CD-Jasco 810 spectrometer, the light source is a 150-W xenon lamp, which is used to produce unpolarised white light, see Figure 9. The unpolarised white light then passes through a monochromator that allows

only monochromatic and linearly polarised light to go through. Then, the light passes through a quarter-wave plate whose optical axis is at 45° with respect to the linear polarisation plane. Unlike a static quarter-wave plate, this is a dynamic quarter-wave plate known as photo-elastic modulator (PEM) which is used to produce right-circularly and left-circularly polarised light switching at 50 kHz. The PEM is a piezoelectric element cemented to a block of fused silica which, under certain circumstances, can influence the silica in such a way that it becomes birefringent. A continuous switching turns the silica into a dynamic quarter-wave plate that is able to produce right and left-circularly polarised light. Right and left-circularly polarised light passes through the sample before hitting a detector. If the sample is not optically active, the detector gives a constant spectrum, otherwise, it gives a non- constant spectrum i.e. a spectrum which shows a difference in intensity between the two circular polarisations, referred to as vAC (voltages Alternating Currents), see Figure 9. The average variations of light intensity, referred to as vDC (voltages Direct Currents), can then be used to calculate the circular dichroism signal by dividing the vAC component by the vDC [40]:

$$\mathrm{CD} = \left(\frac{\mathrm{vAC}}{\mathrm{vDC}}\right) \times \mathrm{G} \quad \text{..... 16}$$

Where G is a calibration-scaling factor to provide either ellipticity or differential absorbance.

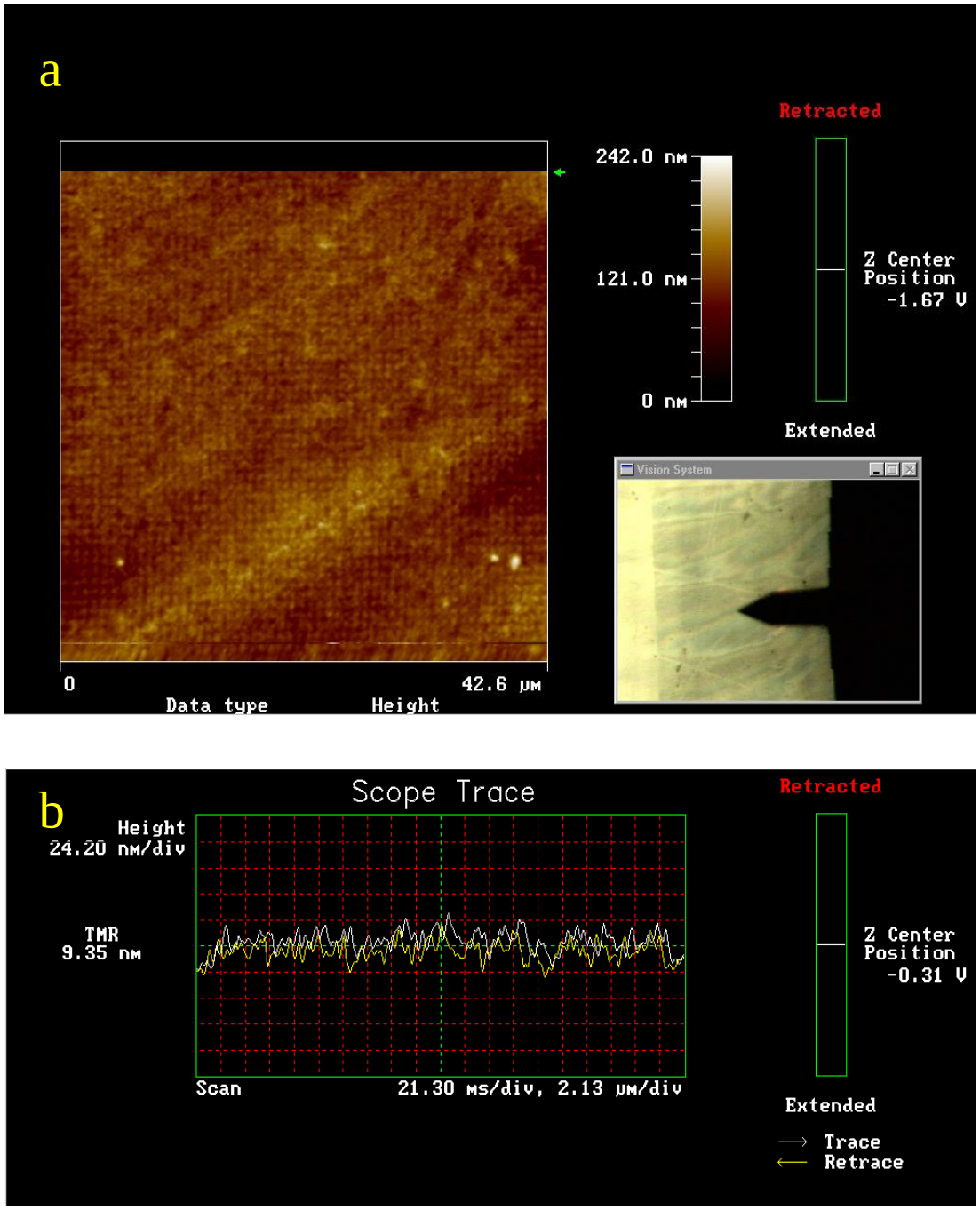

Figure 5: AFM images for 70 µl droplet of 1mg/ml FMN deposited on 100nm gold crosses fabricated on quartz substrate. **a** shows a picture of the AFM tip (on the bottom right corner) scanning an area of (40x40)µm^2 of FMN on quartz (image on the left) which was evaporated from aqueous solution. **b** shows the real time scanning trace of the sample shown in **a**. Note the homogeneity of the FMN film which we concluded from the homogeneity of its trace spectrum.

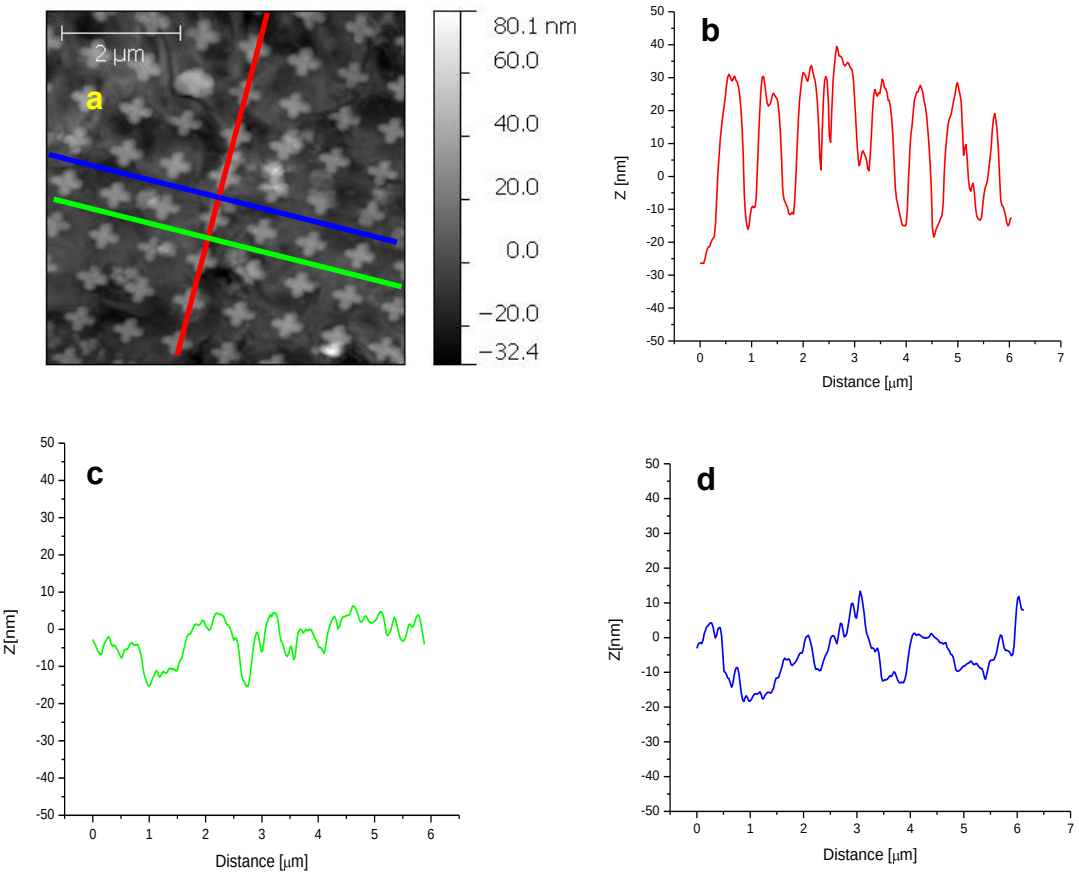

Figure 6: This Figure illustrates the homogeneity of the FMN film deposited on the surface of the sample. **a** represents an AFM image of a drop casted FMN film with surface density of 70 µg / cm^2 deposited on the surface of the gold crosses. **b**, **c**, and **d** represent the thickness profile of the green, blue and red lines of the **a,** respectively.

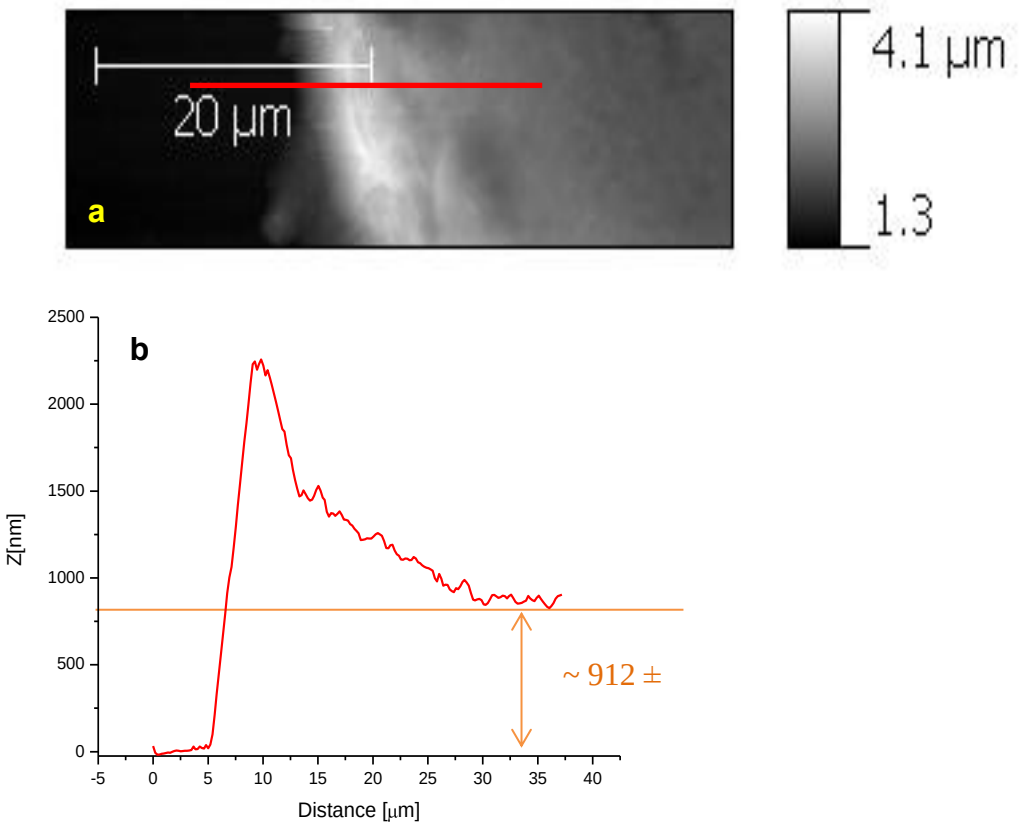

Figure 7: AFM image and a profile of 70 µg /cm^2 FMN layer on quartz substrate. **a** represents an AFM image of FMN film, which was formed by deposition of FMN droplet next to the abrupt edge. This to allow a well- defined step to be produced in the FMN film enabling the thickness of the film to be determined precisely. **b** shows the profile of the red line in the image **a.** Note that the thickest region of the FMN is the region next to the abrupt area, but this is rapidly tailed off to produce a uniform film with a thickness of 912 ± 53nm.

Figure 8: CD spectrometer JASCO-810 which we have used in Glasgow University. It is designed to be operated and controlled by the computer located nearby.

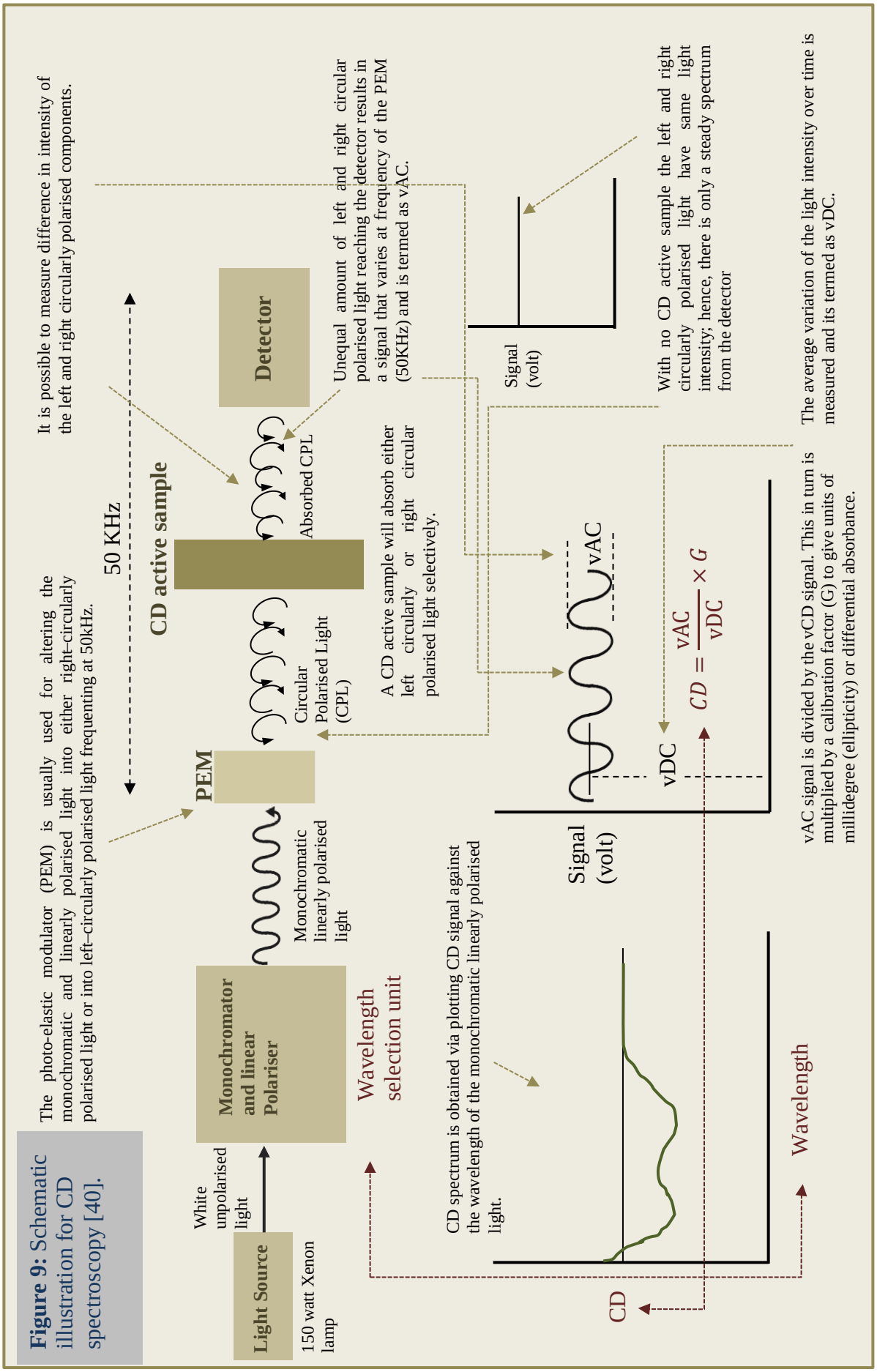

Figure 9: Schematic illustration for CD spectroscopy [40].

4.4. Results

4.4.1. Effect of material optical activity on chirality induction

One of the most important requirements for the radiation coupling model is to use a chiral molecule with high ORD value; otherwise the chiral induction will not occur. This fact was theoretically predicted and then experimentally evidenced. In Figure 10 below, we show a theoretical estimation, carried out by the Govorov group, for the chirality induction raised by different ORD values (given by Re ($\xi c(\omega_{plasmon})$ value) from the spherical-shell model (shown in the same Figure). From this Figure, it is clear that the chirality induction increases proportionally with increasing the ORD values. Therefore, upon considering ß-Lactogloblin (red) and Tryptophan (blue) molecules, which possess small ORD values (i.e. Re ($\xi c(\omega_{plasmon})$) ~ 0) at the plasmonic frequency (~670nm); we see no chiralic induction peak in their CD spectra, see Figure 11 below. However, with FMN molecule, which possesses high ORD value (i.e. Re ($\xi c(\omega_{plasmon})$) ≠ 0) (black) at the plasmonic frequency (~670nm); we note that its chirality induction peak is much bigger than the chirality induction peak for ß-Lactoglobuline (red) and for the Tryptophan (blue), see Figure 14b, and this is why we decided to have FMN as a source of chirality. Having that means, upon using molecules with larger ORD (larger Re ($\xi c(\omega_{plasmon})$) one would expect to see larger chirality induction effect and so forth. Indeed, upon using chlorophyll which possesses higher ORD value in plasmonic frequency than the one for the FMN [6] we have found that the chirality induction peak for chlorophyll is much bigger (~ -8 mdeg for $7\mu gm/cm^2$ on 100nm gold thick crosses, see Figure 12) than the chirality induction peak for the FMN (~ +5 mdeg for $70\mu gm/cm^2$ on 100nm gold thick crosses, see Figure 14b).

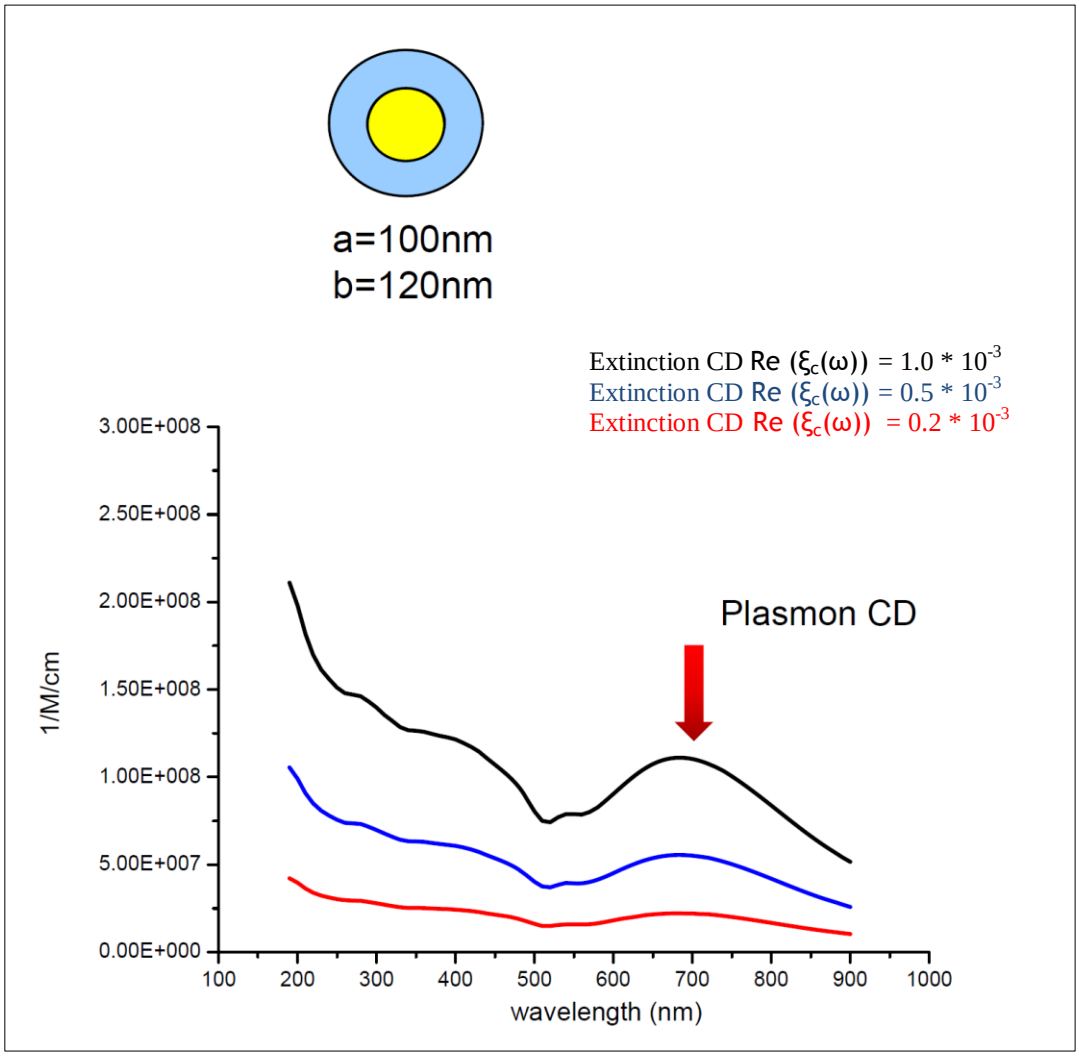

Figure 10: Theoretical estimations for the chirality induction on the surface of spherical-shell model showing the effectiveness of large ORD value on the chirality induction process. Note that CD peak is proportional to the strength of the chirality which estimated here through the real part of the frequency dependent chirality parameter Re ($\xi_c(\omega)$). Red, blue and black lines represent β-Lactogloblin, Tryptophan and FMN molecules, respectively.

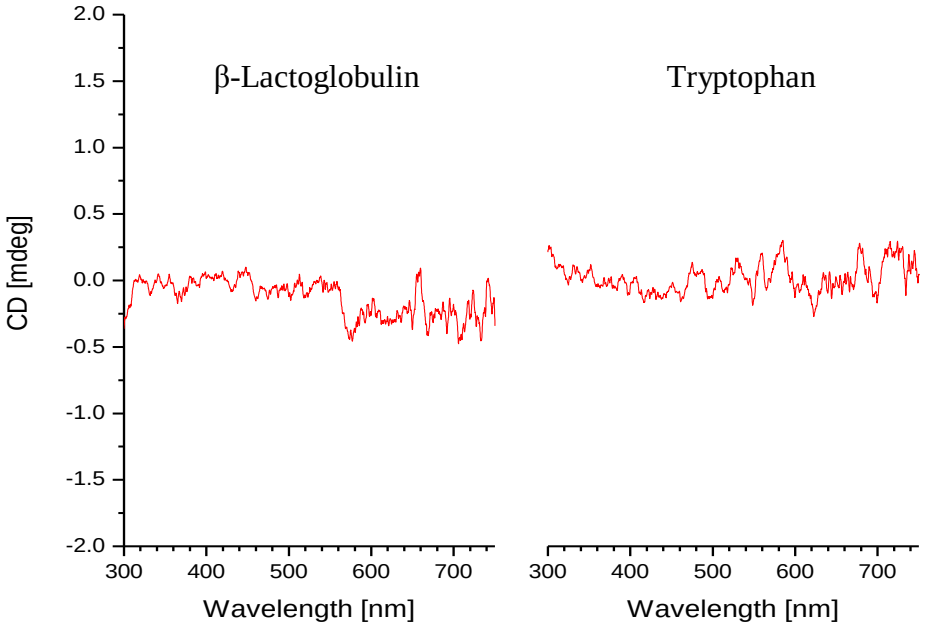

Figure 11: Two CD spectra for chiral molecules with relatively small ORD response. The left and the right panels show the CD spectra for 70µgm/cm^2 film of β-Lactoglobulin and 70µgm/cm^2 film Tryptophan applied on the crosses.

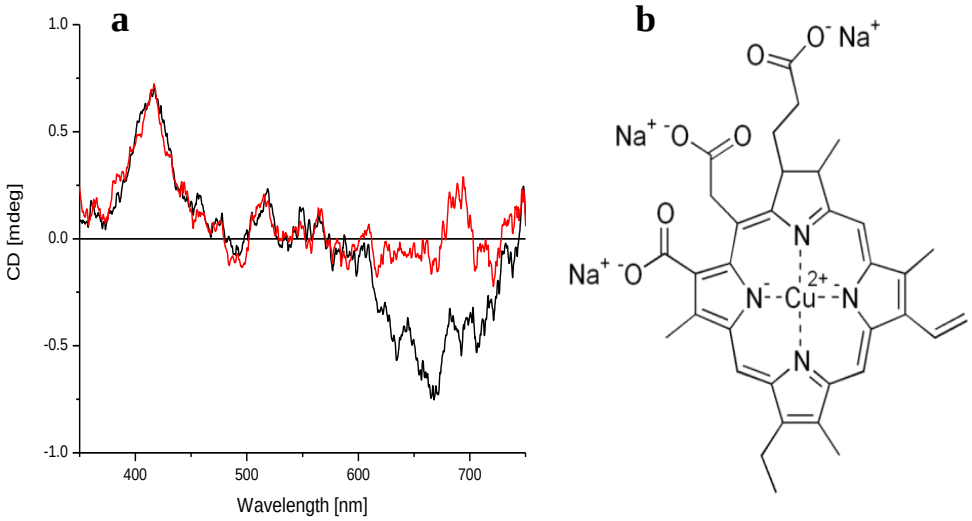

Figure 12: CD spectrum and the chemical formula for the Chlorophyll molecule. **a** represents the CD spectrum for 7µg/cm^2 film deposited on 100nm gold crosses (black) and on a plain glass (red). The cross substrate shows the induction of the chirality into the plasmonic area (~ 670nm). **b** shows the chemical formula of the Chlorophyll molecule which possesses large optical rotation, and hence larger Re (ξc (ω)) than the one for the FMN molecule[41,42] .

4.4.2. Configure extinction spectra for the crosses

We used several types of samples for extinction spectroscopic measurements to evidence our observations. For instance, we collected a number of measurements from the bare crosses, a plain quartz substrate, an FMN film on a quartz substrate and an FMN film on crosses. In Figure 13 below, we show the absorption measurements for the bare crosses. **a** shows the theoretical model and **b** shows the experimental measurements. **a** shows that there are two main plasmonic resonance in the visible region. The plasmon in ~570 nm is caused by plasmon resonance oscillations along the short axis of the cross arms, while the plasmon in ~760 nm is caused by plasmon resonance oscillations across the long axis of the cross arms. The plasmon in the UV region is much stronger than the one in the visible region [6,39]. **b** shows the experimental absorption measurements, which are in good agreement with others results [6, 43]. They are also in a good agreement with the theoretical estimation model in **a**. Regarding the CD spectrum; the sample did not show any differentiation in absorption for the left or right circularly polarised transmitted light. This is expected since the crosses are non-chiral objects.

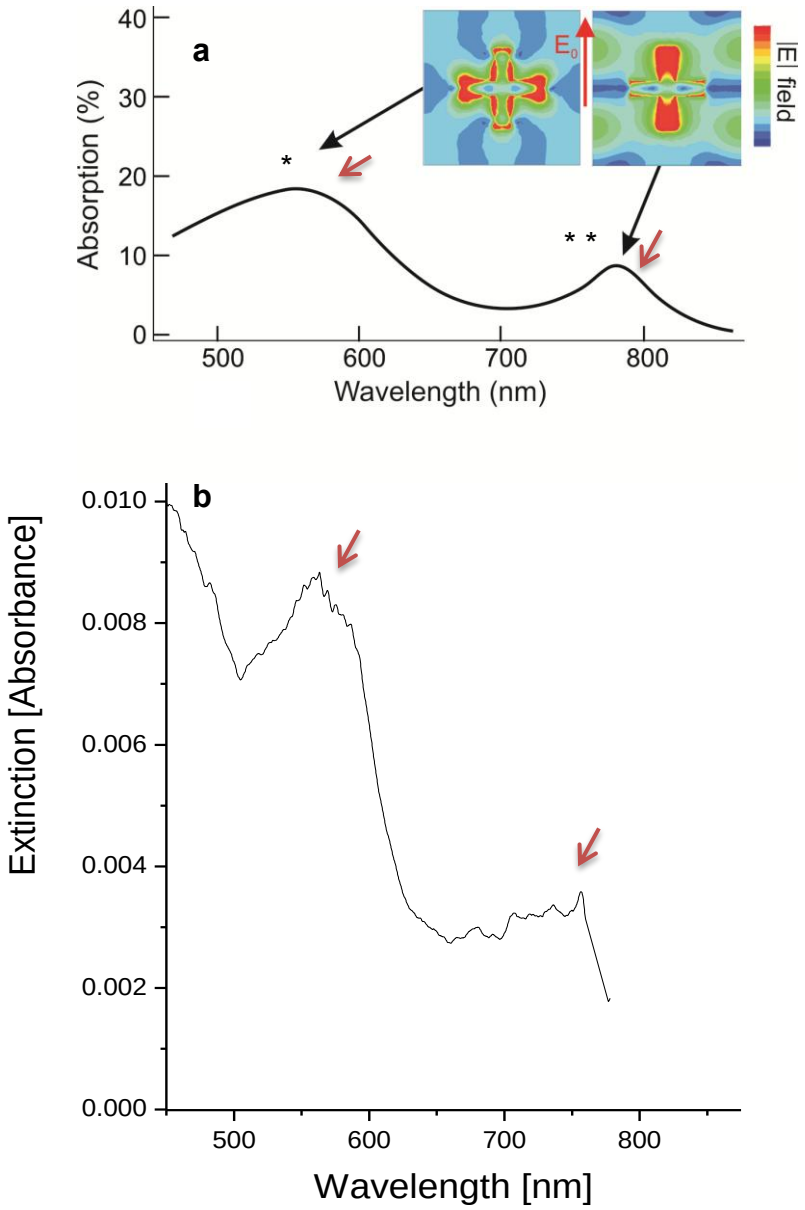

Figure 13: Simulated and experimental absorption spectrum for the bare Crosses on quartz substrate. **a** shows the theoretical electromagnetic model spectrum estimated by the finite element modelling. It represents the time –averaged electric fields of the two plasmon modes. The red area represents a time –averaged field enhancement of eight times the incident field of E_O [41]. **b** shows the experimental absorption spectrum. Note the two main peaks in **a** and **b** of the plasmonic resonance in near UV and in Visible area. The near UV area, at ~570nm, correspond the short axis of the Crosses arms which is much stronger than the longone. Also note the agreement between the theoretical and the experimental results for the peaks pointed with red arrows.

4.4.3. Configure extinction and CD spectra for FMN on quartz and the crosses substrates

In Figure 14 below, we present two types of spectra; these are the extinction spectra in **a** and the CD spectra in **b**, for FMN films deposited on the quartz substrate (red) and on the crosses (black). Both extinction and CD spectra show a strong resonance near the UV region. It is believed that this is caused by molecular electronic transitions [6]. From this Figure, one can see how the molecular resonance in (350-480) nm is identical for the quartz and the achiral crosses; which implies that the molecular resonance intensity is similar on quartz and on crosses for the same surface densities on either. Having that means, there is no significant enhancement for the molecular resonances coming from the plasmon oscillations of the crosses. Fundamentally, it has previously been shown that the enhancement for the molecular resonances occurred if the spectrum of the absorbed molecule is overlapped with the spectrum of the metallic nanoparticles [44]. From Figure 14 (**b**), below, we can see that there is no significant spectral overlap of the gold nanoparticles of the crosses (blue) and the molecular resonance of the FMN (black). Therefore, we would not expect any enhancement for the molecular resonance coming from the metallic plasmon.

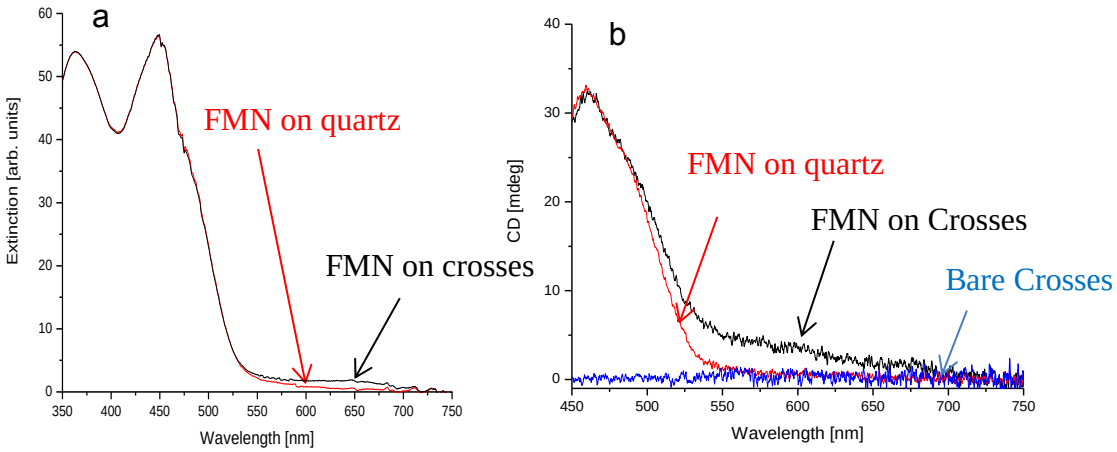

Figure 14: Extinction cross sections for the FMN on the quartz substrate, as well as on the gold crosses. **a** represents the extinction spectra of 70 μg cm^{-2} FMN on quartz substrate (red) and on crosses (black). **b** represents the CD spectra of 70 μg cm^{-2} FMN on quartz substrate (red) and on the crosses (black) . **b** also represents the CD spectrum of the bear crosses (blue). Note the distinct resonances in (350-380) nm which correspond the molecular electronic transitions.

4.4.4. Control measurments

As a control, we have performed measurements in which we replaced the FMN by achiral dyes to prove that the origin of the chiral induction is really coming from a chiral source. We then replaced the crosses by non-plasmonic dye to prove that the chiral induction is enhanced by a plasmonic environment. As such, we performed our measurements with achiral dyes like crystal violet and Rhodamine 6G on the crosses to satisfy the FMN replacement. These dyes have an optical absorption at the same region of FMN resonance, see Figure 15a below. As expected, after the deposition of 70 μg/cm^2 of each, on the surface of the crosses, they showed no CD peaks in their CD spectra. This is shown in Figure 15b below. We also performed measurements with a non-plasmonic dye of crystal violet to satisfy the crosses replacement. Hence, 70 μg/cm^2 of FMN and 70 μg/cm^2 of Crystal violet were both deposited on a quartz substrate (layer after layer). As expected they showed no CD peaks in the plasmonic area, indicating that the chiral induction comes from the plasmonic environment, see Figure 15c below.

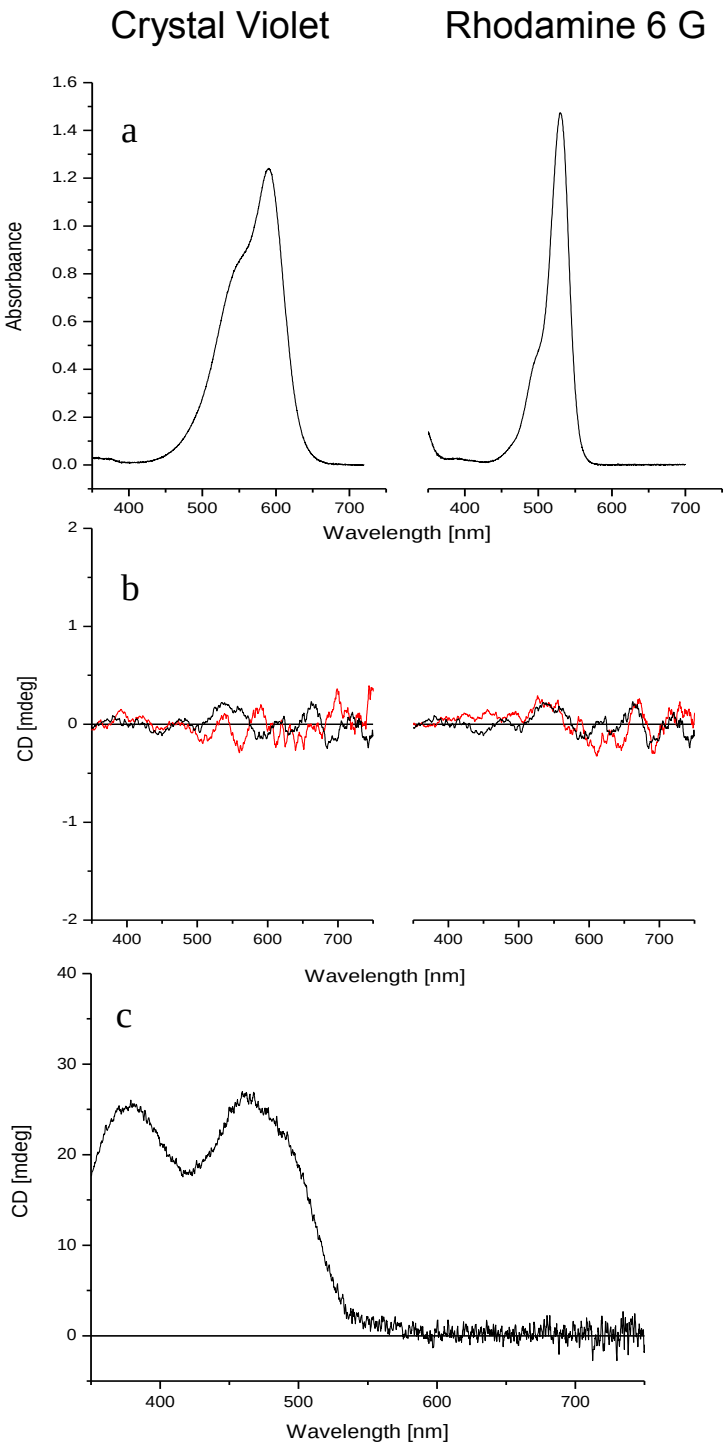

Figure 15: Extinction spectra for the crystal violet and the Rhodamine 6G. **a** shows the absorption spectra of 1mM solutions of the crystal violet and the Rhondamine 6G. **b** shows the CD spectra for a 70µg/cm^2 of crystal violet and Rhandomine 6G deposited on the crosses (black) , also it shows the CD spectrum for the bare crosses (red). **c** shows the CD spectra for 70 µ g/cm^2 of FMN deposited on70 µ g/cm^2 of Crystal violet on quartz substrate. The spectrum is identical to the one shown in Figure 12b.

4.4.5. Configure near-field length scale

Also in Figure 14, and regarding FMN molecular band in the visible region, the extinction spectrum of the FMN film on the crosses shows a broad resonance in the 500-700 nm regions but does not show similar behaviour on the glass substrate. Basically, we know from Figure (13a- pointed with *) that this region corresponds to the plasmonic resonance of the bare crosses on the substrate. Thus, we believe that the FMN film deposition, with a typical dielectric constant to a molecular film ~2 [6], might cause as broad resonance. In particular, the broad resonance is red-shifted in wavelength in comparison with the original one at *, see Figure 13a. For such high dielectric constant, it is reasonable for the plasmon wavelength to be shifted from ~570nm to ~650nm. We have found that the maximum shift for the absorption peak is achieved by FMN surface density of 7 μg/cm^2 which supports ~80nm film thickness, see Figure 16 below. This indicates that the near-field localised surface plasmon falloffs at length scale ~ 80 nm.

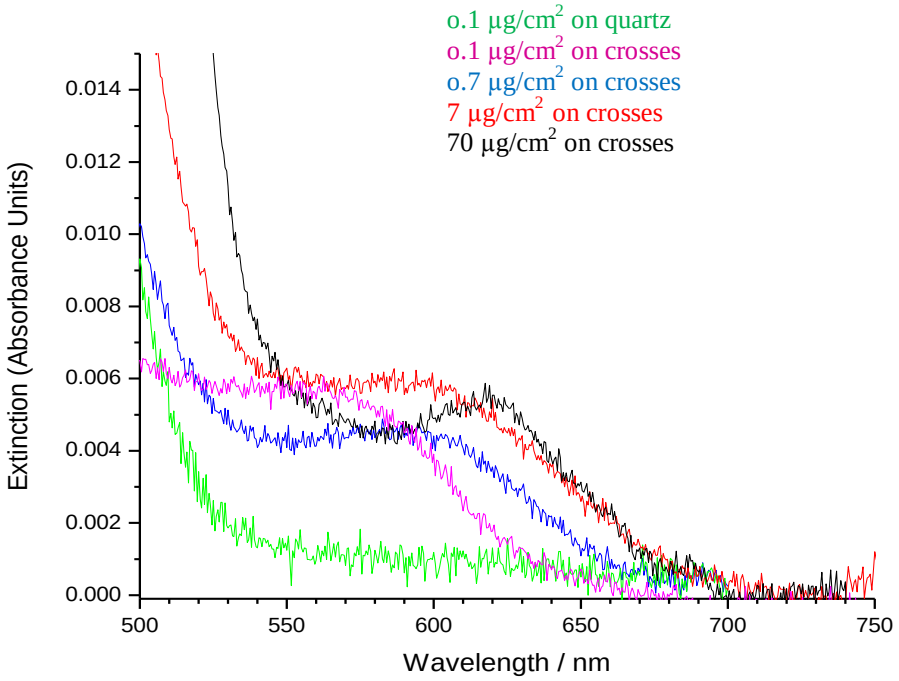

Figure 16: The effect on the extinction spectra causing by different FMN coverage on the surface of the crosses and the plain quartz. The green and the magenta tracks represent the o.1 μg/cm^2 film of FMN on a quartz and crosses substrates respectively. The blue, red and black tracks represent the 0.7 μg/cm^2 (~8nm), 7 μg/cm^2 (~80nm) and 70 μg/cm^2 (~800nm) on the crosses substrates.

4.4.6. Configure FMN coverage densities on the crosses substrate

We have also studied the effect of different FMN coverage densities (and hence different FMN film thickness) that could have on the CD spectra of the crosses. This is shown in Figure 17 below. It is clear that the induced chiral plasmonic peak increases proportionally with the amount of the FMN that is deposited on the surface of the crosses. Clearly, the induced chiral plasmonic peaks are enhanced by the plasmonic fields of the crosses, besides; they stay at the same position, which support our concept about the far field electromagnetic coupling.

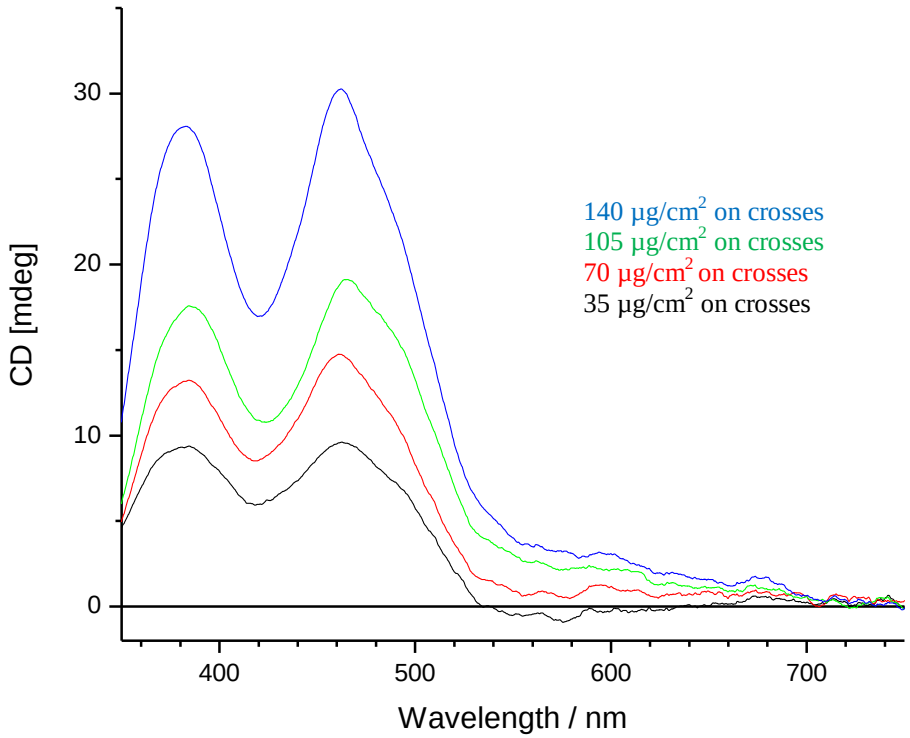

Figure 17: The effect on the CD spectra (i.e. induced chiral plasmonic peak) causing by different FMN coverage densities on the surface of the crosses. The black, red, green and blue tracks represent the 35 µg/cm^2, 70 µg/cm^2, 105 µg/cm^2 and 140 µg/cm^2 respectively.

4.4.7. Anisotropic factor (g factor) considerations

Another way to compare different FMN coverage on different samples is to plot some comparative variations in terms of the anisotropy factor. This is shown in Figure 18 below. The anisotropy factor, termed as a `g ` factor, characterises the strength of the chiroptical response for a particular object, as shown in equation 7 above. In **a** we plot with a g factor of 50nm gold thick crosses against different coverage density of FMN films. We note that the g factor increases as FMN coverage increases. This means that the level of CD induction arises from increasing coverage density of FMN film on the surface. Thus, the maximum induction achieved in the visible region is by the thickest layer of FMN. This is because the g factor approaches an order of 10^{-3} at 570nm wavelength for surface density $\geq$ 70μmg/cm^2 FMN coverage. Indeed, we performed the CD measurement for a single layer of FMN and we got no measurable induction. In addition, we demonstrate the same relation in a different fashion; by showing the effectiveness of the different FMN coverage densities on different substrates. This is shown in Figure 19 below. In Figure 18 **b** we plot a relation driven from panel **a** for the g factor at a wavelength of 575 nm against the coverage density of FMN films. We note that there is a proportional relationship between the g factor and the coverage density of FMN films. In **c** we investigate the effect of 70 μg/cm^2 FMN deposition on different gold thickness of the crosses. We note that as the gold thickness increases, the intensity of the CD peak increases accordingly. Similarly, in **d,** which represents the variations of the g factor driven from **c**, we note that as the gold thickness increases the intensity of the CD peak increases as well, to an order of 10^{-2}. From these four plots, we conclude that in **c** and **d,** as the CD peak intensity increases, its plasmon resonance remains in the same region, since we have the same FMN coverage. Whilst in **a,** as the CD peak increases, its plasmon shifts towards the red wavelengths since we use different FMN coverage density. Another point is the order of g magnitude. The chirality induction arises about ten times by the thickest crosses more than the chirality induction arises by the thickest FMN coverage.

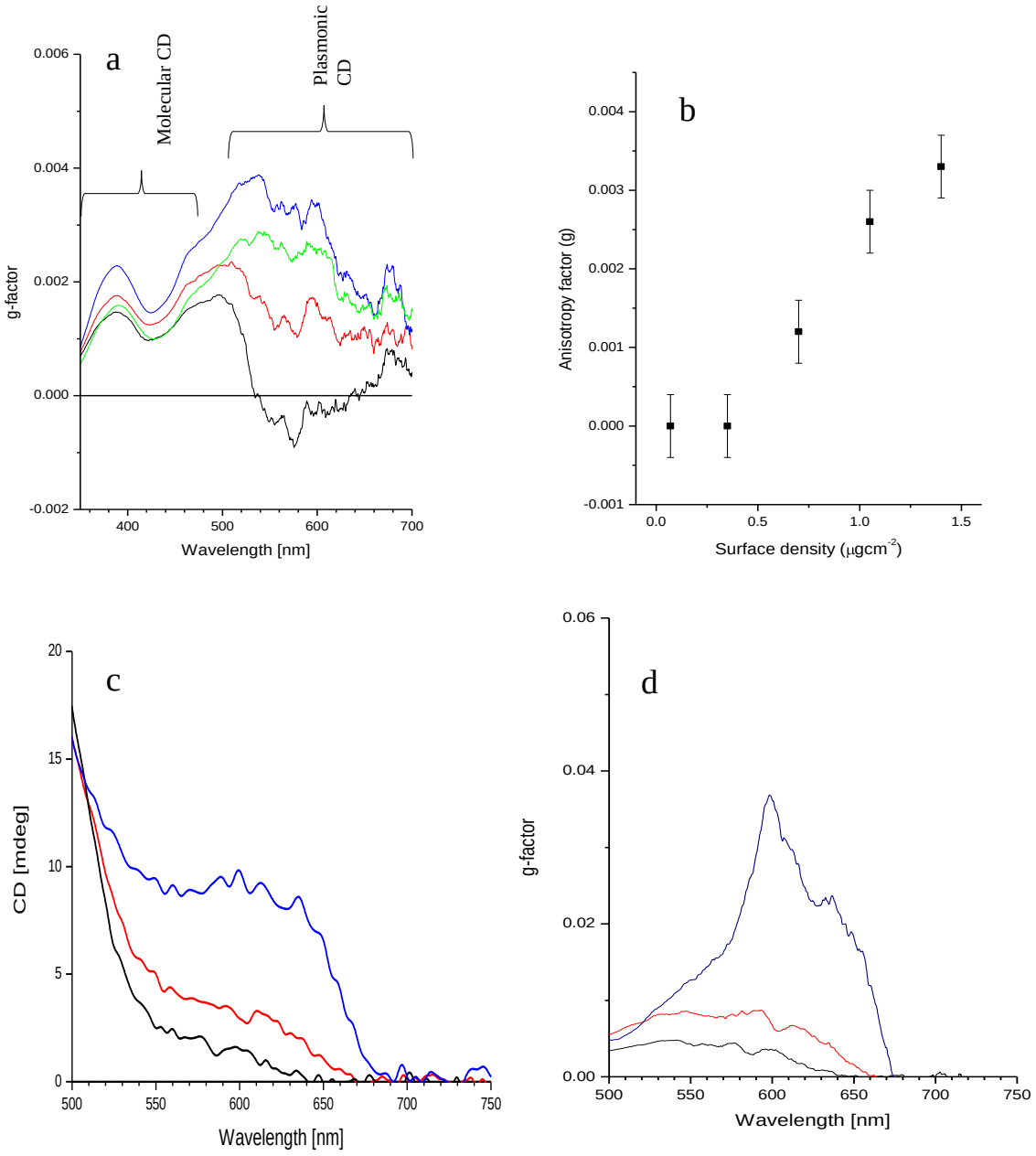

Figure 18: This Figure illustrates different forms of comparisons of anisotropic factor (g) with different variations. **a** represents the g factor derived from CD measurements which is plotted in different wavelengths for different FMN coverage densities. The black, red, green and blue represent the 35 μg/cm^2, 70 μg/cm^2 105 μg/cm^2 and 140 μg/cm2 respectively. **b** represents the relationship between the g factor and the coverage densities at a wavelength of 575nm derived from panel **a**. **c** represents the CD spectra of 70 μg/cm^2 FMN film deposited on different crosses substrates possessing different gold thickness. The black, red and navy tracks represent the gold thickness of 50nm, 100nm and 130nm respectively. **d** represents the g factor driven from **c** and re-plotted with wavelength dependency.

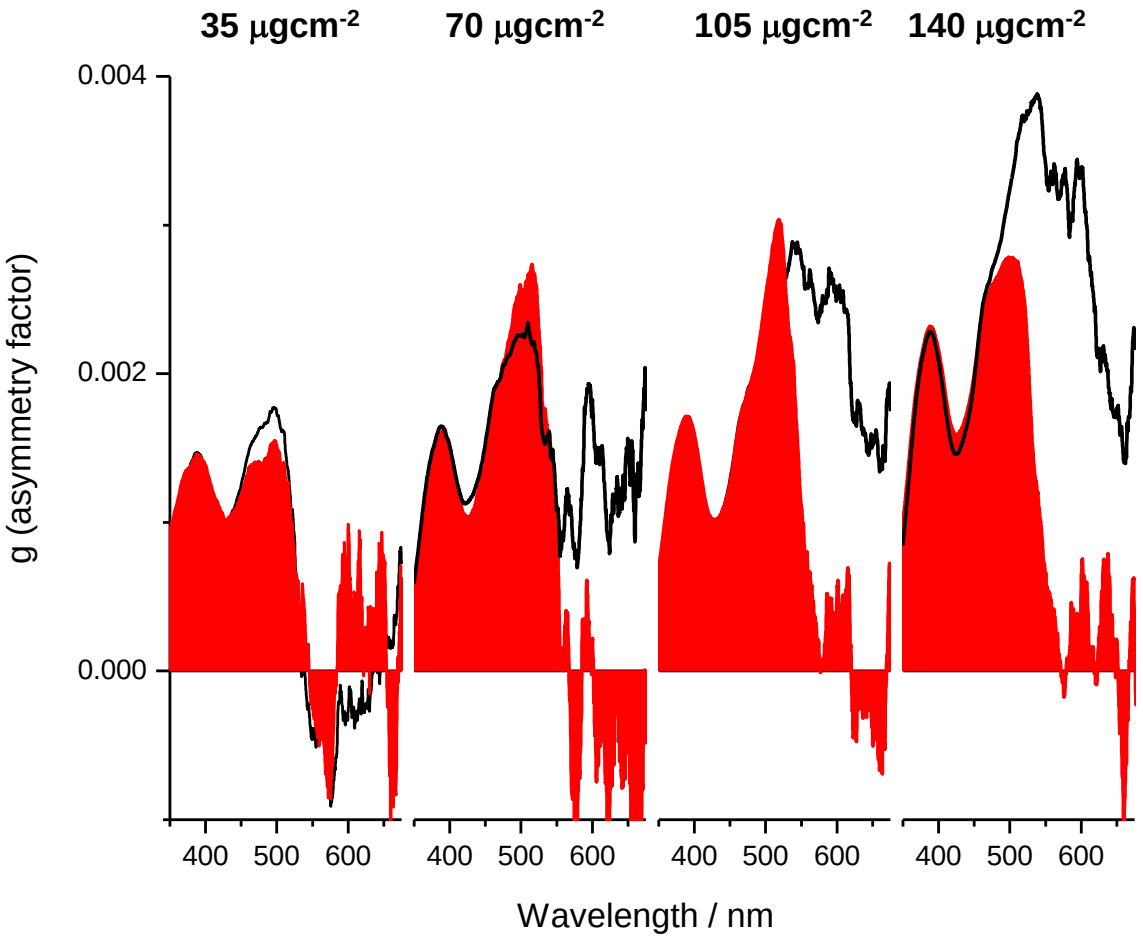

Figure 19: Development of the chirality induction arises as a result of the variation in FMN coverage densities on different substrates. The black expanse represents the g factor shown in Figure 18a above. The red expanse represents the same sense of the black one but with glass substrate instead of crosses.

4.5. Conclusion

We conclude that the chirality can be induced on achiral plasmonic surface via electromagnetic field coupling arising through far field radiative system. Coupling only succeeds with a system consisting of chromophores which possess absorption bands in the UV region of the electromagnetic spectrum and plasmonic surface absorption bands in the visible region. As such, we believe that the physics associated with our model for chirality induction is qualitatively and quantitatively different from the physics associated with the near field dipole–dipole system. This is based on our theoretical model, which shows that chirality induction is a result of the resonant plasmonic nanostructure and is achieved by a different mechanism [6,4,30]. As it already has been mentioned, the plasmon-induced electromagnetic mechanism of CD was estimated by solving Maxwell's equations for the chiral medium deposited on the plasmonic nanostructure. The main difference in the radiation induction mechanism is that the electromagnetic CD is proportional to the thickness of the chiral shell, which implies that the CD peak is actually originated from the large amount of molecules expanding along a distance of the order of λ of the incident light. Thus, the chirality induction is considered to be an accumulative effect, resulting from the formation of chiral plasmon-polariton modes in metal structure covered with a chiral material. The case with dipole-dipole system is fundamentally different, since the chirality induction is originated from molecules in the vicinity of the surface, i.e. laid along only few nanometers from the nanoparticles and hence, chirality induction is raised near the local plasmonic hot spot [6,4,30]. In general, we believe that our method is simple, flexible and offers reproducible results with high level of reliability. The work presented here, which has been published in reference [6], is a pioneering experimental study into far field electromagnetic coupling.

4.6. References

1. Nafie L. A., "Vibrational Optical Activity: Principles and Applications", *John Wiley & Sons, Ltd*, 2011, 1st edition.
2. Singh O.N. and Lakhtakia A., "Electromagnetic Fields in Unconventional Materials and Structures", *john Wiley & Sons, new York*, 2000.
3. Valev V. K., Baumberg J. J., Sibilia C. and Verbie T., *Advanced Materials*, 2013, Vol.25, pp (2517-2534).
4. Govorov A. O., Fan Z. Y., Hernadez P., Slocik J. M. and Naik R. R., *Nano Lett*. 2010, Vol.10, pp (1374-1382).
5. Gérard V. A., Gun'ko Y. K., Defrancq E. and Govorov A. O., *Chem. Commun*., 2011, Vol.47, pp (7383-7385).
6. Abdulrahman N. A., Fan Z., Tonooka T., Kelly S. M., Gadegaard N., Hendry E., Govorov A. O. and Kadodwala M., *Nano Lett.*, 2012, Vol.12, pp (977-983).
7. Kosuda K. M., Bingham J. M., Wustholz K. L. and Van Duyne R. P., *Comprehensive Nanoscience and Technology*, 2011, Vol.3, pp (263-301).
8. Hendry E., Carpy T., Johnston J., Popland M., Mikhaylovskiy R. V., Lapthorn A. J., Kelly S. M., Barron L. D., Gadegaard N. and Kadodwala M., *Nature Nanotechnology*, 2010, Vol.5, pp (783-787).
9. Willets K. A. and Van Duyne R. P., *Annu. Rev. Phys.Chem*, 2007, Vol.58, pp (267-297).
10. Eustis S. and El-Sayed M. A., *Chem. Soc. Rev.*, 2006, Vol.35, pp (209-217).
11. Tang Y. and Cohen A. E., Phys. Rev. Lett., 2010,Vol.104, No.16, pp (163901-163904).
12. Gansel J. K., Thiel M., Rill M. S., Decker M., Bade K., Saile V., Von Freymann G., Linden S. and Wegener M., *Science*, 2009, Vol.325, pp (1513-1515).
13. Schwanecke A. S., Krasavin A., Bagnall D. M., Potts A., Zayats A. V. and Zheludev N. I., *Phys. Rev. Lett.*, 2003, Vol. 91, pp (247404- (1-4)).
14. Kuwata-Gonokami M., Saito N., Ino Y., Kauranen M., Jefimovs K., Vallius T., Turunen J. and Svirko Y., *Phys. Rev. Lett.*, 2005, Vol.95, pp227401(1-4)).
15. Corrêa D. H. and Ramos C. H., *African J. of Biochemistry Research*, 2009, Vol.3 No.5, pp (164-173).
16. Pendry J. B., Science, 2004, Vol.306, pp (1353-1355).
17. Zhang S., Park Y. S., Li J. S., Zhang W. L. and Zhang X., *Phys. Rev. Lett.*, 2009, Vol.102, pp (023901(1-4)).

18. Huray P. G., " Maxwell`s Equations", *John Wiley & Sons, Inc. John Wiley& sons, New Jersey, USA*, 2010, printed dook.
19. Barron L. D., "Molecular Light Scattering and Optical Activity", *Cambridge University press, Cambridge*, 2004, 2nd edition, printed book.
20. Bohren C. F., *Chemical Physics Letter*, 1974, Vol.29, pp (458-462).
21. Bohren C. F. and Huffman D. R., " Absorption and Scattering of Light by Small Particles", *John Wiley and Sons: Weinheim, Germany*, 2004, pp 29, printed book.
22. Bohren C. F. and Huffman D. R., " Absorption and Scattering of Light by Small Particles", *Wiley-VCH Verlag GmbH & Co.KGaA, Weinheim*, 2004, pp287, printed book.
23. Maoz B. M., Chaikin Y., Tesler A. B., Elli O. B., Fan Z., Govorov A. O. and Markovich G., *American Chemical Society, Nano Lett.*, 2013, Vol.13, pp (1203-1209).
24. Govorov A. O., Gun'ko Y. K., Slocik J. M., Gerard V. A., Fan Z. and Naik R. R., *J. Mater Chem.*, 2011, Vol.21, pp (16806-16818) .
25. Gautier C. and Burgi T. J., *Am. Chem. Soc.*, 2006, Vol.128, pp (11079-11087).
26. Kitaev V., *J. Mater. Chem.*, 2008, Vol.18, pp (4745- 4749).
27. Guerrero-Martinez A., Auguie B., Alonso-Gomez J.L., Dzˇolic Z., Gomez-Grana S.,Zinic M., Cid M. M. and Liz-Marzan L. M., *Angew. Chem. Int. Ed.*, 2011, Vol. 50, pp (5499 -5503).
28. Govorov A.O. and Fan Z., *ChemPhysChem*, 2012, Vol.13, pp (2551-2560).
29. Xia Y., Yunlong Zhou Y. and Tang Z., *Nanoscale*, 2011, Vol.13, pp (1374-1382).
30. Govorov A. O., *J. Phys. Chem. C*, 2011, Vol.115, pp (7914-7923).
31. Slocik M., Govorov A. O. and Naik R. R., *Nano Lett.*, 2011, Vol.11, pp (701-705).
32. Jackson J. D., "Classical Electrodynamics", *Wiley: NewYork*, 1998, 3rd edition, printed book.
33. Berova N., Nakanishi K. and Woody R. W., " Circular Dichroism: Principles and Applications", *Wiley-VCH: New York*, 2000, 2nd edition, printed book.
34. Tesler A. B., Chuntonov L., Karakouz T., Bendikov T. A., Haran G., Vaskevich A. and Rubinstein I., *J. Phys. Chem. C*, 2011, Vol.115, pp (24642-24652).
35. Karakouz T., Holder D., Goomanovsky M., Vaskevich A. and Rubinstein I.,Chem. Mater., 2009, Vol.21, pp (5875-5885).
36. Reference of this information is available to view on the web of Protein Data Bank at (cited in 2013): http://www.rcsb.org/pdb/ligand/ligandsummary.do?hetId=FMN

37. Reference of this information available at Reference of this information is available to view on the web of The Drug Bank database at (cited in 2013): http://www.drugbank.ca/drugs/DB00140
38. Sugawara Y., Kelf T. A., Baumberg J. J., Abdelsalam M. E. and Bartlett P. N., *Phys. Rev. Lett.*, 2006, Vol.97, pp (266808 (1-4)).
39. Kelly S. M., Jess T. J., Price N. C., *Biochimica et Biophysica Acta*, 2005, Vol.1751, pp (119-139).
40. An introduction to circular dichroism spectroscopy © 2011 Applied Photophysics Ltd : Registered Company England 1006739. Find this information in the website (cited in 2014):

    http://www.photophysics.com/tutorials/circular-dichroism-cd-spectroscopy

41. Numerical simulations of electromagnetic fields were performed using a commercial finite-element package (Ansoft HFSS, version11.0) with a mesh size of 4.0 nm. Permittivity values for gold were taken from reference 42.
42. Palik E. D., "Handbook of Optical Constants of Solids", *Academic Press: New York*, 1985, printed book.
43. Edmondon D. E. and Tollin G., *Biochemistry*, 1971, Vol.10, pp (113-124).
44. Lieberman I., Shemer G., Fried T., Kosower E. M. and Markovich G., *Ange. Chem. Int. Ed*., 2008, Vol.47, pp (4855-57).

Chapter 5: The origin of off-resonance non-linear optical activity of a gold chiral nanomaterial

Abstract

In this chapter, experimental optically active (OA)-second harmonic generation (SHG) measurements (abbreviates to OA-SHG) based on the non-linear optical activity of 2D chiral plasmonic metamaterials will be presented. The nanostructured substrates used in this work consisted of left- and right-handed gammadion-type structures (referred to throughout as either gammadions or gammas), as well as a racemic mixture (50:50 ratio) of both structures. This study demonstrates the capability of OA-SHG measurements, under off-resonance conditions, to predict the microscopic origin of chiroptical SHG signals. The experimental work was based on measuring the dependence of the s- and p-polarised components of the SHG emission on the orientation of linearly polarised light impinging on the sample at an incident angle of 60^{o}. The theoretical treatment employed here, i.e. the plane wave based formalism, is sensitive to the chirality of 2D array of gold nanostructures. It was established that the non-linear optical activity of the chiral plasmonic nanostructures used in this work shares a common origin with that of aligned chiral molecules i.e. electric dipolar excitation. This is despite the fact that the nanostructures are substantially larger (e.g. hundreds of nanometres across) than molecules. This is a surprising finding, since it might have been expected that non-localised higher multipolar excitation (e.g. electric quadrupole and magnetic dipole contributions) would dominate the optical activity of these relatively large nanostructures. As such, this work suggests that the dominance of electric dipole excitation in OA-SHG is a generic phenomenon implies in a length scale spans from the molecular level to hundreds of nanometres. This work also suggests that the plasmonic excitation enhancement is not prerequisite for an intense OA-SHG signal [1].

5.1. Introduction

Second harmonic generation (SHG) is a nonlinear optical phenomenon that occurs when two photons with fundamental frequency of ω combine together to form a single photon of frequency 2ω (i.e. half the wavelength of the incident light). All the second harmonic waves should propagate in the same phase in order to produce intense waves via constructive interference. In addition, according to the dipole approximation (λ >> atoms), SHG is allowed only within non-centrosymmetric materials, whereby the Cartesian coordinates change sign across their inversion symmetry plane [2, 3].

Linear and non-linear optical techniques have been used for several decades to scrutinise the three-dimensional structure of (bio) molecules. Examples of linear optical techniques include CD (Circular Dichroism) and ORD (Optical Rotary Dispersion), while SHG-CD, SHG-ORD, SHG-LD (Linear Dichroism) and SHG-OA (Optical Activity) are examples of non-linear techniques that exploit second harmonic generation [2,4,5], the work in this chapter was based on the latter i.e. SHG-OA (some references including this project refer to it as OA-SHG), which is several orders of magnitude more sensitive than its linear counterpart [2]. SHG is potentially a much more powerful technique for the detection of adsorbed (bio) molecules on account of its sensitivity to surface phenomena. Nevertheless, intense laser pulses are required to generate SHG signals due to the fact that the SHG process itself is inherently weak. This is because the intensity of the second-harmonic field ($I(2\omega)$) is proportional to the square of its amplitude ($E(2\omega)$), see equation 20 [6, 7].

SHG-based optical techniques are increasingly being used as sensitive tools to probe surface chirality, especially those associated with the metallic surfaces such as metamaterials. These include artificial chiral plasmonic nanostructures which may negatively refract light or as act as broad band polarisers as well as many other applications [8-10]. As the capability to manufacture high resolution nanostructures has advanced in recent years, the non-linear optical properties of these chiral plasmonic metamaterials has become an attractive area for study, and especially those associated with SHG spectroscopy like, such as OA-SHG [11]. The OA-SHG phenomenon has been used via a number of methods to probe

materials with chiral structures such as biological molecules [12,13, 14-18]. Also, it has been used to study the capability of chiral adsorbates to convey chiral perturbations upon the electronic structure of achiral metal surfaces via specific adsorption geometry arrangements, where at least three non-equivalent groups are in close proximity to the surface [19-21]. However, only a few studies have investigated the OA-SHG generated by the chiral metamaterials and these studies have involved sensing the chirality of the structure rather than investigating the origins of their non-linear optical activity [5,11, 22-31]. This chapter addresses the origin of the non-linear optical activity phenomenon displayed by chiral plasmonic nanostructures using the OA-SHG technique under off-resonant conditions. We investigate the optical properties of an array of 2D chiral gold nanostructures, lithographically sculpted into left- and right-handed gammadion-type shapes, as well as a racemic mixture of both.

In principle, the optical activity of the chiral nanostructures originates via different source of excitation, like the electric dipole, the electric quadrupole or the magnetic dipole [32-37]. The electric dipolar excitation dominates the contribution to non-linear optical activity of molecular systems [12]; this aspect has been concluded from the large asymmetry observed in non-linear optical activity of a molecular monolayer [38], and has been verified experimentally [3,39,40] and theoretically [36]. In general, it is typical to refer to the electric quadrupolar and the magnetic dipolar contributions as a single combined multipolar term, since it is not possible to distinguish between them experimentally [3, 9, 10,35, 41,42].

The work in this chapter demonstrates that the non-linear optical activity of our chiral plasmonic nanostructures and the non-linear optical activities of adsorbed chiral molecules originate via the same source, namely the *electric dipolar excitation*. As mentioned above, this is expected for molecular chiral media, but it is not expected for the nanostructures since non-localised higher multipolar contributions (e.g. electric quadrupole and magnetic dipole) may be expected to dominate the optical activity, especially the nanostructures are significantly larger and are comparable in scale to the wavelength of the incident light. As such, this work suggests that electric dipolar excitation is a generic phenomenon which is not limited to sub-wavelength molecules and assemblies.

We investigated the microscopic origin of non-linear optical activity displayed by gold metamaterial under off-resonance conditions. The off-resonance conditions means the conductive plasmon electrons remain unexcited, and hence no evanescent field (an electric field oscillating in the vicinity of excited plasmonic electrons (see chapter 2)) will be formed. In principle, the formation of the evanescent field supports the formation of the `Hot Spots` which affects the properties of the surface, and hence, apply strong spatial variations over a length scale of wavelength. This causes the second order susceptibility tensors $\chi^{(2)}$ to be varied across the surface and hence the molecular frame, which assumes homogenous $\chi^{(2)}$, will not be applicable [1].

Practically, in off-resonance conditions the field across the nanostructures (and hence $\chi^{(2)}$) was assumed to be homogenous. Therefore, the *plane wave based formalism* (theoretical treatment used to determine the microscopic origin of off-resonance OA-SHG signal in molecular system) is capable to determine the microscopic origin of the OA-SHG signal coming from our samples.

This chapter consists of four sections. In section 2, we presented general theoretical aspects associated with the SHG signal, as well as general definitions of related terminologies. In section 3, we described our experimental work. In section 4, we presented our results and discussions. We then derived our conclusions in Section 5.

5.2. Theory and background

In this section, some general theoretical aspects of second harmonic generation from surfaces will be described. A comprehensive theoretical description is beyond the scope of the present work, and more details can be found elsewhere [41]. This section begins with a brief description of linear and nonlinear processes. Subsequently, theoretical aspects of second harmonic generation from chiral surfaces will be discussed. Finally, a brief description of the SHG signals arising from plasmonic surfaces is presented.

5.2.1. Linear and non-linear interactions of electromagnetic waves with surfaces

As an electromagnetic wave strikes a polarisable surface, a macroscopic polarisation (P) is induced as a result of the deflection of electrons from their equilibrium positions. The macroscopic polarisation may lead to refraction or reflection of the electromagnetic wave, depending on the strength of the incoming electromagnetic field (E). The interaction between light and matter is described by the constant χ, known as the `susceptibility tensor`. This is expressed by the following equation [43]:

$$P = \varepsilon_o [\, \chi^{(1)}E + \chi^{(2)}E^2 + \chi^{(3)}E^3 \,] \quad \ldots\ldots\ldots\ldots\ldots\ldots\ldots\ldots\ldots\ldots\ldots\ldots\ldots\ldots\ldots\ldots\ldots\ldots \quad (1)$$

When:
P represents the polarisation of the system.
ε_o represents the vacuum permittivity constant = 8.86×10^{-14} As/V.cm (A: Ampere, s: second, V:volt).
$\chi^{(sth)}$ represents the susceptibility tensor of the material in order of s.
E represents the strength of the electromagnetic field.

For an incident electromagnetic field of moderate intensity, the components of the first term only ($\chi^{(1)}$, the first order susceptibility tensor) will dominate the oscillations of the corresponding frequency. This leads to linear phenomena such as Stokes Raman scattering, anti-Stokes Raman scattering and Rayleigh scattering [44]. Whilst for an incident electromagnetic field of high intensity, such as those generated by nano- or femtosecond pulsed lasers, the components of the second ($\chi^{(2)}$, the second order susceptibility tensor) and the third (($\chi^{(3)}$, the third order susceptibility tensor) terms start to contribute significantly to the oscillations at the corresponding frequency. This leads to phenomena such as `second harmonic generation`, which results in the combination of two photons with frequency ω to generate a single new photon with frequency 2ω (see Figure 1b below), in addition to `third harmonic generation` which is the combination of three photons with frequency ω to generate a single new photon with frequency 3ω (see Figure 1c below). In these higher order phenomena, the incident electromagnetic field is physically changed during the interaction, and hence this is why it is considered a non-linear event [2,11,45].

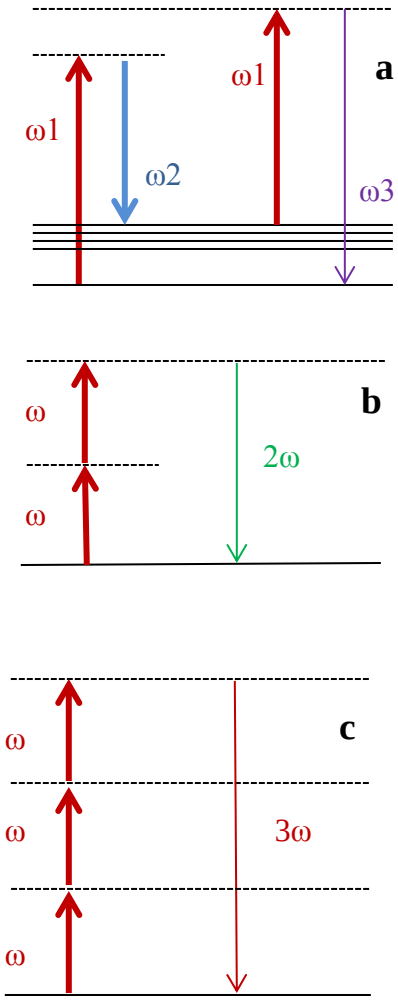

Coherent anti- Stokes Raman scattering CARS

Second harmonic generation SHG

Third harmonic generation THG

Figure 1: Energy diagrams describing various non-linear processes. Thick arrows represent the input energy. Thin arrows represent the output energy that returns the system to the initial state. **a** represents the irradiation of the coherent anti-Stokes Raman scattering (CARS). **b** represents the second harmonic generation SHG which results in the generation of double frequency photons. **c** represents the third harmonic generation THG which results in the generation of triple frequency photons [11, 45, 46].

5.2.2. Theoretical aspects of the second harmonic generation signal from chiral surfaces

Theoretically, it is typical to estimate the SHG signal from a chiral surface from the microscopic response of single molecules, in which the classical wave equation of electron motion is quantified considering the effect of a monochromatic electric field incident with fundamental frequency ω. The electron motion induces a hyperpolarisibility state to the incident electric field; and hence, via averaging this induction over the molecules within the system, one can estimate the macroscopic nonlinear susceptibilities to calculate the SHG signal from the surface. In principle, only the electric field is considered since the magnetic field propagates orthogonally with respect to the electric field vector [41].

It is important to consider the geometry of the SHG signal from the chiral surface. Briefly, three angles should be considered in order to predict the magnitude of SHG signals. These are: θ, γ, and φ, see Figure 2 below [21]. θ represents the angle of the incident vector of the beam ($\hat{k}_i$) on the surface of the sample. θ and ($\hat{k}_i$) are both in the x-z plane, which is considered as the incident plane and it is normal to the surface. The plane of scattering, i.e. the surface, is considered to be the x-y plane, with y axis expands into the plane of the page. The laser beam is incident upon the surface with an original frequency of ω and is reflected with a new frequency of 2ω in the x-z plane; with a propagation vector of ($\hat{k}_r$). The direction of the electric field vector (which can be determined by the right hand thumb rule) is either parallel to the incident plane, referred to as p-polarised radiation, or perpendicular to the incident plane, (parallel to the surface) referred to as s-polarised radiation. Considering p-polarised radiation, γ represents the rotation angle of the fundamental electric field vector ($\vec{E}_{Fp}$) around the electromagnetic field vector of the incident beam ($\hat{k}_i$), see Figure 2b. φ represents the rotation angle of the reflected electric field vector ($\vec{E}_{Rp}$) around the electromagnetic field vector of the reflected beam ($\hat{k}_r$), see Figure 2c. $\vec{E}_{Rp}$ denotes the electric field vector of the SHG radiation. The magnetic field of the incident light is represented by (H), and propagates orthogonally to the electric field (E).

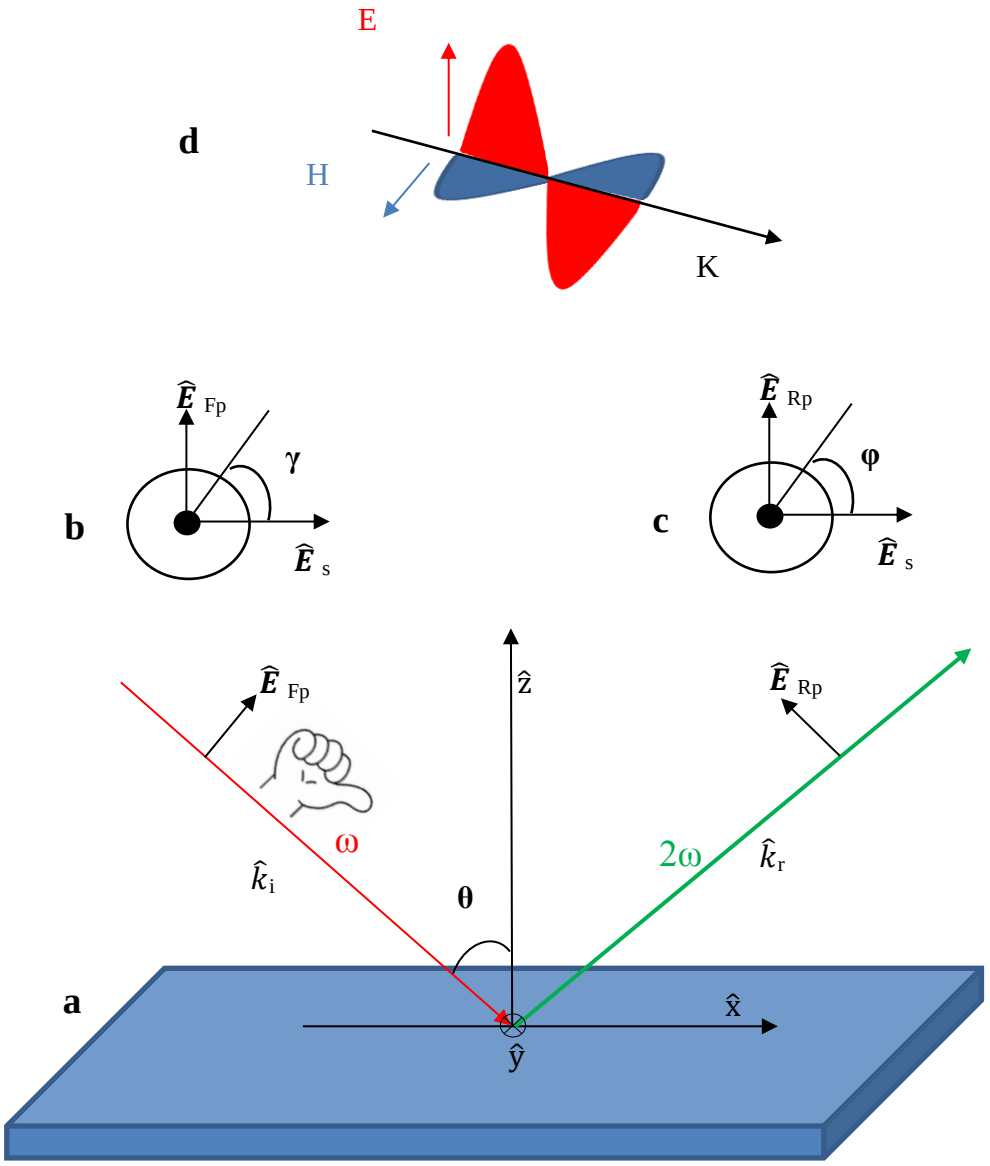

Figure 2: Schematic diagram of SHG from a chiral surface. **a** shows the laser beam striking the surface at θ^o. The beam itself propagates in x-z incident plane with frequency ω. The z-plane is normal to the surface. The propagating incident beam vector is denoted by $\hat{k}_i$. Only the electric field is considered here, and its vector is determined by the right handed thumb rule. $\hat{E}_{Fp}$ refers to the fundamental electric field vector which is polarised parallel to the x-z plane, (**b**). The beam is then reflected from the x-y surface at frequency 2ω and polarisation angle of φ (**c**). The propagating reflected vector is $\hat{k}_r$. $\hat{E}_{Rp}$ denotes the reflected electric field vector which is polarised in parallel to the x-z plane (**c**). y propagates into the page; this is denoted by the crossed circle. **d** denotes the electromagnetic field vector K, which consists of two orthogonal components, the electric field, E, and the magnetic field, H.

Intense incident light effectively induces an electronic polarisation expressed by the following equation [32]:

$$P_i(2\omega) = \chi_{ijk}^{eee} E_j(\omega)\, E_k(\omega) + \chi_{ijk}^{eem} E_j(\omega)\, B_k(\omega) + \chi_{ijkl}^{eeq} E_j(\omega) \nabla_k E_l(\omega) \quad \text{..... (2)}$$

The 2ω and ω refer to the second harmonic frequency and the fundamental frequency, respectively. χ^{eee} represents the susceptibility tensor of the allowed electric dipole. χ^{eem} represents the susceptibility tensor of the electric and the allowed magnetic dipoles. χ^{eeq} refers to the electric quadrupole interactions which include the contribution of the nonlocal electric field gradient $\nabla E(\omega)$. The subscript elements are used to represent the Cartesians of each component in x, y and z directions for the third-rank elements, and similarly but with the addition to the polar vector for the fourth-rank elements.

Also, the generated electric field could be affected to have a state of magnetisation, which is expressed by the following equation:

$$M_i(2\omega) = \chi_{ijk}^{mee} E_j(\omega)\, E_k(\omega) \quad \text{..... (3)}$$

The χ^{mee} represents *the* susceptibility tensor of the allowed magnetic dipoles.

In addition to those, we have also the state of quadrupolarisation:

$$Q_{ij}(2\omega) = \chi_{ijkl}^{qee} E_k(\omega)\, E_l(\omega) \quad \text{..... (4)}$$

The χ^{qee} represents *the* susceptibility tensor of the allowed quadrupolarisation.

From these expressions and considering three terms in *P* (χ^{eee}, χ^{eem} and χ^{eeq}), one term in *M* (χ^{mee}) and one term on *Q* (χ^{qee}), also, considering that the second harmonic field $E(2\omega)$ is a function of the state of the polarisation of the fundamental beam, one would expect the total electric field of the SHG signal to be decomposed as following [17]:

$$E(2\omega) = E^{eee} + E^{eem} + E^{eeq} + E^{mee} + E^{qee} \quad \text{..... (5)}$$

The magnitude of the second harmonic electric field in OA-SHG experiment can be expressed as [47, 48]:

$$E_i(2\omega) = f_i E_p^2(\omega) + g_i E_s^2(\omega) + h_i E_p\, E_s(\omega) \quad \text{..... (6)}$$

E_p and E_s refer to the electric field vectors polarised parallel or perpendicularly with respect to the plane of the incident beam, respectively. The f_i, g_i and h_i refer to the field coefficients that depend linearly on the components of the susceptibility tensors in i polarised state (i = s- or p-). In order to estimate the origin of the SHG signal, the coefficients f_i, g_i and h_i have been derived; to include the electric dipolar, the magnetic dipolar and the electric quadrupolar contributions [3, 33, 35, 41, 44]. For simplicity, the fourth ranking elements (i.e. l in equation 2) will not be involved here; therefore we will limit our discussion to the following equations:

$$f^{Rs} \propto \sin\theta(-2\chi_{xyz}^{eee}\cos\theta - \chi_{xzx}^{eem} + \chi_{zzz}^{mee}\sin^2\theta + \chi_{zxx}^{mee}\cos^2\theta \pm 2\chi_{xxz}^{mee}\cos^2\theta \quad \text{..... (7)}$$

$$g^{Rs} \propto \sin\theta(\chi_{xxz}^{eem} + \chi_{zxx}^{mee}) \quad \text{..... (8)}$$

$$h^{Rs} \propto \sin\theta[2\chi_{xxz}^{eee} - (\chi_{xzy}^{eem} + \chi_{xyz}^{eem})\cos\theta \pm 2\chi_{xyz}^{mee}\cos\theta) \quad \text{..... (9)}$$

$$f^{Rp} \propto \sin\theta(\chi_{zzz}^{eee}\sin^2\theta + \chi_{zxx}^{eee}\cos^2\theta \pm 2\chi_{xxz}^{eee}\cos^2\theta - \chi_{zxy}^{eem}\cos\theta \pm \chi_{xzy}^{eem}\cos\theta + 2\chi_{xyz}^{mee}\cos\theta \quad \text{..... (10)}$$

$$g^{Rp} \propto \sin\theta\left(\chi_{zxx}^{eee} - \chi_{zxy}^{eem}\cos\theta \pm \chi_{xyz}^{eem}\cos\theta\right), \quad \text{..... (11)}$$

$$h^{Rp} \propto \sin\theta\,[\pm 2\chi_{xyz}^{eee}\cos\theta + (\chi_{zzz}^{eem} - \chi_{zxx}^{eem})\sin^2\theta \pm (\chi_{xzx}^{eem} + \chi_{xxz}^{eem})\cos^2\theta - 2\chi_{xxz}^{mee}] \quad \text{..... (12)}$$

R_s represents the reflected light in the s- polarisation state and R_p represents the reflected light in the p- polarisation state. The terms χ^{eee}, χ^{eem} and χ^{mee} are

usually determined by the orientation average of all the relative molecules on the surface, in which each one is characterised by the molecules hyperpolarisability factors represented by: α_i, β_i, γ_i, δ_i and ε_i (these will be defined later). The upper and lower signs of $\pm$ correspond respectively to +45° and -45° linear polarizations with respect to the p-polarized direction. The subscript elements appearing in equations 7-12 are used to represent the second order susceptibility tensors of the material, which are represented by the 27 elements shown below:

$$\begin{pmatrix} xxx & xyy & xzz & xyz & xzy & xzx & xxz & xxy & xyx \\ yxx & yyy & yzz & yyz & yzy & yzx & yxz & yxy & yyx \\ zxx & zyy & zzz & zyz & zzy & zzx & zxz & zxy & zyx \end{pmatrix} \quad \ldots\ldots\ldots\ldots (13)$$

Some of these elements are associated with chirality, but the others are not. For instance, elements with three different terms, like xyz, reflect the chirality coming from the electric dipole tensor element χ^{eee}. Also, elements with two or more similar terms, like xzx and xxz reflect the chirality coming from the magnetic tensor elements of χ^{eem} and χ^{mee} respectively. In principle, chiral elements are equivalent in magnitude but are different in sign [32, 42].

Theoretically, the majority of these elements approach the zero value, in which the SHG signal disappears, and only a few of them become non-vanishing. This depends on the circumstance surrounding the event, such as the polarisation state of the radiation beam, the incident angle and the material used. Considering the latest, the material refers to the material of the surface i.e. is it metal or molecular layer (?) if either, are they chiral or achiral? Thus, in some cases it might be reduced to 18 elements. For example, in the case of a chiral adsorbate layer, the polarisation state of the incident radiation highly affects the generation of the SHG signal. Hence, if the electric field component of the radiation is p- polarised (which means the electric field vector is parallel to the plane of the incident light i.e. x-z plane) then the magnetic component will be

polarised in the y direction, and vice versa. Therefore, only the following electric dipole elements will be non-vanishing:

$$\begin{pmatrix} 0 & 0 & 0 & 0 & xxz & 0 \\ 0 & 0 & 0 & 0 & -yxz & 0 \\ zxx & 0 & zzz & 0 & 0 & 0 \end{pmatrix} \quad \ldots\ldots\ldots\

Table 1: This table includes the susceptibility tensors and their corresponding Cartesian components. Note some components are chirally sensitive and the others are not. This depends on the symmetry conditions of each tensor in each location on the sample surface.

The susceptibility tensors	The Cartesian components	The chiral components	The achiral components
X^{eee}	zzz zxx xxz xzy	xzy	zzz zxx xxz
X^{mee}	zzz zxx xxz xzy	zzz zxx xxz	xzy
X^{eem}	zzz zxx xxz xzx zxy xyz xzy	zzz zxx xxz xzx	zxy xyz xzy

The electric field vectors of the perpendicular and the parallel elements of the incident field are represented by the E_s and E_p, respectively. This is expressed by the following equations [49, 50 pp167]:

$$E_s = E \sin\theta \quad \ldots\ldots\ldots\ldots\ldots\ldots \quad (16)$$

$$E_p = E \cos\theta \quad \ldots\ldots\ldots\ldots\ldots\ldots \quad (17)$$

Considering $I = E^2$ and by substituting equations 16 and 17 in equation 6, one can derive equation 18 below, which represents the variation of the SHG intensity with the variation of its own transition polarisation states [20]:

$$I_i(2\omega) = E^2(\omega)[|f_i|^2 \cos^4\theta + |g_i|^2 \sin^4\theta + (h_i g_i^* + h_i^* g_i)\sin^3\theta\cos\theta + (h_i f_i^* + h_i^* f_i)\sin\theta\cos^3\theta + (f_i g_i^* + f_i^* g_i + |h_i|^2)\sin^2\theta\cos^2\theta] \quad \ldots\ldots\ldots\ldots\ldots\ldots\ldots\ldots (18)$$

Experimentally, this equation can be simplified by defining the following mathematical expressions of the real coefficients:

$$\alpha_i = E^2(\omega)|f_i|^2, \quad \ldots\ldots\ldots\ldots\ldots\ldots\ldots \quad (18\ a)$$

$$\beta_i = E^2(\omega)(f_i g_i^* + f_i^* g_i + |h_i|^2) \quad \ldots\ldots\ldots\ldots \quad (18\ b)$$

$$\gamma_i = E^2(\omega)|g_i|^2, \quad \ldots\ldots\ldots\ldots\ldots\ldots\ldots \quad (18\ c)$$

$$\delta_i = E^2(\omega)(h_i f_i^* + h_i^* f_i), \quad \ldots\ldots\ldots\ldots\ldots\ldots \quad (18\ d)$$

$$\varepsilon_i = E^2(\omega)(h_i g_i^* + h_i^* g_i) \quad \ldots\ldots\ldots\ldots\ldots \quad (18\ e)$$

Here, the α_i, β_i, γ_i, δ_i and ε_i represent different hyperpolarisation elements which depend on different polarisation transition states. When these tensors are plugged into equation 18 again, the following expression can be derived [51]:

$$I_i(2\omega) = \alpha_i \cos^4\theta + \beta_i \sin^2\theta \cos^2\theta + \gamma_i \sin^4\theta + \delta_i \sin\theta \cos^3\theta + \varepsilon_i \sin^3\theta \cos\theta$$

$$\ldots\ldots\ldots\ldots\ldots\ldots

5.2.3. The SHG signals from the plasmonic surfaces

Excited surface plasmons significantly enhance the SHG signal whether it is localised or propagated [2]. Yet, for the work of this chapter it has been selected a wavelength for the fundamental and the SHG light to be out of surface plasmon resonance i.e. off resonance surface plasmon. Primarily because of the reason we already mentioned in the introduction above. Besides, the excited surface plasmon might support a broad background, and hence decreases the signal to noise ratio i.e. attenuate the SHG signal; this previously evidenced by Martin et.al (Figure 3) [53]. Another reason for this choice of wavelength is to reduce the chance of damage to the sample as previously reported by Verbiest *et al*. [37].

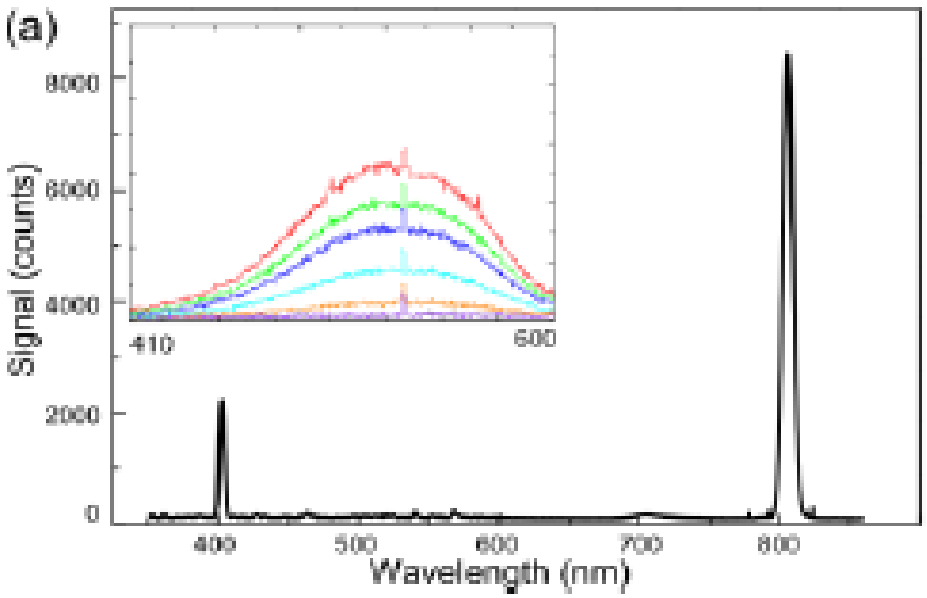

Figure 3: SHG signal profiles of the double resonance antenna (DRA). The main spectrum (black) shows the SHG profile of the fundamental beam. The inset spectra shows the SHG signal overlapped with the resonance of the plasmon. Note as the power increases from 90 mJ to 200mJ the background of the plasmon resonance increases and hence perturbs the SHG signal [53].

5.3. Experimental work

In this section we demonstrate our methodology for the OA-SHG measurements which is based on the non-linear optical activity originating from chiral plasmonic metamaterials. Our methodology was previously applied to chiral molecular monolayer systems [12-21, 32, 54]. A number of chiral nanostructured surfaces were used, namely arrays of left- and right- handed gammadion shapes, as well as a racemic mixture of both structures. We demonstrate the optical activity associated with the off-resonance fundamental and SHG wavelengths.

In the experiments described in this section, the dependence of the SHG emission on the polarisation state of the incident light was measured with the light striking the sample at an incident angle of 60^{o} (thus $\theta = 60^{o}$ all the time). The resulting SH light was either perpendicular (s-) or parallel (p-) polarised with respect to the incident plane x-z. We performed our measurements by rotating the γ angle from zero to cover a full rotation of 360^{o} in 2.5 degree increments. We then measured the intensity of the SHG signals, which are polarised at an angle of φ, as a function of each rotating degree. This is to establish the effect of the γ rotation on the intensity of the SHG signals, which we show with polar plots presented in section 5.4. A pulsed Nd-YAG laser (Quanta Ray Coherent Ltd) was used as the light source. The linearly polarised incident laser beam propagates with a fundamental wavelength of 1064 nm. Each laser pulse has a width of 8 ns and an energy density of 5.3 $mJcm^{-2}$; exposed to an area of ~ 1 cm^{2} on the sample.

It is important to stress that the energy of the laser pulses used in this work was insufficient to damage the samples. This was verified by imaging the nanostructures by SEM microscopy prior to and after the measurements. Some of these SEM images are shown in Figure 4. In this Figure we present six SEM images including both left and right gammadion nanostructures and a racemic mixture of both. In **a** and **b** we show the left handed gammadions after they have been used in the SHG measurements. Similarly, the **c** and **d** we show the racemic gammadions at different size scales. In addition, **e** and **f** we show the right handed gammadions. The scale bar of each image has been shown on its bottom left corner.

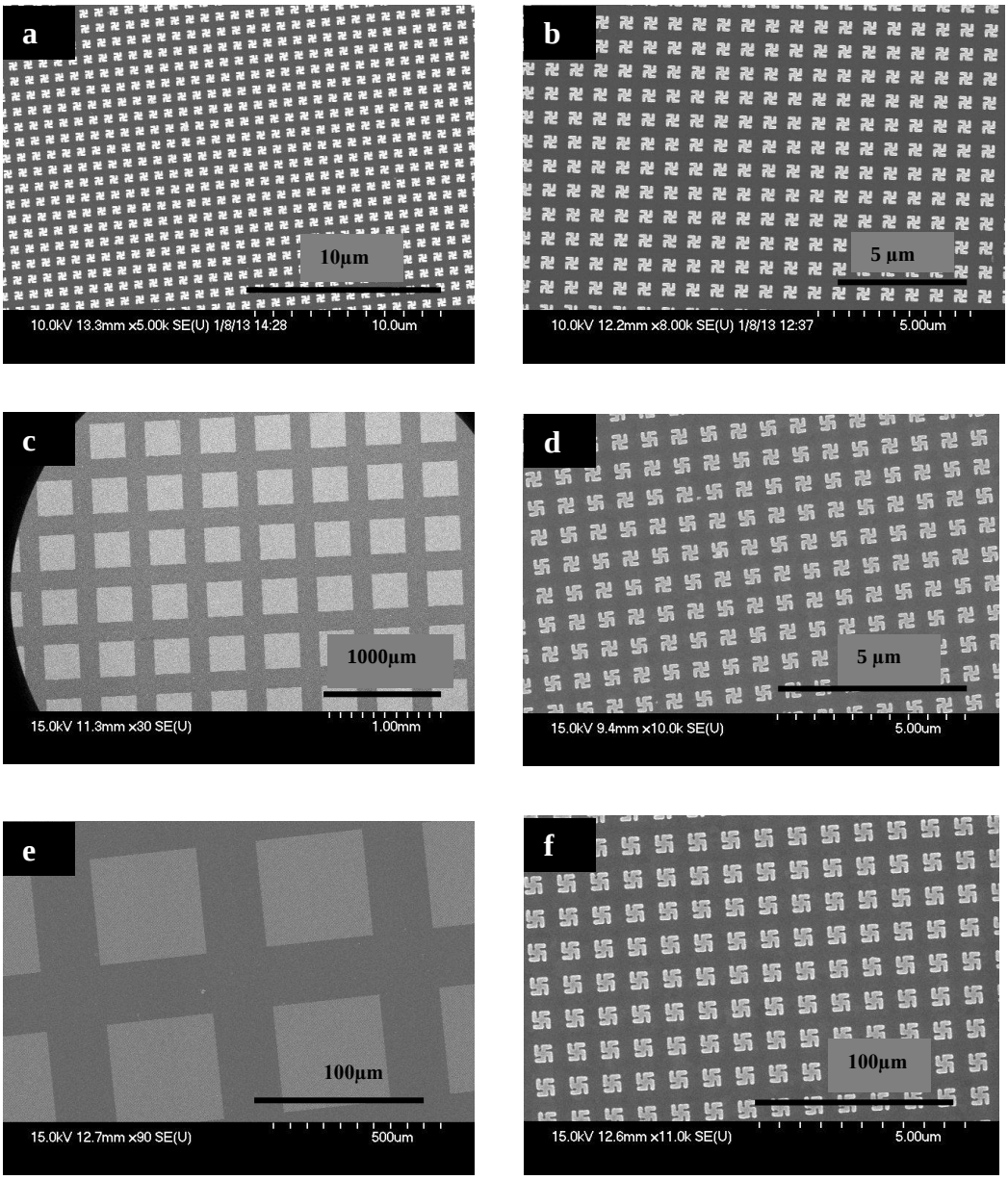

Figure 4: SEM images for the left and right gammadions and a racemic mixture of both after they have been used in the SHG experiment. Scale bars are shown in the bottom right corner of each image. **a** and **b** show the left handed gammadions. **c** and **d** show the racemic mixture. **e** and **f** show the right-handed gammadions.

Finally, the off-resonance conditions was verified by the extinction and ORD spectra (Figure 13) shown in section 4. In the forthcoming subsections (5.3.1 and 5.3.2) details of the samples and the instrumental set-up are described, and are supported by SEM images and photograph pictures.

5.3.1. Sample characterisation

We have used 2D planar chiral metamaterials covered with 60 nm gold film. The metamaterials consist of left-handed gammadion shapes (referred to henceforth as L gammas), right-handed gammadion shapes (R gammas) and a racemic mixture of both (R_4 gammas), see Figure 5 below. The racemic mixture consists of a 50:50 mixture of left and right handed gammadions shapes, and has been used as a control. We also used another control consisting of a 60 nm thick gold layer, without any nanostructured features. For all patterns, each nanostructure was 400 nm in size, with line widths of 80 nm, and periodically replicated every 800 nm in an array of 400 x 400 nanofeatures covering a square of 320 x 320 μm. The whole array of 15x15 squares represents a total area of 4.8 x 4.8 mm^2. In addition, all the nanostructures are made out of gold at 130 nm thick, with a 5 nm Ti adhesion layer, and deposited on a polished silicon wafer substrate. All samples were fabricated by electron beam lithography in the JWNC cleanroom facility at the University of Glasgow.

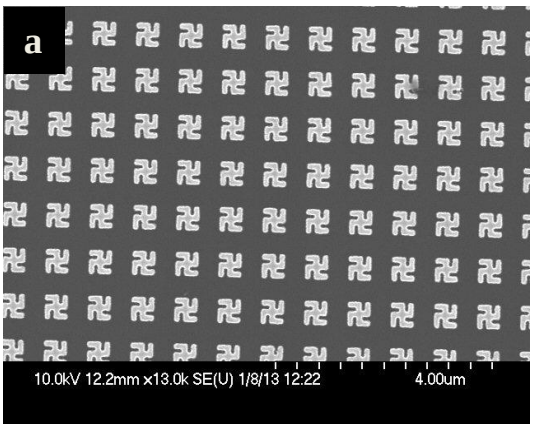

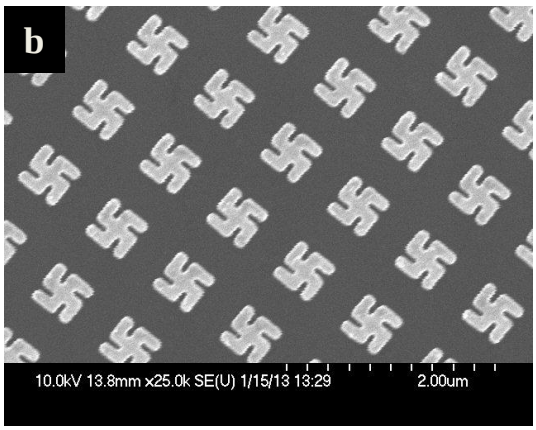

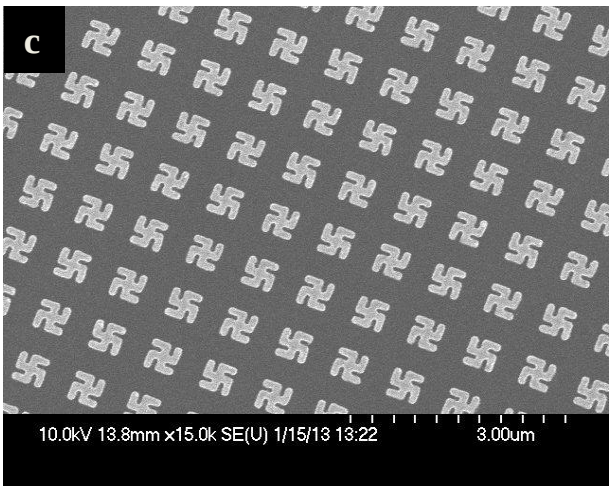

Figure 5 SEM images for the gammas set. **a** represents the left handed gama (L gama), **b** represents the right handed gama(R gama) and **c** represents the racemic gama (R_4 gama). All these samples have been fabricated in JWNC cleanroom/Glasgow University

5.3.2. The optics

The Second Harmonic Generation experiments were conducted using the instrumental scheme shown in Figure 6 below.

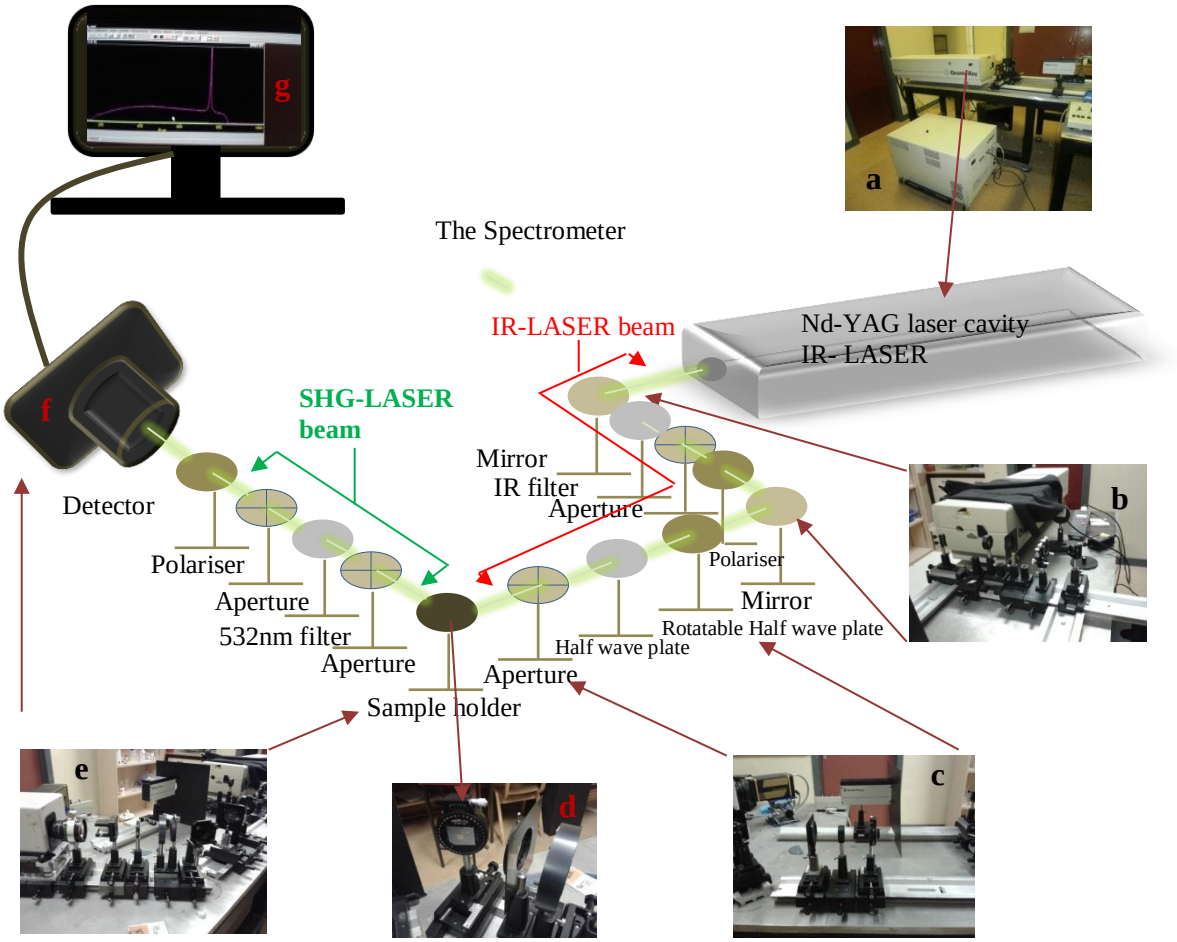

Figure 6: Schematic overview of the SHG instrumental set-up. The instrument comprises three main sections which are described in detail in Figures 7-9. **a** shows a photo of the Nd-YAG laser (1064 nm) cavity. The path of the laser beam is depicted in light green. **b** shows the optics used in the first section of the SHG instrument. **c** shows optics used in the second section of the SHG instrument. **d** shows the sample holder, with the sample substrate attached. **e** shows a photo of the third section of the SHG instrument. **f** shows a cartoon of the detector. **g** shows a photo of a real time SHG signal. Note that the fundamental laser beam (1064nm) is propagates through sections 1 and 2, whilst the SHG signal from the sample (532nm) propagates through section 3 only. The SHG signal was usually detecting by a photomultiplier operating in photon counting mode.

The SHG scheme consists of three main sections. The first section consists of five elements, see Figure 7 below. The first element in the optical path is a high-efficiency mirror which reflects the laser beam at 45°. The second element is a filter which allows only 1064 nm light to be transmitted. The third element is an aperture of ~0.5cm in diameter, which is usually used to align and guide the laser beam. The fourth element is a polariser which was fixed in all experiments, to produce an s- polarised beam. The fifth element is a second mirror, which reflects the beam at 45° toward the second section.

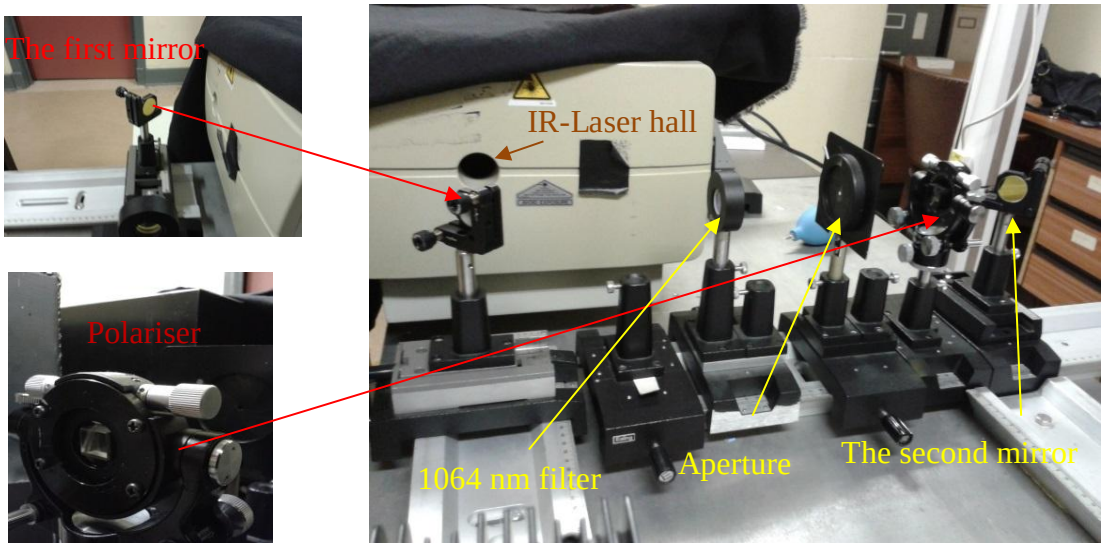

Figure 7: First section of the SHG spectrometer. The 1064 nm laser beam starts its journey from the IR laser hole. The beam is reflected at 45° from the first mirror which faces the hole, and passes through a 1064 nm filter. This is then aligned by the aperture, which guides the beam through the polariser. A second mirror directs to the beam into the second section of the SHG instrument.

The second section consists of three optical elements, see Figure 8 below. The first one is the rotatable half wave plate, which is used to control the polarisation state of the incident beam during the measurements. Each angular increment was 2.5° for an entire 360° rotation. The second element is a mobile half wave plate. This is used to determine the position of the SHG signal on the detector as it generates a strong SHG signal. It is removed when we want to

determine the SHG signal coming from the sample. The third element is another aperture, which helps with the beam alignment.

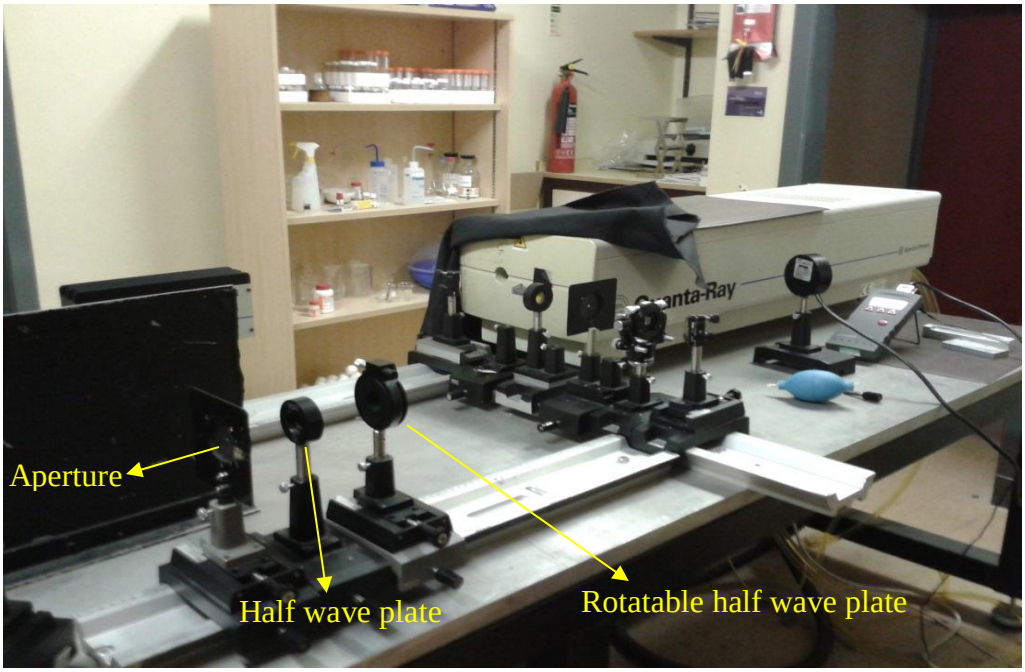

Figure 8: Second section of the SHG spectrometer. After the beam is reflected from the second mirror in Section 1, it passes through a rotatable half wave plate and then a mobile half wave plate followed by another aperture which guides the beam towards the sample and the third section of the instrument.

The third section consists of six elements, see Figure 9 below. The first is the sample holder, which receives and then reflects the laser beam at an incident angle of 60°. The second is another aperture for beam alignment. The third is a filter which allows only the SHG light at 532nm to be transmitted. The fourth is another aperture. The fifth is the analyser, which is set to either (p-) polarisation for P_{out} polarised measurements, or at (s-) polarisation for S_{out} polarised measurements. The final element in the optical path is a series of lenses which help to focus light into the spectrometer. Inside the spectrometer, the SHG light is refracted through a 532 nm grating before passing through a final lens which focusses light onto the CCD camera.

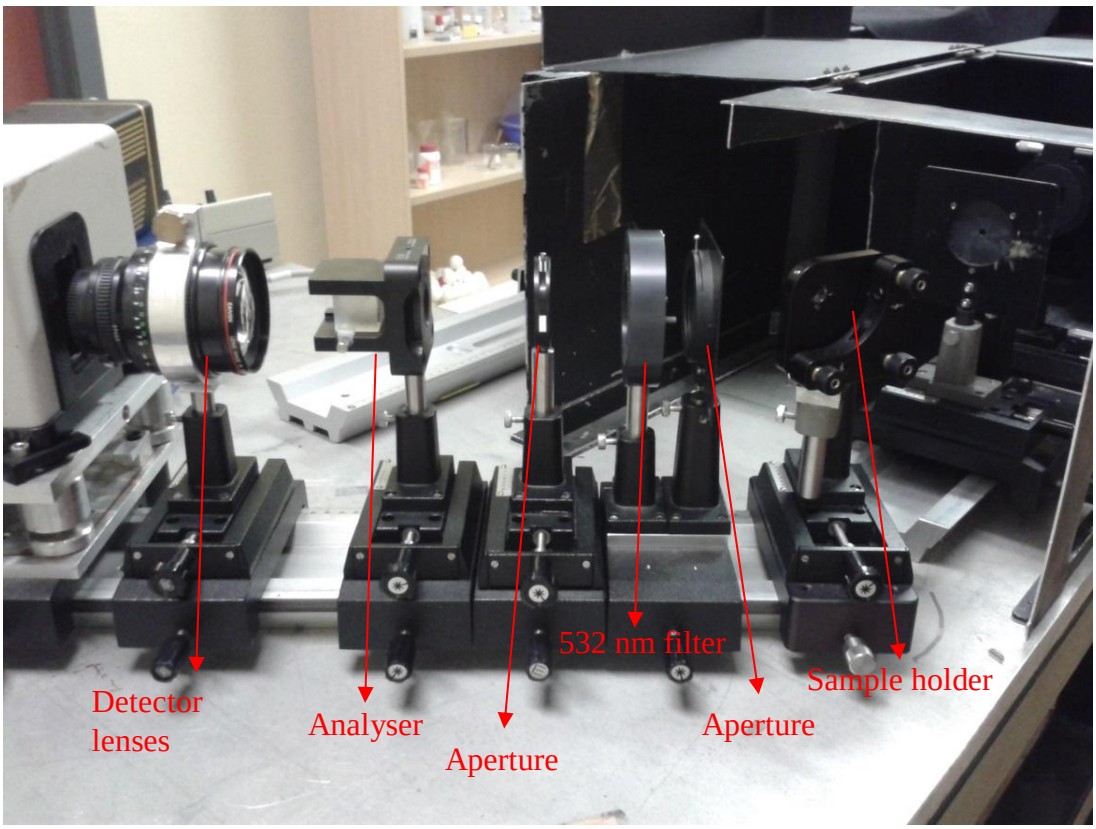

Figure 9: Third panel of the SHG spectrometer. The collimated beam strikes the sample at an incident angle of 60°. Scattered light then passes through aperture followed by a 532nm filter. The 532nm light is guided by another aperture before entering the analyser. Finally, the beam is focused into the spectrograph by a series of lenses. Inside the spectrograph, the light passes through a grating and is focused by another lens on to the detector operating in photon counting mode.

In p-polarised measurements we used a laser power of 3.5-4.5 mJ at a gain of 255 for 400 accumulations. Whilst for s-polarised measurements, we used the same power at the same gain but for 700 accumulations due to the lower intensity of the s-polarised signal.

Room temperature was maintained at 18°C throughout the measurements to ensure that the optical elements remained as stable as possible. Also, because the detector is very sensitive to extraneous photons; the instrument was covered

and the room lights were switched off during the measurements. The complete SHG instrument is shown in Figure 10.

Optical alignments were checked using an IR sensor card. This is shown in Figure 11 in which we demonstrate how we have used the IR laser sensor card to track, and hence align the laser beam. Laser alignment normally took several hours; however it is crucial for such an experiment, since a small mis-alignment could lead to a large drop in the SHG signal.

Figure 12 shows two images which correspond to the sample before (a) and during (b) exposure to the incident of the laser beam. Interestingly, the beam scattered on the surface of the nanostructures only, but not the rest of the substrate, which simply reflects the interference with the plasmon of the gold surface.

Finally, we monitored the power variation of the laser beam during the experiment, and it was fluctuating within a scale of the second digit only, which reflects its stable conditions all the time.

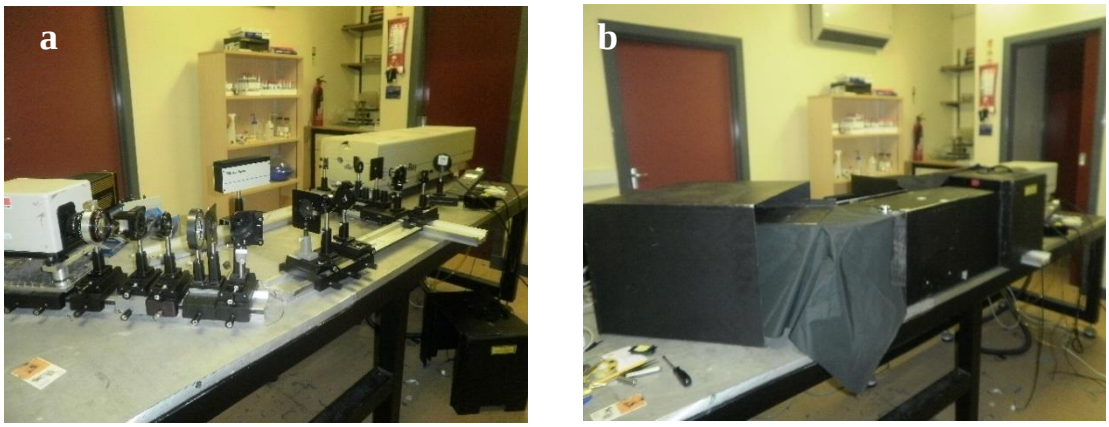

Figure 10: The SHG instrument before (a) and after (b) covering up the optics, which is necessary during the experiment.

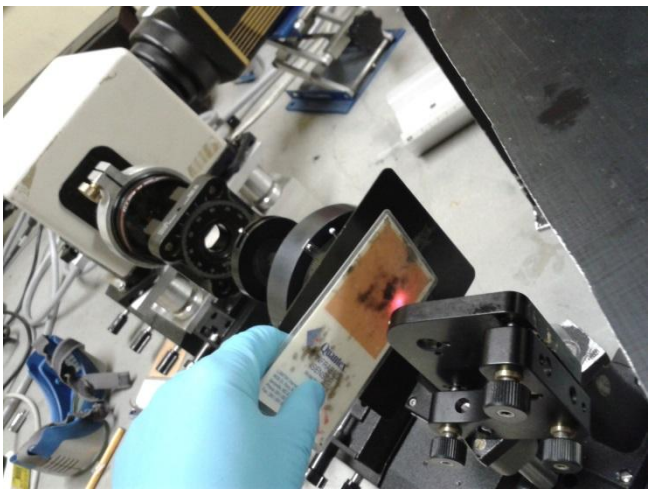

Figure 11: Demonstration of how to use the IR laser sensor card to track the beam during alignment.

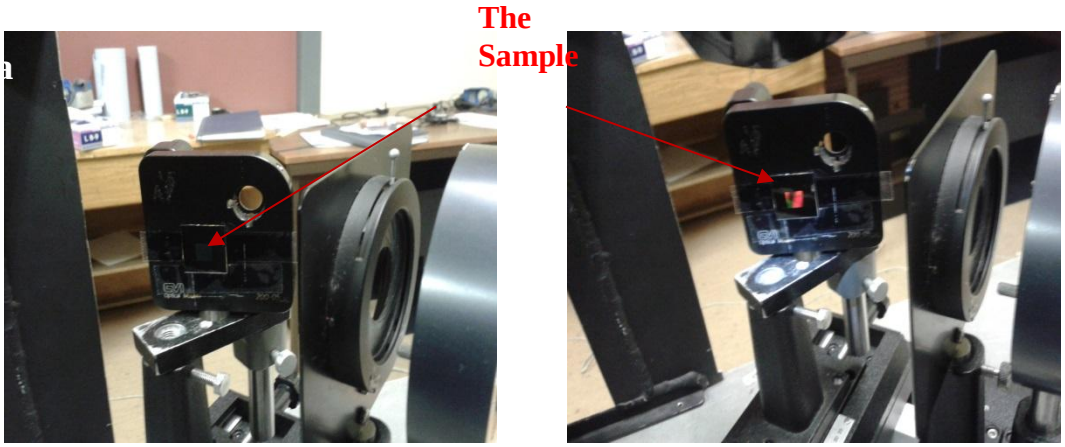

Figure 12: The sample attached to the sample holder. Note the sample before (a) and during (b) experiencing the IR laser beam.

5.4. Results and Discussion

In this section we present our spectroscopic data for S_{out} and P_{out} measurements for the various gammadion sets. Two main issues are discussed in this section, namely the sensitivity of S_{out} and P_{out} measurements towards chirality, and the origin of the SHG signal originating from the samples. The conclusions are derived using the theory presented in section 2 above.

5.4.1. The Off-Resonances Configurations

As mentioned, we chose to perform our measurements at off-resonance conditions of plasmonic nanomaterials. This means, during the measurements the fundamental and the SH energy did not excite the plasmonic mode of the nanomaterial. The off-resonance conditions have been verified by the optical rotation dispersion (ORD) and the extinction (scattering + absorption) spectra, shown in Figure 13 below. These spectra were collected by a member of our group via reflection mode using unpolarised light. In **a,** the ORD spectra for the left and the right-handed gammadions shapes are shown. In **b** the extinction spectrum for the left-handed gammadions shapes is shown. The extinction spectrum in **b** shows two plasmonic peaks: at 623nm and 935nm, which do not overlap with either the fundamental wavelength at 1064nm or with the SHG wavelength at 532nm. However, an intense extinction (~0.8) appeared in 532nm which is comparable with the extinction of the 623nm (~1). We believe that this is attributed to the light scattering rather than plasmonic excitation absorption. This was indicated by the ORD spectra in **b;** which shows chiral asymmetry only at 623nm but not at 532nm. The chiral asymmetry apparent at 623nm is due to *Cotton effect* which is a `*Circular dichroism, together with the anomalous optical rotary dispersion which accompanies it in the absorption region*` [55^{pp6}]. The anomalous optical rotary dispersion peaks occur in the region of the maximum of an electronic absorption band, which represented here by the excited plasmonic electrons, i.e. this indicates CD existence at 623nm which appears only in excited plasmonic resonance. Another indication for unexcited plasmon resonance in 532nm region, is that Hendry et al. [10] have previously

shown a theoretically modelled CD spectrum for similar structure exhibiting excited plasmon resonance at ~ 623nm region, which is in agreement with the spectrum in **b**. Follows that, there is no clear evidence for excited plasmon in 532nm area.

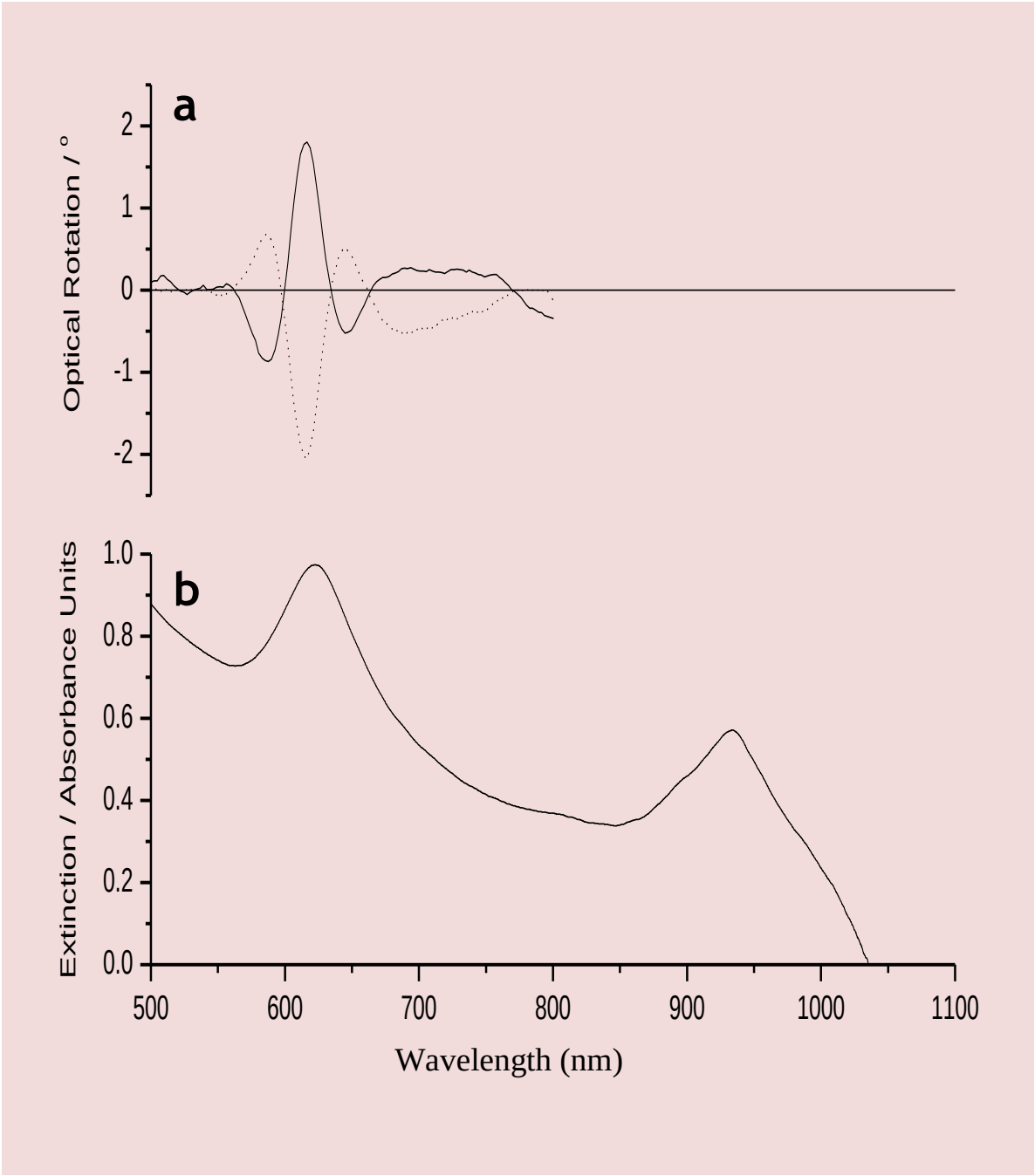

Figure 13: Optical Rotation Dispersion and the extinction spectra for our samples. **a** shows the ORD spectra for the left and the right handed gammadion shapes. **b** shows the extinction spectrum for the left handed gammadion shape.

5.4.2. Samples reference and SHG signal errors configurations

OA-SHG measurements were performed on a substrate of 60nm Au film which we used as a reference for our samples. Its polar spectra are represented by the blue line plots shown in **a** and **b** of Figure 14 below. This substrate has no nanostructures on its surface, however its corresponding samples (i.e. our nanostructures) have check board patterns; and therefore only 50 % of its (i.e. 60nm Au film substrate) total area has been considered. In order to have the spectra of the SHG signal coming from this substrate comparable to the spectra of the SHG signal coming from our nanostructures, the SHG intensity for the 60nm Au film substrate has been reduced by 50 %.

Another important issue to be pointed out is that, in general, the intensity of s-polarised emission is an order of magnitude less than for p-polarised emission. As such, s-out profiles exhibit a greater degree of variation between experiments than p-out profiles. Importantly, the errors associated with the fits for s-emission data are not significantly greater than those for the p-emission data. We concluded this in depending on the error bars appeared in the s-out and p-out profiles, shown in black font bars in Figure 14 **a** and **b**, respectively.

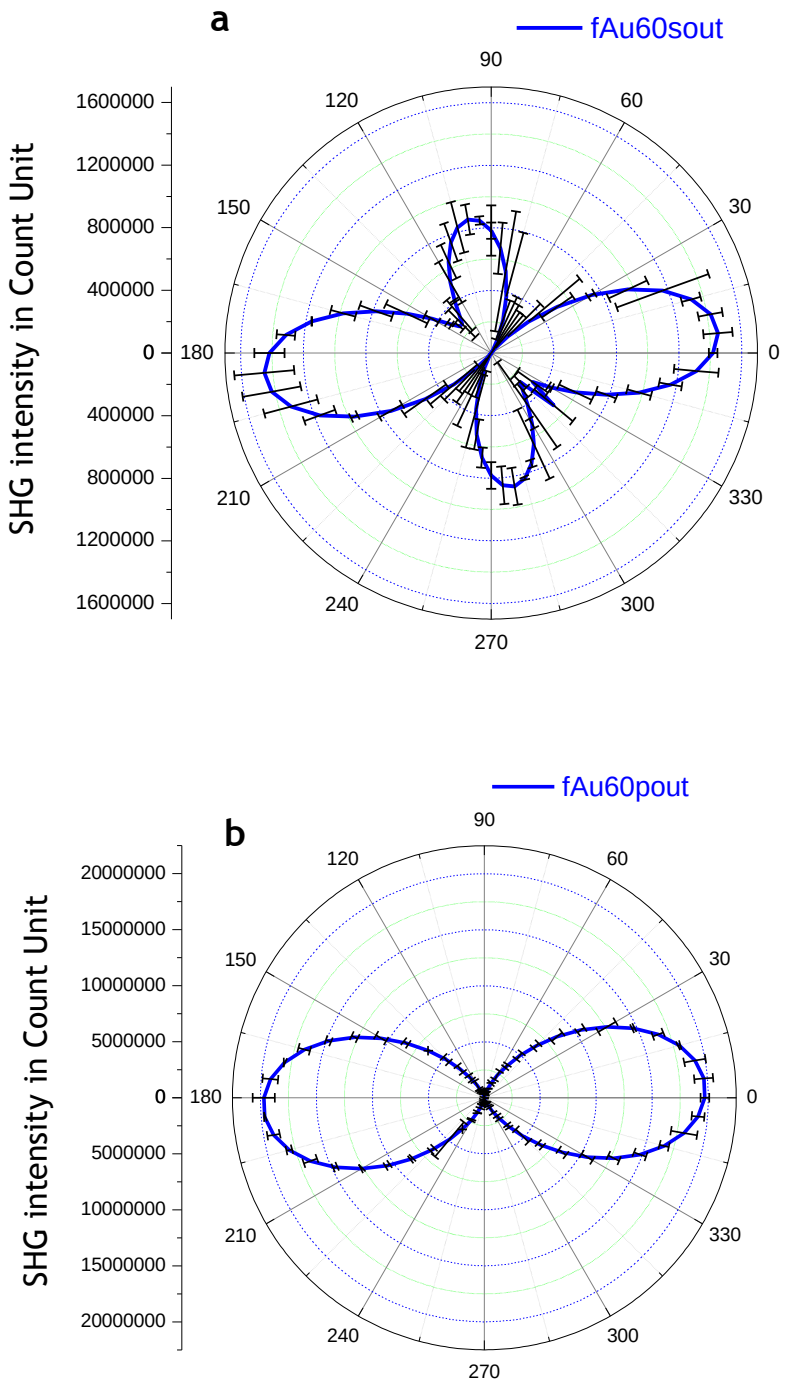

Figure 14 This figure shows the profiles of s-out in **a** and p-out in **b,** both are in blue lines; with their correspondent error bars in black lines. This is for pure 60nm Au film, which we have used as a reference for our measurements. Note the large error bars appeared in **a**, which evidence the data scattering during the measurements, this is due to the intrinsic weakness of the SH signal generated by s-out set up.

5.4.3. SHG signal from the gammadion patterns

This includes the configurations of the SHG signal from the surfaces of the left, Right and racemic gammadions. In Figure 15 we show polar plots for the s-polarised (**d**, **e** and **f**) and p-polarised (**a**, **b** and **c**) SH emission for the: 60nm Au film, left, right and racemic gammadion patterns. We applied equation 19 to achieve the best fitting to our experimental spectra, and hence, derive these plots. The scattered (black) and the solid (red) plots represent the experimental data of SH emissions and their fits, respectively. The blue solid lines represent the fits of 60nm Au film substrate (similar to those shown in Figure 14). The red solid lines represent the fits of the samples with left, Right and racemic nanostructures. For the s-polarised racemic plot (shown in **e**), the experimental data (black) has been compared with the average of the left- and Right-handed s-polarised profiles (green). This is to check if the racemic sample produces similar profile to that produced by the average of the left and right handed gammadion profiles. Since both resulting profiles are almost identical, this suggests that the samples were behaving as expected and were of high quality. In fact, the racemic profile is equivalent to a 50:50 mixture of those obtained from the left and the right handed nanostructures, with a small fraction of unavoidable defects. The unavoidable defects could be scaled on atomic scale or even larger, which might contribute to the SHG signal via *multipolar bulk emission*. However, since the racemic profile is exactly equivalent to a 50:50 mixture of left and right handed nanostructure profiles, the three samples of left, right and racemic gammadions are assumed to have a very similar level of defects. Fitting the experimental spectra to equation 19 reveals the best values of α_i, β_i, γ_i, δ_i and ε_i. By comparing these values all together, one can conclude the source of the contribution associated with the observed SHG signal. Concluding the source of the contribution associated with the observed SHG signal means investigating whether the origin of the SHG signal is chiral or achiral, or whether it is electric dipole or multipolar excitation. In this section, we will verify the origin of the SHG signal from chiral and achiral surfaces; this is to see if our SHG signals are sensitive enough to chirality, and hence to decide if our SHG signals

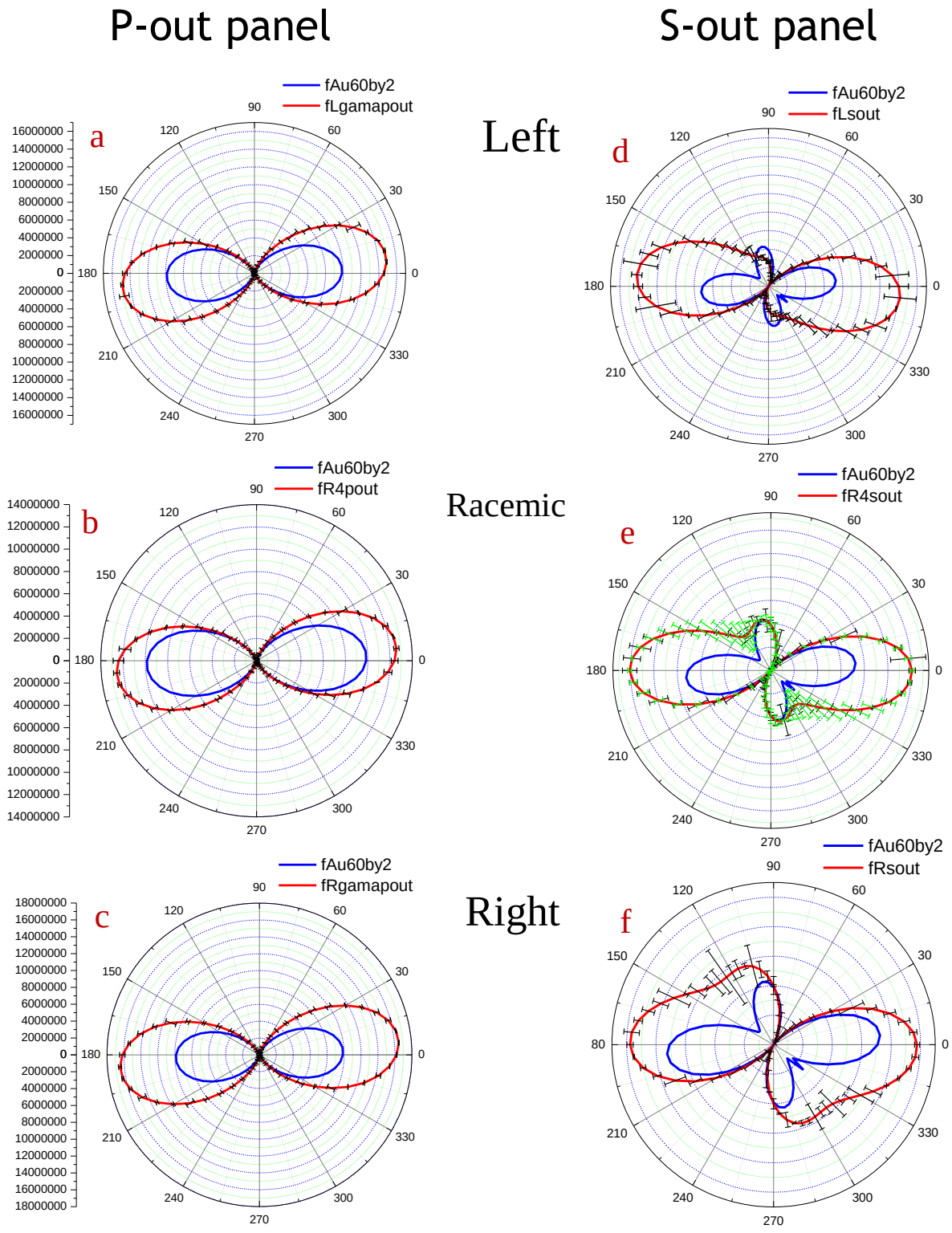

Figure 15: Polar plots and their corresponding fits (derived from equation 19) for s-polarised (**d**, **e** and **f**) and p-polarised (**a**, **b** and **c**) SH emissions; from chiral and achiral substrates. The scattered (black) and the solid (red) plots represent the emission and the fits profiles, respectively, associated with the s- and p- polarised light. The blue solid lines represent the fits of the pure 60 nm Au film (as a reference (shown in Figure 15 above)). The red solid lines represent the fits of the samples with left, right and racemic nanostructures. Note the SH intensity was reduced by 50% for the 60 nm Au film, which has no nanostructures. For the s-polarised racemic plot (**e**) experimental data (black) is compared with the average of the left- and right-handed s-polarised profiles (green).

are readable to distinguish between enantiomers (section 4.3.1). Then we will verify whether the origin of our SHG signal is electric dipole or multipolar excitation, and hence predict the microscopic origin of our OA-SHG signal (section 4.3.2).

5.4.3.1. Schematic and theoretical treatments to determine the enantiomer sensitivity from the s-out and p-out measurements

Determination the enantiomer sensitivity from the s-out and p-out measurements could be verified via ***schematic treatments***. For this purpose, we compared the SHG signals for all the six plots in Figure 15 (a-f) and henceforth, we observed asymmetry about the scattering plane (0 on the plots) for the s-out and p-out measurements, this was for the samples with the nanostructures (red line plots) as well as for the sample with the 60 nm Au film (the blue line plots). Similar behaviour was observed in a previous SHG study on plasmonic nanostructured materials [56]. On account of this observation, one may realised that it is not possible to discriminate between the chirality of the left and right nanostructures from the p-out measurements, as they do not display a significant asymmetry between the different handed nanostructures (see **a** and **c**). In contrast, the s-out measurements are fairly sensitive to chirality, since they displayed a clear and large asymmetry between the different handed nanostructures (shown in **d** and **f**).

Moreover, determination of the enantiomer sensitivity from the s-out and p-out measurements could be verified via ***theoretical treatments***. For this purpose, we start with the verification of the origin of the SHG signal from chiral and achiral surfaces and used the 60nm Au film as an example to demonstrate how we performed our investigations for the other samples. We fitted our experimental data of s-polarised profile for 60nm gold film with the all coefficients above (i.e. α_i, β_i, δ_i and ε_i); apart from γ_i who was fixed to zero for s-out and p-out measurements. Our fitting revealed large value (in comparison with other coefficients) for β_s, which indicates its dominant contribution to the SHG signal coming from 60nm Au film, see table 2 below. In this table, we

present the contributions of α_s, β_s, γ_s, δ_s and ε_s coefficients which represent the fitted data of: 60nm Au film, left, right and the racemic gammadion patterns, all for the S_{out} set up. For comparison purposes, we normalised all data to β_s for the 60nm Au film since it has the largest contribution, and since it considers the contribution of both dipolar and multipolar excitations. According to the second column of table 2 (i.e. 60nmAu film), we believe that β_s value is large since it is four times larger than δ_s and it is significantly higher than the others. This is expected since, in theory, if it is compared with α_s, δ_s and ε_s; β_s has the largest susceptibility tensor to generate the SHG signal from an achiral surface. This fact could be realised if we look at equations (18a - 18e), equations (7-12) and Table 1 (all are mentioned in section 2 above) as following: From 18b, β_s is proportional to $|h_i|^2$, which has no chiral elements at all, this could be realised via comparing the susceptibility tensors appeared in equation 9, i.e. : $\chi_{xxz}^{eee}, \chi_{xzy}^{eem}, \chi_{xyz}^{eem}, \chi_{xyz}^{mee}$ with their correspondent Cartesian components that are listed in table1. For example, if we want to figure out if χ_{xxz}^{eee} is chiral or achiral, we should look at χeee in the first column of table 1 and compare it with its correspondent Cartesian component i.e. xxz and see if it is listed under the third column which includes the chiral components or under the fourth column which includes the achiral components. Clearly, xxz is listed under the fourth column which includes achiral components. From all that, with such achiral surface, one may illustrate the reason why β_s of 60nm Au film has such big value. From the same equation (i.e. 18b), β_s is also proportional to$(f_i g_i^* + f_i^* g_i)$. Similarly to above, from equations (7-12) and Table 1, one may observe comparable chiral contributions coming from f_s and g_s. This indicates the probability of chiral contribution, which we believe it comes from the gold lattice and, crucially, it does not affect our investigations of the SHG signal sensitivity to chiral nanostructures; first because it (gold lattice) has small contribution (in comparison of 400nm features) and second because it is a characteristic which is shared with all other samples (i.e. 60nm Au film, left, Right and racemic gammadions). However, similar analysis for the p- polarised profiles of 60nm Au film reveals different results. This is also as expected, and suggests that the SHG signal is mostly coming from the symmetry allowed coefficient, which is represented here by α_p, β_p, see table 3 below. In table 3, we present the contributions of α_p, β_p, γ_p, δ_p and ε_p coefficients which represent

the fitted data of: 60nm Au film, left, right and the racemic gammadion patterns. These coefficients have been derived via fitting our p-out experimental data to equation 19 above. Although α_p for 60nm Au film is the largest coefficient this time, the data was normalised to β_p instead of α_p ; first because β_p considers contributions from both dipolar and multipolar excitations, and second to enable a meaningful comparison with the other data (as we will see later). Again, following similar route to investigate the reason why α_p have the biggest value, one may look at equations (18a - 18e), equations (7-12) and Table 1: From 18a, α_p is proportional to $|f_i|^2$, which has no chiral elements at all, this could be realised via comparing the susceptibility tensors appeared in equation 10, i.e. : χ_{zzz}^{eee} , χ_{zxx}^{eee}, χ_{xxz}^{eee}, χ_{zxy}^{eem}, χ_{xzy}^{eem}, χ_{xyz}^{mee} with their correspondent Cartesian components that are listed in table1. Once again, if we want to figure out if χ_{zzz}^{eee} is chiral or achiral, we should look at χeee in the first column of table 1 and compare it with its correspondent Cartesian component i.e. zzz and see if it is listed under the third column (for chiral components) or under the fourth column (for achiral components), obviously zzz is listed under the fourth column which includes achiral components. Again, from all that, with such achiral surface, one may illustrate the reason why α_p of 60nm gold film has such big contribution. For β_p however, its contribution is five times less than α_p (see table 2), again, one may look at equations (18a - 18e), equations (7-12) and Table 1 to illustrate the reason of such difference, which we found it is the same reason that we illustrated for β_s above, but with having chiral and achiral contributions coming from $(f_p\ ,\ g_p\ ,\ h_p)$ reversed; since the chiral elements of $f_s\ ,\ g_s\ ,\ h_p$ will reversed to be achiral elements for $f_p\ ,\ g_p\ ,\ h_s$.

Table 2: This table displays the α_i, β_i, γ_i, δ_i and ε_i coefficients for equation 19 for s-polarised SH emission from the various gammadion sets.

Coefficient	60 nm Au film	Left	Right	Racemic
α_S	0.08±0.00	0.19±0.00	0.14±0.00	0.13±0.00
β_S	1	0.52±0.00	0.52±0.01	0.59±0.01
γ_S	0±0	0±0	0±0	0±0
δ_S	0.23±0.03	0.36±0.00	0.12±0.01	0.28±0.00
ε_S	0.02±.03	0.06±0.01	0.04±0.01	0.02±0.01

Table 3: This table displays the α_i, β_i, γ_i, δ_i and ε_i coefficients used in equation 19 fitting for p-polarised SH emission from the various gammadion sets.

Coefficient	60 nm Au film	Left	Right	Racemic
α_P	6.92±0.8	5.18±0.6	5.75±0.76	4.40±0.57
β_P	1	0.83±0.05	0.78±0.05	0.66±0.03
γ_P	0±0	0±0	0±0	0±0
δ_P	0±0	1.44±0.14	1.35±0.13	0.91±0.07
ε_P	0.11±0.1	0.08±0.05	0.12±0.04	0.01±0.04

Now, we will consider the SHG signal from the left, Right and racemic gammadions on the way to investigate the probability of having the SHG signal carrying information about the chirality of our nanostructures (i.e. to verify whether the origin of the SHG signal is chiral or not). Starting with ***s-polarised system***, in this system α_s, β_s, δ_s and ε_s coefficients are considered to be chiral sensitive. Once again, this fact could be realised if we look at equations (18a - 18e), equations (7-12) and Table 1 as following: ***first***, considering $\boldsymbol{\alpha_s}$, from 18a, α_s is proportional to $|f_i|^2$, which has fully chiral elements, this could be realised via comparing the susceptibility tensors appeared in equation 7, i.e.: $\chi_{xyz}^{eee}, \chi_{xzx}^{eem}, \chi_{zzz}^{mee}, \chi_{zxx}^{mee}, \chi_{xxz}^{mee}$ with their correspondent Cartesian components that are listed in table1. Clearly, they are all listed under the third column in table 1 which includes the chiral components. Despite the fact of having such chiral surface, yet α_s is unreadable to differentiate between enantiomers and this is why in table 4 one would observe the small dissymmetry between left and Right species. In this table, we present the dissymmetry between the left and Right species for α_i, β_i, γ_i, δ_i and ε_i coefficients for the s-out and p-out measurements; which they were derived from the data of tables 2 and 3 above. In fact, we believe that the reason for the small dissymmetry (for α_s) between the left and Right species is because $|f_i|^2$ is an absolute square quantity which obscures the sign of the chiral element, and hence obscures the differentiation between enantiomers. ***Second***, considering $\boldsymbol{\beta_s}$, from 18b, β_s is proportional to $(f_i g_i^* + f_i^* g_i + |h_i|^2)$, which is a combinations between chiral and achiral elements. This could be realised via comparing the susceptibility tensors appeared in equation 7, i.e.: $\chi_{xyz}^{eee}, \chi_{xzx}^{eem}, \chi_{zzz}^{mee}, \chi_{zxx}^{mee}, \chi_{xxz}^{mee}$ equation 8, i.e.: $\chi_{xxz}^{eem}, \chi_{zxx}^{mee}$ and equation 9, i.e.: $\chi_{xxz}^{eee}, \chi_{xzy}^{eem}, \chi_{xyz}^{eem}, \chi_{xyz}^{mee}$ with their correspondent Cartesian components that are listed in table1. Clearly, the correspondent Cartesian components appeared in equation 7 and 8 are listed under the third column in table 1 which includes the chiral components. However, the correspondent Cartesian components appeared in equation 9 are listed under the fourth column in table 1 which includes the achiral components. Despite the fact of having such combination between chiral and achiral elements, with considerable chiral contribution (0.52 for left and Right handed gamma (see table 2)), yet β_s is also unreadable to differentiate between enantiomers; simply because it was influenced equally from the left and Right

features and therefore implied zero dissymmetry between the left and the Right handed gammadions, this is shown in table 4. ***Third***, considering δ_s, from 18d, δ_s is proportional to $(h_i f_i^* + h_i^* f_i)$, which is a combination between chiral and achiral elements. This could be realised via comparing the susceptibility tensors appeared in equation 7, i.e.: $\chi_{xyz}^{eee}, \chi_{xzx}^{eem}, \chi_{zzz}^{mee}, \chi_{zxx,}^{mee} \chi_{xxz,}^{mee}$ and equation 9, i.e.: $\chi_{xxz}^{eee}, \chi_{xzy}^{eem}, \chi_{xyz}^{eem}, \chi_{xyz,}^{mee}$ with their correspondent Cartesian components that are listed in table1. Again, the correspondent Cartesian components appeared in equation 7 are listed under the third column in table 1 which includes the chiral components and the correspondent Cartesian components appeared in equation 9 are listed under the fourth column in table 1 which includes the achiral components. In contrast to β_s, and despite the fact of having such combination between chiral and achiral elements, with lower chiral contribution (0.36 for left and 0.12 for Right (see table 4)), yet δ_s is considered to be cable to differentiate between enantiomers; simply because it was influenced unequally from the left and Right features; which implied a nonzero (0.24) dissymmetry between left and the Right handed gammadions, this is shown in table 4. **Finally**, Considering ε_s, from 18e, ε_s is proportional to $(h_i g_i^* + h_i^* g_i)$, which is a combination between chiral and achiral elements. This could be realised via comparing the susceptibility tensors appeared in equation 8, i.e.: $\chi_{xxz}^{eem}, \chi_{zxx}^{mee}$ and equation 9, i.e.: $\chi_{xxz}^{eee}, \chi_{xzy}^{eem}, \chi_{xyz}^{eem}, \chi_{xyz,}^{mee}$ with their correspondent Cartesian components that are listed in table1. Again, the correspondent Cartesian components appeared in equation 8 are listed under the third column in table 1 which includes the chiral components and the correspondent Cartesian components appeared in equation 9 are listed under the fourth column in table 1 which includes the achiral components. Despite the fact of having such combination between chiral and achiral elements, ε_s in general has a very low contribution; that make it unable to show any kind of effect, whether chiral or achiral or differentiate between enantiomers.

Table 4: This table displays the differential values of α_i, β_i, γ_i, δ_i and ε_i coefficients calculated between the left and the right gammadions for s-out and p-out measurements. Note the small differences between the left and right gammas apart from δ_s in s-out measurements, which shows a large value within the error level.

The fitting coefficients	L-R/ s-out	L-R/ p-out
α	0.05 ± 0.00	0.75 ± 1.36
β	0.00 ± 0.01	0.05 ± 0.10
δ	0.24 ± 0.01	0.09 ± 0.27
ε	0.02 ± 0.02	0.04 ± 0.09

Continuously to above and considering ***p-polarised system***, in this system β_p, δ_p and ε_p coefficients are considered to be chiral sensitive. Once again, this fact could be understood if we look at equations (18a - 18e), equations (7-12) and Table 1 as following: **first**, considering $\boldsymbol{\beta_p}$, from 18b, β_p is proportional to $(f_i g_i^* + f_i^* g_i + |h_i|^2)$, which is combinations between chiral and achiral elements. This could be understood via comparing the susceptibility tensors appeared in equation 10, i.e.: χ_{zzz}^{eee} , χ_{zxx}^{eee}, χ_{xxz}^{eee}, χ_{zxy}^{eem}, χ_{xzy}^{eem}, χ_{xyz}^{mee}, equation 11, i.e.: χ_{zxx}^{eee}, χ_{zxy}^{eem} , χ_{xyz}^{mee} and equation 12, i.e.: χ_{xyz}^{eee} , χ_{zzz}^{eem} , χ_{zxx}^{eem} , χ_{xzx}^{eem} , χ_{xxz}^{eem} χ_{xxz}^{mee}, with their correspondent Cartesian components that are listed in table1. Clearly, the correspondent Cartesian components appeared in equation 10 and 11 are listed under the fourth column in table 1 which includes the achiral components. However, the correspondent Cartesian components appeared in equation12 are listed under the third column in table 1 which includes the chiral components (apart from χ_{xxz}^{mee} which is listed under the achiral column). Despite the fact of

having such combination between chiral and achiral elements, with considerable contributions (0.83 for left and 0.78 for Right (see table 3)), yet β_p is unreadable to differentiate between enantiomers; simply because it showed small (scaled within error) dissymmetry between the left and the Right handed gammadions, this is shown in table 4. **Second**, considering **δ_p**, from 18d, δ_p is proportional to $(h_i f_i^* + h_i^* f_i)$, which is a combination between chiral and achiral elements. This could be understood via comparing the susceptibility tensors appeared in equation 10, i.e.: χ_{zzz}^{eee} , χ_{zxx}^{eee}, χ_{xxz}^{eee}, χ_{zxy}^{eem}, χ_{xzy}^{eem}, χ_{xyz}^{mee}, and equation 12, i.e.: χ_{xyz}^{eee} , χ_{zzz}^{eem} , χ_{zxx}^{eem} , χ_{xzx}^{eem} , χ_{xxz}^{eem} χ_{xxz}^{mee}, with their correspondent Cartesian components that are listed in table1. Again, the correspondent Cartesian components appeared in equation 10 are listed under the fourth column in table 1 which includes the achiral components and the correspondent Cartesian components appeared in equation 12 are listed under the third column in table 1 which includes the chiral components (apart from χ_{xxz}^{mee} which is listed under the achiral column). In contrast to δ_s, and despite the fact of having such combination between chiral and achiral elements, with considerable contribution (1.44 for left and 1.35 Right handed gamma (see table 3)), yet δ_p is considered to be unable to differentiate between enantiomers; simply because it showed small (scaled within error) dissymmetry between the left and the Right handed gammadions, this is shown in table 4. **Finally**, Considering **ε_p**, from 18e, ε_p is proportional to $(h_i g_i^* + h_i^* g_i)$, which is a combination between chiral and achiral elements. This could be realised via comparing the susceptibility tensors appeared in equation 11, i.e.: χ_{zxx}^{eee}, χ_{zxy}^{eem}, χ_{xyz}^{mee} and equation 12, i.e.: χ_{xyz}^{eee} , χ_{zzz}^{eem} , χ_{zxx}^{eem} , χ_{xzx}^{eem} , χ_{xxz}^{eem} χ_{xxz}^{mee}, with their correspondent Cartesian components that are listed in table1. Again, the correspondent Cartesian components appeared in equation 11 are listed under the fourth column in table 1 which includes the achiral components and the correspondent Cartesian components appeared in equation 12 are listed under the third column in table 1 which includes the chiral components (apart from χ_{xxz}^{mee} which is listed under the achiral column). Despite the fact of having such combination between chiral and achiral elements, ε_s in general has a very low contribution that make it unreadable to show any kind of effect; whether chiral or achiral or differentiate between enantiomers.

From all that, the clear message is that $\boldsymbol{\delta_s}$ ***is the only coefficient which could be relied on to discriminate between our left and the Right handed nanostructures.*** In the coming paragraphs we will present a comparison between δ_s and δ_p, taking in account the effect of the bulk contribution; in order to demonstrate that the effect we have observed (about the reliability of δ_s to distinguish between enantiomers) is really influenced by the handedness of our nanostructures and not by the bulk of these nanostructures.

Back to table 4 above, from this table, as we already mentioned, δ_s coefficient shows a substantial difference between the left and right nanostructures, also, the δ_s coefficient obtained for the racemic mixture (shown in table 2) is approximately intermediate between the δ_s coefficient obtained for the left and the right nanostructures, which is clearly, an indication of chiral sensitivity. In general, the contribution of δ_s could be given by:

$$\delta_s = \delta_s^{bulk} \pm \delta_s^{chiral}$$

Here the:

δ_s^{bulk} Represents the contributions coming of the multipolar bulk emission (mentioned above) and δ_s^{chiral} represents the contributions coming from the chiral surface. Theoretically, δ_s is non-zero for the left and right nanostructures (with its sign changes according to the handedness of the sample), and it is zero for the racemic nanostructure. We calculated the ratio between the δ_s^{chiral} and the δ_s^{bulk} in order to examine the contribution coming from the multipolar bulk emission and its effect on the SH signal. As we already assumed, δ_s^{bulk} is similar for left and right gammadions, and hence the ratio in question could be calculated as following:

$$\frac{\delta_s^{chiral}}{\delta_s^{bulk}} = \frac{left - right}{left + right} = \frac{0.24 \pm 0.01}{0.48 \pm 0.01} = 0.5 \pm 0.01$$

Clearly, the fraction of dissymmetry, which equals to the half of the total contribution, reflects the chirality effectiveness to the SHG signal, which is again, an indication of chiral sensitivity. Generally speaking and in contrast to s-

polarised system, the variation in the SHG response coming from the left, right and racemic gammadions is very slight in p-polarised system. This is because, as we already concluded, the chiral sensitive coefficients β_p, δ_p and ε_p showed very small differences between the left and the right species, see Table 4 above. Considering δ_p values, the ratio between the δ_p^{bulk} and the δ_p^{chiral} gives a low value (scaled with error) in comparison to similar ratio that is calculated in s-polarised system we discussed above:

$$\frac{\delta_p^{chiral}}{\delta_p^{bulk}} = \frac{left - right}{left + right} = \frac{0.09 \pm 0.27}{2.79 \pm 0.27} = 0.032 \pm 0.08$$

Indeed, such ratio reflects the domination of the multipolar bulk emission, which might illustrate the reason behind the small dissymmetry variation between the left and the right nanostructures.

5.4.3.2. Theoretical treatments to determine electric dipole excitation- induced SHG signal from s-out measurements

Following similar theoretical treatments of section 4.3.1, it is possible to verify the origin of the SHG signal whether it has electric dipole, or multipolar contributions. For space limitation, in this section, we will only consider δ_s since it is the only coefficient who showed enantiomer sensitivity. Once again, equation 18d illustrates the dependency of δ_s coefficient upon $(h_i f_i^* + h_i^* f_i)$, which implies the dependency on the following susceptibility tensors: $\chi_{xyz}^{eee}, \chi_{xzx}^{eem}, \chi_{zzz}^{mee}, \chi_{zxx}^{mee}, \chi_{xxz}^{mee},$ from equation 7 and $\chi_{xxz}^{eem}, \chi_{zxx}^{mee}$ from equation 8. Obviously, this indicates a combination of electric dipole excitation and multipolar excitation which influence the SHG signal. At this point, it is crucial to decide which one of these excitations has dominated and influenced our SHG signal more effectively and why?

In order to answer this question it is useful to estimate the contribution of each tensor that is found in equation 18d (i.e $\chi_{xyz}^{eee}, \chi_{xzx}^{eem}, \chi_{zzz}^{mee}, \chi_{zxx}^{mee}, \chi_{xxz}^{mee},$

$\chi_{xxz}^{eem}, \chi_{zxx}^{mee}$) according to the equivalent tensor which could be found in different equations for different coefficients, especially, coefficients that are showed high contribution to the SHG signal. Starting with α_s, since this coefficient is proportional to $|f_i|^2$ (eq. 18a) only, we believe that α_s is not useful (for this particular case) to provide extra information, and therefore we have not considered it. Our second candidate however, which is represented by β_s seem to be more useful; first because it reflects chiral contribution and second because it is proportional to f_i, a common coefficient between β_s and δ_s. In fact, our final candidate, which is represented by ε_s, is also useful; again, because it reflects chiral contributions and because it is proportional to g_i, a common coefficient between β_s and ε_s. Having these facts means ε_s is, indirectly, linked to δ_s through g_s. The essential fact that ε_s has a very low contribution ($\cong$ zero) see table 2 and table4, which implies that the susceptibility tensors of δ_s that equivalent their correspondent tensors in ε_s will be low as well. This is because $\chi_{xxz}^{eem} \cong \chi_{xzx}^{eem}$, $\chi_{zxx}^{mee} \cong \chi_{zzz}^{mee}$, $\chi_{zxx}^{mee} \cong \chi_{zxx}^{mee}$, and $\chi_{zxx}^{mee} \cong \chi_{xxz}^{mee}$ **.This indicates that *the contribution of multipolar excitation in δ_s is $\cong$ zero***. On the other hand, β_s has a very high contribution, see table 2. Since g_s has a very small contribution, we believe that the main contribution for β_s is essentially coming from f_s only, i.e. from its susceptibility tensor χ_{xyz}^{eee} . As we already mentioned, χ_{xyz}^{eee} represents the contribution coming from the electric dipole excitations, therefore we conclude that ***the only excitation that dominates the δ_s contribution to the SHG signal coming from our nanostructures essentially to be the electric dipole excitation***.

5.5. Conclusion

In conclusion, it is possible to discriminate between left- and right-handed chiral nanostructures via off-resonance; nonlinear optically active SHG spectroscopy (OA-SHG). We have found that the non-linear optical activity of our 2D chiral metamaterials is dominated by electric dipolar excitation rather than non-localised multipolar excitation. This conclusion is in line with the dominance of electric dipolar contributions in the non-linear optical activity of adsorbed chiral monolayers. This is perhaps a surprising result since there is almost three orders of magnitude difference between the size of the nanostructures used in this work and the size of the molecules in previous work where the electric dipolar contribution was found to be dominant. Therefore we conclude that the dominance of the electric dipole contribution to the non-linear optical activity is a generic phenomenon; since it extends from molecular length scales to hundreds of nanometres. This is an important finding since it demonstrated how novel chiral nanostructures can be used to rationalise the non-linear optical properties of plasmonic metamaterials without considering the multipolar excitation; which significantly simplifying the experimental measurements. This implies practical applications for effective potentials of plasmonic metamaterials via dipolar coupling detection system, in particular those displayed by large proteins; such as protein fibrils. Finally, our work also suggests that the plasmonic excitation enhancement is not prerequisite for intense OA-SHG signal.

5.6. References

1. Abdulrahman A., Syme C. S., Jack C., Karimuallh A., Barron L. D., Gadegaard N. and Kadodwala M., *The Royal Society of Chemistry*, *Nanoscale*, 2013, Vol.5, pp (12651-12657).

2. Valev V. K., *Langmuir, American Chemical Society*, 2012, Vol.28, pp (15454-15471).
3. Siltanen M., Vuorimaa E., Lemmetyinen H., Ihalainen P., Peltonen J. and Kauranen M., *J. Phys. Chem. B*, 2008, Vol.112, pp (1940-1945).
4. Schanne-Klein M.C., Hache F., Roy A., Flytzanis C., and Payrastre C., *Journal of Chemical Physics*, 1998, Vol.108, pp (9436-9443).
5. Huttunen M. J., Bautista G., Decker M., Linden S., Wegener M. and KauranenM., *Optical Materials Express*, 2011, Vol.1, pp (46-56).

6. Byers J. D., Yee H. I. and Hicks J. M., *J.Chem. Phys*., 1994, Vol.101, pp (6233-6241).
7. Verbiest T., Elshocht S. V., Kauranen M., Hellemans L., Snauwaert J., Nuckolls C., Katz T.J., Persoons A., *Science*,1998, Vol.282, pp (913-915).
8. Pendry J. B., *Science*, 2004, Vol.306**,** pp(1353-1355).
9. Gansel J. K., Thiel M., Rill M. S., Decker M., Bade K., Saile V., Freymann G. V., Linden S. and Wegener M., *Science*, 2009, Vol.325**,** pp (1513-1515).
10. Hendry E., Carpy T., Johnston J., Popland M., Mikhaylovskiy R. V., Lapthorn A. J., Kelly S. M., Barron L. D., Gadegaard N. and Kadodwala M., *Nature Nanotechnology*, 2010, Vol.5, pp (783-787).
11. Kauranen M. and Zayats A. V. , *Nature Photonics*, 2012, Vol.6, pp (737-748).

12. Simpson G. J., *Chemphyschem*, 2004, Vol.**5,** pp (1301-1310).
13. Petralli-Mallow T., Wong T. M., Byers J. D., Yee H. I. and Hicks J. M., *Journal of Physical Chemistry*, 1993, Vol.97**,** pp (1383-1388).

14. Fischer P. and Hache F., *Chirality*, 2005, Vol.17, pp (421-437).
15. Persechini L. and McGilp J. F., *Physica Status Solidi B-Basic Solid State Physics*, 2012, Vol.249**,** pp (1155-1159).
16. DeWalt E. L., Begue V. J, Ronau J. A., Sullivan S. Z., Das C. and Simpson G. J., *Acta Crystallographica Section D-Biological Crystallography*, 2013, Vol.69, pp (74-81).
17. Verbiest T., Kauranen M., Persoons A., Ikonen M., Kurkela J. and Lemmetyinens H., *Journal of the American Chemical Society*, 1994, Vol.116**,** pp (9203-9205).
18. Kauranen M., Verbiest T., Maki J. J. and Persoons A., *Journal of Chemical Physics*, 1994, Vol.101**,** pp (8193-8199).
19. Bovet N., McMillan N., Gadegaard N. and Kadodwala M., *Journal of Physical Chemistry B*, 2007, Vol.111, pp (10005-10011).
20. Mulligan A., Lane I., Rousseau G. D., Johnston S. M., Lennon D. and Kadodwala M., *Journal of Physical Chemistry B*, 2006, Vol.110, pp (1083-1090).
21. Mulligan A., Lane I., Rousseau G. D., Johnston S. M., Lennon D. and Kadodwala M., *Angewandte Chemie-International Edition*, 2005, Vol.44, pp (1830-1833).

22. Valev V. K., Silhanek A. V., Verellen N., Gillijns W., Van Dorpe P., Aktsipetrov O. A., Vandenbosch G. E., Moshchalkov V. V. and Verbiest T., *Physical Review Letters*, 2010, Vol.104, pp (127401(1-4))
23. Mamonov E. A., Murzina T. V., Kolmychek I. A., Maydykovsky A. I., Valev V. K., Silhanek A. V., Verbiest T., Moshchalkov V. V. and Aktsipetrov O. A., *Optics Express*, 2012, Vol.20**,** pp (8518-8523).
24. Valev V. K., Clercq B. D., Zheng X., Denkova D., Osley E. J., Vandendriessche S., Silhanek A. V., Volskiy V., Warburton P. A., Vandenbosch G. E., Ameloot M., Moshchalkov V. V. and Verbiest T., *Optics Express*, 2012, Vol.20**,** pp (256-264).
25. Mamonov E., Kolmychek I., Murzina T., Maydykovsky A., Aktsipetrov O., Valev V., Verbiest T., Silhanek A. and Moshchalkov V., *Asia-Pacific Interdisciplinary Research Conference*, 2012, Vol. 352.
26. Valev V. K., Smisdom N., Silhanek A. V., De Clercq B., Gillijns W., Ameloot M., Moshchalkov V. V. and Verbiest T., *Nano Letters*, 2009, Vol.9**,** pp (3945-3948).
27. Huttunen M. J., Virkki M., Erkintalo M., Vuorimaa E., Efimov A., Lemmetyinen H. and Kauranen M., *J. Phys. Chem. Lett.*, 2010, Vol.1, pp (1826-1829).
28. Huttunen M. J., Erkintalo M. and Kauranen M., *Journal of Optics a-Pure and Applied Optics*, 2009, Vol.11**,** pp (1- 6).
29. Husu H., Canfield B. K., Laukkanen J., Bai B., Kuittinen M., Turunen J. and Kauranen M., *Applied Physics Letters*, 2008, Vol.93**,** pp (183115(1-3)).
30. Czaplicki R., Zdanowicz M., Koskinen K., Laukkanen J., Kuittinen M. and Kauranen M., *Optics Express*, 2011, Vol.19**,** pp (26866-26871).
31. Canfield B. K., Canfield B. K., Kujala S., Laiho K., Jefimovs K., Turunen J. and Kauranen M., *Optics Express*, 2006, Vol.14**,** pp (950-955).
32. Kauranen M., Verbiest T., Maki J. J. and Persoons A., *Journal of Chemical Physics*, 1994, Vol.101, pp (8193-8199).
33. Pershan P. S., *Physical Review*, 1963, Vol.130, pp (919- 929).
34. Maki J. J., Verbiest T., Kauranen M., Elshocht S. V. and Persoons A., *Journal of Chemical Physics*, 1996, Vol.105, pp (767-772).
35. Maki J. J., M. Kauranen and A. Persoons, *Physical Review B*, 1995, Vol.51, pp (1425-1434).
36. Hecht L. and Barron L. D., *Journal of Molecular Structure*, 1995, Vol.348, pp (217-220).
37. Verbiest T., Kauranen M., Maki J. J., Teerenstra M. N., Schouten A. J., Nolte R. and Persoons A., *Journal of Chemical Physics*, 1995, Vol.103, pp (8296-8298).
38. Belkin M. A., Shen Y. R. and Flytzanis C., *Chemical Physics Letters*, 2002, Vol.363, pp (479-485).
39. Fischer P. and Albrecht A. C., *Bulletin of the Chemical Society of Japan*, 2002, Vol.75, pp (1119-1124).
40. Fischer P. and Albrecht A. C., *Laser Physics*, 2002, Vol.12, pp (1177-1181).
41. Hache F., Mesnil H. and Schanne-Klein M. C., *Journal of Chemical Physics*, 2001, Vol.115, pp (6707-6715).
42. Mulligan A., *PhD.Thesis, University of Glasgow*, 2004.
43. Rubahn H. G., `Laser Applications in Surface Science and Technology`, *John Wiley & Sons Ltd*, 1999, printed book.

44. Smith E. and Dent G., "Modern Raman Spectroscopy", *John Wiley & Sons Ltd.*, 2005, printed book.
45. Miyata K., Umemura N. and Kato K., *OPTICS LETTERS*, 2009, Vol.34, pp (500-502).
46. Olivier N., Luengo-Oroz M. A., Duloquin L., Faure E., Savy T., Veilleux I., Solinas X., Débarre D., Bourgine P., Santos A., Peyriéras N. and Beaurepaire E. *Scince*, 2010, Vol. 329, pp (969-971).
47. Mitchell S. A., Mcaloney R. A., Moffatt D., Diez M. N., Zgierski M. Z., *The Journal of Chemical Physics*, 2005, Vol.122, pp (114707- 114715).
48. This reference is available to view at the following website http://www.chem.queensu.ca/people/faculty/Stolow/Research/NLOChi2.html (cited in 2013).
49. Nappa J., Revillod G., Russier-Antoine I., Benichou E., Jonin C. and Brevet P. F., *Physical Review B*, 2005, Vol.**71,** pp (165407(1-4)).
50. Bohren C. F. and Huffman D. R., "Absorption and Scattering of Light by Small Particles", *John Wiley & Sons Ltd*, 2004, printed book.
51. Bachelier G., Russier-Antoine I., BenichouE., Jonin C. and Brevet P. F., *Journal of the Optical Society of America B-Optical Physics*, 2008, Vol.25**,** pp (955-960).
52. Siltanen M., Cattaneo S., Vuorimaa E., Lemmetyinen H., Katz T. J., Philips K. and Kauranen M., *Journal of chemical physics*, 2004, Vol.121, pp (1- 4).
53. Thyagarajan K., Rivier S., Lovera A. and Martin O. J. F., *OPTICS EXPRESS*, 2012, Vol. 20, pp (12860-12865).
54. Mulligan A., Lane I., Rousseau G. D., Hecht L., Johnston S. M., Lennona D. and Kadodwala M., *Chemical Communications*, 2004, Vol.21, pp (2492-2493).
55. Barron L. D., "Molecular Light Scattering and Optical Activity", *Cambridge University press*, *Cambridge*, 2004, 2nd edition, printed book.
56. Capretti A., Walsh G. F., Minissale S., Trevino J., Forestiere C., Miano G. and Negro L. D., *Optics Express*, 2012, Vol.20, pp (15797-15806).

Chapter 6: Femtosecond Laser Irradiation for Hot Spots Mapping on the Surface of Plasmonic Nanostructures

Abstract

In this chapter, a novel method for visualising plasmonic `hot spots` is presented; hot spots are defined here as regions of localised high intensity electromagnetic fields. Upon irradiation with 800 nm femtosecond laser pulses, which may be linearly or circularly polarised, it is possible to reveal the location of plasmonic hot spots since the nanostructures are physically damaged i.e. undergo melting by the intense heat generated by femtosecond laser pulse irradiation. SEM microscopy may be used subsequently to map the surface to show which areas have been damaged, and hence reveal where the hot spots are. 2D arrays of quadric units (arranged in a racemic fashion) consisting of two patterns, gammadions and G-like shapes, have been used as plasmonic chiral nanostructures. It has been found that irradiation with *linearly* polarised light affected segments that are perpendicular to the polarisation direction of the incident beam. However, irradiation with *circularly* polarised light affected both horizontal and vertical segments of the nanostructures regardless of the sense of individual features (i.e. left-handed or right-handed) or the sense of the circular polarisation of the incident beam (i.e. clockwise or counter-clockwise). As such, no enantio-selectivity was observed.

6.1. Introduction

Mapping the activity of plasmonic structures is an area of great interest for an increasing number of researchers, especially with recent advanced in technology [1-5].The term `hot spot` is a region of high intensity electromagnetic field (such as that generated in femtosecond laser pulses) produced by plasmonic excitation [6,7]. Principally, the beam of femtosecond laser pulses is a flux of ultra-short laser pulses on the order of 10^{-15} seconds, and therefore it is

considered as an ultrafast event. Such short laser pulses make it possible to monitor ultrafast dynamics like electron motion in atoms and molecules [8]. Femtosecond lasers can be used to generate terahertz radiation, which has the advantage of being of low enough energy to be applied in medical imaging such that it does not damage living cells or tissue, or DNA [9], more applications for femtosecond laser pulses could be found in references [8,10,11]. In this chapter, we have taken advantage of the high energy that femtosecond laser pulses are characterised by, to provoke an optical response referred to as *Highly Localised Electromagnetic (EM) field* i.e. *Hot Spots*. The work in this chapter involves visualising (imprinting) these hot spots on the surface of plasmonic chiral nanostructures. The process of imaging the imprinted hot spots with microscopy is usually called the `hot-spot mapping`.

Hot-spot mapping is a flexible, high resolution 3D imaging technique for visualising electric fields on the surface of plasmonic metamaterials [12, 13]. Hot-spot mapping was originally envisaged to be used as a writing tool, for example to prepare tips in scanning probe microscopy [12]. Also, hot-spot mapping could be used to characterise the conditions required for growth processes in electronic storage media, and hence it could be used in data storage applications [13]. The findings presented in this chapter demonstrate the validity of hot-spot mapping as a novel technique to visualise plasmonic activity. Reference [6, 14] showed that imaging of plasmonic nanostructures by SHG and AFM microscopies were in excellent agreement with theoretical simulations. This is especially for nanostructures made out of nickel, palladium and gold. Essentially for work in these reference, all AFM images reveal `nanobumps` in the same locations as those predicted theoretically and/or detected by SHG microscopy, clearly indicating the origin of these nanobumps as highly localised electromagnetic fields. Similar phenomena are described in this work, despite the fact that different experimental conditions were employed from that employed by reference [6, 14]. For example, the nanostructures used here are made out of gold (held by Titanium), not nickel, or palladium, or gold (held by nickel). Also, 800 nm femtosecond laser pulses were manually focused onto the plasmonic surfaces instead of using an SHG microscope. Besides, this work involved the use of SEM microscopy as opposed to AFM microscopy. In addition,

theoretical simulations were performed using finite-element modelling instead of MAGMAS and RSoft`s DiffractMOD. In fact, hot-spot mapping can generate higher resolution images than SHG imaging, which is limited in its optical resolution (~200 nm). Similarly, SEM microscopy has some advantages over AFM microscopy. AFM microscopy is time consuming, requires very high resolution tips, and can only image regions on the order of a few microns. SEM microscopy is easier to use, faster to perform, can image much larger areas (up to the millimetre range), and a much wider resolution range (between >1 nm to 1 mm).

Indeed, a (15 x 15) mm Si wafer substrate can have at least 25 different patterns fabricated in a single writing job, which may be completed within a few hours or less (depending on the pattern). The mapping strategy described in this work involves irradiating each pattern for just a few seconds (~5 sec), and subsequently imaging them using SEM microscopy (within 2-4 hours), without the need for prior theoretical modelling. What is more, although hot-spot mapping damages the hot-spot regions, this might be considered as an advantage, since as well as the applications mentioned later in this chapter, one may also use the same sample at different times without any changes occurring to the affected regions, thus allowing analyses from previously characterised plasmonic surfaces.

The main hypothesis for this work was to see hot spots from our nanostructures first and to determine if they were enantio- selective or not. This is in order to be in line with research involving hot-spot mapping of plasmonic metamaterials. Intense fields such as those revealed by hot-spot mapping behave essentially as `lenses` for concentrating the field of the light [7]. Considering the amount of energy retained in a single location for each hot spot, one can imagine the amount of energy reserved in an array of thousands of nanostructures, and hence the energy reserved within larger areas (e.g. 1.6x1.6 mm). Potentially, this energy could be channelled into electronic circuits or used to initiate/influence chemical reactions etc. in a controlled manner. One might also create plasmonically controlled `switches` for nanoscale devices, such as a chirality switching system as recently described by researchers of reference [6].

Also, by fabricating hot spots in specific patterns (which could be improved by the aid of such a chirality switching system), one might enhance the surface-enhanced Raman scattering (SERS) properties of the hot spot regions and hence increase sensitivity for various detection applications. Thought, over recent years, different applications have been demonstrated to show the general potential of hot spots as ` miniature molecular reactors` which could be used in Raman scattering; which can be increased up to fourteen orders of magnitude [7, 15, 16], catalytic reactions [7, 17,18], chemical transformations [19] and photochemical reactions [7, 20].

6.2. Theory and background

Hot-spot mapping is associated with a vast amount of theoretical background that cannot be adequately presented in a single chapter. Therefore, this section is limited to the discussion of various theoretical aspects that are necessary to clarify the experimental work and data analysis presented in this chapter.

6.2.1. Hot spot imprinting

After electromagnetic waves impinge on a surface consisting of plasmonic nanostructures, surface electrons start to oscillate in parallel to the oscillations of the electromagnetic waves (see chapter 2), which in turn leads to the plasmonic electrons (confined within the shape of the nanostructures) being driven to the edges of the features. As such, the electron density at the edges will increase and hence the electric field, referred to as the `near field`, will increase as well. Such `near fields` are usually generated as a result of the electron motion, meaning that at the region of highest electron density (i.e. the edges of the features) the near fields will be very high as well, and hence start to condense as a hot spot. This is the case with the normal intensity light in the visible region for silver and gold surfaces. However, for a very intense light such as that generated in femtosecond laser pulses, the density of the plasmonic electrons will be very high at the edges of the feature segments (Figure 1a) that

leads to charge separation (Figure 1b), whereby an electric current could be triggered (Figure 1c). Subsequently, Ohmic losses cause the temperature of the metal surface to increase (at the edges), which in turn causes the metal structures to melt and eventually to imprint hot spots [6, 21, 14].

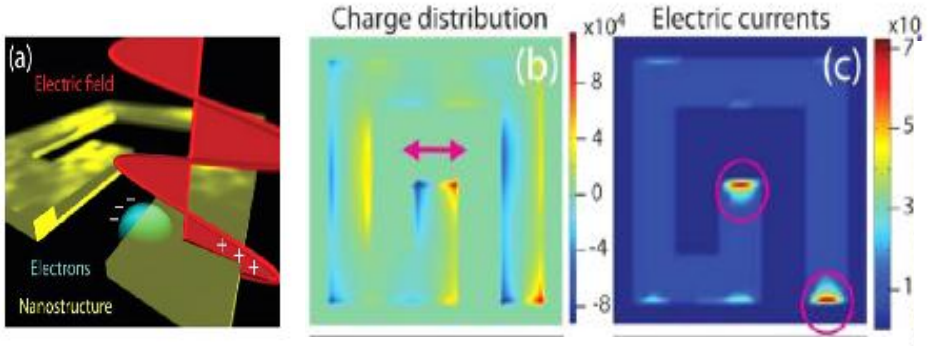

Figure 1: Hot spots formation and imprinting. **a** represents a schematic of the electromagnetic wave oscillating on the surface of the plasmonic nanostructure (G like shape); which drive the plasmonic electrons to be separated into positive and negative charges. **b** represents the theoretical simulations for the charge distributions. **c** represents the theoretical simulations for the electric currents formation. The polarisation state of the incident electric field is represented by the magenta arrow in **b**. All images are taken from reference [6].

6.2.2. Electromagnetic modelling for hot spots mapping

Hot spot mapping reveals important information about the locations of the intense *electric field (near field),* intense *electric currents* and intense *chiral field* that are distributed on the surface of the plasmonic chiral structures [6, 22, 23]. In fact, hot-spot mapping is a direct tool for having the theoretical simulation for these fields to be seen in real life. For example, a previous study [22] has shown two theoretical simulations for the locations of the electric field (near field) and for the chiral field, which are all distributed on the surface of a left-handed gold gammadion structure (see Figure 2 below). In another study [6], another two theoretical simulations for the locations of the electric field (near field) and for the electric currents are shown, which are all distributed on the surface of gold G-like shapes (see Figure 3 below). In [6], the author presented SHG micrographs and AFM images that corresponding the hot spots mapping (referred to as `nanobumps`) for the real locations of the electric

fields (near field) and the electric currents, and they were in good agreement with their corresponding theoretical simulations. In this chapter, as it will be presented later, SEM images have shown similar hot spot mapping but in a different fashion i.e. not as nanobumps, instead, as damaged regions. Generally speaking, from these two studies, it is clear that the theoretical distributions for the electric field (near field), the electric current and the chiral field all have nearly similar patterns for a certain shape made out of a certain metal. In fact, despite the fact that the hot spots originate as a result of the near field enhancement [6], it was not possible to assign mapped hot spots to a specific field. So, mapped hot spots may indicate the existence of one, two or all three fields mentioned above.

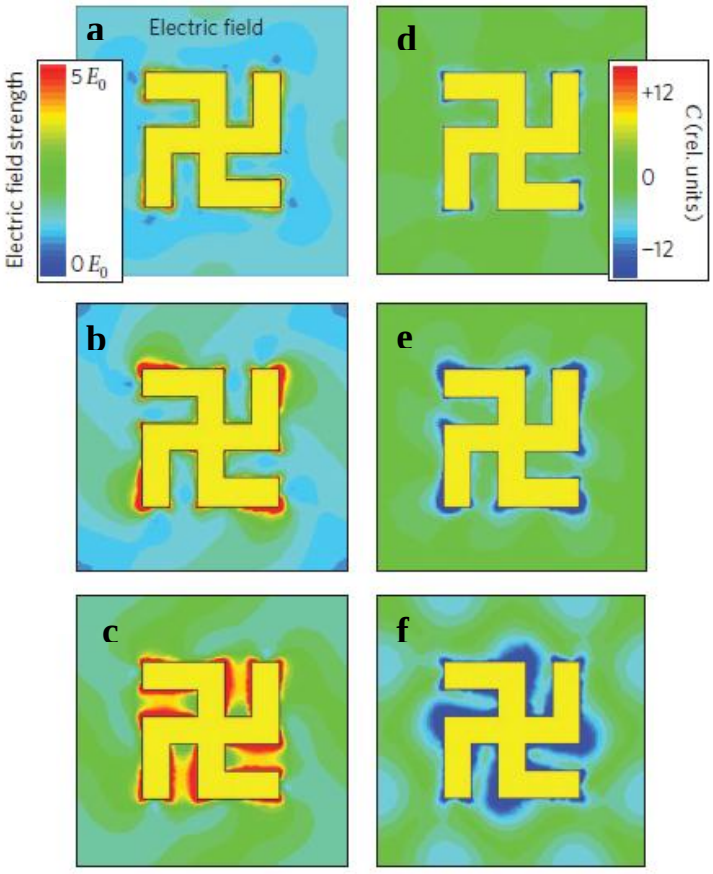

Figure 2: Theoretical simulations for the electromagnetic fields around the gammadions in compression to experimental results. **a**, **b** and **c** represent the electric field (near fields) with strength increasing from **a** to **c**. Then **d**, **e** and **f** represent the local optical chirality (chiral field) around the gammadions with strength increasing from **d** to **f**. The incident light was circularly polarised. Images are taken from reference [22].

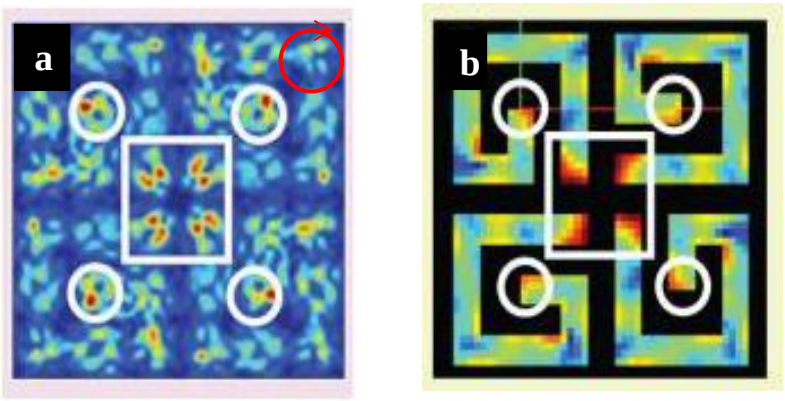

Figure 3: Theoretical simulations for the electromagnetic fields around the G like shapes in compression to experimental results. **a** represents the electric field (near fields). **b** represents the electric currents around the G like. The incident light was circularly polarised. Images are taken from reference [6].

6.3. Experimental work

Different samples were irradiated for a few seconds (~ 5 sec) with an 800 nm femtosecond pulsed laser beam. The beam had a diameter of ~5 mm and was focused by a lens with a focal length of about 25 cm, with pulse duration of 20 fs. The beam was set up to be incident upon the substrate at an angle of 90 degrees. The incident beam has been used with three different polarisation states; these are: linearly (vertically) polarised light, left handed circularly polarised light and right handed circularly polarised light. The circularly polarised light was generated by a quarter wave plate.

All samples were fabricated via electron beam lithography in JWNC /Glasgow University (see chapter 2). Silicon substrates have been used to provide a dielectric environment which supports the formation for the hot spots. Two patterns have been used, namely racemic gammadions and left-handed quadrics of G-like shapes. The pattern of the racemic gammadions consists of 50:50 mixtures of left- and right-handed features (see chapter 2). This pattern is a 2D array of quadric units each 4.4 μm. The quadric unit itself consists of four gammadions; each one was sized in 1μ and separated by 0.2μm from sides; and hence each unit occupied an area of (2.2 x 2.2) μm. The pattern of the left

handed quadrics of G letter like shapes consists of four features rotated anti-clock wise by 90^{o} starting from left, towards underneath, then right and above (Figure shown in nanofabrication chapter). This pattern is also a 2D array of quadric units that repeated each 2.4 μm. Again, the quadric unit itself consists of four features with G letter like shapes, each one was sized in 1μ and separated by 0.2 μm from sides; and therefore each unit occupied an area of (2.2 x 2.2) μm. For sample imaging, SEM Hitachi S4700 has been used; taking in account all considerations that are detailed in chapter 2.

6.4. Results and discussion

In this section a number of SEM images will be presented to show: the track of the laser beam spot on the surface of the nanostructures, the dependency of this track on the polarisation and the orientation of the incident beam, the selected areas for carrying out investigation and how these areas were affected gradually (anticipated from Gaussian beam spot), also, how results are in good agreements with theoretical models, how the hot-spot mapping looks like in case of using linearly and/or circularly polarised laser beam, and finally, how results are in good agreements with results from other literatures.

6.4.1. The damage morphology (or The beam spot track (BST))

As it is mentioned above, the locations of plasmonic hot spots were indicated from the physically damaged (melted) regions on the surface of the nanostructures, which they are considered to be tracks with specific morphology containing important information about the intensity distribution across the beam spot. We referred to this track as the ` Beam Spot Track` or BST for short. From various BST configurations, it is possible to determine the range (how far) of the affected area which leads to the determination of the range of the affected nanostructures. This is necessary to be presented here to show that we have only considered areas that showed gradual and/or consistent effects (this is explained later). Via SEM images, it has been found that the morphology of the

BST varies depending on the power of the laser beam (see Figure 4) in addition to the polarization state (i.e. linear or circular) of the laser beam (compare Figure 4 with Figure 5). However, the morphology of the BST alone was insufficient to show the exact orientation of the polarised light (see Figure 5), an observation which agrees with findings of reference [24]. In Figure 4, SEM images of the BST originating from irradiation with vertically polarised femtosecond laser light are shown. In a, three blocks (A, B and C) were irradiated with laser pulses at different powers. The laser power was increased from A towards B then C. Note the BST observed on the block with the lowest power (i.e. A) (its magnified image is shown in e) was distributed with expansions into two orthogonal directions, along the horizontal direction and along the vertical direction, with the former being much more intense than the latter. As the power was increased in B (its magnified image is shown in d); the contrast of the BST between the horizontal and the vertical directions became clearer; which simply indicates higher intensity in the horizontal direction than the vertical one. In C (its magnified image shown in c), only the horizontal direction is observed, with regular fading across the horizontal opposite sides; emphasised by the violet rectangle; which shows the area between C and B (its magnification image is shown in b). In Figure 5, SEM images of the BST originating from irradiation with circularly polarised femtosecond laser pulses are shown. In **a,** four blocks (A, B, C and D) have been irradiated with either right- or left-handed circularly polarised light (direction is indicated by the text next to the corresponding block). **b** and **c** are magnified images of the C and D blocks, respectively. Having these two images with opposite contrasts does not mean that they have been irradiated with two differently orientated polarised beams. This was indicated by the two images shown in d and e, which are magnifications of b and c, respectively. Clearly, with colour modes the opposite contrasts disappeared. From the literature, BST is an effect of the so called `Ultrafast phase transformation`, which is associated with laser material processing [10]. Over the past few decades, ultrafast laser pulses have become increasingly important in the processing of the various materials. When strongly absorbing materials are treated with extremely short laser pulses that are sufficiently intense enough to produce extremely steep temperature gradients, phase transitions including melting and evaporation processes can occur. Extremely fast heating with extremely fast cooling leads to effective heating conduction

that enormously broadens the applications for ultrafast phase transformations [10]. However, ultrafast phase transformation is a very wide field that is beyond the scope of this chapter.

As has already been mentioned, only areas which showed gradual or consistent effects were considered, in Figure 6, SEM images are presented of the BST edges created by irradiation with polarised (circularly or linearly) light from the femtosecond pulsed laser. In **a**, the area very close to the centre of the BST is shown in which the majority of the features are damaged. This level of damage, close to the centre of the spot, was seen within all the samples used. In **b** and **c,** the selected areas are a few microns away from the centre of the BST wherein less affected (in **b**) and unaffected (in **c**) features could be seen. Apparently, regions containing the less affected features were used for analysis, as they show what may be referred to as a `gradual effect` rather than a full or zero effect. The gradual effect is a view of moderately affected areas, wherein each represents a specific level of effectiveness. Deep examination for several samples has shown that each level may expands over an area of (100 – 25) μm^2. To make this effect clear, Figure 7 contains three SEM images showing the gradual effect over racemic mixtures of gammadions upon irradiation with linearly polarised light. In **a,** the effect is much bigger than in **b,** which in turn is much bigger than the effect observed in **c**. Further evidence of this effect could be seen in Figure 8. This is a single SEM image illustrates the gradual effect upon irradiation with circularly polarised light, with intensity range decreasing from left to right. Having the gradual effect to be consistent over tens of microns, for each level, means that something regular had happened and not random or accidental. In Figure 9 we present three SEM images that demonstrating a consistent effect across three different magnifications for a single level of effectiveness; which ranged between (10 ~ 100) μ^2.

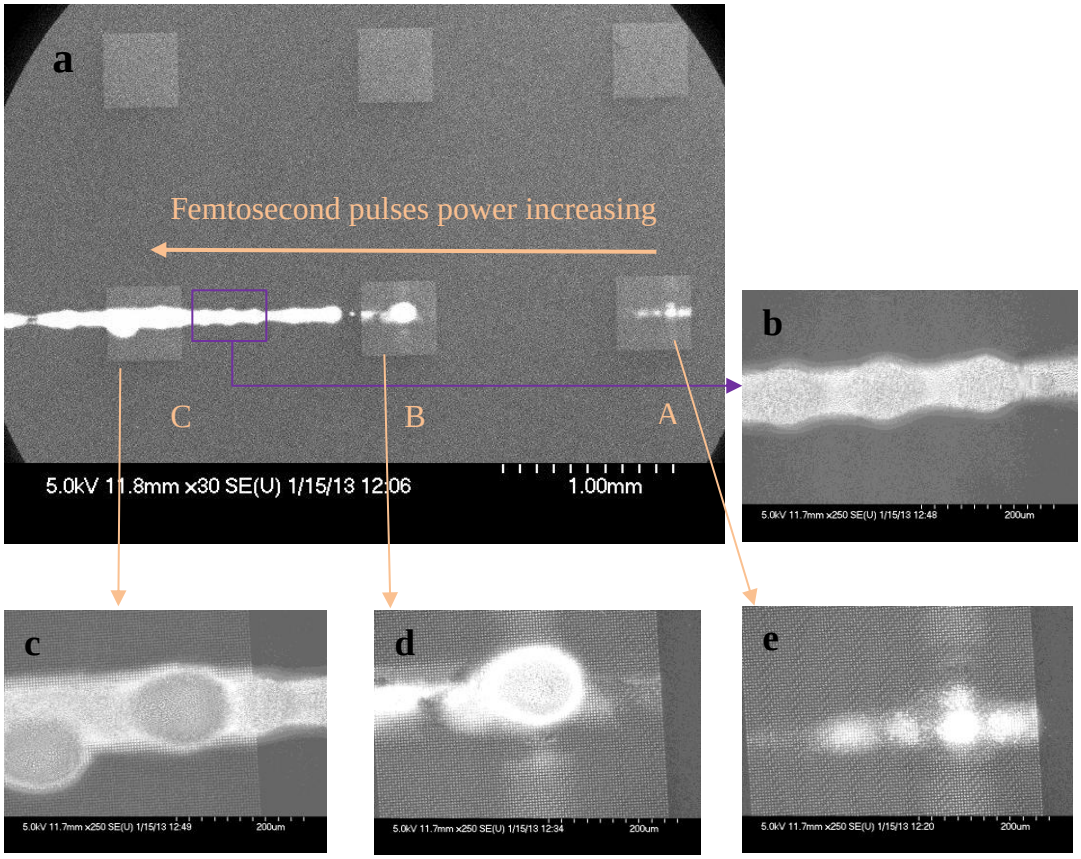

Figure 4: SEM images for the BST originated upon few seconds irradiation with 30mW vertically polarised femtosecond laser beam. In **a** three blocks these are: A, B and C have been irradiated with femtosecond laser beam have three different powers. The laser power was increased from A towards B then C. Note the BST observed on the block with the lowest power (i.e. A) was distributed with expansions in four orthogonal directions; two along the opposite sides of the horizontal directions and two along the opposite sides of the vertical directions; with the former much intense than the later. As the power was increased in B the contrast of the BST between the horizontal and the vertical directions turn out to be clearer; which simply indicates higher intensity in the horizontal directions than the vertical one. In C only the horizontal one observed; with regular vanishing across the horizontal opposite sides; emphasised by the violet rectangle; which showed the area between C and B. **b** is the magnification image of the area between C and B blocks. **c, d** and **e** are the magnification images of the BST in blocks C, B and A, respectively.

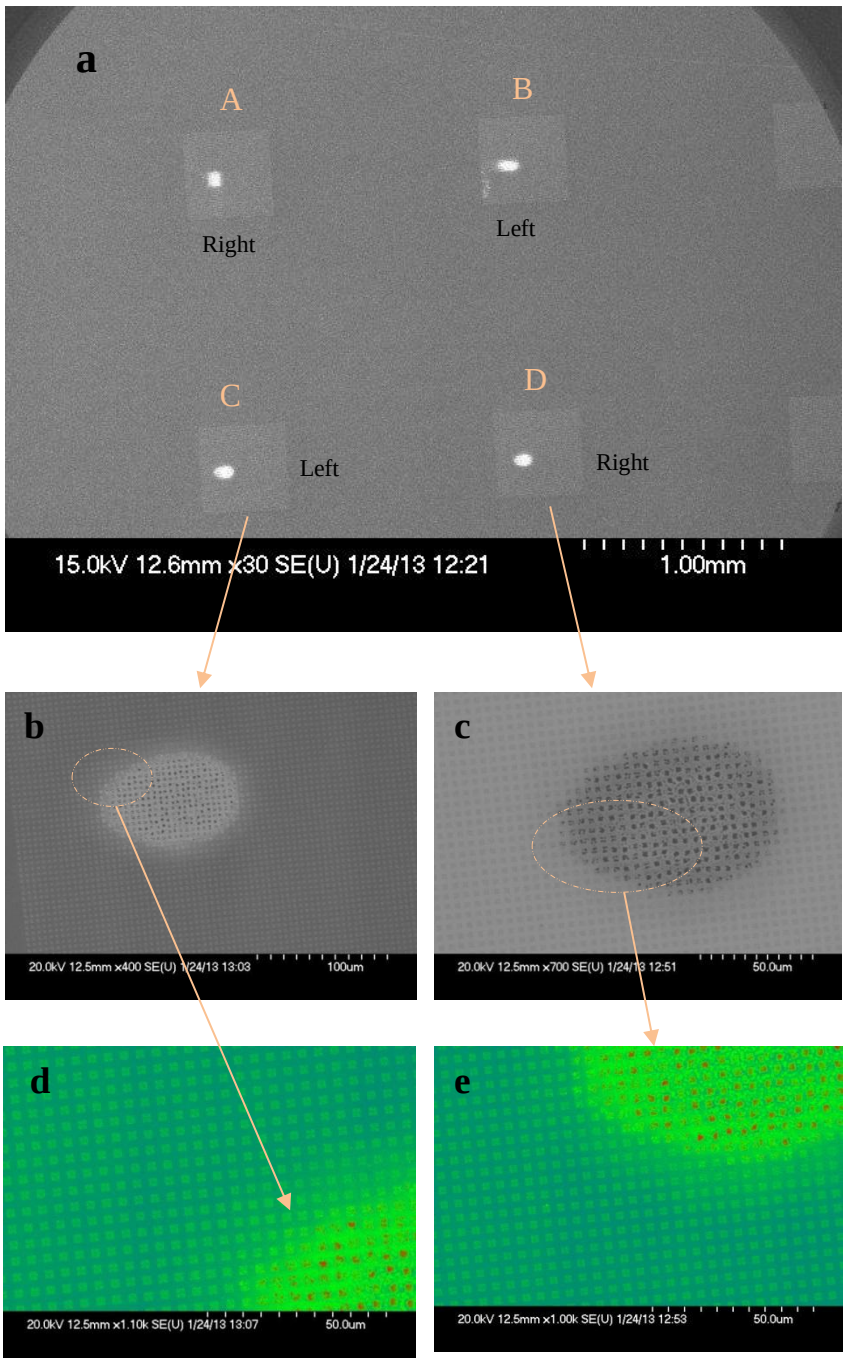

Figure 5: SEM images of the BST originated upon the irradiation with 30mW focused circularly polarised femtosecond laser beam for few seconds. In **a** four blocks these are: A, B, C and D have been irradiated with either Right or Left handed circularly polarised beam (indicated by the words `Right` or `Left` written next to the corresponding block). **b** and **c** represent the magnification images of the C and D blocks, respectively. **d** and **e**, represent the magnification images of **b** and **c**, respectively. Note with colour modes the opposite contrasts disappeared.

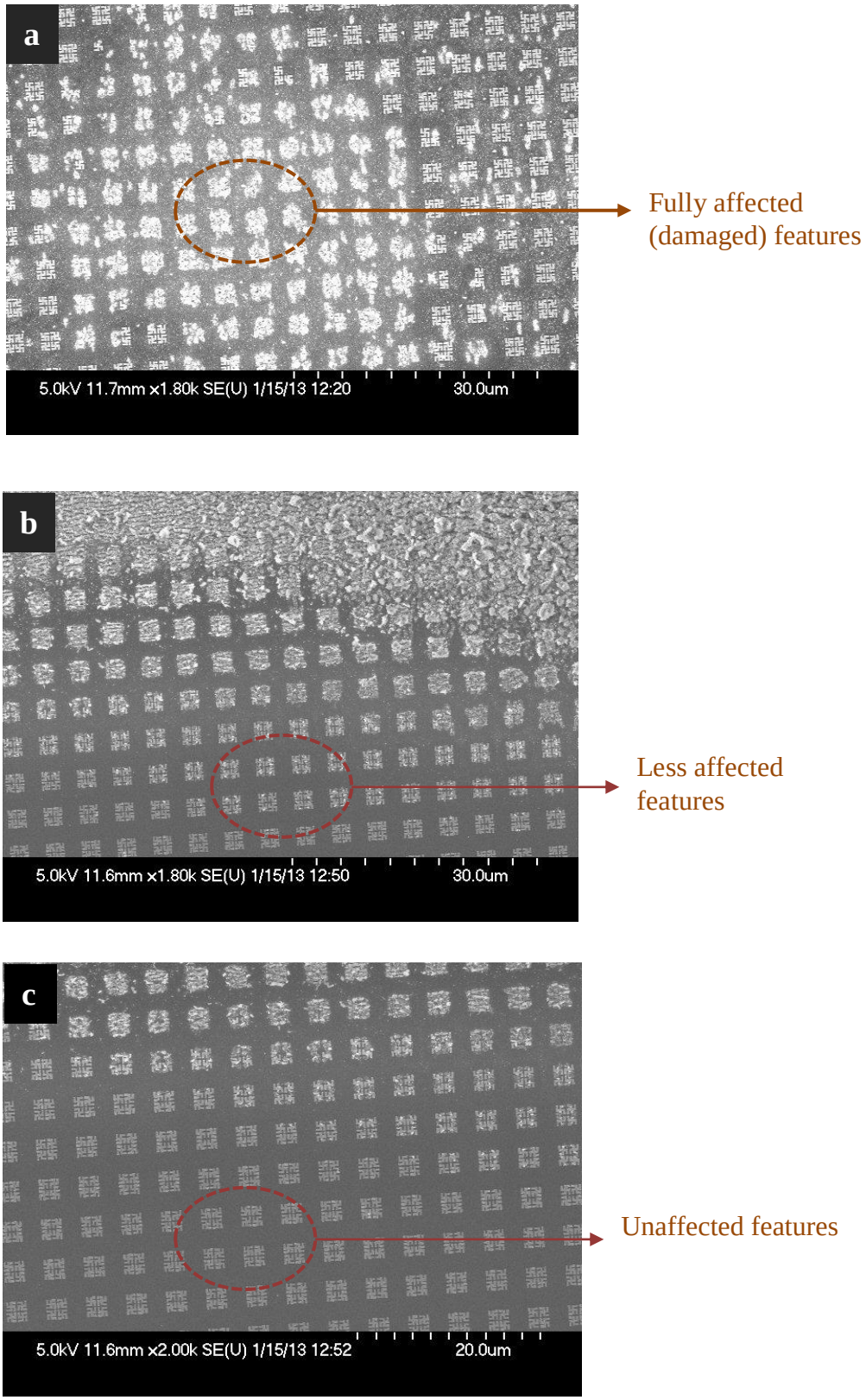

Figure 6: Three SEM images illustrate three different affected areas, which have been irradiated with 30mW femtosecond laser beam for few seconds. **a** fully affected area, **b** less affected area and **c** unaffected area.

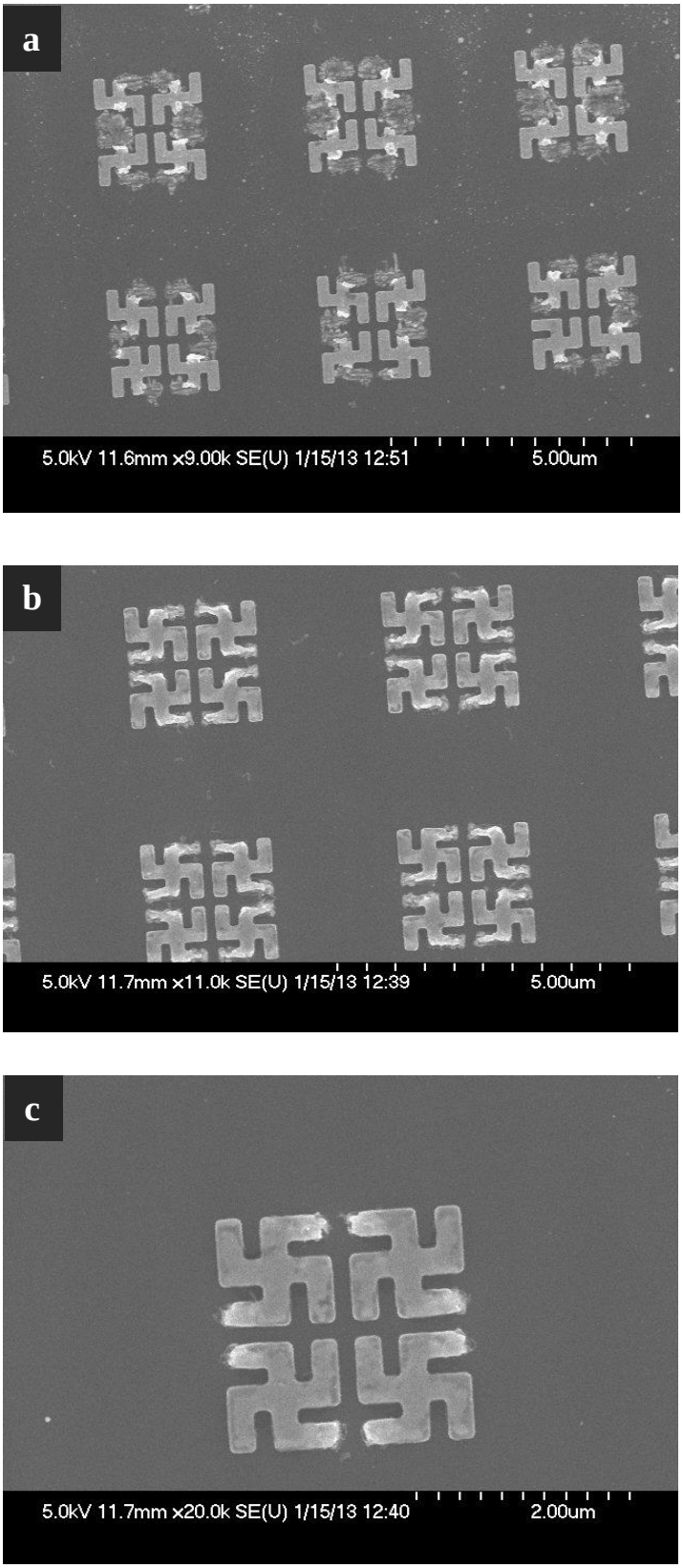

Figure 7: SEM images for the gammadions indicating the graduated effect upon irradiation with linearly polarised femtosecond laser beam. Laser power decreases from **a** to **c**.

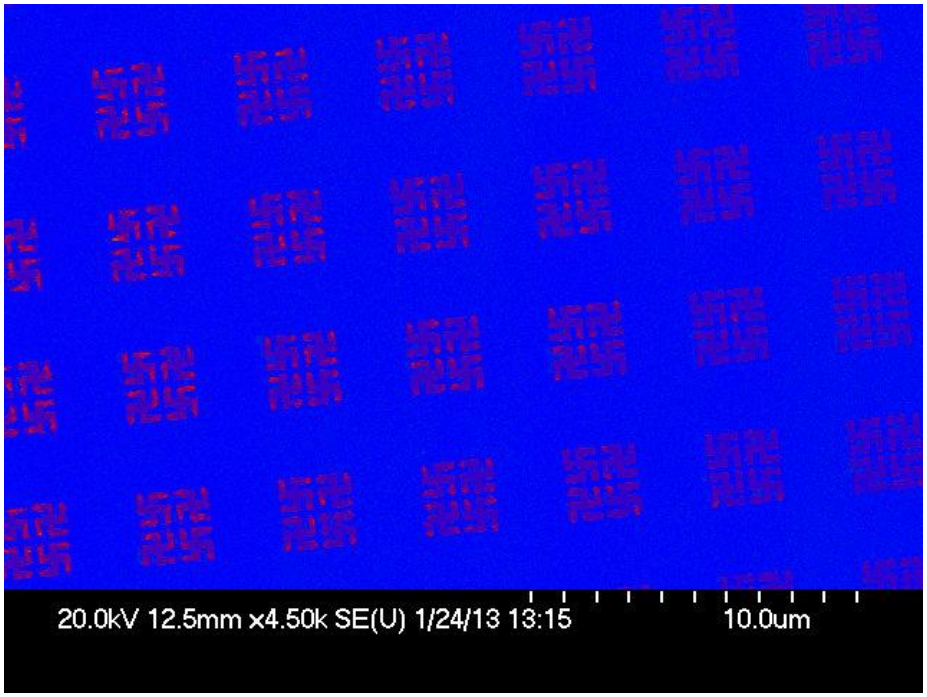

Figure 8: SEM images for the gammadions indicating the graduated effect upon irradiation with focused circularly polarised femtosecond laser beam. Laser power decreases from left to right**.**

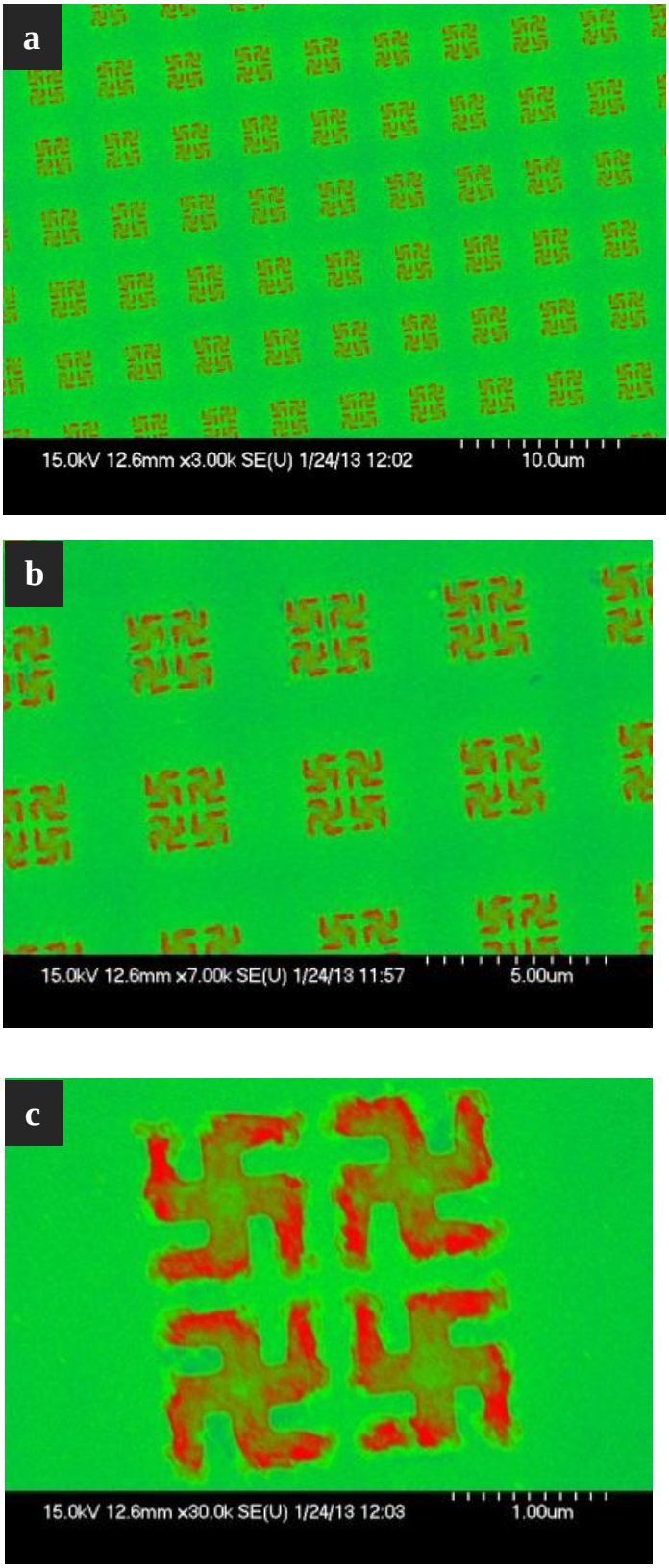

Figure 9: SEM images demonstrate the consistent effect across three different magnifications (**a**, **b** and **c**) for a single level of effectiveness. Note the consistency ranged from (10 – 100) μ^2.

6.4.2. Results are in good agreements with theoretical models

SEM images have shown that hot-spot mapping on the surface of the gammadion shapes and that hot-spot mapping on the surface of the G shapes are in good agreement with theoretical simulations shown in Figure 2 and Figure3. In Figure 10a, SEM image is presented for the gammadion shapes which show hot-spot mapping similar to that shown in Figure 2(a-f) above. In Figure 10b, SEM image is presented for the G like shapes which show hot-spot mapping similar to that are shown by Figure 3 (a, b). According to these Figures one would conclude that hot-spot appear on the surfaces of the nanostructures, rather than the surface of the substrate, indicating the existence of near fields on the edges of these nanostructures which, as theoretically shown, could be electric fields or chiral fields.

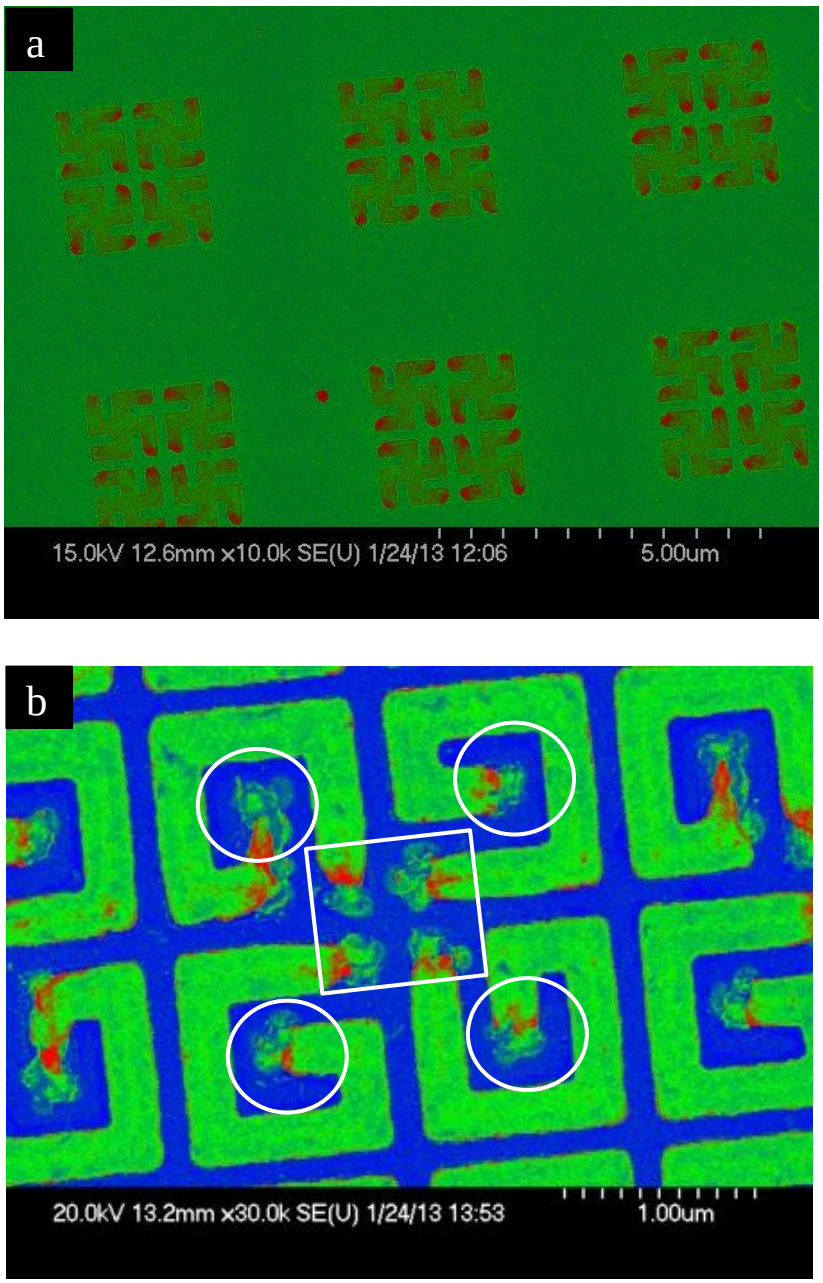

Figure 10: Hot-spot mapping on the surface of the gammadion shapes and G like shapes. **a** illustrates hot-spot mapping on the surface of the gammadion shapes. Note how this hot spots mapping is in good agreement with theoretical simulations shown in Figure 2 (a-f) above. **b** illustrates hot-spot mapping on the surface of the G like shapes (emphasised with four white circles and single white square. Note how this hot-spot mapping is in good agreement with theoretical simulations that are shown in Figure 3(a, b) above.

6.4.3. Hot-spot mapping by using linearly polarised laser beam

Irradiation with linearly polarised light leads to damage on the edges of the segments that are perpendicular to the direction of the light polarisation. Thus, irradiation with vertically polarised light has damaged the horizontal segments of the gammadions regardless of the sense (handedness) of the individual features; this is shown in Figure 11. In this Figure, SEM image for the racemic gammadions after it has been irradiated with vertically polarised femtosecond laser beam (indicated with red arrow) is presented. Hot-spot appearance on the horizontal rather than the vertical segments is because as the electric wave vector is oscillating parallel to the surface normal (since it is vertically polarised) it drives the plasmonic electrons on the surface of the horizontal edges in similar manner that is shown in Figure 1a above, and hence, influences positive and negative charges by way of theoretical simulations for the charge distribution (shown in Figure 1b) suggests, to eventually, triggers electric currents that melt up this particular area via Ohmic losses high temperature by way of another theoretical simulations for the electric currents formation (shown in Figure 1 c) suggests. This finding is in line with previously published work [6, 14] in which left- and right-handed quadrics of G-like shapes, made out of nickel and gold were used.

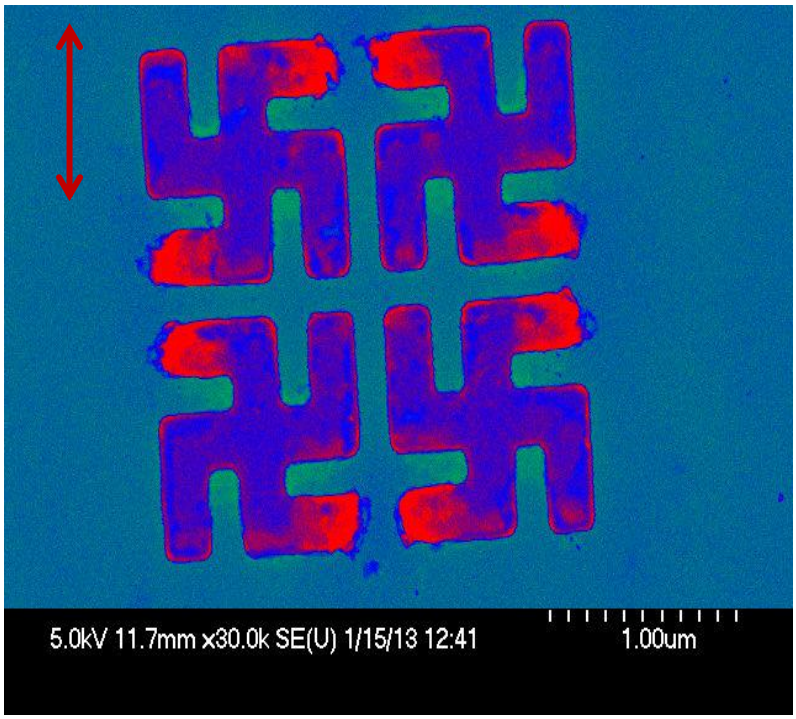

Figure 11: SEM images for the racemic gammadions after it has been irradiated with vertically polarised femtosecond laser beam (indicated with red arrow). Note the hot spots appearance on the horizontal rather than the vertical segments indicating a good agreement with reference [6, 14].

6.4.4. Hot spot mapping by using circularly polarised laser beam

Irradiation with circularly polarised light leads to damage of the horizontal and vertical segments of the gammadions regardless of the sense (handedness) of the individual features or the direction of the CPL incident light; this is shown in Figure 12. In this Figure, SEM images for the racemic gammadions after they have been irradiated with left and right circularly polarised femtosecond laser beam (indicated with red oriented circles) are presented. Equal hot-spot appearance on the horizontal and the vertical segments could be attributed to the equal amounts of the horizontally and the vertically polarised incident light, which represent the two components of the circular polarised light. Similarly to the illustration that is presented in section 4.2.above, hot-spot appearance on the horizontal and the vertical segments is because as the electric wave vector is oscillating parallel and perpendicularly to the surface normal (since it vertically and horizontally polarised) it drives the plasmonic electrons on the surface of the horizontal and the vertical edges in similar manner that is shown

in Figure 1a above, and hence, induces positive and negative charges at these edges. In Figure 1b, theoretical simulation for the charge distribution is shown illustrating bespoke positive and negative charges induction. This eventually triggers electric currents that melt up these particular areas via Ohmic losses high temperature in similar manner of another theoretical simulations for the electric currents formation (shown in Figure 1 c) suggests.

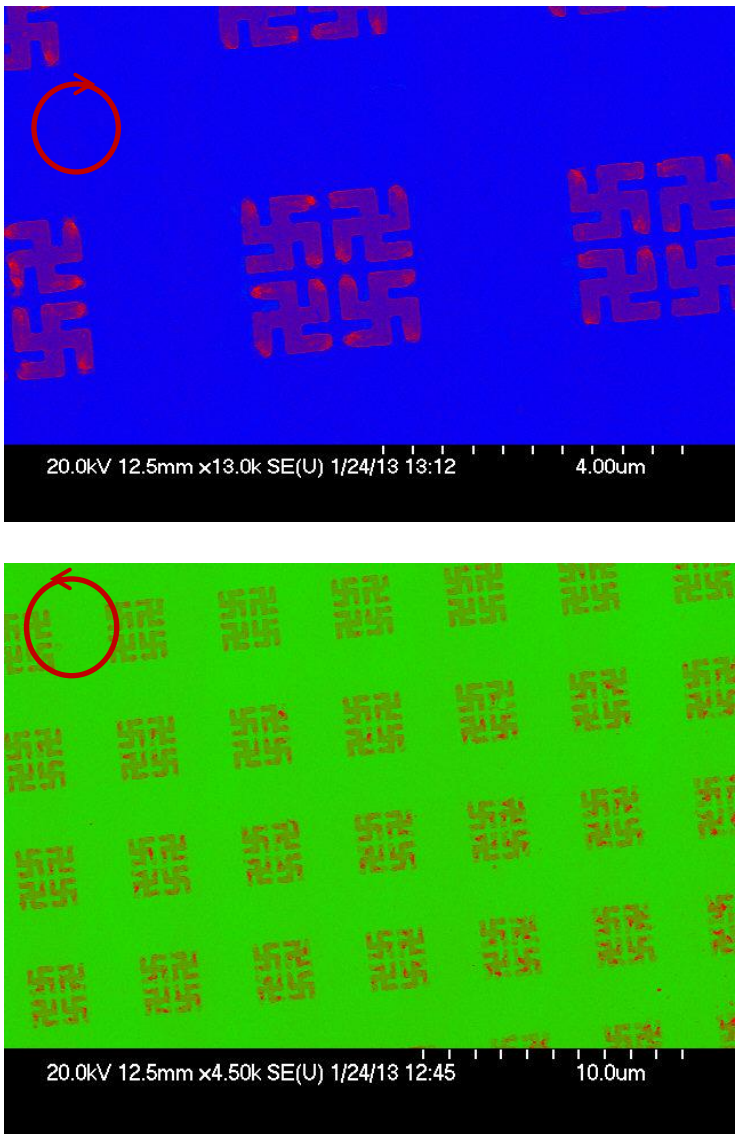

Figure 12: SEM images for the racemic gammadions after they have been irradiated with left and right circularly polarised femtosecond laser beam (indicated with red oriented circles). Note the hot spots appearance on the horizontal and the vertical segments regardless the orientation of the incident beam.

6.4.5. Comparison of results to the literature

Irradiation with circularly polarised light leads to damage at the edges of the G-like shapes, closely matching the locations of hot spots detected by SHG microscopy for similar units also irradiated with circularly polarised incident light [25], shown in Figure13. In this Figure, SEM and SHG microscope images are presented. In a, SEM image for the G quadric units after they have been irradiated with right circularly polarised femtosecond laser beam (sense indicated with red oriented circle) is shown. In b, SHG microscope image (taken from reference [25]) for a similar unit is shown. Hot-spot appearance on the centre of the unit cell, as well as on the non-centred horizontal and vertical segments for individual features, indicates chiral coupling occurrence in the centre of the unit cell; which appears to be similar behaviour that was suggested by Valev group [6, 25]. An important issue to be pointed out here is the different resolution of hot-spot mapping via SEM and SHG images. Clearly, hot spots that are imaged via SEM microscope (shown in a) have much higher resolution than hot spots that are imaged via SHG microscope (shown in b). This is one of the advantages of hot spot mapping via imprinting over hot spot mapping via SHG microscopy, a view we shared with Valev group [7].

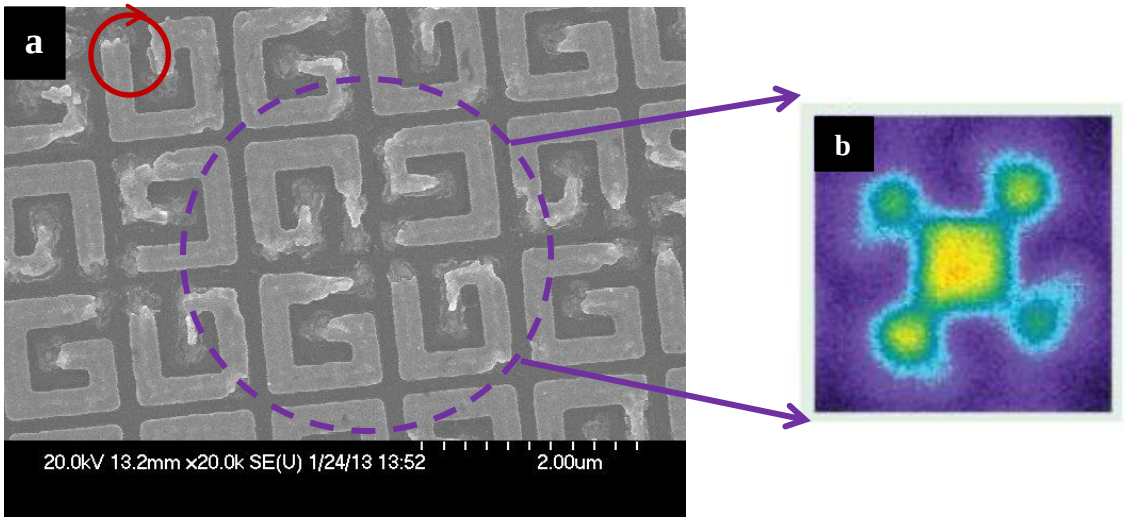

Figure 13: a SEM image for the G quadric units after they have been irradiated with right circularly polarised femtosecond laser beam (indicated with red oriented circle). **b** SHG microscope image, from reference [25], for similar unit cell shown in **a**. Note the hot spots appearance on the centre of the unit cell in addition to the non-centred horizontal and vertical segments for individual feature. This observation could be attitude to the chiral coupling occurrence in the centre of the unit cell [6, 25].

6.5. Conclusion

In conclusion, our strategy for hot-spot mapping is capable of revealing important information regarding the optical and electronic properties of plasmonic metamaterials. The findings presented in this chapter are in close agreement with those described by other research groups currently active in this area. Hot-spot mapping by using linearly polarised laser beam showed different results to the hot-spot mapping by using circularly polarised laser. Nevertheless, hot spots mapping agree with theory. No enantio-selectivity was observed. Despite of variety findings, they are in good agreement with literatures.

6.6. References

1. Steen W. M., "Laser Material Processing", *Springer*, 2003, 3rd eddition, pp(1-8), printed book.
2. Valev V. K., Zheng X., Biris C. G., Silhanek A. V., Volskiy V., De Clercq B., Aktsipetrov O. A., Ameloot M., Panoiu N. C., Vandenbosch G. A. E. and V. V. Moshchalkov, *OPTICAL MATERIALS EXPRESS*, 2011, Vol.1, pp (36-45).
3. Chen H., Shao L., Li Q. and Wang J., *The Royal Society of Chemistry*, 2013, Vol.42, pp (2679-2724).
4. Anceau C., *OPTICS LETTERS*, 2003, Vol. 28, pp (713-715).
5. Borys N. J., Waller M. J. and Lupton J. M., *Physical Review*, 2009, Vol.B80, pp (161407- (1-3)).
6. Valev V. K., *Langmuir, American Chemical Society*, 2012, Vol.28, pp (15454-15471).
7. Valev V. K., Baumberg J. J., Sibilia C. and Verbie T., *Advanced Materials*, **2013**, Vol.25, pp (2517-2534).
8. Diels J., Rudolph W., "Ultrashort laser pulse phenomena: fundamentals, techniques, and applications on a femtosecond time scale", *AP Elsevier*, 2006, 2nd eddition, pp (xvii-xxi), printed book.
9. Tonouchi M., *Nature Photonics*, 2007, Vol.1, pp (97 - 105).
10. Kaiser W., "Ultrashort Laser Pulses: Generation and Applications", *Springer-Verlag, Berlin*, 1993, printed book.
11. Rulliere C., "Femtosecond Laser Pulses / Principles and Experiments", *Springer Science + Bisness Media, LLC*, 2005, 2nd eddition, printed book..
12. Valev V. K., Silhanek A.V., Jeyaram Y., Denkova D., De Clercq B., Petkov V., Zheng X., Volskiy V., Gillijns W., Vandenbosch G. A. E., Aktsipetrov O. A., Ameloot M., Moshchalkov V.V. and Verbiest1 T., *American Physical Society*, 2011, Vol.106, pp (2268031-2268034).
13. Kao T. S., Jenkins S. D., Ruostekoski J. and Zheludev N. I., *American Physical Society*, 2011, Vol.106, pp (085501- 085504).
14. Valev V. K., Denkova D., Zheng X., Kuznetsov A. I., Reinhardt C., Chichkov B. N., Tsutsumanova G., Osley E. J., Petkov V., De Clercq B., Silhanek A. V., Jeyaram Y., Volskiy V., Warburton P. A., Vandenbosch G. A. E., Russev S., Aktsipetrov O. A., Ameloot M., Moshchalkov V.V. and Verbiest T., *Advanced Optical Materials*, 2012, Vol. 24, pp(29-35).
15. Kneipp K., Wang Y., Kneipp H., Perelman L. T., Itzkan I., Dasari R. R. and Feld M. S., *Physical Review Letter*, 1997, Vol.78, pp (1667-1670).
16. Nie S. and Emory S. R., *SCIENCE*, 1997, Vol. 275, pp(1102- 1106)
17. Nitzan A. and Brus L. E., *The Journal of Chemical Physics*, 1981, Vol.75, pp (2205- 2214).
18. Chen C. J. and Osgood R. M., *The American Physical Society*, 1983, Vol.50, pp (1705- 1709).

19. Chen T., Wang H., Chen G., Wang Y., Feng Y., Teo W., Wu T. and Chen H., *American Chemical Society Nano*, 2010, Vol. 4, pp (3087-3094).
20. Dostert K., lvarez M. A., Koynov K., Campo A., Butt H. and Kreiter M., *Lamgmuir*, 2012, Vol.28, pp (3699−3703).
21. Valev V. K., De Clercq B., Biris C. G., Zheng X., Vandendriessche S., Hojeij M., Denkova D., Jeyaram Y., Panoiu N. C., Ekinci Y., Silhanek A. V., Volskiy V., Vandenbosch G. A. E., Ameloot M., Moshchalkov V. V. and Verbiest T., *Advanced Optical Materials*, 2012, Vol. 24, pp (208-215).
22. Hendry E., Carpy T., Johnston J., Popland M., Mikhaylovskiy R. V., Lapthorn A. J., Kelly S. M., Barron L. D., Gadegaard N. and Kadodwala M., *Nature Nanotechnology*, 2010, Vol.5, pp (783-787).
23. Dickreuter S., Gleixner J., Kolloch A., Boneberg J., Scheer E. and Leiderer P., *Beilstein Journal of Nanotechno,* 2013, Vol.4, pp (588- 602).
24. Ma B., Zhang Y., Ma H., Jiao H., Cheng X, and Wang Z., *APPLIED OPTICS*, 2014, Vol.53, pp (A96-A102).
25. Lekner J., *JOURNAL OF OPTICS A: PURE AND APPLIED OPTICS*, 2003, Vol.5, pp (6-14).

Chapter 7: Conclusion and Future work

As the work in this thesis has hopefully demonstrated clearly, light can be manipulated to gain insight into the potential of optically active plasmonic nanostructures surfaces, and in particular how such plasmonic nanostructures might be employed in biosensing technologies. Recent advances in nanotechnology have played a key role in this thesis, especially regarding nanofabrication by electron beam lithography. Via EBL it is possible to create effective nanoelectronic biosensing platforms made out of various materials, such as gold.

The work described in this thesis has included the 3D structural characterisations for biomolecules at the picogram level. It was also possible to distinguish between proteins with mainly α–helical or β-sheet secondary structures, and between two proteins that differ at the quaternary structure level. In addition, it was also possible to sense different stages of α-synuclien fibril growth.

Also, it has been demonstrated that chirality could be induced on achiral plasmonic nanostructures surfaces via electromagnetic field coupling arising via a far field radiative system. This is true with a system consisting of chromospheres and plasmonic surfaces that strongly absorb UV and visible light, respectively. Our investigations for such systems of chirality induction were based on theoretical models which consisted of plasmonic objects embedded into chiral shells, theorised by Gorovov et al. . Prior to this work, the far field radiative coupling had not been considered before. As such, this part of the thesis provides experimental evidences for far field radiative coupling for the first time; and has resulted in a publication arising directly from this work [1].

The work on nonlinear optically active SHG spectroscopy (performed at off-resonance conditions) revealed that chiral molecules and chiral plasmonic nanostructures share similar excited states when they interact with light, namely via electric dipolar excitation. This is an important finding since it demonstrates how the novel chiral plasmonic nanostructures could be used to rationalise the non-linear optical properties of chiral metamaterials without considering multipolar excitation; which is anticipated to highly affect

measurements with large contributions, and hence this finding could significantly simplify future experimental measurements on similar systems. Once again, this new experimental evidence resulted in a new publication [2].

Moreover, this work has demonstrated high resolution 3D imaging of plasmonically active areas i.e. hot spots on plasmonic nanostructures surfaces. Hot spots imaging is important for a number of reasons including, but not limited to, improving applications associated with Raman scattering, catalytic reactions, chemical transformations, photochemical reactions etc.

For the future, the work described in this thesis anticipates the possibility to expand spectroscopic investigations towards yet more biological species like sugars, proteins, DNA, collagen, fibrils, fibrils aggregations and viruses. Further, the flexibility of nanofabrication work offers unlimited designs and patterns that could be used to characterise and hence exploit more types of plasmonic surfaces of potential use in a vast array of applications across many scientific disciplines.

Appendix A : List of Tables

List of Tables in chapter 2

List of Tables in chapter 3

List of Tables in chapter 5

Appendix B: List of Figures

List of Figures of chapter 1

List of Figures of chapter 2

List of Figures of chapter 3

List of Figures of chapter 4

List of Figures of chapter 5

List of Figures of chapter 6

Appendix B